Development of highly efficient electrocatalysts for fresh and seawater electrolysis under high current density

by

Nutthaphak Kitiphatpiboon

Graduate School of Science and Technology

Hirosaki University

2023

ABSTRACT

Hydrogen production via electrochemical water splitting is a clean and secure technology. Water electrolysis consists of two main reactions, i.e., Hydrogen Evolution Reaction (HER) and Oxygen Evolution Reaction (OER). However, the sluggish OER kinetics and high-cost of commercial nobel metal based catalysts such as Pt and RuO_2 based ones limit the practical application of this technology. Especially, to meet the practical industrial-scale requirements, the electrocatalysts should be operated at a high current density to achieve a high hydrogen production rate under long-term operation. Besides, using seawater directly to replace freshwater for the hydrogen production is attracting more and more attention for sustainable energy development because seawater is abundant. However, utilizing seawater based electrolyte remains great challenge due to the existence of competitive reactions between chlorine evolution reaction (ClER) and OER at the anode in the presence of Cl^- in the seawater, which always results in catalyst degradation and serious electrode erosion. In this dissertation study, the objective is to develop highly efficient electrode for water splitting with minimized operation cost, especially at a high current density even in a natural seawater based solution.

Firstly, $CuVO_x$ nanobelt@NiO nanosheet is successfully synthesized using a facile one-step hydrothermal process combined with a calcination method. The obtained $CuVO_x$@NiO composite electrode exhibits remarkable HER activity in alkaline freshwater solution with an overpotential as low as 74 mV at 10 mA cm^{-2}, which also shows excellent stability and a fast kinetic reaction with a Tafel slope of 60.8 mVdec^{-1}. Moreover, it can maintain the potentials at difference constant current densities up to 300 mA cm^{-2}. Such a higher electrocatalytic performance could be attributed to the generation of real active (VO_x-Cu_2O) species during HER with increased O vacancies. Besides, lamellar NiO shell could also provides a large number of active sites and super-hydrophilic surface, which effectively facilitates the H_2O adsorption and decomposition to H_{ads} intermediates. It is found that the intrinsic reaction activity for the conversion of H_{ads} to H_2 could be improved by the VO_x-Cu_2O core with rich O vacancy defects. This pioneer work provides a novel catalyst structure and superb properties for the HER in the alkaline electrolyzer.

Secondly, *in-situ* growing of $FeNiS_x/NiFe(OH)_x$ on nickel form (NF) is successfully realized using a facile corrosion engineering followed by a fast and mild sulfurization process. The obtained electrode requires only a low overpotential of 270 mV at a high current density of 100 mA cm^{-2} in alkaline simulated seawater (1 M KOH + 0.5 M NaCl) and maintains mechanical stability at an industrial-level current density of 1 A cm^{-2} without catalyst corrosion. Density functional theory (DFT) calculations reveals that the $FeNiS_x/NiFe(OH)_x$ has high oxygen evolution reaction (OER) against chlorine evolution reaction (ClER) since S substitution on O site can effectively decrease the free energy gap between *OH to *O, making OER more efficient. For overall seawater electrolysis using it as the bifunctional electrocatalyst, the electrolyzer only requires a low cell voltage of 1.60 V at 10 mA cm^{-2} and can sustain stable at the industrial-level current density of 1 A/cm^2 with a cell voltage of 2.81 V for 100 h, achieving a high hydrogen productivity without the catalyst deterioration.

Lastly, a $MnCo_2O_4$ nanowire coated with NiFe-Layered Double Hydroxide (NiFe-LDH) layer ($MnCo_2O_4$@NiFe-LDH) composite electrocatalyst prepared by a simple two-step hydrothermal method is applied for the seawater electrolysis, which exhibits low overpotentials of 219 and 245 mV for OER at a high current density of 100 mA cm^{-2} in alkaline simulated and natural seawaters, respectively. It is found that the NiFe-LDH layer on the $MnCo_2O_4$ nanowire can serve as Cl^- protective layer to hinder the ClER and anode erosion and simultaneously improve the active surface area and intrinsic properties of $MnCo_2O_4$ nanowires, allowing for faster kinetics. While, the high valence states of Mn^{3+}, Co^{3+}, Ni^{3+} and Fe^{3+} play a crutial role for OER. In addition, when it is used as the bifunctional electrocatalyst for the overall natural seawater splitting, the $MnCo_2O_4$ @NiFe-LDH (-)||$MnCo_2O_4$ @NiFe-LDH(+) pair in a two-electrode cell only requires a low voltage of 1.56 V@10 mA cm^{-2} and simultaneously maintains excellent stability at a high current density of 100 mA cm^{-2} for over 100 h. Such an electrocatalyst could be a promising candidate for practical seawater splitting.

ACKNOWLEDGEMENTS

TABLE OF CONTENTS

LIST OF TABLES

LIST OF FIGURES

xii

CHAPTER 1 Introduction

A most promising energy carriy for a decarbonized global energy system is hydrogen. As reported by International Renewable Energy Agency, the hydrogen market will reach $ 155 billion by 2022, and the market share of water electrolysis for hydrogen production is expected to reach 22% by 2050 [1]. Especially, the hydrogen production via water electrolysis is a promising option in the environmental friendly way without green house gas emission. The reaction takes place in a unit called an electrolyzer. There are many types of electrolyzers categorized by charge carrier, operation temperature and electrolytes including alkaline electrolysis, polymer electrolyte membrane electrolysis (PEMWE) and solid oxide electrolysis (SOE) [2]. In this study, the electrochemical decomposition of water at a low temperature (below 100ºC) with an aqueous electrolyte is chosen due to its low operating cost and safety. Theoretically, water electrolysis involves two half-cell reactions, i.e., hydrogen evolution reaction (HER) at the cathode and oxygen evolution reaction (OER) at the anode , in which HER and OER have thermodynamic quilibrium potentials of 0 V and 1.23 V *vs.* RHE, respectively (Figure 1.1). Because water splitting is not a spontaneous reaction, the input voltage should be high enough to overcome the overpotentials of the HER/OER reactions in order to split water molecule into hydrogen and oxygen [3].

Precious metals (e.g., Ir, Ru) and their oxide compounds (e.g., IrO_2, and RuO_2) are currently used as the benchmark electrocatalysts on the anode side in water splitting. While, Pt based ones is widely used on the cathode side. However, their scarcity, high cost and poor durability from metal dissolution after long-term operation limit their large-scale applications [4, 5]. Therefore, non-precious metal-based catalysts with superior performance and low price are required.

The major obstacle of electrolyzer efficiency is the overvoltage or overpotential

for OER at the anode because of the sluggish kinetics caused by the 4-electron transfer step. Thus, it is more important to develop OER electrocatalysts. To date, only a few electrodes can meet the criteria for an industrial application, by which OER can work stably at an extremely high current density ($\geq$500 mA cm^{-2}) with a low overpotential ($\leq$ 300 mV) for a long-period [6]. Many electrocatalytic systems based on acidic, alkaline, and neutral freshwater electrolytes have been explored. Recently, utilizing the earth abundant seawater (96.5% water resouces on earth) to replace freshwater attracts more and more interests for promoting the sustainable energy development goals (SDGs). However, it is full of challenges relating to high energy cost and serious chlorine erosion in seawater environment. More than 3.5% of salts consisting of Na^+, Cl^-, Ca^{2+}, Mg^{2+}, and so on in the seawater, which could affect both HER and OER. In the alkaline condition, the formation of insoluble compounds can poison the electrocatalysts at both the cathode and anode, resulting in catalyst deterioration and deactivation, lowering electrocatalytic activity and stability [7].

The barrier for utilizing the natural seawater is that the aggressive Cl⁻ anions can lead to chlorine evolution reaction (ClER) with the formation of hypochlorite at an overpotential about 480 mV in an alkaline electrolyte. As such, the competitive reaction between OER and ClER always occur since ClER is more kinetically favorable via a two-electron transfer pathway [8, 9]. The competitive reaction between OER and ClER on the anode site can be suppressed by limitimg the OER overpotential lower than 480 mV under alkaline condition (pH >7.5) [10]. To date, long-term stability at an industrial current density of ~1 A cm^{-2} is still not applied in seawater splitting [9]. While, it is expected to have ideal bifunctional electrocatalysts with low-cost, highly activity, long-term durability for HER/OER and cost-effective preparation method for practical application [29].
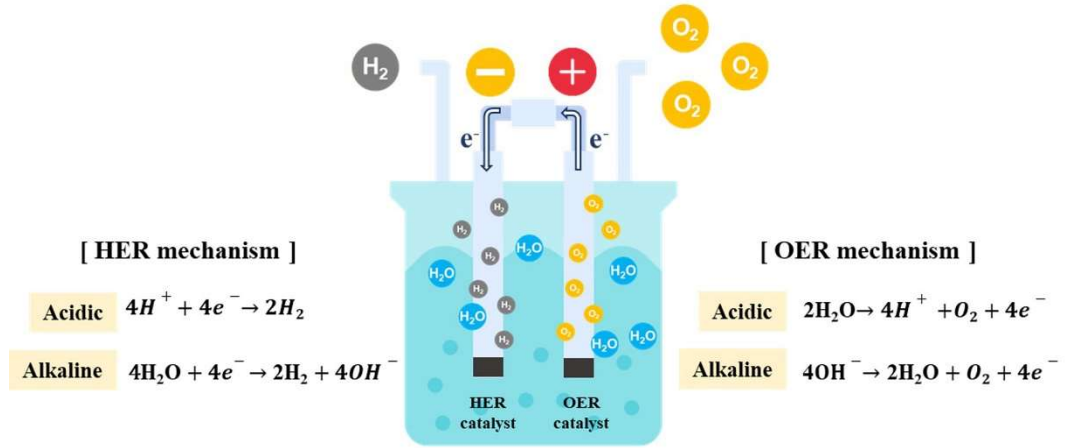
Figure 1.1 Schematic illustration of water electrolyzer with two half-reactions under acidic and alkaline conditions.

1.1 REACTION MECHANISM OF WATER ELECTROCATALYSIS

1.1.1 Theoretical of hydrogen evolution reaction (HER)

HER is kinetically favourable in acidic solution because of high proton concentration. In acidic solution, HER performance is related with hydrogen adsorption (H_{ad}), which follows Volmer/Heyrovsky or Volmer/Tafel steps as indicated below [11]

$$Volmer\ step: H^+ + e^- \rightarrow H_{ad} \qquad\qquad (Eq.1)$$

$$Heyrovsky: H^+ + e^- + H_{ad} \rightarrow H_2 \qquad\qquad (Eq.2)$$

$$Tafel\ step: 2H_{ad} \rightarrow H_2 \qquad\qquad (Eq.3)$$
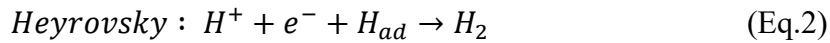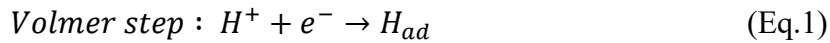
In the alkaline solution, The Volmer step refers to the reduction of water molecule on the catalyst surface to form adsorbed hydrogen atoms and hydroxide anion. Consequently, two possible mechanisms could occur : (i) Heyrovsky step, in which the adsorbed hydrogen (H_{ad}) atom from the volmer step is reacted with another water molecule, producing a H_2 molecule and a OH⁻ (Volmer-Heyrovsky) and (ii) Tafel step, in which two adsorbed hydrogen atoms from volmer step can be combined to generate

a H_2 molecule (Volmer-Tafel) as shown in the following equations [12, 13]:

$$Volmer\ step : H_2O + e^- \rightarrow H_{ad} + OH^- \qquad (Eq.4)$$

$$Heyrovsky : H_2O + H_{ad} + e^- \rightarrow H_2 + OH^- \qquad (Eq.5)$$

$$Tafel\ step : 2H_{ad} \rightarrow H_2 \qquad (Eq.6)$$
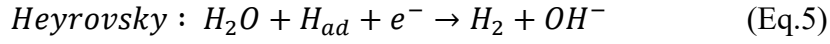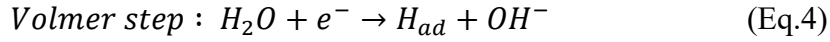
The whole reaction rate is mostly based on the the hydrogen adsorption free energy (ΔG_H). The adsorption (Volmer) step will hinder the whole reaction rate if the H_2 molecule weakly adsorbs on the surface of catalyst. On the other hand, the desorption via Heyrovsky or Tafel step will reduce the reaction rate if the hydrogen binding is so strong on the surface of catalyst. Therefore, the highly active HER catalyst should have $\Delta G_H \approx 0$ (but inadequate) with optimal binding energy between reaction intermediate and catalyst surface [14].

1.1.2 Theoretical of oxygen evolution reaction (OER)

A 4-proton-coupling electron transfer step is involved in OER, which is always the bottleneck for water splitting. There are two possibles mechansims for OER, including (i) adsorbate evolution mechanism (AEM) and (ii) lattice-oxygen-mediated mechanism (LOM) [15].

The conventional AEM has been proved by the Sabatier principle, that is, the oxygen adsorption energy on catalyst surface [16]. AEM is being considered to be involved in 4-electron transfer pathway on the active metal sites. For this mechanism, the H_2O molecule is first binded on the metal active sites with the generating of an adsorbed OH^* on the metal sites (*). Subsequently, *OH couples with proton with an electron removal process to generate *O intermediates. Following the formation of O-O bond, *O can combine with another H_2O molecule to generate *OOH, which will be finally,

oxidized, leading to the O₂ release and the regeneration of the initial Metal active sites as illustrated in the following equations:

$$H_2O + * \rightarrow *OH + H^+ + e^- \quad ; \Delta G_1 \qquad \text{(Eq.7)}$$

$$OH^* \rightarrow O^* + H^+ + e^- \quad ; \Delta G_2 \qquad \text{(Eq.8)}$$

$$O^* + H_2O \rightarrow OOH^* + H^+ + e^- \quad ; \Delta G_3 \qquad \text{(Eq.9)}$$

$$OOH^* \rightarrow * + O_2 + H^+ + e^- \quad ; \Delta G_4 \qquad \text{(Eq.10)}$$
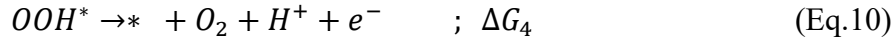
Where, the * denotes as a catalytic active sites on the catalyst surface while OOH^*, O^* and OH^* represent three adsorption intermediates. Theoretical OER potential is 1.23 V at the standard condition with the overall reaction Gibbs free energy (ΔG) of 4.92 eV. In the equilibrium state, however, from the above equations, each step should be related to a specific binding energy corresponding to the intermediates.The rate-determining step (RDS) is the step with the largest free energy gap (ΔG = max [$\Delta G_1, \Delta G_2, \Delta G_3, \Delta G_4$]), and the theoretical overpotential of the reaction can be calculated by $\eta_{OER} = \frac{\Delta G_{max}}{e} - 1.23V$ equation [17, 18].

Lattice-oxygen-mediated mechanism (LOM) is attributed to the dynamic catalyst surface, not only active sites at the metal centers but also lattice oxygen. The first two steps of LOM are similar to AEM by forming O^*. Then, O^* will interact with the lattice oxygen to generate a O₂ molecule, forming a lattice oxygen vacancy. Finally, the migration of OH^- from the solution can refill the oxygen vacancy. According to this mechanism, oxygen species in the lattice functions as the intermediate and thereby, there is no OOH^* to be formed in this pathway. Thus, the lattice oxygen evolved in OER plays a crutial role for boosting the OER activity. Theoretically, the $\Delta G^{OER} = 1.23\ eV$, however, there is a difference between theoretical and experimental values caused by inappropiate electrocatalyst O-bonding forces, which makes OER more sluggish. The RDS for OER can be investigated from the Tafel slope. The first reaction

is the rate-controlling step if Tafel slope is around 120 mV dec^{-1} (Eq. 7). At the same time, if the Tafel slope is approximately 40 mV dec^{-1}, the second reaction performs as a rate-determining step (Eq. 8) [19].

In acidic solution

Overall oxidation reaction under the standard condition (pressure = 1 bar and T = 298.15 K) in acidic solution ca be expressed as below ;

$$H_2O \rightarrow O_2 + 4H^+ + 4e^- \qquad ; \ \Delta G_0 = 4.92 \ eV \qquad \text{(Eq.11)}$$

where ΔG refers to Gibbs free energy. The reaction mechanism consists of 4 steps ;

$$H_2O + * \ \rightarrow * OH \ + H^+ + e^- \qquad ; \ \Delta G_1 \qquad \text{(Eq.12)}$$

$$OH^* \rightarrow O^* + H^+ + e^- \qquad ; \ \Delta G_2 \qquad \text{(Eq.13)}$$

$$O^* + H_2O \rightarrow OOH^* + H^+ + e^- \qquad ; \ \Delta G_3 \qquad \text{(Eq.14)}$$

$$OOH^* \rightarrow * \ + O_2 + H^+ + e^- \qquad ; \ \Delta G_4 \qquad \text{(Eq.15)}$$
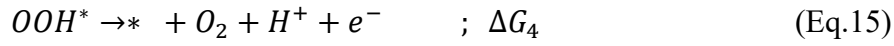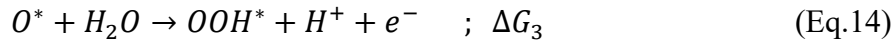
where the * denotes catalytic active sites on the catalyst surface, and OOH^*, O^* and OH^* represent adsorption intermediates.

In alkaline solution

Overall oxidation reaction under standard condition (pressure = 1 bar and T = 298.15 K) in alkaline solution can be given by [20]

$$4OH^- \rightarrow O_2 + 2H_2O + 4e^- \qquad \text{(Eq.16)}$$

In this case, the OER mechanism under alkaline condition can be described by 4 steps using the equations below [20]:

$$OH^- + * \ \rightarrow OH^* + e^- \qquad \text{(Eq.17)}$$

$$OH^* + OH^- \rightarrow O^* + H_2O + e^- \qquad \text{(Eq.18)}$$

$$O^* + OH^- \rightarrow OOH^* + e^- \qquad\qquad\qquad\qquad \text{(Eq.19)}$$

$$OOH^* + OH^- \rightarrow * \ + O_2 + H_2O + e^- \qquad\qquad \text{(Eq.20)}$$
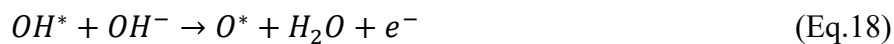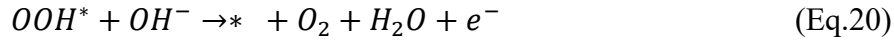
According, OER is more kinetically sluggish in a water electrolysis cell, and OER is always a crucial reaction in controlling the overall efficiency of overall water splitting [21].

1.1.3 Overall water splitting

To complete the overall water splitting reaction, electrocatalysts must perform well on both cathode and anode sides. The overall reaction can be described in the following equations[22]:

Overall reaction ;

$$H_2O \rightarrow H_2 + \frac{1}{2}O_2 \qquad\quad ; \ \Delta G^0 = +237.2 \ kJ/mol \qquad \text{(Eq.21)}$$

In acidic solution ;

HER (Cathode) : $\ 2H^+ + 2e^- \rightarrow H_2$ $\qquad\qquad\qquad\qquad$ (Eq.22)

OER (Anode): $\ H_2O + \frac{1}{2}O_2 \rightarrow 2H^+ + 2e^-$ $\qquad\qquad$ (Eq.23)

In alkaline solution ;

HER (Cathode) : $\ 2H_2O + 2e^- \rightarrow H_2 + 2OH^-$ $\qquad\qquad$ (Eq.24)

OER (Anode) : $\ 2OH^- \rightarrow \frac{1}{2}O_2 + H_2O + 2e^-$ $\qquad\quad$ (Eq.25)
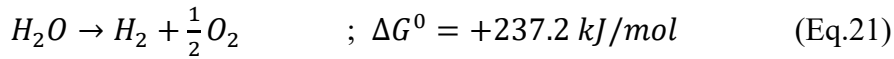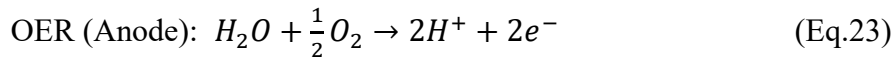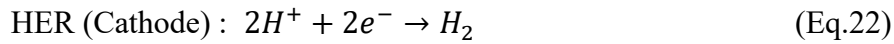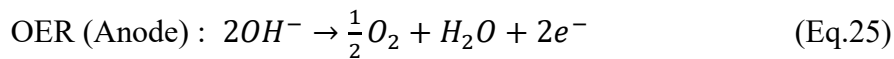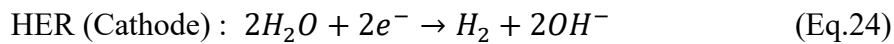
The thermodynamic equilibrium potential for the overall water splitting is 1.23 V under standard temperature and pressure (STP) conditions (T = 25°C and P = 1 atm) with 0 and 1.23 V *vs*. RHE for cathodic and anodic, respectively. Nevertheless, the practical cell voltage (V_{oc}) of water electrolysis is far from this theoretical potential. Thus, the overpotentials for cathode (η_c) and anode (η_a), and the extra potential to compensate for internal resistance loss (η_Ω) need to be considered as indicated in Eq. 26:

$$V_{oc} = 1.23 \text{ V} + |\eta_c| + \eta_a + \eta_{\Omega} \qquad \text{(Eq.26)}$$

1.1.4 Chlorine Evolution reaction (ClER)

In the seawater splitting, two-electron transfer reaction of ClER is more kinetically favorable than OER. Thus, directly using seawater remains challenge. Pourbaix diagram is commonly used to explain the thermodynamic behavior of chlorine species in various pH values [23], in which the thermodynamic gap in each pH value should be considered in order to avoid the occurring of ClER.

1.1.4.1 Seawater electrolysis at low pH value

The competitive reaction between OER and ClER at the anode side must be taken into account especially in the acidic solution (pH<3). In this case, the formation of chlorine is illustrated in Eq. (27). As shown in Figure 1.2, the overpotential gap between OER and ClER is less than 330 mV, and it is obvious that the chlorine is more easily generated in the electrolyte with a low pH.

1.1.4.2 Seawater electrolysis at neutral pH value

As shown in Figure 1.2, increasing the pH of the solution (3 < pH < 7.5) causes the formation of hypochlorous acid (Eq. (28)). However, because of the sluggish kinetics of water dissociation in neutral/near-neutral solutions, improving catalytic performance and OER selectivity at this pH range is more difficult.

1.1.4.3 Seawater electrolysis at high pH value

In alkaline solution, the thermodynamic gap between potentials required for OER and formation of ClO⁻ is about 480 mV for ClER, with a larger gap than the case with a lower pH value (Figure 1.2). In summary, the formation of HClO/ClO⁻ is commonly simplified as described below [24]:

(i) Chloride migration to the anode, where it is oxidized to gaseous chlorine

$$2Cl^-_{aq} \rightarrow Cl_{2(g)} + 2e^- \qquad \text{(Eq.27)}$$

(ii)   Chlorine hydrolysis results in the formation of hypochlorous acid (pH <3)

$$Cl_2 + H_2O \rightarrow HClO + H^+ + Cl^- \qquad \text{(Eq.28)}$$

(iii)   pH-dependent equilibrium between hypochlorous and hypochlorite ion (3 <pH<7.5)

$$HClO \rightarrow ClO^- + H^+ \qquad \text{(Eq.29)}$$

(iv)   Competive reaction between OER and ClER at the anode side in alkaline solution (7.5 <pH<14) ; [25]

$$Cl^- + 2OH^- = ClO^- + H_2O + 2e^- \; ; \; E^0 = 1.72V - 0.059 * pH \qquad \text{(Eq.30)}$$

$$4OH^- = 4e^- + 2H_2O + O_2 \; ; \; E^0 = 1.23V - 0.059 * pH \qquad \text{(Eq.31)}$$
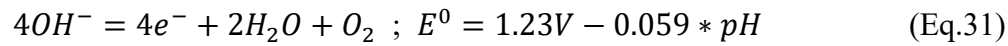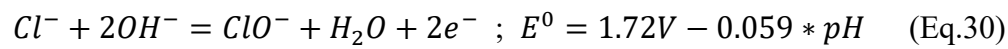
According to Eqs. (30) and (31), the potential difference between OER and ClER in the alkaline solution is ca. 480 mV at the pH range of 7.5-14. Hence, if OER overpotential is lower than 480 mV, ClER could be avoided. The ClER generation mechanisms in various pH values can be found in Table 1.1.
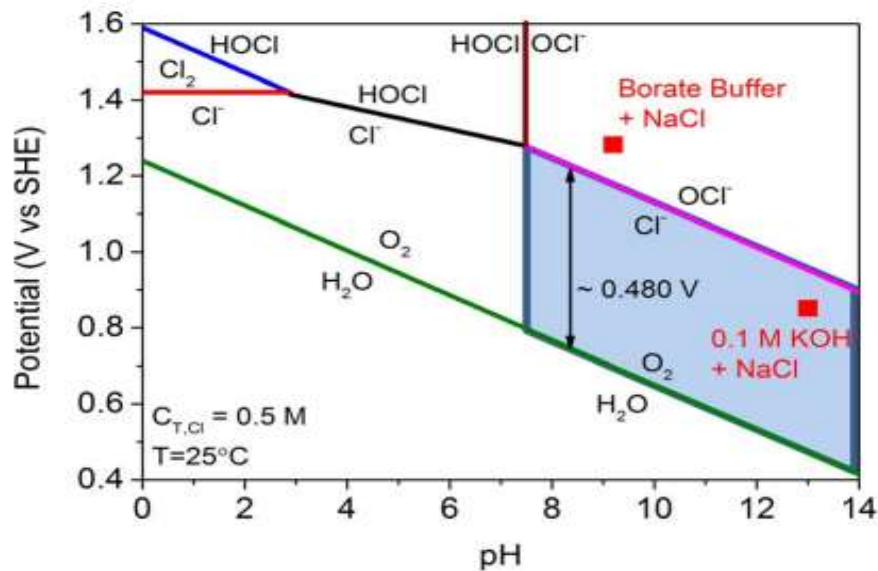
Figure 1.2 Computed Pourbaix diagram for artificial seawater model [9].

Table 1.1 Reaction mechanism in a different conditions[26].

Electrolyte	pH values	Half-cell reaction	E^0 (V)
Acid solution	pH < 3	$2Cl^- \rightarrow Cl_2 + 2e^-$	+1.36
Neutral solution	3 < pH<7.5	$Cl^- + H_2O \rightarrow HClO + H^+ + 2e^-$	+1.61
Alkaline solution	pH ~14	$Cl^- + 2OH^- \rightarrow ClO^- + H_2O + 2e^-$	+0.89

The presence of chloride ions in natural seawater have an effect on both anode and cathode. Chloride ions on the anode may hinder HER by adsorption on the catalyst active sites, promoting catalyst degradation. On the other hand, high OER selectivity need to be considered for designing the potential electrode for OER at the anode. As a result, developing highly efficient bifunctional electrocatalysts for seawater splitting remains challenging.

1.2 CATHODE MATERIAL DESIGN FOR HER

1.2.1 Transition metal oxides (TMOs) and Hydroxides (TMOHs)

Transition metal oxides have been applied for HER owing to their abundant crystal structures and excellent activity. For example, Gong *et al.* [27] mentioned that Ni@NiO/Cr$_2$O$_3$ had excellent HER activity and stability comparable to Pt based electrocatalysts since the chemically stable Cr$_2$O$_3$ can prevent oxidation and aggregation of Ni core, and maintain abundant NiO/Ni active sites for HER in alkaline solution. Lu *et al.* [28] reported that Mn-doped nickle oxide/Ni (Mn-NiO/Ni) heterostructure also had Pt-like performance with a low onset potential even in natural seawater (pH ~8.2). Wu *et al.* [29] demonstrated that incorporating Ru into CoO$_x$/NF can effectively improve catalytic activity at large current densities. This electrode required only 252 mV overpotential at a large current density of 1 A cm^{-2}, which is better than that of Pt/C (444 mV). Moreover, the catalytic activity remains constant for

100 h, indicating that it is a highly durable electrode [29]. Jiang *et al.* [30] prepared NiFe-LDH/FeOOH on nickel foam substrate via an electrodeposition process, which showed a low overpontential of 181.9 mV @10 mA cm^{-2} for HER in 1 M KOH + 0.5 M NaCl solution. The results proved that the formation of NiOOH species during reaction and strong interaction between FeOOH and NiFe-LDH are able to improve catalytic activity.

1.2.2 Transition metal alloys (TMAs)

Precious metals and their alloys like Pt and Pd alloys have been studied for HER in alkaline solution due to excellent catalytic activity and electrical conductivity. However, high cost limits their large-scale application. As such, cost reduction through the the modification of nobel metals with transition metal alloys is widely considered. According to Brewer-Engel theory, d-orbital atoms in a half- or full-space state should be more beneficial for the adsorption of H atom, and electrons are able to activate H_2O molecule via the d orbitals so that the O-H bond is broken. Thus, alloying of Pt with various transition metals could vary the performance of HER [31, 32]. As indicated above, the HER activity in seawater splitting is extremely challenging since its intrinsic corrosive nature [28]. Thus, many strategies have been studied for improving the electrocatalytic activity and stability in seawater solution. For example, It was discovered that altering the nobel metal catalyst electronic structure by doping foreign atoms like Ni, Fe, Mo, Co, Cr and so on could mitigate the influence of Cl_2 on Pt performace effectively with the enhanced stability While, it can also facilitate the charge transfer process and effectively enhance the activity, particularly in seawater solution [33]. Zheng *et al.* [34] reported that Ti supported PtPd alloy electrode exhibited an onset potential of 52 mV with an excellent efficiency for HER because the alloying of Ni with Pt has a potential to tune electronical structure and change the transfer of

charge while more active sites could be exposed on the nanostructure, thereby improving HER performance. While, the Ti/PtMo electrode showed a low overpotential of 254.6 mV to achieve 10 mA cm^{-2} in seawater solution. Moreover, it is found that the the competitive dissolution reaction between Mo and Pt in seawater that produces Cl_2 is advantageous for increasing the durability of PtM alloy electrodes. As such, the optimized PtMo alloy catalyst maintained the initial current density about 91.13% over 172 h in seawater. Besides, $PtNi_5$ electrode was used to catalyze the HER reaction in seawater solution, which displayed the most excellent performance with a minimum starting potential of 380 mV and maintained stable for more than 12 h [35]. Ros *et al.* [36] proposed an electrocatalyst of Ni-Mo-Fe trimetallic coated on graphitic carbon felt for HER in real seawater, by which a two-electrode cell required 1.58 and 2.16 V at 10 and 100 mA cm^{-2}, respectively.

1.2.3 Transition metal sulfides (TMS)

Theoretically, in the layered MS_2 with a sandwich structure, one metal layer bonds to two sulfur layers. Because van der Waals forces are relatively weak, each MS_2 unit cell is vertically stacks on top of others, allowing MS_2 to be exfoliated down to single layers. They are calssified into several phase types including 1T, 2H, and 3R phases (here, the digit represents the number of layer; T, H and R respectively refer to tetragonal, hexagonal and trigonal lattices) based on MS_2 bonding configurations. The electronical structure of MS_2 varies with the configuration [37]. Transition metal sulphides with high electrical conductivity can be utilized for HER. In this case, to achieve higher electrocatalytic activity, the synthesis method and various modified strategies have been proposed. For example, doping a transition metal into sulphide-based materials can effectively increase active sites and optimize the 3d electronic configuration [38]. He *et al.* [39] used a cationic doping strategy to tune

electrocatalyst`s electronical structure as well as the free energy of the adsorbed intermediate. They synthesized Zn-doped Ni_3S_2, which displayed a low overpotential of 78 mA @10 mA cm^{-2} and maintained stably for at least 18 h in alkaline solution, implying its high HER activity and durability. To explore the reaction mechanism during HER, DFT calculations are always applied to investigate the adsorption/desorption ability of intermediates on the active sites during the reaction. For example, Zhang *et al.* [40] studied the electrocatalytic activity of Ni_3S_2 toward HER, and DFT calculation results demonstrated that S-rich surfaces and several stoichiometric of Ni_3S_2 surfaces are thermodynamically stable, thereby increasing HER activity. Pan *et al.* [41] synthesized pentagonal 2D transition metal sulphide monolayer such as FeS, MnS and VS. Among them, FeS and VS monolayers exhibited superior activity for HER in acidic electrolyte, and it is found that they had lower Gibbs free energies when compared to other materials. Xie *et al.* [42] synthesized MoS_2 using a defect engineering strategy and found that the molar concentration of Mo to S played a significant role in the determing of the number of active sites. Thus, the defect-abundant MoS_2 demonstrated remarkable HER activity with an onset potential as low as 120 mV. However, it is found that there was limited the active sites in the bulk MoS_2. To solve this issue, they tried to expose more active sites of MoS_2 by incorporating oxygen into MoS_2 nanosheets, by which a large number of defects were generated. Notably, the generation of defects could provide more active sites whereas the O doping could increase electrical conductivity [43]. Duraisamy *et al.* [44] synthesized MoS_2/MoO_3 by a one-step hydrothermal synthesis. It is found that the $1T/2H$-MoS_2 and $1T$-MoS_2/MoO_3 have rich defects, which effectively enhanced the HER activity in acidic solution. Moreover, rich S vacancies in substoichiometric MoS_{2-x} and rich O-vacancies in substoichiometric MoO_{3-x} edge sites of nanosheets serve as active sites for HER.

13

1.2.4 Transition metal phosphides (TMPs)

TMPs have been applied for hydrogen production due to their excellent conductivity, high corrosion resistance and high catalytic activity. Herein, the electronegative P atoms can accelerate H_2 dissociation and the optimal atomic ration between metal and P can improve condiuctivity and P alloying can enhance the corrosion resistance and chemical stability for HER [45, 46]. Moreover, bimetallic phosphides (such as NiCoP, CoFeP, and CoMoP) are more active than monometallic phosphides. For example, Pan *et al.* [47] mentioned that multi-phase heterostructure CoNiP/Co$_x$P/NF catalysts exhibited an overpotential as low as 36 mV@10 mA cm^{-2}, outperforming commercial Pt/C. According to DFT calculations, the strong electronical interaction at CoNiP/CoP heterointerface could be attained by transferring of electron from CoNiP to the heterointerface, which can promote water dissociation at the heterointerface and enhance the desorption of hydrogen from CoNiP, resulting in high activity and stability under alkaline seawater solutions. Wu *et al.* [48] proposed a Ni$_2$P-Fe$_2$P/NF electrode for alkaline seawater splitting, which needed only low overpotentials of 252 and 389 mV at 0.1 and 1A/cm^2, respectively. This 2D nanosheet structure contained abundant of active sites, which played a crutial function for improving the activity. Furthermore, the Ni and Fe species could help to improve stability and corrosion resistance, which is advantageous for seawater solutions.

Many strategies such as interface engineering, doping, and defect engineering are usually applied to modify the electronical structures of TMPs in order to improve catalytic activity. Especially, interface engineering is immensely used to optimize activity by tuning the electronical structure of catalyst, increasing active sites, and promoting mass transfer [49]. Recently, it is reported that TMPs had superior activity and stability in seawater splitting. For example, Chang *et al.* [50] successfully

synthesized Fe, P-NiSe$_2$ electrocatalyst, which required only 120 and 180 mV at 0.1 and 0.5 A/cm^2, respectively, in 0.5 M KOH + seawater solution with 90% IR correction. Herein, the P-NiSe$_2$ active sites should be formed by Fe cation doping whereas the P anions resulted in the formation of a passivation layer containing P-O bonds, improving electronical conductivity and preventing selenide dissolution. Yu *et al.* [51] prepared a sandwich-like NiCoN|Ni$_x$P|NiCoN microsheet array based electrode, which also displayed superior HER performance with a low overpotential of 165 mV @10 mA cm^{-2} in natural seawater electrolyte, and can be operated for 24 hour under seawater electrolysis (@10 mA cm^{-2}). Herein, the superior performance and stability could be attributed to (i) high chlorine-corrosion resistance from Ni$_x$P skeleton and (ii) anti-corrosive NiCoN nanoparticles [51].

1.2.5 Transition metal carbides and nitrides (MXenes)

The new class materials of 2D transition metal carbides, nitrides and carbonitrides are named as MXenes, which are especially suitable for engineering in order to achieve multi-functional catalytic interfaces with high active surface area [52]. MXenes is generally expressed as M$_{n+1}$X$_n$T$_x$ (n = 1-4), where M represents early transition metal atoms (i.e. Ti, Zr, Nb, and V), X is C or N, T$_x$ is the surface termination group (i.e. –F, –OH, –O, –Cl or –Se) and M layers cover the X layers in [MX]$_n$M arrangement [53]. MXene interlayer spacing is typically in the 1 nm range and it can be determined by the value of n in MXenes (M$_{n+1}$X$_n$T$_x$) [54]. The surface termination groups can induce hydrophilic surface and the layered structure could provide a large surface area. Thus, it has been suggested as a potential candidate for water electrolysis [55]. Moreover, the molecular sheets produced from transition metals carbides and nitrides can offer a high carrier mobility and intrinsic layered structure, indicating inherently superior conductivity and excellent volumetric capacitance. As such, the electrocatalytic

performance of MXene should depend on transition metal type, morphology, surface termination groups, adsorption and desorption ΔG_H values, and elemental doping state. Recently, it is reported that MXenes have great potentials as the electrocatalysts for water electrolysis because of its some special advantages including large surface area, excellent metallic conductivity (up to $10,000 \, \mathrm{S \, cm^{-1}}$), good hydrophilicity and adjustable structure [56]. For example, Tian *et al.*[57] synthesized FeCo-LDHs on a single-layered MXene ($Ti_3C_2T_x$), which showed an overpotential as low as 268 mV @10 mA $\mathrm{cm^{-2}}$ for OER in alkaline solution. Herein, the MXene effectively stabilized the LDH structure against aggregation with a synergistic effect with FeCo-LDH and especially, the high conductivity of MXene sheet can accelerate the redox process during the OER reaction, thereby leading to an excellent electrocatalytic activity. Haiyuan *et al.* [58] synthesized a hirerarchical porous NiCuS/$Ti_3C_2T_x$ electrocatalyst using a metal-organic framework (MOF) precursor. It is found that the interfacial interaction between NiCuS and Ti-MXene sheets effectively increased active sites, enhanced charge transfer rate and facilitated the electrolyte diffusion in the open structure. As a result, outstanding OER activity with an overpotential of 365 mV @ 10 mA $\mathrm{cm^{-2}}$ was achieved. Sun *et al*. [1] used a NiCo@C/MXene on CF anode coupling with a hydrazine degradation to generate H$_2$. This electrode exhibited a best HER activity with low overpotentials of 49 and 235 mV at 10 and 500 mA $\mathrm{cm^{-2}}$, respectively. The higher performance could be attributed to (i) the superior conductivity of $Ti_3C_2T_x$ MXene, (ii) the abundance -O and -OH groups on MXene surface, which can effectively facilitate the water as well as hydrazine molecules attractions onto the interface via hydrogen bonding, and (iii) hydrophilic properties, which can accelerate the overall kinetics. Moreover, it can work stably and produce H$_2$ gas at a rate of 9.2 mol $\mathrm{h^{-1} \, g_{cat}^{-1}}$ for 140 h at 0.5 A $\mathrm{cm^{-2}}$ with an excellent Faradaic efficiency, implying high mechanical

robustness in corrosive seawater splitting with 30-52% cost reduction at the hight current density. To impove HER performance in natural seawater, Wu *et al.* [59] designed a multifunctional $Co_xMo_{2-x}C$/MXene/NC electrode by using a cooperative catalytic interface strategy, which only requiresd the overpotentials of 81, 126 and 75 mV at 10 mA cm^{-2} for HER in 0.5 M H_2SO_4 (pH 0.3), 0.1 M phosphate buffer (PBS, pH 7.01) and 1.0M KOH (pH 13.8), respestively. Herein, the extremely conductive MXene can accelerate the transportation of charges across the triple-phases interface (catalyst-electrolyte-gas) and enhance H^+/water adsorption on the catalyst with a lower kinetic barrier for water dissociation. While, the $Co_xMo_{2-x}C$ provided highly exposed active surface area with substantial exposure active sites for promoting the HER. Therefore, the collaborative interface between $Co_xMo_{2-x}C$, hybridized carbon and MXene can effectively enhance the kinetics of initial Volmer step balance adsorption/desorption (H* and H_2) and maintain the stability in a wide pH range and natural seawater with 98% Faradaic efficiency.

1.3 ANODE MATERIAL DESIGN FOR OER

1.3.1 Transition metal oxides/hydroxides/ oxyhydroxides

Transition metal oxides or (oxy) hydroxides, especially first-row of transition metals (e.g., Mn, Fe, Co and Ni) base ones have been intensively studied for a OER since oxygen in the metal oxides and (oxy)hydroxides lattices could associate with the surface reaction and play a crutial role for modulating the catalytic performance [60]. For example, in the alkaline condition, it was mentioned that an amorphous $NiFe(OH)_x$/CP electrode exhibited a low overpotential of 303 mV @ 0.1 A cm^{-2} with a small Tafel slope of 33.8 mV dec^{-1} [61]. Herein, the superior activity toward OER could be attributed from the generation of oxygen vacancies, synergistic function between Ni and Fe species with an optimal Ni/Fe ratio. Recently, He *et al*. [62] reported that Mo

doing in NiFe (oxy)hydroxide can effectively improve oxygen activity via a lattice-oxygen-mediated (LOM) pathway. By using the metal-oxygen bond strength as a representative of oxygen activity for DFT calculation, it is proved that doping of Mo can weaken the metal-oxygen bonds and activated the lattice oxygen due to the upshift of O 2p, refering to deeper penetration of Fermi level into the O 2p band, which enhances the electron movement from oxygen sites, allowing lattice oxygen to be released from lattice more easily, thereby promoting the formation of oxygen vacancies. Jana *et al*. [63] developed $ZnO/Ni(OH)_2$ composite via a polyvinylpyrrolidone and dopamine (PVP -DA) assisted hydrothermal method, which showed a low overpotential of 170 mV @ 10 mA cm^{-2} in alkaline solution. Notably, the current density increased during the first 4 hours due to the generation of oxy(hydroxide) real active species. During OER, some irreversible/reversible reactions were found to occur on the surface of the catalyst due to the harsh condition on the anode side. As a result, the real active species could be generated after surface evolution or self-reconstruction during the oxidation reaction [64]. Similarly, the generation of oxy(hydroxide) active species during OER has also been reported by Yuan *et al*. [65]. It revealed that hybrid NiFeOOH/NF electrode had exceptional performance in the alkaline solution by using cell voltages of 1.51 and 1.55 V at 0.5 and 1 A cm^{-2}, respectively. Herein, the active Fe-OOH and Ni-OOH phases involved in the OER process were identified by using *in situ* electrochemical Raman spectroscopy. According to the XPS analysis results, the oxidation state of Ni was altered from Ni^{2+} to Ni^{3+} during the OER reaction, indicating that NiOOH acted as active centers for OER. In addition, the experimental results from Babar *et al*. [66] reported that the NiFe-OOH/NF electrode had a higher performance than NiFe-OH/NF electrode. Particularly, the NiFeOOH/NF electrode reached 0.4 A cm^{-2} at 280 mV, 10 times greater than that of NiFe-OH/NF electrode (40 mA cm^{-2}).

Moreover, the overpotential exhibited negligible change after continue the reaction for 75 h at 50 mA cm^{-2}, indicating its high mechanical robustness. Herein, the nanosheet NiFeOOH electrocatalysts enhanced the catalytic performance due to the metastable structure and long-range disorder atomic arrangement with rich defects and vacancies including void spaces,cation and anion vacancies and cluster gaps, which are advantageous for rapid diffusion of protons and fast transferring of charge. In addition, the abundant intrinsic defects generated by those randomly oriented bonds with high-energy can promote the adsorbing of intermediates on the surface of catalyst, and the amorphous structure's high flexibility can effectively improve electrocatalytic performance [66].

1.3.2 Transition metal layered double hydroxides (TM-LDHs)

Transition metal layered double hydroxides (TM-LDHs) have a basic formula of $[\ M_{1-x}^{2+}\ \ M_{x}^{3+}(OH)_{2}\ ]_{x}^{+}\ (A^{n-})x/n \cdot m\,H_{2}\,O$, where M^{2+} represents a bivalent, M^{3+} represents a trivalent TM cation and A^{n-} refer to charge balancing anion [67]. TM-LDHs like NiCo-LDH, NiFe-LDH, NiMn-LDH and NiV-LDH always have a flexible open structure with chemical versatility and remarkable electrocatalytic properties, which are commonly used as an electrode for water electrolysis. For example, 2D ultrathin nanosheet NiCo-LDH/NiCoS was synthesized via a MOF-involving sulfidation [68]. The synthesized electrode exhibited a low overpotential of 308 mV@0.1 A cm^{-2} with a low Tafel slope (48 mV dec^{-1}) value in alkaline solution. The hydrid arrays with rich interfaces between NiCo-LDH and NiCoS can promote the generation of oxygen containing intermediates, accelerating OER kinetics, thereby allowing this electrode to operate for 25 h without degradation. Herein, the *in situ* growth technique can minimize charge transfer resistance, provide more active sites and improve the interactions among solid, liquid and gas phases on the electrode surface, thereby increasing OER activity.

Currently, many studies on the modified TM-LDHs for seawater electrolysis have recently been reported. For example, Strasser *et al*. [69] firstly reported that NiFe-LDH electrocatalyst should meet the above alkaline design criterion. As a result, it achieved a high Faradaic efficiency of ~100% for OER in imitated seawater solution (0.1 M KOH+0.5 M NaCl ; pH = 13) [69]. Dong *et al*. [70] used a mild chemical technique to produce NiFe-LDH on O_2-plasma-treated carbon cloth (NiFe-LDH/CC). This electrode required a low overpotential of 252 mV @ 0.1 A cm^{-2} in alkaline solution, which is inferior than that of commercial RuO_2 for OER. It is considered that such a high OER activity should be attributed to partial redistribution among Ni and Fe atoms caused by bridging O^{2-}, resulting in the formation of rich active sites, which can facilitate electronical transferring and improve the adsorption/desorption capacity of oxygenated intermediates on the surface of catalyst. As a result, there was no chlorine detected during the reaction, suggesting ClER was completely suppressed by strong interaction between NiFe-LDH and carbon cloth (CC) substrate. Besides, NiFe-LDH/CC maintained its initial potential for 450 and 165 hours for fresh water (pH = 13.8) and seawater (pH = 13.5) based electrolytes at a current density of 0.1 A cm^{-2}, respectively. Cheng *et al.* utilized CoFe-LDH/Ti for seawater electrolysis (pH = 8.0). This electrode require an overpotential of ~530 mV@10 mA cm^{-2} for OER [71]. Liu *et al.* [72] modified CoFe-LDH with a high-valence state of Zr^{4+}, which improved the electronic structure, optimized the O intermediates, increased the electrochemical active surface area and reduced crystallinity, allowing the low overpotential as 159 and 233 mV at 10 mA cm^{-2} for HER and OER in alkaline electrolyte, respectively. Furthermore, in alkaline imitated seawater (1 M KOH+0.5 M NaCl), this catalyst needed a low overpotential of 303 mV @ 0.1 A cm^{-2}. You *et al.* [73] also found that doping Ir into $Ni(OH)_2$ remarkably changed the electron density of Ir and Ni sites, accelerating the

generation of *O and *OOH intermediates, thereby resulting in a high seawater splitting performance. In alkaline seawater, the monolayer NiIr-LDH worked stably for 650 hours at 0.5A cm^{-2} without noticeable change with ~99% Faradaic efficiency, indicating that it is applicable for large-scale application. Moreover, multimetallic LDH (NiFe-CuCo-LDH) was proposed as a potential candidate for highly efficient seawater oxidation (e.g., for 6 M KOH seawater electrolyte), which required overpotentials of 259 and 283 mV at 0.1 and 0.5 A cm^{-2}, respectively. This electrode exhibited high OER selectivity (97.4 % Faradaic efficiency for O_2 production at 500 mA cm^{-2}) and good durability for 500 hours in 6 M KOH electrolyte at 0.5 A cm^{-2} [74].

1.3.3 Spinel family

In a spinel oxide with a formula of AB_2O_4 (A,B = Fe, Co, Mn, Ni, Cu, etc.), A is a divalent cation at tetrahedral sites, B is a trivalent cation at octahedral sites and O is an anion. Spinel oxide's crystal structure is made up of metallic ions in tetrahedral and octahedral site centers and oxygen anions arranged at the polyhedral vertexes. Spinel oxide-based electrocatalysts are widely used due to their controllable composition, structure, valence, and morphology. Especially, this structure provides surface redox centers for oxygen adsorption, which is beneficial for OER [75]. Notably, the metal cation in the octahedral site plays a crutial function for OER because of substantially overlapping of highly layed 3d orbital in the octahedrally coordinating metal ions with an O 2p orbital and the weakly overlapped 3d orbital in the tetrahedrally coordinating metal ions with an oxygen atom. Furthermore, the surface of octahedral cation is more easily exposed, implying that it is easier to contact with the reactants [76, 77]. In addition, spinel compounds are excellent electrical conductor with active sites and stable in base solution at a high potential [78]. Generally, multimetallic spinel oxides (MFe_2O_4 ; M = Co,Ni,Cu, etc.) have higher OER activity than monometallic one [79].

Among spinel oxide family, cobalt-based binary spinel-type metal oxides such as $MnCo_2O_4$, $CuCo_2O_4$, $NiCo_2O_4$, etc., have been proposed for OER owing to their redox stability and synergistic interaction between the metal species and mixed variance states of metals. It was discovered that the distribution balance of M^{3+}/M^{2+} species in octahedral and tetrahedral sites as well as bond strength between M and oxygen atoms can control active sites [80]. For example, Li $et\ al.$ [81] reported that spinel Co_2MnO_4 had low activation barrier comparable to IrO_2 benchmark due to the ideal binding energies of oxygen evolution reaction intermediates. Moreover, it is found that this catalyst can suppress the catalyst dissolution during long-term operation for over 1,500 hours at 200 mA cm^{-2}.

However, some spinal oxides such as $MnCo_2O_4$ have low electrical conductivity. To solve this issue, various strategies such as hetero-atom doping, incorporation of O vacancy and deposition of it on the conductive material have been considered. For example, Yang $et\ al$. [82] found that $MnCo_2O_4$-rGO nanocomposites generated from bimetal-MOFs had a low onset potential of 1.56 V vs RHE with high electron transfer number, which is comparable to that of Pt/C [82]. Bahadur $et\ al.$ [83] also sulfurized $CoMn_2O_4$ to improve electrical conductivity and to lower the oxidation state of cobalt, leading to excellent activity and stability with a low overpotential of 300 mV@10 mA cm^{-2}. Wang $et\ al.$ [84] improved the conductivity and ion diffution rate of cobalt ferrite ($CoFe_2O_4$) by incorporating NiO. In alkaline solution, the obtained NiO-$CoFe_2O_4$/NF electrode required only a low overpotential of 157 mV@10 mA cm^{-2}. Herein, the outstanding OER activity can be attributed to the presence of bimetallic active sites of $CoFe_2O_4$ and NiO. Wen $et\ al.$ [85] recently immobilized iridium-single atoms (Ir-SAs) in spinel $Ni_xMn_{3-x}O_4$ for alkaline seawater electrolysis. At 0.1 and 0.2 A cm^{-2}, this electrocatalyst achieved low overpotentials of 330 and 350 mV, respectively. Herein,

the immobilized Ir-SAs not only improved the intrinsic activity, facilitated surface charge kinetics and stabilized *OOH intermediate but also destabilized chloride ions adsorption on the electrode surface.

1.3.4 Transition metal sulfides (TMS)

Transition metal sulfides (TMS)-based electrocatalysts have been investigated for water electrolysis, especially for OER due to their distinctive structure with abundant exposed active sites, high activity, high conductivity and excellent durability. There are distinct classes of TMSs including layered TMS (MS_2) and non-layered TMS (M_xS_y). Corresponding to the periodic table, TMSs in groups 4-7 (M=Mo,W, Mn, Nb, *etc*.) always crystallize with a graphite-like layered structure where as TMSs in groups 8-12 (M=Fe, Co, Ni, Zn, *etc*.) crystallize as a non-layered structure. The different configurations could affect the electronic and electrochemical properties [19]. Generally, the layered ones can be employed as excellent HER electrocatalysts because of their well-exposed edge sites with high electrical conductivity and high intrinsic activity. While, the non-layered ones are effective for OER. Generally, the basal plane and edge plane of the layered TMS have anisotropic properties. The in-plane electrical conductivity of layered MS_2 is approximately 2200 times higher than that of the interlayer one, while the edge plane contributes to fast electron transfer, resulting in an improved electrocatalytic performance [86, 87]. Among TMSs, Ni/Fe-based ones such as NiS and FeS are more efficient for overall water splitting. For instance, Zhang *et al.* [88] reported that the FeS/NiS *in-situ* growing on the nickel foam exhibied low overpotentials of 144 and 203 mV at10 mA cm^{-2} in 1 M KOH solution for HER and OER, respectively. According to the high conductivity of FeS and NiS with the high active surface area, only a cell voltage of 1.618 V@10 mA cm^{-2} was required for overall water splitting. Pan *et al.* [89] enhanced the performance of layered MoS_2

catalyst by covalent Ni and P doping into 1T-enriched MoS_2. By this way, it efficiently activated the basal planes, expanded the interlayer spacing, and increased the edge density of MoS_2 in 2D nanostructure. Moreover, ternary and quaternary non-layered TMSs such as Ni-Co-S, Fe-Co-S and Ni-Fe-S with higher electrical conductivity and faster redox reactions also exhibited excellent activity [90]. For example, Li *et al.* [91] successfully synthesized 3D trimetallic sulfide $FeCo_2S_4$-$NiCo_2S_4$ on the Ti mesh. This electrode exhibited a low overpotential as 230 mV at 10 mA cm^{-2} for OER. Herein, the synergistic between $FeCo_2S_4$ and $NiCo_2S_4$ can significantly facilitate the charge transfer whereas the NiCoFe-S formation results in abundant active sites and increased conductivity. Notably, for the TMSs, there are many strategies such as modification with transition metal based oxides, heteroatomic doping and edge sites engineering to expose more active sites, thereby improving intrinsic activity. For example. Ghouri *et.al.*[92] synthesized hybrid graphene $MnFeCoO_4$/$Mn_2S_2(CO)_7$ by a one-step hydrothermal way, which diplayed good performance with a low overpotential as ~310 mV at 10 mA cm^{-2} toward OER in neutral seawater solution (1 M PB + 0.6 M NaCl, pH 7.0). Chen *et al.* [93] applied a one-step calcination step to dope N anions on Ni_3S_2 (N-Ni_3S_2/NF). To achieve a current density of 0.1 A cm^{-2}, the prepared electrode needed a low overpotential of 330 mV. Herein, the introduction of N anions can improve electrical conductivity, optimize hydrogen and water adsorption energies, and increase abundant active sites, resulting in high activity as well as durability.

Many reports have mentioned that TMSs are unstable at an oxidizing potential and easily converted to oxides/(oxy)hydroxide during the OER process. Surprisingly, the post-oxidized catalyst is more stable with higher catalytic activity than the initial fresh catalyst [94]. For instance, Hu *et al.* [95] mentioned that $FeCo_2S_4$/NF electrode required only 290 mV@100 mA cm^{-2} due to formation of CoFe-(oxy)hydroxides layer on the

24

surface, which acted as a real active species, leading to high activity and stability. Yang *et al.* [96] also reported that Ni(Fe) OOH-FeS$_x$ electrocatalyst displayed excellent activity with a low overpotential of 220 mV@10 mA cm^{-2}. Herein, the incorporation of Fe-S on the Ni(Fe)OOH can strengthen the bond between Fe and the active *O intermediate, which is the rate-controlling step, and significantly reduce the adsorption free energy gap.

1.3.5 Transition metal phosphides (TMPs)

TMPs always demonstrate excellent OER performance owing to the high conductivity, corrosion resistance and catalytic activity. Recently, TMPs have received more attentions because they have shown excellent properties and high durability for seawater electrolysis application. For instance, Ren *et al.* [48] proposed a Ni$_2$P-Fe$_2$P/NF electrode for alkaline seawater splitting, which required only low overpotentials of 305 and 431 mV at 0.1 and 1 A cm^{-2}, respectively. Such a bimetallic phosphide with a high transfer coefficient always performs a phase transformation during OER to form Ni/Fe oxide/hydroxide phases on the surface, which can optimize adsorption intermediates. While, alloying Ni and Fe with P atoms improved the corrosion resistance in seawater solution. Yang *et al.* [50] designed iron and phosphor dual-doped nickel selenide (Fe,P-NiSe$_2$ NFs) for seawater electrolysis. Herein, doping with Fe cations increased OER selectivity and faradaic efficiency whereas doping with P anions improved the conductivity and prevented catalyst dissolution during long-term operation by generating a passivation layer containing P-O species. In a natural seawater electrolyzer, this catalyat required only 1.8 V@0.8A cm^{-2} and worked consistently for over 200 hours [50]. Qi *et al.* [97] fabricated NiFeP/P-rGO on the nickel foam, which displayed a low overpotential of 290 mV@100 mA cm^{-2} with a Tafel slope of 71.9 mA dec^{-1} in seawater solution (1 M KOH+1 M NaCl). In addition, this catalyst exhibited high durability for

more than 450 hours at 35 mA cm^{-2} without current loss. Herein, the highly active NiFeP and conductive rGO could be responsible for the high activity and stability.

1.4 Bifunctional electrocatalyst design for overall water splitting

Designing bifunctional electrocatalysts for overall water especially seawater splitting is difficult because most electrocatalysts can be only effective at anode or cathode. Recently, some bifunctional electrodes were developed for overall water seawater splitting in various conditions.

1.4.1 Transition metal sulfide (TMS) based electrocatalysts

Transition metal sulfides (TMS) based electrocatalysts could be applied as the bifunctional electrocatalysts for overall water especially seawater electrolysis. For example, Zhao *et al.* [98] revealed that Ni_3N/Ni_3S_2 should be a promising candidate for large-scale water/seawater electrolysis due to the existence of interfacial NiNS between Ni_3N/Ni_3S_2 which can act as the real active species for accelerate dissociative adsorption water molecule, resulting high overall catalytic activity as the bifunctional electrocatalysts. Li *et al.* [99] synthesized Ni_3S_2-1 T-MoS_2-Ni_3S_2 multi-layered electrocatalyst coated on Ni foam substrate using a two-step hydrothermal process, which required a stable cell voltage of 1.82 V @ 100 mA cm^{-2} for 100 hours in an electrolyte solution containing 1 M KOH + seawater. Herein, the Ni_3S_2 sandwiched structure provided a protective layer against chloride anions, enhancing the durability of this electrode. While, the MoS_2 interlayer can improve electrocatalytic performance [99]. Wang *et al.* [100] fabricated S-$NiMoO_4$@NiFe-LDH core-shell structure on the Ni foam, in which the NiFe-LDH and S-$NiMoO_4$ are beneficial for OER and HER in imitated alkaline seawater, respectively. By using this bifunctional electrocatalyst, the two-electrode cell needed a voltage of 1.68 V @ 0.1 A cm^{-2}. Seenivasan *et al.* [101] mentioned that multimetallic transition metal sulfide-based electrocatalyst such as

$NiCo_2S_4/NiMo_2S_4/NiO$ (NCMS/NiO) can effectively against chloride corrosion without hypochlorite formation under seawater electrolysis because dual active sites of M-S and M-OOH have remarkable corrosion resistance to chloride ions during seawater electrolysis.

1.4.2 Transition metal phosphide (TMP)-based electrocatalysts

Transition metal phosphide (TMP)-based electrocatalysts could be also utilized as the bifunctional electrocatalysts for overall water splitting especially for seawater splitting. For example, a heterogeneous bimetallic phosphide of Ni_2P-Fe_2P supported on NF represented excellent electrocatalytic activity and durability for overall seawater splitting, which required only ~ 1.81 and 2.00 V cell voltages at 0.1 and 0.5 A cm^{-2} in alkaline seawater, respectively. Herein, the heterointerfaces between two phases can improve exposed active sites, thereby enhancing intrinsic activity as well as corrosion resistance [48]. Chang *et al.* [102] doped Fe and P on the nickel selenide (Fe, P-NiSe$_2$) to improve the electronical structure and surface composition, resulting in increased activity as well as stability over 200 hours in natural seawater electrolysis. Wang *et al.* [103] doped Co on the Fe_2P electrocatalyst (Co-Fe$_2$P) to change the electronical structure of P for making it more negatively charged, which especially improved HER activity by making it easier to attract protons during HER. As a result, a cell with this bifunctional electrocatalyst (Co-Fe$_2$P // Co-Fe$_2$P) showed excellent activity with a cell voltage of 1.69V@100 mA cm^{-2} for overall seawater electrolysis. Liu *et al.* [47] synthesized CoNiP/Co$_x$P composite bifunctional electrocatalyst on NF (CoNiP/Co$_x$P/NF) by combining electrodeposition and chemical vapor deposition technique, which showed a strong corrosion resistance and abundant exposed active sites, allowing for better catalytic performance and durability for long-term operation. According to the DFT calculations, such a catalyst (CoNiP) has optimal thermodynamic

properties for hydrogen desorption/adsorption, accelerating water dissociation.

1.4.3 Transition metal nitride (TMN) based electrocatalysts

Recently, transition metal nitrides (TMNs) have been reported as the bifunctional electrocatalysts for overall seawater electrolysis application because their high corrosion-resistance, high electrical conductivity and strong mechanical property [104]. For example, the obtained NiMoN@NiFeN core-shell structure required low cell voltages of 1.608 and 1.709 V at 0.5 and 1 A cm^{-2}, respectively, in alkaline seawater solution [105]. Li *et al*. [106] successfully synthesized NiCoN for HER and NiFeN nanosheets for OER anchored on NiTe nanorod arrays by electrodeposition followed by nitridation. The two-electrode cell (NiTe-NiCoN(-) || NiTe-NiFeN (+)) required only a voltage of 1.84 V@0.5 A cm^{-2} for overall seawater splitting.

Table 1.2 Summary of recent studies on the electrocatalysts for HER in alkaline freshwater and alkaline seawater solutions

Catalyst	Electrolyte	η (mV@ mA cm^{-2})	Durability (h)	Ref.
V-Ni$_3$S$_2$/CC	1M KOH	81@10	30	[107]
Ce@NiCo-LDH	1M KOH	134@50	36	[108]
PtMo/Ti mesh	SeawaterF	254.6@10	172	[35]
S-NiMoO$_4$@NiFe-LDH	1 M KOH + 0.5 M NaCl	46@10	20	[100]
	1 M KOH + 0.5 M NaCl	170 @100	20	
	1 M KOH + seawater[a]	220@100	20	
Ni$_2$P-Fe$_2$P/NF	1 M KOH + seawater[b]	252@100	36	[48]
Mo$_5$N$_6$	Natural seawater[c]	257@10	100	[109]
Ni-SA/NC	1 M KOH + seawater[d]	139@10	14	[110]
CoP$_x$@FeOOH	1 M KOH + seawater[b]	190@100	80	[111]
NiCoN|Ni$_x$P|NiCoN	Natural seawater[e]	165@10	24	[51]
Ni$_5$P$_4$@Nickel	1M KOH	87@10	50	[112]
hydr(oxy)oxide	Seawater	144@10		

Note ; [a]: The natural seawater was collected from Stone Oldman sea area of Fushan Bay, Qingdao, China ; [b] : Natural seawater was collected from Galveston Bay, Galveston, Texas, USA; [c] : Natural seawater was collected from Henley Beach, Adelaide, Australia ; [d] : Natural seawater was collected from Sentosa beach, Singapore ; [e] : Natural seawater was collected from Galveston Bay near Houston, Texas, USA.

Table 1.3 Summary of recent studies on the electrocatalysts for OER in alkaline freshwater solutions

Catalyst	Electrolyte	η (mV@ mA cm^{-2})	η_{100} (mV)	Durability (h)	Ref.
Ni$_3$S$_2$ /MnO$_2$	1M KOH	260@10	348	48	[113]
CoFe-OH@FeOOH	1M KOH	200 @50	230	48	[114]
NiCo-LDH@NiCoV-LDH/NF	1M KOH	-	260	40	[115]
NiCo-LDH-V$_{Ni}$/CC	1M KOH	227@10	-	100	[116]
NiCo@NiFe-LDH	1M KOH	-	209		[117]
Co$_3$O$_4$@ NiCo- LDH	1M KOH	279@15	-	20	[118]
Co$_3$O$_4$@ NiFe- LDH	1M KOH	215@10	-	80	[119]
Ce@NiCo-LDH	1M KOH	250@50	-	36	[108]
C-MCO/h-BN	1M KOH	240@10	-	35	[120]

Table 1.4 Summary of recent studies on electrocatalysts for OER in alkaline simulated seawater and natural seawater.

Catalyst	Electrolyte	η_{10} (mV)	η_{100} (mV)	Durability (h)	Ref.
S-NiMoO$_4$@NiFe-LDH	1 M KOH + 0.5 M NaCl	-	273	20	[100]
	1 M KOH + seawater[a]	-	315	20	
Pb$_2$Ru$_2$O$_{7-x}$	Natural Simulated seawater	500	-	5	[121]
FTO/NiO	1 M KOH + 0.5 M NaCl	340	-	100	[122]
NiFe-LDH	0.1 M KOH + 0.5 M NaCl	359	-	120	[9]
		490		6	
	Borate buffer + 0.5 M NaCl				
NiFe-LDH	1 M KOH + 0.5 M NaCl	~270	-	100	[123]
CoFe-LDH	Simulated seawater (pH 8)	530	-	8	[71]
S-(Ni,Fe)OOH	1 M KOH + 0.5 M NaCl		278	100	[124]
	1 M KOH + seawater		300	100	
NiFe/NiS$_x$-Ni	1 M KOH+0.5 M NaCl		~300 (at 400 mA/cm^2)	1000	[125]
NiMoN@NiFeN	1 M KOH + 0.5 M NaCl	-	286	100	[126]
	1 M KOH + seawater	-	307	-	
Ni$_2$P-Fe$_2$P/NF	1 M KOH + seawater[b]		305	36	[48]
NiFeP/P-rGO/NF	1 M KOH + 1M NaCl	-	290	450	[97]
Ir$_2$	0.1 M HClO4 + 3.5 wt% NaCl	243		-	[127]

Electrode	Electrolyte			Durability	Ref.
CoP$_x$@FeOOH	1 M KOH + seawater[b]	283 337(@ 500 mA/cm^2)		80	[111]
NiCo@NiFe LDH	1 M KOH + seawater[b]	-	222	100	[117]

Note ; [a] : The natural seawater was collected from Stone Oldman sea area of Fushan Bay, Qingdao, China ; [b] : Natural seawater was collected from Galveston Bay, Galveston, Texas, USA.

Table 1.5 Summary of recent studies on bifunctional electrocatalysts for overall seawater elecrolysis

Electrode	Electrolyte	Voltage (V)@current density (mA cm^{-2})	Durability (h)	Ref.
NiMoFe	0.5M KOH + seawater[a]	1.59 (at 10 mA cm^{-2})	24	[36]
Ni$_2$P-Fe$_2$P/NF	1M KOH + seawater[b]	1.811 (at 100 mA cm^{-2})	48	[48]
		2.004 (at 500 mA cm^{-2})	38	
Ni$_3$S$_2$-MoS$_2$-Ni$_3$S$_2$@Ni foam (NMN-NF)	1M KOH + 0.5M NaCl	1.80 (at 100 mA cm^{-2})	100	[99]
	1M KOH + seawater	1.82 (at 100 mA cm^{-2})	100	
S-NiMoO$_4$@NiFe-LDH	1M KOH + 0.5M NaCl	1.68 (at 100 mA cm^{-2})	20	[100]
	1M KOH + seawater[c]	1.73 (at 100 mA cm^{-2})	20	
CoP$_x$@FeOOH	1M KOH + seawater[b]	1.710 (at 100 mA cm^{-2})	80	[111]
		1.867 (at 500 mA cm^{-2})		
NiFe/NiS$_x$-Ni	6M KOH + 1.5M NaCl	1.72 (at 400 mA cm^{-2})	1000	[125]
	1M KOH + seawater[d]	2.12 (at 400 mA cm^{-2})	1000	
S,P-(Ni,Mo,Fe)OOH/ NiMoP/Wood aerogel	1M KOH + seawater[e]	1.86 (at 500 mA cm^{-2})	30	[128]
HCl-c-NiFe	1M KOH + 0.5M NaCl	1.62 (at 100 mA cm^{-2})	300	[129]
NF@NiMoO$_4$/N/P (NF@NM-NP)	1M KOH + 0.5M NaCl	1.46 (at 10 mA cm^{-2})	-	[130]
		1.70 (at 100 mA cm^{-2})	-	
RuV-CoNiP/NF	Alkaline seawater	1.538 (at 20 mA cm^{-2})	12	[131]
		1.663 (at 50 mA cm^{-2})	12	
		1.841 (at 100 mA cm^{-2})	12	

Note : [a] : The seawater was collected from the seaside of Barcelona ; [b] : Natural seawater was collected from Galveston Bay, Galveston, Texas, USA; [c] : The natural seawater was taken from Stone Oldman sea area of Fushan Bay, Qingdao, China ; [d] : Seawater was collected from San Francisco Bay ; [e] : The natural seawater was collected from Fushan Bay in Qingdao, Shandong, China.

1.5 SUBSTRATE FOR SUPPORT ELECTROCATALYST

For the large-scale application, the uniformity, accuracy, precision and preparation cost of electrocatalysts need to be considered. There are various techniques to prepare the electrode, which can be divided into two main groups: (i) Preparing of powder-state electrocatalysts and subsequently coated them on current collector (e.g., glassy carbon, NF, and carbon fiber paper) applying a Nafion solution as the binder to enhance electron transportation, and (ii) Binder-free electrode, in which the substrates such as porous metal foam (Ni/Cu foam), carbon paper, carbon cloth, FTO, Ti-foil, etc are always used to replace glassy carbon. In general, by using the binders, it is not suitable for long-term operation because of the deterioration of mechanical strength, electrical conductivity and catalyst peeling-off during a long-term operation [132]. Therefore, directly growing of the electrocatalysts on the substrate is more attractive to prepare the electrode, which is also simple, low cost and reproducible [114]. In this case, it is important to select suitable substrate. In the following, two typical substrates are introduced.

1.5.1 Carbon fiber paper (CP)

Commercial carbon fiber paper is one of the suitable carbon substrates for water splitting application because it has high conductivity, chemical tolerance in acidic/alkaline environments, large surface area and high non-Faradaic background current [133]. Many studies used the carbon paper (CP) as the substrate to improve electrocatalytic performance. For instance, Xiong et al. [134] applied a hydrothermal process to synthesize Ni-Mo bimetal sulfides on Co_3O_4/carbon fibers (Ni-Mo-S@Co_3O_4/CF). At 10 mA cm^{-2}, this electrode displayed a small overpotentials of 85 and 275 mV for HER and OER, respectively. Herein, the 3D hybrid hierarchical heterostructure on CF can be directly connected to the active materials, confirming good electrical conductivity and mechanical stability. A two-electrode cell by using it

demonstrated excellent overall water splitting with a low cell voltage of 1.57 V@10 mA cm^{-2}, as well as excellent durability and stability for 50 hours without noticeable change. Ye *et al*. [135] supported 3D Co-Fe oxide nanoarrays on the carbon fiber paper (Co$_x$Fe$_{3-x}$O$_4$ /CFP) via a facile hydrothermal method , then calcined it in air at 350°C for 2 h. Because of the microporous structure of CFP with high electrical properties, this electrode showed an excellent OER activity and stability, especially at high current density (> 0.5A cm^{-2}).

1.5.2 Nickel foam (NF)

NF is extensively utilized as an electrode support material since it has a large surface area and continuous highly conductive 3D network, which helps to improve electrocatalytic performance [136]. For example, Hao *et al.* [137] prepared FeO$_x$-Ni$_3$S$_2$ on the NF by a one-pot solvothermal reaction, which exhibited a low overpotental of 120 (at 50 mA cm^{-2}) and 470 mV (at 200 mA cm^{-2}) for HER and OER, respectively in alkaline simulated seawater (1 M KOH + 0.5 M NaCl) since the self-supporting configuration achieved a large catalytic specific surface area of nanosheet arrays as well as fast charge transfer capability. Nowadays, *in situ* growing of electrocatalyst on NF substrate is becoming more popular because it can effectively reduce the resistance between the electrocatalyst and substrate, leading to better electrocatalytic performance with a longer stability. For example, Chen *et al.* [138] synthesized FeIr alloy on NF by using a hydrothermal process at 180°C for 12 h. As it was used as a bifunctional electrocatalyst for overall water splitting at a high current density, low overpotentials of 25.6 and 220 mV at 10 mA cm^{-2} were required for HER and OER, respectively. For overall water splitting, it required only a cell voltage of 1.51 V@10 mA cm^{-2}. Moreover, this electrode showed excellent durability for 124 hours even at 1 A cm^{-2} in alkaline solution. Herein, the excellent activity and durability are related to self-supported

volcano-like FeIr alloy on NF, which can significantly enhance intrinsic activity and increase the specific surface. Shin *et al.* [139] successfully synthesized binder-free Fe-Ni hydroxides on NF by a simple corrosion engineering way using a piranha solution (H_2SO_4 and H_2O_2) containing Fe^{3+} precursor, by which the porosity and electrocatalytic active surface area of the electrode were effectively increased while the charge transfer resistance was reduced. Hence, this electrode maintained the OER overpotential as low as 267 mV for 500 h, indicating excellent stability.

1.6 ELECTROCATALYST PREPARATION METHODS

There are numerous methods for growing electrocatalysts on the substrates with excellent performance for water splitting application.

1.6.1 Hydrothermal synthesis method

The hydrothermal synthesis method is a low temperature preparation method that has been generally used for the preparation of metal nanoparticles, metal alloys, metal oxides, and chalogenides with controllable size, shape, and nanostructure. Herein, the morphology of nanoparticles by using this method could be determined by (i) film rigidity of reverse micelle in microemulsion, (ii) the kinetics of crystal growth in a constrained environment, (iii) the water to surfactant molar ratio, (iv) the intermiceller exchange rate, (v) the organic solvent, surfactant, and co-surfactant, and (vi) the packing parameter [140]. The various morphology, physical properties and catalytic activity could be achieved by using this method. For example, Marimuthu *et al.* [141] fabricated Cu_2S thin film by using a hydrothermal synthesis method at 80°C at different reaction periods. The obtained Cu_2S grown for 1 hour exhibited a lowest overpotential as 76 mV at 10 mA cm^{-2}. Yu *et al.* [105] synthesized highly uniform NiFeN nanoparticles on NiMoN nanorods (NiMoN@NiFeN) by a hydrothermal synthesis method at 150°C for 6 h followed by a nitridation process in a tube furnace, which

exhibited low cell voltages of 1.608 and 1.709V at 0.5 and 1 A /cm^2, respectively, for overall seawater electrolysis (60°C).

1.6.2 Chemical bath deposition (CBD) method

Zou *et al.* [142] reported an ultrafast strategy for growing other Ni-based bimetallic hydroxide (Ni–M–OH, M = Ni, Fe, Co, Mn, or Cr) films on Ni$_3$S$_2$/NF using a chemical bath deposition method. Herein, *in-situ* growing of amorphous Ni-Fe-OH on conductive Ni$_3$S$_2$/NF was successfully realized by using a liquid solution containing Fe^{3+} ion at 100°C for 5 s. The obtained electrode exhibited excellent activity and stability for OER at large current densities. Lu *et al.* [143] also proposed a fast sulfurization method to synthesize Ni-CoCHH/NF-S by using Na$_2$S at room temperature. The obtain electrode displayed an overpotential as 100 mV@10 mA cm^{-2} in alkaline solution for HER with almost no change for 25 h.

1.6.3 Chemical vapor deposition (CVD)

Chemical vapor deposition (CVD) is commonly used for preparation of self-standing electrode by deposition of solid compounds onto the substrate's surface. Herein, the key factors for controlling the composition and morphology of electrocatalyst include precursor type, gas flow rate, temperature and pressure [144]. For example, Yang *et al.* [145] prepared Ni@NiO core-shell structure on graphite using a one-step chemical vapor deposition from Bis(cyclopentadienyl)nickel(ii) (NiCp$_2$) precursor. It is found that the deposition temperature could control the thickness of the graphite layer as well as the Ni content. This special core–shell microstructure displayed an overpotential of 330 mV@10 mA cm^{-2} for OER.

1.6.4 Electrodeposition

The electrodeposition technique has been applied for more than two centuries [146], which is one of the most time-saving techniques to synthesize the electrocatalyst with

a high performance [147]. The concept of electrodepositon starts from the reactants which are firstly dissolved in the electrolyte. Then, the oxidized and reduced products can be constantly loaded on the substrate surface by tunning the applied potential. The potential at the working electrode is usually monitord by using a reference electrode. The deposition potential and current, time, pH, temperature and additive are the important parameters for determining size and morphology of the obtained electrocatalysts [148]. Such a method can be used for the synthesis of TM alloy, TM oxides, LDH, TM sulfides and so on. For example, NiO, CuO and Co_3O_4 can be synthesized through electrochemical reduction of NO_3^- at first in order to produce hydroxide precursors, which are further annealed to get transition metal oxides [149]. Herein, the main factors influencing electrode structure are metal salt concentrations, applied potential, applied current and time. However, it could be a high electrical energy consumption process.

1.6.5 Aerosol-spray-assisted method

  Kuai *et al*. [150] reported an aerosol-spray-assisted approach (ASAA) for producing amorphous mixed-metal oxides for OER. This method allows not only for control size of catalyst and composition but also use of low-cost inorganic salts as the precursor, which is economically applicable for a large-scale electrode production. They obtained $Fe_6Ni_{10}O_x$ electrocatalyst by this method, which showed a low overpotential of 286 mV @ 10 mA cm^{-2} for OER. This is the best electrode among Fe-Ni-O_x series. El Emam *et al.* used such an aerosol spray drying method to dope Ni onto $BaTiO_3$ hollow spheres (HS)/RGO. The charge transfer resistance was lowest in Ni doped $BaTiO_3$ HS/RGO, indicating improved electrocatalytic activity toward water oxidation [151].

1.7 KEY PARAMETER RELATED TO REACTION KINETIC

For water splitting, there are many parameters such as operation temperature, type of electrolyte, pH, and applied current, which will affect the activity and durability of electrolysis cell. Therefore, it is necessary to consider the optimum conditions to achieve the best electrocatalytic efficiency.

1.7.1 Temperature

Water electrolysis systems can be classified into two categories based on their operating temperatures: (i) low temperature electrolysis system (below 100°C) such as Proton Exchange Membrane Electrolysis Cell (PEMEC) and Alkaline Electrolysis Cell (AEC) and (ii) high temperature electrolysis system (500-900°C) such as solid oxide electrolysis cell (SOEC). On a practical or industrial scale, it should consider whether the system could be operated at a higher temperature to demonstrate the mechanical robustness of the electrode [152].

1.7.2 Electrolytes

Because proton or hydroxide ions must pass through the electrolyte during the water electrolysis process to enable electrochemical reaction at the electrodes, electrolytes are one of the important parameters that affect the electrocatalytic performance. Because of high proton concentration in the acid solution, HER is more kinetically favorable in it. However, OER prefers to occur in the alkaline electrolyte. Thus, the pH value needs to be considered for calculating the overpotential using the Nernst equation as below[153, 154]:

$$E_{eq} = E^0 + \frac{RT}{nF} ln \left(\frac{a_0}{a_R}\right) \qquad \text{(Eq.32)}$$

where E_{eq} represents the equilibrium potential, R represents the universal gas constant, T represents the temperature, and a_i represents the activity of species i. When Equation (32) is utilized for HER and OER under standard condition, the equilibrium

potentials (E_{eq}) can be obtained on the standard hydrogen electrode (SHE) as following (33)-(34):

$$HER : E_{eq} = -0.059 \times pH \qquad \text{(Eq.33)}$$

$$OER : E_{eq} = -0.059 \times pH + 1.23 \qquad \text{(Eq.34)}$$

Therefore, the equilibrium potentials for HER and OER on the reversible hydrogen electrode (RHE) scale are 0 and 1.23 V, respectively.

1.7.2.1 Acid electrolyte

The acidic condition is commonly used for proton exchange membrane (PEM) electrolysis, particularly for HER, due to its high energy efficiency as well as high hydrogen production rate. Herein, the abundant protons in the acidic electrolyte allow H^+ adsorption on the electrode surface for Volmer reaction, which is beneficial for HER. However, most efficient catalysts for OER are unable to withstand in the acidic condition. For the acidic solution, sulfuric acid (H_2SO_4) and perchloric acid ($HClO_4$) are commonly used, and the pH value of acidic solution is about 0-4 such as 0.5 M H_2SO_4 solution (pH = 0.3) [155].

1.7.2.2 Neutral electrolyte

In neutral or near-neutral condition, 0.1 M Na_2SO_4 or 0.1M $KClO_4$ is usually used to evaluate the water electrolysis performance at pH=7. However, phosphate-buffered saline (PBS, pH ~7), carbonate buffer (CBF, pH~8.6-10.6) or borate-buffered saline (BBS, pH ~8.5-9.2) is generally used for the evalution of the electrocatalysts working at neutral or near-neutral condition for water splitting.   For proton generation, the HER rate, which is determined by the pK_a of the buffering species and the pH of a solution, most likely acts as a proton carrier and directly involved in surface reactions [156]. Similarly, the presence of buffered species can improve the reaction rate of OER by facilitating the removal of generated proton on the electrode surface [157]. In this case,

due to the lower proton/hydroxyl concentration in the solution, the OER has slower kinetics in this condition when compared to alkaline or acidic conditions.

1.7.2.3 Alkaline electrolyte

Alkaline electrolyzer always operates under potassium hydroxide (KOH) or sodium hydroxides (NaOH) containing solutions. Because of its higher conductivity, KOH solution is more commonly used than NaOH to adjust the pH of the electrolyte. The molar ion conductivities of Na^+, K^+, and OH^- are 0.050, 0.073, and 0.198 S L mol^{-1} cm^{-1}, respectively [60]. Generally, the pH of alkaline aqueous solution used in alkaline water splitting ranges between 11 and 14, depending on the molar concentration of KOH or NaOH solution [7].

1.7.2.4 Simulated seawater electrolyte

Addition of 0.5 M NaCl into 1 M KOH solution is usually used for simulate seawater condition since this NaCl concentration is almost the same as that in natural seawater [105, 122, 125]. Moreover, the pH of alkaline imitate seawater solution is about 13-14. In addition, Juodkazytė *et al.* [122] also mimicked the seawater solution by mixing a solution containing 27. 495 g NaCl, 6.912 g MgSO$_4$, 1.1 g CaCl$_2$ and 0.745 g KCl and 1,000 ml of deionized water with 1.0 M KOH to obtain actual concentrations of Na^+, Cl^-, SO_4^{2-}, Mg^{2+}, Ca^{2+} and K^+ close to natural seawater. Herein, adding KOH is one of the pre-treatment steps for seawater without using a membrane because KOH aids in the precipitation of Mg(OH)$_2$ and Ca(OH)$_2$, resulting in a clear solution and preventing the catalyst active sites from being blocked [158]. This condition is now widely used as a preliminary step in the development of an electrocatalyst for seawater electrolysis.

1.7.2.5 Natural seawater electrolyte

Natural seawater contains a variety of ions such as Na^+, Cl^-, SO_4^{2-}, Mg^{2+} and Ca^{2+}, and contaminants, and thus, direct seawater splitting still remains challenge.

The pH of natural seawater is close to a neutral state with pH values ranging between 7.5 and 8.4 [159]. As illustrated in Table 1.6, the majority ions in the natural seawater are Na^+ and Cl^- ions, which could cause electrocatalyst corrosion and deterioration [160, 161]. Thus, the properties of natural seawater will greatly influence the design and operation of water electrolysis process, and sometimes, the pre-treatment process is required before use. There are numerous methods for treating the seawater before it is used as an electrolyte. For example, Zhang *et al.* [162] proposed a hybrid seawater electrolyzer (HSE) that combines seawater electrolysis and sulfion degradation, by which the key development is the reduction of seawater for HER at the cathode while degrading of the sulfion at the anode side, avoiding anode corrosion and Cl^- crossover and allowing fast and efficient degradation of S^{2-} pollutants to sulfur. Sun *et al.* [1] also mentioned that coupling of chlorine-free hybrid seawater splitting with hydrazine degradation can effectively reduce the energy input by 48% while provide high Faradaic efficiency without Cl^- crossover and prevent toxic hydrazine from polluting seawater. In this system, the cathode side is used for HER from seawater while the anode side is supplied with OH^- crossover for hydrazine degradation to reduce salinity, which is separated by an anion exchange membrane (AEM).

The electrolytes used in water water electrolysis cell are summarized in Table 1.7.

Table 1.6 Chemical compositions of natural seawater [160, 161]

Common Name	Elements	Chemical species	Concentration (ppm)
Chloride	Cl	Cl^-	~19500–22014
Sodium	Na	Na^+	~11536–14039
Magnesium	Mg	Mg^{2+}	~1290–1543
Sulfur	S	SO_4^{2-}, $NaSO_4^+$	~905–3273
Calcium	Ca	Ca^{2+}	~378–420
Potassium	K	K^+	~380–470
Bromine	Br	Br^-	~67

Carbon	C	$HClO_3^-$, CO_3^{2-}	~28
Nitrogen	N	NO_3^-, NH_4^+	~12

Table 1.7 Summary of the electrolytes used in electrolysis cell

Electrolyte	pH
Alkaline solution (1M KOH, 1M NaOH)	14
Simulated seawater solution (1M KOH+0.5M NaCl)	13.8
Borate buffer	9.2
Carbonate buffer	8.6
Phosphate buffer	6.4-7
Acidic solution (0.5M H_2SO_4)	3

1.7.3 Input current

1.7.3.1 Continuous current

Continuous electrochemical water electrolysis is a general process for hydrogen production using a constant current input. Acid and alkaline freshwater solutions are usually used as the electrolyte in this system. However, considering the sustainability, using freshwater with higher cost and scarcity is not recommended. While, using renewable energy based electricity should be a sustainable way for water splitting.

1.7.3.2 Intermittent current or power interruption

Water electrolysis can be electrified by intermittent renewable energy sources like solar and wind powers, which can make hydrogen production more environmentally friendly. However, if the electrolyzer is powered by the intermittent renewable energy, frequent power interruption and shutting downs can hasten electrode degradation [163, 164]. In order to simulate power interruption condition, the chronoamperometric test can be used by setting up the power in an on-off condition and measure the current density with a constant applied potential and comparing with the continuous electrolysis. Herein, the corresponding current density is always recorded to verify the electrocatalysis activity and stability.

1.7.3.3 High current density

For the large-scale water electrolyzer, it is necessary to have highly durable electrocatalysts which can be worked at a high current density above 0.5 A cm^{-2} or 1 A cm^{-2} for alkaline electrocatalytic cells or proton exchange membrane [165, 166]. To date, the majority of reported electrocatalysts have been reported at a relatively low current densities (< 0.1 A cm^{-2}), which is incompatible with industrial qualification, but only a few works on OER electrocatalysts have been investigated under harsh conditions [167]. Notably, most developed electrocatalysts are always deactivated during the OER process at a high current density. For example, Zhou *et al.* [168] mentioned that the stability of NiFe-LDH on Cu nanowires is not good at a high current density (0.5 A cm^{-2}) under alkaline condition (1 M KOH solution). Gupta *et al.* [169] used a Co-Fe-O-B electrocatalyst for OER in saline water (1 M KOH + 0.5 M NaCl), which exhibited high activity with a low overpotential of 294 mV@10 mAcm^{-2}, but the current lost nearly 35% after stability test for 20 hours. Besides, the faradaic efficiency was also reduced from nearly 100% to ~74% due to Cl^{-} oxidation at a high current density (e.g., 0.1 A cm^{-2}) [169]. Therefore, seeking for a catalyst which can maintain its initial performance for long-term operation at a high current density is greatly desired for the improvement of electrolysis efficiency for large-scale water splitting.

1.8 EVALUATING PERFORMANCE

1.8.1 Electrocatalytic activity

The activity of electrode is generally characterized by determining overpotential, Tafel slope, and exchange current density via the calculations based on the measured polarization curves [170]. The overpotential (η) is defined as the difference between the applied potentials required to deliver a current density and thermodynamic potential value, which is commonly used to estimated the catalytic activity for water splitting

[171]. The equilibrium potentials for HER and OER are known to be 0 and 1.23 V (both *vs* RHE), respectively. Because of the intrinsic kinetic barrier, an extra potential which is larger than the equilibrium potential is always needed to activate the reactions. Such an extra potential is defined as the overpotential. In generally, linear sweep voltammetry (LSV) and cyclic voltammetry (CV) test can be utilized for determine an electrocatalytic activity. A smaller overpotential means higher electrocatalytic activity [94]. Moreover, the overpotential @10 mA cm^{-2}, which is equivalent to a 10% efficiency of solar-driven water electrolysis, is usually reported as the standard basis for comparison of different electrocatalysts [78].

Owing to the slow kinetics of the four-electron transfer reaction, the OER is the hindrance for scaling-up in a water electrolysis system whereas the HER is just a two-electron transfer reactions. Thus, OER requires more energy (higher overpotential value) to overcome the kinetic barrier [78]. The Tafel slope is an overpotential-dependent criterion, which is associated with catalytic reaction mechanism for both HER and OER in terms of electron-transfer kinetics.The value of Tafel slope refers to certain pathway for the catalytic reaction. As such, if the Tafel slope (mV/decade) is lower meaning that less overpotential is required to get high current and faster kinetics. The Tafel slope can be used to identify the rate-determining step (RDS) for both HER and OER [172]. Theoretically, the Tafel slope for HER is about 40-120 mV dec^{-1}. The rate determining step of the reaction can be determined using the Tafel slope value [173]. The exchange current density (i$_0$) can be used to explain the intrinsic charge transfer under the equilibrium condition. A greater charge transfer rate and a lower reaction barrier are associated with a higher exchange current density. In conclusion, a superior electrocatalyst should have a lower overpotential, a smaller Tafel slope and a higher exchange current density [170, 174].

42

1.8.2 Stability

Catalyst stability is an important criteria for predicting potential industrial-scale application. The commercialized electrode must be able to operate for hundreads to thousands of hours or cycles with negligible change [175]. The applied fixed potential and current can be measured using chronoamperorometry (I-t curve) and chronopotentiometry (E-t curve) over a period of time to determine the stability. There is no benchmark for the stability test, however, numerous studies have been reported stability for at least 10 h at 10 mA cm^{-2} [170]. For large-scale application, the stability should be maintained over 100 hours at high current densities (>500-1000 mA cm^{-2}) [1]. Furthermore, cyclic voltammetry (CV) test with over 5000 cycles, which is also called accelerated degradation test (ADT), is also used to investigate the overpotential gap between before and after the test. Currently, the stability or durability of most electrocatalysts are still not satisfied for the industrial scale application. Kuang *et al.* reported a highly durable electrode for seawater splitting for over 1,000 h in a solar-driven alkaline seawater electrolysis system using the NiFe/NiS$_x$-Ni electrocatalyst, which is the most longest period of time for the electrocatalysts working in an alkaline seawater solution [125]. Recently, sophisciated *in-situ* techniques has been developed to monitor catalyst dissolution during the long-term operation. For example, electrochemical flow cells or the electrochemical quartz microbalance has been applied for a deeper understanding of catalyst degradation mechanism [176, 177].

1.8.3 Faradaic efficiency

Faradaic efficiency is used to describe the efficiency of electron transfer involved in the reaction for both HER and OER. It can be measured from the amount of gas production during the real reaction obtained from experiment and the calculated amount of gas produced theoretically. Herein, the amount of generated gas H_2/O_2 can be

examined by using gas chromatography (GC) measurement or a water displacing technique. It is reported that the amount of O_2 from OER can be defined by using a rotating-disk electrode (RDE) [94]. Faradaic efficiency can be evaluated from the ratio of experimental gas volume to the theoretical gas volume as shown in the following equation [178, 179]:

$$Faradaic\ efficiency\ = \frac{V_{Experimental}}{V_{Theoretical}} = \frac{V_{Experimental}}{\frac{1}{2(4)} \times \frac{Q}{F} \times V_m} \qquad (Eq.\ 35)$$

where, Q is charge passing through the electrode, F is Faraday's constant (96,485.3 C/mol), the numbers of 2 and 4 indicate mol of electrons per mole of H_2 (for HER) and O_2 (for OER), respectively, V_m is the molar volume of gas (24.5 L/mol, 298 K, 101 KPa). The high faradaic efficiency means that the electrode can be stable against oxidation or reduction for HER and OER, respectively. Therefore, a higher faradaic efficiency means a high catalytic efficiency.

1.8.4 Electrochemical active surface area (ECSA)

The intrinsic activity of the electrocatalyst is able to determine by ECSA normalization without the metal loading effect whereas the geometrical area normalized current density always shows a dependence on catalyst loading [180]. There are several methods to investigate the ECSA of catalyst. However, estimating the ECSA from the double layer capacitance (C_{dl}) using the Cyclic voltammetery (CV) method at various scan rates in non-faradic region is more accurate. In this case, the charging current is plotted at the various scan rates [181], and the ECSA can be evaluated using Eq. 36 [182]:

$$ECSA = C_{dl}/CS \qquad (Eq.\ 36)$$

where, C_{dl} (mF) is double layer capacitance from CV test; CS is the estimated specific capacitance of 0.04 mF cm^{-2} in alkaline solution.

1.8.5 Density functional theory (DFT) calculations

To further deep understanding the insight electronic state, coordinate environment of catalytic active sites and catalytic mechanism, density function theory (DFT) calculation is always used [183]. The DFT calculation can understand the adsorption/desorption kinetics, which corresponds to the Gibb's free energies, intermediates during HER/OER reaction, and energy barrier, thereby infering the rate determining step. Theoretically, HER and OER have different reaction mechanism since HER is a 2-electron pathway while OER involves in a four-electron pathway [96]. Therefore, the water adsorption energy and reaction intermediates are different and OER is considerably more complicated [184]. For HER, if adsorption free energy of H* closes to zero, implying higher catalytic activity. In general, the lower energy barrier means the improved kinetics with higher catalytic activity.

1.8.6 Chlorine Determination

Due to the competitive reaction between OER and ClER in the presence of Cl⁻ in the seawater solution, the formation of hydrochloric acid (HCl) and hypochlorous acid (HClO) as follows becomes possible [185, 186] ;

$$Cl_2 + 2H_2O \leftrightarrow HCl + HClO \qquad\qquad\qquad (Eq.\ 37)$$

$$Cl^- + 2OH^- \rightarrow ClO^- + H_2O + 2e^- \ ; pH = 14 \qquad (Eq.\ 38)$$
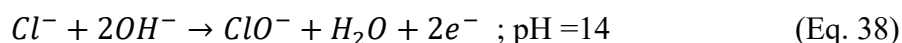
Ko *et al.*, designed an *in-situ* headspace Cl_2 gas detector that decoupled O_2 and Cl_2 generation from a rotating disk electrode. The concentration of Cl_2 is measured using chronoamperometry test during electrolysis [186]. For two-electrode configuration, Yu *et al.,* used 1M KOH + Seawater as electrolyte using Chronopotentiometry test with a constant current density, then removed the gaseous product with a syringe and injected it into a GC-TCD instrument [124].

1.9 OBJECTIVE OF THIS STUDY

According to the above review, for scaling up the experimental results from lab-scale to industrial-level by using natural seawater as a water resource for water splitting, either the electrocatalytic performance or the catalyst preparation step as well as the cost of chemical substances need to be considered. Therefore, searching for earth-abundant and cost-effective electrocatalysts with high electrocatalytic activity and durability, especially at a large current density for seawater electrolysis is still full of challenges. Besides, to meet the practical industrial-scale requirements, the electrocatalysts should be operated at high current density (> 500 mA/cm^2) to achieve a high hydrogen production efficiency. Therefore, the objective of this research focuses on developing earth-abundant and low-cost 3D transition metal-based nanostructured electrocatalysts for highly efficient and durable water electrolysis at a high current density for either HER or OER towards an industrial-scale. It is expected to prepare electrocatalysts with a high intrinsic activity with a low overpotential and Tafel slope, high electrical conductivity with fast electron transport properties, low charge transfer resistance, high electrocatalytic active surface area (ECSA), highly durable and close to theoretical Faradaic efficiency for water splitting in various electrolytes as well as input current densities. While, the reaction mechanism and surface adsorption enegy on the surface of electrodes were clarified.

1.10 SCOPE OF THIS DESSERTATION

Chapter 1 summarizes the reaction mechanism of water electrolysis, introduces current trends of anode/cathode materials, elucidates the effects of substrate and preparation method on the performance of electrocatalysts, emphasizes key kinetic parameters and performance evalution procedures. Finally, the objective of this study is given.

Chapter 2 reports that $CuVO_x$ nanobelt@NiO nanosheet with O vacancy-rich composite is successfully coated on the carbon paper by one-pot hydrothermal method followed by calcination. The morphology and oxidation state of prepared electrodes are examined before and after testing. In alkaline solution, the electrocatalytic activity and stability of HER are evaluated. The electrochemical active surface area is also investigated under the same condition. Furthermore, their electrochemical performance is evaluated and compared to a commercial nobel metal catalyst.

Chapter 3 introduces that the $FeNiS_x/NiFe(OH)_x$ on nickel form (NF) is successfully fabricated using a facile corrosion engineering followed by a fast and mild sulfurization process. In the preliminary step, the preparation time and morphology are investigated. The electrocatalytic performance of the obtained electrode is measured in both alkaline and alkaline simulated seawater solutions. The morphological and chemical states of initial and spent catalysts are characterized. The DFT calculations is also performed in order to elucidate OER mechanism and Cl^- adsorption energy on the electrode surface. This electrode is also used as a bifunctional electrocatalyst for overall seawater splitting, and its electrochemical performance is compared to a commercial electrode (Pt/RuO_2).

Chapter 4 reports that the NiFe-LDH core @$MnCo_2O_4$ shell electrocatalyst is fabricated in order to achieve outstanding electrocatalytic performance and corrosion resistance in an imitate seawater solution. It is found that the synergy of a large active surface area, Mn species with Cl^- blocking capability, and highly active NiFe-LDH can effectively improve activity and extend stability in chloride-containing solutions. The obtained electrode exhibits excellent catalytic activity for OER with low overpotentials of 219 and 460 mV at 100 and 500 mA/cm^2, respectively. Furthermore, it can operate for over 25 hours without corrosion in an imitation seawater solution even at a high current density of 1 A/cm^2 with complete OER selectivity against ClER. Furthermore,

the NiFe-LDH@MnCo$_2$O$_4$ can be used as a bifunctional electrocatalyst for overall seawater splitting, requiring only a low cell voltage of 1.54 V at 10 mA/cm^2 and maintaining its initial potential for 100 hours at a high current density without catalyst degradation and corrosion. Such an electrocatalyst is expected to be a promising candidate for sustaining seawater splitting in an industrial scale.

Chapter 5 summarizes the main results and new finding of this study and future perspective for large scale application is also discussed.

References

[1] F. Sun, J. Qin, Z. Wang, M. Yu, X. Wu, X. Sun, J. Qiu, Energy-saving hydrogen production by chlorine-free hybrid seawater splitting coupling hydrazine degradation, Nature Communications, 12 (2021) 4182.

[2] J. Wang, Y. Gao, H. Kong, J. Kim, S. Choi, F. Ciucci, Y. Hao, S. Yang, Z. Shao, J. Lim, Non-precious-metal catalysts for alkaline water electrolysis: operando characterizations, theoretical calculations, and recent advances, Chemical Society Reviews, 49 (2020) 9154-9196.

[3] J.E. Lee, K.-J. Jeon, P.L. Show, I.H. Lee, S.-C. Jung, Y.J. Choi, G.H. Rhee, K.-Y.A. Lin, Y.-K. Park, Mini review on H_2 production from electrochemical water splitting according to special nanostructured morphology of electrocatalysts, Fuel, 308 (2022).

[4] Z. Cai, Q. Yao, X. Chen, X. Wang, Chapter 14 - Nanomaterials With Different Dimensions for Electrocatalysis, in: X. Wang, X. Chen (Eds.) Novel Nanomaterials for Biomedical, Environmental and Energy Applications, 2019, 435-464.

[5] S. Cherevko, S. Geiger, O. Kasian, N. Kulyk, J.-P. Grote, A. Savan, B.R. Shrestha, S. Merzlikin, B. Breitbach, A. Ludwig, K.J.J. Mayrhofer, Oxygen and hydrogen evolution reactions on Ru, RuO_2, Ir, and IrO_2 thin film electrodes in acidic and alkaline electrolytes: A comparative study on activity and stability, Catalysis Today, 262 (2016) 170-180.

[6] D.L. Smith Rodney, S. Prévot Mathieu, D. Fagan Randal, Z. Zhang, A. Sedach Pavel, J. Siu Man Kit, S. Trudel, P. Berlinguette Curtis, Photochemical Route for Accessing Amorphous Metal Oxide Materials for Water Oxidation Catalysis, Science, 340 (2013) 60-63.

[7] X. Xiao, L. Yang, W. Sun, Y. Chen, H. Yu, K. Li, B. Jia, L. Zhang, T. Ma, Electrocatalytic Water Splitting: From Harsh and Mild Conditions to Natural Seawater, Small, 18 (2022) 2105830.

[8] P.K.L. Tran, D.T. Tran, D. Malhotra, S. Prabhakaran, D.H. Kim, N.H. Kim, J.H. Lee, Highly Effective Freshwater and Seawater Electrolysis Enabled by Atomic Rh-Modulated Co-CoO Lateral Heterostructures, Small, 17 (2021) e2103826.

[9] F. Dionigi, T. Reier, Z. Pawolek, M. Gliech, P. Strasser, Design Criteria, Operating Conditions, and Nickel-Iron Hydroxide Catalyst Materials for Selective Seawater Electrolysis, ChemSusChem, 9 (2016) 962-972.

[10] W. Tong, M. Forster, F. Dionigi, S. Dresp, R. Sadeghi Erami, P. Strasser, A.J. Cowan, P. Farràs, Electrolysis of low-grade and saline surface water, Nature Energy, 5 (2020) 367-377.

[11] C. Hu, L. Zhang, J. Gong, Recent progress made in the mechanism comprehension and design of electrocatalysts for alkaline water splitting, Energy & Environmental Science, 12 (2019) 2620-2645.

[12] W. Sheng, H.A. Gasteiger, Y. Shao-Horn, Hydrogen Oxidation and Evolution Reaction Kinetics on Platinum: Acid vs Alkaline Electrolytes, Journal of The Electrochemical Society, 157 (2010).

[13] J. Mohammed-Ibrahim, X. Sun, Recent progress on earth abundant electrocatalysts for hydrogen evolution reaction (HER) in alkaline medium to achieve efficient water splitting – A review, Journal of Energy Chemistry, 34 (2019) 111-160.

[14] N. Zaman, T. Noor, N. Iqbal, Recent advances in the metal–organic framework-based electrocatalysts for the hydrogen evolution reaction in water splitting: a review, RSC Advances, 11 (2021) 21904-21925.

[15] K. Zhang, R. Zou, Advanced Transition Metal-Based OER Electrocatalysts: Current Status, Opportunities, and Challenges, Small, 17 (2021) 2100129.

[16] Z. Lei, T. Wang, B. Zhao, W. Cai, Y. Liu, S. Jiao, Q. Li, R. Cao, M. Liu, Recent Progress in Electrocatalysts for Acidic Water Oxidation, Advanced Energy Materials, 10 (2020) 2000478.

[17] I.C. Man, H.-Y. Su, F. Calle-Vallejo, H.A. Hansen, J.I. Martínez, N.G. Inoglu, J. Kitchin, T.F. Jaramillo, J.K. Nørskov, J. Rossmeisl, Universality in Oxygen Evolution Electrocatalysis on Oxide Surfaces, ChemCatChem, 3 (2011) 1159-1165.

[18] Z. Shi, X. Wang, J. Ge, C. Liu, W. Xing, Fundamental understanding of the acidic oxygen evolution reaction: mechanism study and state-of-the-art catalysts, Nanoscale, 12 (2020) 13249-13275.

[19] M. Wang, L. Zhang, Y. He, H. Zhu, Recent advances in transition-metal-sulfide-based bifunctional electrocatalysts for overall water splitting, Journal of Materials Chemistry A, 9 (2021) 5320-5363.

[20] Q. Liang, G. Brocks, A. Bieberle-Hütter, Oxygen evolution reaction (OER) mechanism under alkaline and acidic conditions, Journal of Physics: Energy, 3 (2021) 026001.

[21] J. Song, C. Wei, Z.-F. Huang, C. Liu, L. Zeng, X. Wang, Z.J. Xu, A review on fundamentals for designing oxygen evolution electrocatalysts, Chemical Society Reviews, 49 (2020) 2196-2214.

[22] X.-P. Li, C. Huang, W.-K. Han, T. Ouyang, Z.-Q. Liu, Transition metal-based electrocatalysts for overall water splitting, Chinese Chemical Letters, 32 (2021) 2597-2616.

[23] M. Maril, J.-L. Delplancke, N. Cisternas, P. Tobosque, Y. Maril, C. Carrasco, Critical aspects in the development of anodes for use in seawater electrolysis, International Journal of Hydrogen Energy, 47 (2022) 3532-3549.

[24] C.A.R.M.A.S.O. Martinez-Huitle, Electrochemical Water and Wastewater Treatment, (2018).

[25] S. Feng, Y. Yu, J. Li, J. Luo, P. Deng, C. Jia, Y. Shen, X. Tian, Recent progress in seawater electrolysis for hydrogen evolution by transition metal phosphides, Catalysis Communications, 162 (2022) 106382.

[26] S. Khatun, H. Hirani, P. Roy, Seawater electrocatalysis: activity and selectivity, Journal of Materials Chemistry A, 9 (2021) 74-86.

[27] M. Gong, W. Zhou, M.J. Kenney, R. Kapusta, S. Cowley, Y. Wu, B. Lu, M.C. Lin, D.Y. Wang, J. Yang, B.J. Hwang, H. Dai, Blending Cr_2O_3 into a NiO-Ni electrocatalyst for sustained water splitting, Angew Chem Int Ed Engl, 54 (2015) 11989-11993.

[28] X. Lu, J. Pan, E. Lovell, T.H. Tan, Y.H. Ng, R. Amal, A sea-change: manganese doped nickel/nickel oxide electrocatalysts for hydrogen generation from seawater, Energy & Environmental Science, 11 (2018) 1898-1910.

[29] D. Wu, D. Chen, J. Zhu, S. Mu, Ultralow Ru Incorporated Amorphous Cobalt-Based Oxides for High-Current-Density Overall Water Splitting in Alkaline and Seawater Media, Small, 17 (2021) 2102777.

[30] K. Jiang, W. Liu, W. Lai, M. Wang, Q. Li, Z. Wang, J. Yuan, Y. Deng, J. Bao, H. Ji, NiFe Layered Double Hydroxide/FeOOH Heterostructure Nanosheets as an Efficient and Durable Bifunctional Electrocatalyst for Overall Seawater Splitting, Inorganic Chemistry, 60 (2021) 17371-17378.

[31] B.E. Conway, G. Jerkiewicz, Nature of electrosorbed H and its relation to metal dependence of catalysis in cathodic H_2 evolution, Solid State Ionics, 150 (2002) 93-103.

[32] B.E. Conway, G. Jerkiewicz, Relation of energies and coverages of underpotential and overpotential deposited H at Pt and other metals to the 'volcano curve' for cathodic H_2 evolution kinetics, Electrochimica Acta, 45 (2000) 4075-4083.

[33] S. Jiang, H. Suo, T. Zhang, C. Liao, Y. Wang, Q. Zhao, W. Lai, Recent Advances in Seawater Electrolysis, Catalysts, 12 (2022).

[34] J. Zheng, Binary platinum alloy electrodes for hydrogen and oxygen evolutions by seawater splitting, Applied Surface Science, 413 (2017) 72-82.

[35] J. Zheng, Y. Zhao, H. Xi, C. Li, Seawater splitting for hydrogen evolution by robust electrocatalysts from secondary M (M = Cr, Fe, Co, Ni, Mo) incorporated Pt, RSC Advances, 8 (2018) 9423-9429.

[36] C. Ros, S. Murcia-López, X. Garcia, M. Rosado, J. Arbiol, J. Llorca, J.R. Morante, Facing Seawater Splitting Challenges by Regeneration with Ni−Mo−Fe Bifunctional Electrocatalyst for Hydrogen and Oxygen Evolution, ChemSusChem, 14 (2021) 2872-2881.

[37] Y. Guo, T. Park, J.W. Yi, J. Henzie, J. Kim, Z. Wang, B. Jiang, Y. Bando, Y. Sugahara, J. Tang, Y. Yamauchi, Nanoarchitectonics for Transition-Metal-Sulfide-Based Electrocatalysts for Water Splitting, Advanced Materials, 31 (2019) 1807134.

[38] S. Nouseen, P. Singh, S. Lavate, J. Chattopadhyay, A.M. Kuchkaev, D.G. Yakhvarov, R. Srivastava, Transition metal based ternary hierarchical metal sulphide microspheres as electrocatalyst for splitting of water into hydrogen and oxygen fuel, Catalysis Today, 397-399 (2022) 618-630.

[39] W. He, H. Liu, J. Cheng, J. Mao, C. Chen, Q. Hao, J. Zhao, C. Liu, Y. Li, L. Liang, Designing Zn-doped nickel sulfide catalysts with an optimized electronic structure for enhanced hydrogen evolution reaction, Nanoscale, 13 (2021) 10127-10132.

[40] B. Zhang, X. Fu, L. Song, X. Wu, Surface selectivity of Ni_3S_2 toward hydrogen evolution reaction: a first-principles study, Physical Chemistry Chemical Physics, 22 (2020) 25685-25694.

[41] K.L. Ao, Y. Shao, I.N. Chan, X. Shi, Y. Kawazoe, M. Yang, K.W. Ng, H. Pan, Design of novel pentagonal 2D transitional-metal sulphide monolayers for hydrogen evolution reaction, International Journal of Hydrogen Energy, 45 (2020) 16201-16209.

[42] J. Xie, H. Zhang, S. Li, R. Wang, X. Sun, M. Zhou, J. Zhou, X.W. Lou, Y. Xie, Defect-Rich MoS_2 Ultrathin Nanosheets with Additional Active Edge Sites for Enhanced Electrocatalytic Hydrogen Evolution, Advanced Materials, 25 (2013) 5807-5813.

[43] J. Xie, J. Zhang, S. Li, F. Grote, X. Zhang, H. Zhang, R. Wang, Y. Lei, B. Pan, Y. Xie, Controllable Disorder Engineering in Oxygen-Incorporated MoS_2 Ultrathin Nanosheets for Efficient Hydrogen Evolution, Journal of the American Chemical Society, 135 (2013) 17881-17888.

[44] S. Duraisamy, A. Ganguly, P.K. Sharma, J. Benson, J. Davis, P. Papakonstantinou, One-Step Hydrothermal Synthesis of Phase-Engineered MoS_2/MoO_3 Electrocatalysts for Hydrogen Evolution Reaction, ACS Applied Nano Materials, 4 (2021) 2642-2656.

[45] Y. Li, Z. Dong, L. Jiao, Multifunctional Transition Metal-Based Phosphides in Energy-Related Electrocatalysis, Advanced Energy Materials, 10 (2020) 1902104.

[46] Y. Shi, B. Zhang, Recent advances in transition metal phosphide nanomaterials: synthesis and applications in hydrogen evolution reaction, Chem Soc Rev, 45 (2016) 1529-1541.

[47] D. Liu, H. Ai, M. Chen, P. Zhou, B. Li, D. Liu, X. Du, K.H. Lo, K.-W. Ng, S.-P. Wang, S. Chen, G. Xing, J. Hu, H. Pan, Multi-Phase Heterostructure of $CoNiP/Co_xP$

for Enhanced Hydrogen Evolution Under Alkaline and Seawater Conditions by Promoting H2O Dissociation, Small, 17 (2021) 2007557.

[48] L. Wu, L. Yu, F. Zhang, B. McElhenny, D. Luo, A. Karim, S. Chen, Z. Ren, Heterogeneous Bimetallic Phosphide Ni_2P-Fe_2P as an Efficient Bifunctional Catalyst for Water/Seawater Splitting, Advanced Functional Materials, 31 (2021) 2006484.

[49] Y. Cao, X. Zheng, H. Zhang, J. Zhang, X. Han, C. Zhong, W. Hu, Y. Deng, Interface engineering of NiS_2/CoS_2 nanohybrids as bifunctional electrocatalysts for rechargeable solid state Zn-air battery, Journal of Power Sources, 437 (2019) 226893.

[50] J. Chang, G. Wang, Z. Yang, B. Li, Q. Wang, R. Kuliiev, N. Orlovskaya, M. Gu, Y. Du, G. Wang, Y. Yang, Dual-Doping and Synergism toward High-Performance Seawater Electrolysis, Adv Mater, 33 (2021) e2101425.

[51] L. Yu, L. Wu, S. Song, B. McElhenny, F. Zhang, S. Chen, Z. Ren, Hydrogen Generation from Seawater Electrolysis over a Sandwich-like $NiCoN|Ni_xP|NiCoN$ Microsheet Array Catalyst, ACS Energy Letters, 5 (2020) 2681-2689.

[52] L. Xiu, W. Pei, S. Zhou, Z. Wang, P. Yang, J. Zhao, J. Qiu, Multilevel Hollow MXene Tailored Low-Pt Catalyst for Efficient Hydrogen Evolution in Full-pH Range and Seawater, Advanced Functional Materials, 30 (2020) 1910028.

[53] B. Anasori, M.R. Lukatskaya, Y. Gogotsi, 2D metal carbides and nitrides (MXenes) for energy storage, Nature Reviews Materials, 2 (2017) 16098.

[54] I. Ihsanullah, Potential of MXenes in Water Desalination: Current Status and Perspectives, Nano-Micro Letters, 12 (2020) 72.

[55] M. Zubair, M.M. Ul Hassan, M.T. Mehran, M.M. Baig, S. Hussain, F. Shahzad, 2D MXenes and their heterostructures for HER, OER and overall water splitting: A review, International Journal of Hydrogen Energy, 47 (2022) 2794-2818.

[56] S. Bai, M. Yang, J. Jiang, X. He, J. Zou, Z. Xiong, G. Liao, S. Liu, Recent advances of MXenes as electrocatalysts for hydrogen evolution reaction, npj 2D Materials and Applications, 5 (2021) 78.

[57] M. Tian, Y. Jiang, H. Tong, Y. Xu, L. Xia, MXene-Supported FeCo-LDHs as Highly Efficient Catalysts for Enhanced Electrocatalytic Oxygen Evolution Reaction, ChemNanoMat, 6 (2019) 154-159.

[58] H. Zou, B. He, P. Kuang, J. Yu, K. Fan, Metal–Organic Framework-Derived Nickel–Cobalt Sulfide on Ultrathin Mxene Nanosheets for Electrocatalytic Oxygen Evolution, ACS Applied Materials & Interfaces, 10 (2018) 22311-22319.

[59] X. Wu, S. Zhou, Z. Wang, J. Liu, W. Pei, P. Yang, J. Zhao, J. Qiu, Engineering Multifunctional Collaborative Catalytic Interface Enabling Efficient Hydrogen Evolution in All pH Range and Seawater, Advanced Energy Materials, 9 (2019) 1901333.

[60] L. Zhang, Q. Fan, K. Li, S. Zhang, X. Ma, First-row transition metal oxide oxygen evolution electrocatalysts: regulation strategies and mechanistic understandings, Sustainable Energy & Fuels, 4 (2020) 5417-5432.

[61] S. Wang, X. Ge, C. Lv, C. Hu, H. Guan, J. Wu, Z. Wang, X. Yang, Y. Shi, J. Song, Z. Zhang, A. Watanabe, J. Cai, Oxygen vacancy-rich amorphous porous $NiFe(OH)_x$ derived from $Ni(OH)_x$/Prussian blue as highly efficient oxygen evolution electrocatalysts, Nanoscale, 12 (2020) 9557-9568.

[62] Z. He, J. Zhang, Z. Gong, H. Lei, D. Zhou, N. Zhang, W. Mai, S. Zhao, Y. Chen, Activating lattice oxygen in NiFe-based (oxy)hydroxide for water electrolysis, Nature Communications, 13 (2022) 2191.

[63] J. Jana, K.C. Bhamu, Y.-L.T. Ngo, S.G. Kang, J.S. Chung, S.H. Hur, Designing a bimetallic transition metal oxide/hydroxide composite for effective electrocatalytic oxygen evolution reaction, Applied Surface Science, 562 (2021) 150253.

[64] J. Huang, Y. Li, Y. Zhang, G. Rao, C. Wu, Y. Hu, X. Wang, R. Lu, Y. Li, J. Xiong, Identification of Key Reversible Intermediates in Self-Reconstructed Nickel-Based Hybrid Electrocatalysts for Oxygen Evolution, Angewandte Chemie International Edition, 58 (2019) 17458-17464.

[65] J. Yuan, X. Cheng, C. Lei, B. Yang, Z. Li, K. Luo, K.H. Koko Lam, L. Lei, Y. Hou, K.K. Ostrikov, Bimetallic Oxyhydroxide as a High-Performance Water Oxidation Electrocatalyst under Industry-Relevant Conditions, Engineering, 7 (2021) 1306-1312.

[66] P. Babar, K. Patil, D.M. Lee, V. Karade, K. Gour, S. Pawar, J.H. Kim, Cost-effective and efficient water and urea oxidation catalysis using nickel-iron oxyhydroxide nanosheets synthesized by an ultrafast method, Journal of Colloid and Interface Science, 584 (2021) 760-769.

[67] X. Long, Z. Wang, S. Xiao, Y. An, S. Yang, Transition metal based layered double hydroxides tailored for energy conversion and storage, Materials Today, 19 (2016) 213-226.

[68] J. Li, L. Wang, H. He, Y. Chen, Z. Gao, N. Ma, B. Wang, L. Zheng, R. Li, Y. Wei, J. Xu, Y. Xu, B. Cheng, Z. Yin, D. Ma, Interface construction of NiCo LDH/NiCoS based on the 2D ultrathin nanosheet towards oxygen evolution reaction, Nano Research, (2022).

[69] F. Dionigi, T. Reier, Z. Pawolek, M. Gliech, P. Strasser, Design Criteria, Operating Conditions, and Nickel–Iron Hydroxide Catalyst Materials for Selective Seawater Electrolysis, ChemSusChem, 9 (2016) 962-972.

[70] G. Dong, F. Xie, F. Kou, T. Chen, F. Wang, Y. Zhou, K. Wu, S. Du, M. Fang, J.C. Ho, NiFe-layered double hydroxide arrays for oxygen evolution reaction in fresh water and seawater, Materials Today Energy, 22 (2021).

[71] F. Cheng, X. Feng, X. Chen, W. Lin, J. Rong, W. Yang, Synergistic action of Co-Fe layered double hydroxide electrocatalyst and multiple ions of sea salt for efficient seawater oxidation at near-neutral pH, Electrochimica Acta, 251 (2017) 336-343.

[72] W. Liu, K. Jiang, Y. Hu, Q. Li, Y. Deng, J. Bao, Y. Lei, Zr-doped CoFe-layered double hydroxides for highly efficient seawater electrolysis, Journal of Colloid and Interface Science, 604 (2021) 767-775.

[73] H. You, D. Wu, D. Si, M. Cao, F. Sun, H. Zhang, H. Wang, T.-F. Liu, R. Cao, Monolayer NiIr-Layered Double Hydroxide as a Long-Lived Efficient Oxygen Evolution Catalyst for Seawater Splitting, Journal of the American Chemical Society, (2022).

[74] L. Yu, J. Xiao, C. Huang, J. Zhou, M. Qiu, Y. Yu, Z. Ren, C.W. Chu, J.C. Yu, High-performance seawater oxidation by a homogeneous multimetallic layered double hydroxide electrocatalyst, Proc Natl Acad Sci U S A, 119 (2022) e2202382119.

[75] G. Janani, Y. Chae, S. Surendran, Y. Sim, W. Park, J.K. Kim, U. Sim, Rational Design of Spinel Oxide Nanocomposites with Tailored Electrochemical Oxygen Evolution and Reduction Reactions for ZincAir Batteries, Applied Sciences, 10 (2020).

[76] T.W. Kim, M.A. Woo, M. Regis, K.-S. Choi, Electrochemical Synthesis of Spinel Type $ZnCo_2O_4$ Electrodes for Use as Oxygen Evolution Reaction Catalysts, The Journal of Physical Chemistry Letters, 5 (2014) 2370-2374.

[77] J. Liu, H. Bao, B. Zhang, Q. Hua, M. Shang, J. Wang, L. Jiang, Geometric Occupancy and Oxidation State Requirements of Cations in Cobalt Oxides for Oxygen Reduction Reaction, ACS Applied Materials & Interfaces, 11 (2019) 12525-12534.

[78] N.-T. Suen, S.-F. Hung, Q. Quan, N. Zhang, Y.-J. Xu, H.M. Chen, Electrocatalysis for the oxygen evolution reaction: recent development and future perspectives, Chemical Society Reviews, 46 (2017) 337-365.

[79] M. Li, Y. Xiong, X. Liu, X. Bo, Y. Zhang, C. Han, L. Guo, Facile synthesis of electrospun MFe_2O_4 (M = Co, Ni, Cu, Mn) spinel nanofibers with excellent electrocatalytic properties for oxygen evolution and hydrogen peroxide reduction, Nanoscale, 7 (2015) 8920-8930.

[80] M. Harada, F. Kotegawa, M. Kuwa, Structural Changes of Spinel MCo_2O_4 (M = Mn, Fe, Co, Ni, and Zn) Electrocatalysts during the Oxygen Evolution Reaction Investigated by In Situ X-ray Absorption Spectroscopy, ACS Applied Energy Materials, 5 (2022) 278-294.

[81] A. Li, S. Kong, C. Guo, H. Ooka, K. Adachi, D. Hashizume, Q. Jiang, H. Han, J. Xiao, R. Nakamura, Enhancing the stability of cobalt spinel oxide towards sustainable oxygen evolution in acid, Nature Catalysis, 5 (2022) 109-118.

[82] H. Yang, M. Zhu, X. Guo, C. Yan, S. Lin, Anchoring MCo_2O_4 Nanorods from Bimetal-Organic Framework on rGO for High-Performance Oxygen Evolution and Reduction Reaction, ACS Omega, 4 (2019) 22325-22331.

[83] A. Bahadur, W. Hussain, S. Iqbal, F. Ullah, M. Shoaib, G. Liu, K. Feng, A morphology controlled surface sulfurized $CoMn_2O_4$ microspike electrocatalyst for water splitting with excellent OER rate for binder-free electrocatalytic oxygen evolution, Journal of Materials Chemistry A, 9 (2021) 12255-12264.

[84] X. Wang, Z. Liu, Z. Guo, L. Ge, Z. Liu, $NiO–CoFe_2O_4$ electrocatalyst prepared on Ni foam by one-step hydrothermal method for efficient overall water splitting, Journal of Materials Science, 56 (2021) 8575-8587.

[85] N. Wen, Y. Xia, H. Wang, D. Zhang, H. Wang, X. Wang, X. Jiao, D. Chen, Large-Scale Synthesis of Spinel $Ni_x Mn_{3-x} O_4$ Solid Solution Immobilized with Iridium Single Atoms for Efficient Alkaline Seawater Electrolysis, Adv Sci, (2022) 2200529.

[86] X. Chia, A.Y.S. Eng, A. Ambrosi, S.M. Tan, M. Pumera, Electrochemistry of Nanostructured Layered Transition-Metal Dichalcogenides, Chemical Reviews, 115 (2015) 11941-11966.

[87] C. Zhu, D. Gao, J. Ding, D. Chao, J. Wang, TMD-based highly efficient electrocatalysts developed by combined computational and experimental approaches, Chemical Society Reviews, 47 (2018) 4332-4356.

[88] R. Zhang, Z. Zhu, J. Lin, K. Zhang, N. Li, C. Zhao, Hydrolysis assisted in-situ growth of 3D hierarchical FeS/NiS/nickel foam electrode for overall water splitting, Electrochimica Acta, 332 (2020) 135534.

[89] U.N. Pan, T.I. Singh, D.R. Paudel, C.C. Gudal, N.H. Kim, J.H. Lee, Covalent doping of Ni and P on 1T-enriched MoS_2 bifunctional 2D-nanostructures with active basal planes and expanded interlayers boosts electrocatalytic water splitting, Journal of Materials Chemistry A, 8 (2020) 19654-19664.

[90] X.Y. Yu, X.W. Lou, Mixed Metal Sulfides for Electrochemical Energy Storage and Conversion, Advanced Energy Materials, 8 (2018) 1701592.

[91] D. Li, Z. Liu, J. Wang, B. Liu, Y. Qin, W. Yang, J. Liu, Hierarchical trimetallic sulfide $FeCo_2S_4$–$NiCo_2S_4$ nanosheet arrays supported on a Ti mesh: An efficient 3D bifunctional electrocatalyst for full water splitting, Electrochimica Acta, 340 (2020) 135957.

[92] Z.K. Ghouri, K. Elsaid, M. Mahmoud Nasef, A. Badreldin, Y. Wubulikasimu, A. Abdel-Wahab, Incorporation of manganese carbonyl sulfide (($Mn_2S_2 (CO)_7$) and mixed metal oxides-decorated reduced graphene oxide ($MnFeCoO_4$/rGO) as a selective anode

toward efficient OER from seawater splitting under neutral pH conditions, Renewable Energy, 190 (2022) 1029-1040.

[93] P. Chen, T. Zhou, M. Zhang, Y. Tong, C. Zhong, N. Zhang, L. Zhang, C. Wu, Y. Xie, 3D Nitrogen-Anion-Decorated Nickel Sulfides for Highly Efficient Overall Water Splitting, Advanced Materials, 29 (2017) 1701584.

[94] Y. Guo, T. Park, J.W. Yi, J. Henzie, J. Kim, Z. Wang, B. Jiang, Y. Bando, Y. Sugahara, J. Tang, Y. Yamauchi, Nanoarchitectonics for Transition-Metal-Sulfide-Based Electrocatalysts for Water Splitting, Adv Mater, 31 (2019) 1807134.

[95] J. Hu, Y. Ou, Y. Li, D. Gao, Y. Zhang, P. Xiao, $FeCo_2S_4$ Nanosheet Arrays Supported on Ni Foam: An Efficient and Durable Bifunctional Electrocatalyst for Overall Water-Splitting, ACS Sustainable Chemistry & Engineering, 6 (2018) 11724-11733.

[96] H. Yang, L. Gong, H. Wang, C. Dong, J. Wang, K. Qi, H. Liu, X. Guo, B.Y. Xia, Preparation of nickel-iron hydroxides by microorganism corrosion for efficient oxygen evolution, Nature Communications, 11 (2020) 5075.

[97] L. Qi, A. Li, M. Wang, Y. Zhang, K. Zhang, X. Li, Stable and Efficient Oxygen Evolution from Seawater Enabled by Graphene-Supported Sub-Nanometer Arrays of Transition Metal Phosphides, Advanced Materials Interfaces, 9 (2022) 2101720.

[98] Y. Zhao, B. Jin, A. Vasileff, Y. Jiao, S.-Z. Qiao, Interfacial nickel nitride/sulfide as a bifunctional electrode for highly efficient overall water/seawater electrolysis, Journal of Materials Chemistry A, 7 (2019) 8117-8121.

[99] Y. Li, X. Wu, J. Wang, H. Wei, S. Zhang, S. Zhu, Z. Li, S. Wu, H. Jiang, Y. Liang, Sandwich structured Ni_3S_2-MoS_2-Ni_3S_2@Ni foam electrode as a stable bifunctional electrocatalyst for highly sustained overall seawater splitting, Electrochimica Acta, 390 (2021) 138833.

[100] H. Wang, L. Chen, L. Tan, X. Liu, Y. Wen, W. Hou, T. Zhan, Electrodeposition of NiFe-layered double hydroxide layer on sulfur-modified nickel molybdate nanorods for highly efficient seawater splitting, Journal of Colloid and Interface Science, 613 (2022) 349-358.

[101] S. Seenivasan, D.-H. Kim, Engineering the surface anatomy of an industrially durable $NiCo_2S_4/NiMo_2S_4/NiO$ bifunctional electrode for alkaline seawater electrolysis, Journal of Materials Chemistry A, 10 (2022) 9547-9564.

[102] J. Chang, G. Wang, Z. Yang, B. Li, Q. Wang, R. Kuliiev, N. Orlovskaya, M. Gu, Y. Du, G. Wang, Y. Yang, Dual-Doping and Synergism toward High-Performance Seawater Electrolysis, Advanced Materials, 33 (2021) 2101425.

[103] S. Wang, P. Yang, X. Sun, H. Xing, J. Hu, P. Chen, Z. Cui, W. Zhu, Z. Ma, Synthesis of 3D heterostructure Co-doped Fe_2P electrocatalyst for overall seawater electrolysis, Applied Catalysis B: Environmental, 297 (2021) 120386.

[104] Y. Zhang, B. Ouyang, J. Xu, S. Chen, R.S. Rawat, H.J. Fan, 3D Porous Hierarchical Nickel–Molybdenum Nitrides Synthesized by RF Plasma as Highly Active and Stable Hydrogen-Evolution-Reaction Electrocatalysts, Advanced Energy Materials, 6 (2016) 1600221.

[105] L. Yu, Q. Zhu, S. Song, B. McElhenny, D. Wang, C. Wu, Z. Qin, J. Bao, Y. Yu, S. Chen, Z. Ren, Non-noble metal-nitride based electrocatalysts for high-performance alkaline seawater electrolysis, Nature Communications, 10 (2019) 5106.

[106] R. Li, Y. Li, P. Yang, P. Ren, D. Wang, X. Lu, R. Xu, Y. Li, J. Xue, J. Zhang, M. An, J. Ma, B. Wang, H. Liu, S. Dou, Synergistic interface engineering and structural optimization of non-noble metal telluride-nitride electrocatalysts for sustainably overall seawater electrolysis, Applied Catalysis B: Environmental, 318 (2022) 121834.

[107] L. Ma, K. Zhang, S. Wang, L. Gao, Y. Sun, Q. Liu, J. Guo, X. Zhang, Vanadium doping over Ni_3S_2 nanosheet array for improved overall water splitting, Applied Surface Science, 489 (2019) 815-823.

[108] H.N. Dhandapani, D. Mahendiran, A. Karmakar, P. Devi, S. Nagappan, R. Madhu, K. Bera, P. Murugan, B.R. Babu, S. Kundu, Boosting of overall water splitting activity by regulating the electron distribution over the active sites of Ce doped NiCo–LDH and atomic level understanding of the catalyst by DFT study, Journal of Materials Chemistry A, 10 (2022) 17488-17500.

[109] H. Jin, X. Liu, A. Vasileff, Y. Jiao, Y. Zhao, Y. Zheng, S.-Z. Qiao, Single-Crystal Nitrogen-Rich Two-Dimensional Mo_5N_6 Nanosheets for Efficient and Stable Seawater Splitting, ACS Nano, 12 (2018) 12761-12769.

[110] W. Zang, T. Sun, T. Yang, S. Xi, M. Waqar, Z. Kou, Z. Lyu, Y.P. Feng, J. Wang, S.J. Pennycook, Efficient Hydrogen Evolution of Oxidized $Ni-N_3$ Defective Sites for Alkaline Freshwater and Seawater Electrolysis, Advanced Materials, 33 (2021) 2003846.

[111] L. Wu, L. Yu, B. McElhenny, X. Xing, D. Luo, F. Zhang, J. Bao, S. Chen, Z. Ren, Rational design of core-shell-structured CoP @FeOOH for efficient seawater electrolysis, Applied Catalysis B: Environmental, 294 (2021).

[112] Y. Huang, L. Hu, R. Liu, Y. Hu, T. Xiong, W. Qiu, M.S. Balogun, A. Pan, Y. Tong, Nitrogen treatment generates tunable nanohybridization of Ni_5P_4 nanosheets with nickel hydr(oxy)oxides for efficient hydrogen production in alkaline, seawater and acidic media, Applied Catalysis B: Environmental, 251 (2019) 181-194.

[113] Y. Xiong, L. Xu, C. Jin, Interface-Engineered Atomically Thin Ni_3S_2/MnO_2 Heterogeneous Nanoarrays for Efficient Overall Water Splitting in Alkaline Media, Applied Catalysis B: Environmental, 254 (2019).

[114] P. Babar, K. Patil, J. Mahmood, S.-j. Kim, J.H. Kim, C.T. Yavuz, Low-overpotential overall water splitting by a cooperative interface of cobalt-iron hydroxide and iron oxyhydroxide, Cell Reports Physical Science, 3 (2022) 100762.

[115] L. Xu, B. Yuan, L. Min, W. Xu, W. Zhang, Preparation of NiCo-LDH@NiCoV-LDH interconnected nanosheets as high-performance electrocatalysts for overall water splitting, International Journal of Hydrogen Energy, 47 (2022) 15583-15592.

[116] W. He, D. Cao, D. Ma, Y. Li, C. Chen, L. Liang, H. Liu, Engineering nickel vacancies in NiCo LDH nanoarrays accelerates hydrogen evolution and oxygen evolution reactions, Chemical Communications, 58 (2022) 7757-7760.

[117] F. Zhang, Y. Liu, L. Wu, M. Ning, S. Song, X. Xiao, V.G. Hadjiev, D.E. Fan, D. Wang, L. Yu, S. Chen, Z. Ren, Efficient alkaline seawater oxidation by a three-dimensional core-shell dendritic NiCo@NiFe layered double hydroxide electrode, Materials Today Physics, 27 (2022) 100841.

[118] R. Que, S. Liu, Y. Yang, Y. Pan, Core-shell structure Co_3O_4@NiCo LDH was used as a high efficiency catalyst for overall water splitting, Materials Letters, 288 (2021) 129364.

[119] L. Meng, H. Xuan, J. wang, X. Liang, Y. Li, J. Yang, P. Han, Flower-like Co_3O_4@NiFe-LDH nanosheets enable high-performance bifunctionality towards both electrocatalytic HER and OER in alkaline solution, Journal of Alloys and Compounds, 919 (2022) 165877.

[120] A.K. Shah, M. Qureshi, In Situ Grown Cuboidal $MnCo_2O_4$/h Boron Nitride Heterojunction: A Noble Metal-Free Approach Based on Efficient Hole Extraction for Electrochemical Oxygen Evolution Reaction, ACS Applied Energy Materials, 5 (2022) 1551-1559.

[121] P. Gayen, S. Saha, V. Ramani, Selective Seawater Splitting Using Pyrochlore Electrocatalyst, ACS Applied Energy Materials, 3 (2020) 3978-3983.

[122] J. Juodkazytė, B. Šebeka, I. Savickaja, M. Petrulevičienė, S. Butkutė, V. Jasulaitienė, A. Selskis, R. Ramanauskas, Electrolytic splitting of saline water: Durable nickel oxide anode for selective oxygen evolution, International Journal of Hydrogen Energy, 44 (2019) 5929-5939.

[123] S. Dresp, F. Dionigi, S. Loos, J. Ferreira de Araujo, C. Spöri, M. Gliech, H. Dau, P. Strasser, Direct Electrolytic Splitting of Seawater: Activity, Selectivity, Degradation, and Recovery Studied from the Molecular Catalyst Structure to the Electrolyzer Cell Level, Advanced Energy Materials, 8 (2018).

[124] L. Yu, L. Wu, B. McElhenny, S. Song, D. Luo, F. Zhang, Y. Yu, S. Chen, Z. Ren, Ultrafast room-temperature synthesis of porous S-doped Ni/Fe (oxy)hydroxide electrodes for oxygen evolution catalysis in seawater splitting, Energy & Environmental Science, 13 (2020) 3439-3446.

[125] Y. Kuang, M.J. Kenney, Y. Meng, W.H. Hung, Y. Liu, J.E. Huang, R. Prasanna, P. Li, Y. Li, L. Wang, M.C. Lin, M.D. McGehee, X. Sun, H. Dai, Solar-driven, highly sustained splitting of seawater into hydrogen and oxygen fuels, Proc Natl Acad Sci U S A, 116 (2019) 6624-6629.

[126] L. Yu, Q. Zhu, S. Song, B. McElhenny, D. Wang, C. Wu, Z. Qin, J. Bao, Y. Yu, S. Chen, Z. Ren, Non-noble metal-nitride based electrocatalysts for high-performance alkaline seawater electrolysis, Nat Commun, 10 (2019) 5106.

[127] J.S. Ko, J.K. Johnson, P.I. Johnson, Z. Xia, Decoupling Oxygen and Chlorine Evolution Reactions in Seawater using Iridium-based Electrocatalysts, ChemCatChem, 12 (2020) 4526-4532.

[128] H. Chen, Y. Zou, J. Li, K. Zhang, Y. Xia, B. Hui, D. Yang, Wood aerogel-derived sandwich-like layered nanoelectrodes for alkaline overall seawater electrosplitting, Applied Catalysis B: Environmental, 293 (2021) 120215.

[129] S. Duan, Z. Liu, H. Zhuo, T. Wang, J. Liu, L. Wang, J. Liang, J. Han, Y. Huang, Q. Li, Hydrochloric acid corrosion induced bifunctional free-standing NiFe hydroxide nanosheets towards high-performance alkaline seawater splitting, Nanoscale, 12 (2020) 21743-21749.

[130] P. Yang, M. Ren, C. Jin, H. Xing, Facile Synthesis of N and P Co-Doped $NiMoO_4$ Hollow Nanowires and Electrochemical Deposition of NiFe-Layered Double Hydroxide for Boosting Overall Seawater Splitting, Journal of The Electrochemical Society, 169 (2022) 046511.

[131] Q. Ma, H. Jin, F. Xia, H. Xu, J. Zhu, R. Qin, H. Bai, B. Shuai, W. Huang, D. Chen, Z. Li, J. Wu, J. Yu, S. Mu, Ultralow Ru-assisted and vanadium-doped flower-like CoP/Ni_2P heterostructure for efficient water splitting in alkali and seawater, Journal of Materials Chemistry A, 9 (2021) 26852-26860.

[132] H. Wang, H.W. Lee, Y. Deng, Z. Lu, P.C. Hsu, Y. Liu, D. Lin, Y. Cui, Bifunctional non-noble metal oxide nanoparticle electrocatalysts through lithium-induced conversion for overall water splitting, Nat Commun, 6 (2015) 7261.

[133] M. Cong, D. Sun, L. Zhang, X. Ding, In situ assembly of metal-organic framework-derived N-doped carbon/Co/CoP catalysts on carbon paper for water splitting in alkaline electrolytes, Chinese Journal of Catalysis, 41 (2020) 242-248.

[134] T. Xiong, G. Li, D.J. Young, Z. Tan, X.-H. Yin, Y. Mi, F. Hu, In-situ surface-derivation of Ni-Mo bimetal sulfides nanosheets on Co_3O_4 nanoarrays as an advanced overall water splitting electrocatalyst in alkaline solution, Journal of Alloys and Compounds, 791 (2019) 328-335.

[135] Z. Ye, C. Qin, G. Ma, X. Peng, T. Li, D. Li, Z. Jin, Cobalt-Iron Oxide Nanoarrays Supported on Carbon Fiber Paper with High Stability for Electrochemical Oxygen Evolution at Large Current Densities, ACS Applied Materials & Interfaces, 10 (2018) 39809-39818.

[136] N.K. Chaudhari, H. Jin, B. Kim, K. Lee, Nanostructured materials on 3D nickel foam as electrocatalysts for water splitting, Nanoscale, 9 (2017) 12231-12247.

[137] W. Hao, J. Fan, X. Xu, Y. Zhang, H. Lv, S. Wang, S. Deng, S. Weng, Y. Guo, Sulfur doped FeO_x nanosheet arrays supported on nickel foam for efficient alkaline seawater splitting, Dalton Transactions, 50 (2021) 13312-13319.

[138] J. Chen, Y. Wang, G. Qian, T. Yu, Z. Wang, L. Luo, F. Shen, S. Yin, In situ growth of volcano-like FeIr alloy on nickel foam as efficient bifunctional catalyst for overall water splitting at high current density, Chemical Engineering Journal, 421 (2021) 129892.

[139] C.-H. Shin, Y. Wei, G. Park, J. Kang, J.-S. Yu, High performance binder-free Fe–Ni hydroxides on nickel foam prepared in piranha solution for the oxygen evolution reaction, Sustainable Energy & Fuels, 4 (2020) 6311-6320.

[140] A. Das, A.K. Ganguli, Design of diverse nanostructures by hydrothermal and microemulsion routes for electrochemical water splitting, RSC Adv, 8 (2018) 25065-25078.

[141] T. Marimuthu, R. Yuvakkumar, P. Senthil Kumar, G. Ravi, X. Xu, D. Velauthapillai, D.V. N. Vo, Cost effective and facile low temperature hydrothermal fabrication of Cu_2S thin films for hydrogen evolution reaction in seawater splitting, International Journal of Hydrogen Energy, 22 (2021), 30819-30829.

[142] X. Zou, Y. Liu, G.-D. Li, Y. Wu, D.-P. Liu, W. Li, H.-W. Li, D. Wang, Y. Zhang, X. Zou, Ultrafast Formation of Amorphous Bimetallic Hydroxide Films on 3D

Conductive Sulfide Nanoarrays for Large-Current-Density Oxygen Evolution Electrocatalysis, Advanced Materials, 29 (2017) 1700404.

[143] W. Lu, X. Li, F. Wei, K. Cheng, W. Li, Y. Zhou, W. Zheng, L. Pan, G. Zhang, Fast sulfurization of nickel foam-supported nickel-cobalt carbonate hydroxide nanowire array at room temperature for hydrogen evolution electrocatalysis, Electrochimica Acta, 318 (2019) 252-261.

[144] A.C. Jones, M.L. Hitchman (Eds.), Chapter 1 Overview of Chemical Vapour Deposition : Chemical Vapour Deposition: Precursors, Processes and Applications, The Royal Society of Chemistry 2009, 1-36.

[145] M. Yang, H. Zhu, Y. Zheng, C. Zhang, G. Luo, Q. Xu, Q. Li, S. Zhang, T. Goto, R. Tu, One-step chemical vapor deposition fabrication of Ni@NiO@graphite nanoparticles for the oxygen evolution reaction of water splitting, RSC Advances, 12 (2022) 10496-10503.

[146] S.S. Ray, R. Gusain, N. Kumar, Chapter three - Water purification using various technologies and their advantages and disadvantages, in: Carbon Nanomaterial-Based Adsorbents for Water Purification, Elsevier 2020, 37-66.

[147] C.N. Gonsalves, A.C. Hegde, Electrochemical water electrolysis using electrodeposited (NiMo) coatings from a low concentration bath, Chemical Data Collections, 34 (2021).

[148] Z. Yan, H. Liu, Z. Hao, M. Yu, X. Chen, J. Chen, Electrodeposition of (hydro)oxides for an oxygen evolution electrode, Chem Sci, 11 (2020) 10614-10625.

[149] M. Jing, T. Wu, G. Zou, H. Hou, X. Ji, Chapter 9 - Nanomaterials for electrochemical energy storage, in: A.J. Wain, E.J.F. Dickinson (Eds.) Frontiers of Nanoscience, 421-484.

[150] L. Kuai, J. Geng, C. Chen, E. Kan, Y. Liu, Q. Wang, B. Geng, A reliable aerosol-spray-assisted approach to produce and optimize amorphous metal oxide catalysts for electrochemical water splitting, Angew Chem Int Ed Engl, 53 (2014) 7547-7551.

[151] H.k. El Emam, S.I. El-Dek, W.M.A. El Rouby, Aerosol Spray Assisted Synthesis of Ni Doped $BaTiO_3$ Hollow Porous Spheres/Graphene as Photoanode for Water Splitting, Journal of The Electrochemical Society, 168 (2021) 050540.

[152] F.M. Sapountzi, J.M. Gracia, C.J. Weststrate, H.O.A. Fredriksson, J.W. Niemantsverdriet, Electrocatalysts for the generation of hydrogen, oxygen and synthesis gas, Progress in Energy and Combustion Science, 58 (2017) 1-35.

[153] J.N. Hausmann, B. Traynor, R.J. Myers, M. Driess, P.W. Menezes, The pH of Aqueous NaOH/KOH Solutions: A Critical and Non-trivial Parameter for Electrocatalysis, ACS Energy Letters, 6 (2021) 3567-3571.

[154] T. Shinagawa, K. Takanabe, Towards Versatile and Sustainable Hydrogen Production through Electrocatalytic Water Splitting: Electrolyte Engineering, ChemSusChem, 10 (2017) 1318-1336.

[155] Z.-p. Lu, L. Sepunaru, Electrodeposition of iron phosphide film for hydrogen evolution reaction, Electrochimica Acta, 363 (2020) 137167.

[156] T. Naito, T. Shinagawa, T. Nishimoto, K. Takanabe, Water Electrolysis in Saturated Phosphate Buffer at Neutral pH, ChemSusChem, 13 (2020) 5921-5933.

[157] T. Shinagawa, M.T.-K. Ng, K. Takanabe, Electrolyte Engineering towards Efficient Water Splitting at Mild pH, ChemSusChem, 10 (2017) 4155-4162.

[158] J. Mohammed-Ibrahim, H. Moussab, Recent advances on hydrogen production through seawater electrolysis, Materials Science for Energy Technologies, 3 (2020) 780-807.

[159] C. Ros, S. Murcia-Lopez, X. Garcia, M. Rosado, J. Arbiol, J. Llorca, J.R. Morante, Facing Seawater Splitting Challenges by Regeneration with Ni-Mo-Fe Bifunctional Electrocatalyst for Hydrogen and Oxygen Evolution, ChemSusChem, 14 (2021) 2872-2881.

[160] S.A. Mangi, A. Makhija, M.S. Raza, S.H. Khahro, A.A. Jhatial, A Comprehensive Review on Effects of Seawater on Engineering Properties of Concrete, Silicon, 13 (2020) 4519-4526.

[161] H. Zhang, Y. Luo, P.K. Chu, Q. Liu, X. Liu, S. Zhang, J. Luo, X. Wang, G. Hu, Recent advances in non-noble metal-based bifunctional electrocatalysts for overall seawater splitting, Journal of Alloys and Compounds, 922 (2022) 166113.

[162] L. Zhang, Z. Wang, J. Qiu, Energy-Saving Hydrogen Production by Seawater Electrolysis Coupling Sulfion Degradation, Advanced Materials, 34 (2022) 2109321.

[163] X. Lu, Q. Zhang, Y.H. Ng, C. Zhao, Reversible ternary nickel-cobalt-iron catalysts for intermittent water electrolysis, EcoMat, 2 (2020).

[164] B.H.R. Suryanto, Y. Wang, R.K. Hocking, W. Adamson, C. Zhao, Overall electrochemical splitting of water at the heterogeneous interface of nickel and iron oxide, Nat Commun, 10 (2019) 5599.

[165] Y. Luo, L. Tang, U. Khan, Q. Yu, H.-M. Cheng, X. Zou, B. Liu, Morphology and surface chemistry engineering toward pH-universal catalysts for hydrogen evolution at high current density, Nature Communications, 10 (2019) 269.

[166] S. Xue, Z. Liu, C. Ma, H.M. Cheng, W. Ren, A highly active and durable electrocatalyst for large current density hydrogen evolution reaction, Science Bulletin, (2020).

[167] L. Zhang, Z. Shi, Y. Lin, F. Chong, Y. Qi, Design Strategies for Large Current Density Hydrogen Evolution Reaction, Front Chem, 10 (2022) 866415.

[168] H. Zhou, F. Yu, Q. Zhu, J. Sun, F. Qin, L. Yu, J. Bao, Y. Yu, S. Chen, Z. Ren, Water splitting by electrolysis at high current densities under 1.6 volts, Energy & Environmental Science, 11 (2018) 2858-2864.

[169] S. Gupta, M. Forster, A. Yadav, A.J. Cowan, N. Patel, M. Patel, Highly Efficient and Selective Metal Oxy-Boride Electrocatalysts for Oxygen Evolution from Alkali and Saline Solutions, ACS Applied Energy Materials, 3 (2020) 7619-7628.

[170] S. Wang, A. Lu, C.-J. Zhong, Hydrogen production from water electrolysis: role of catalysts, Nano Convergence, 8 (2021) 4.

[171] Q. Zhang, W. Chen, G. Chen, J. Huang, B. Ouyang, D. Chen, E. Kan, T. Lan, C. Li, H.-S. Choi, K.K. Ostrikov, Trimetallic Octahedral Ni–Co–W Phosphoxide Sprouted from Plasma-Defect-Engineered Ni–Co Support for Ultrahigh-Performance Electrocatalytic Hydrogen Evolution, ACS Sustainable Chemistry & Engineering, 9 (2021) 7454-7465.

[172] S. Anantharaj, S. Noda, M. Driess, P.W. Menezes, The Pitfalls of Using Potentiodynamic Polarization Curves for Tafel Analysis in Electrocatalytic Water Splitting, ACS Energy Letters, 6 (2021) 1607-1611.

[173] F. Bao, E. Kemppainen, I. Dorbandt, R. Bors, F. Xi, R. Schlatmann, R. van de Krol, S. Calnan, Understanding the Hydrogen Evolution Reaction Kinetics of Electrodeposited Nickel-Molybdenum in Acidic, Near-Neutral, and Alkaline Conditions, ChemElectroChem, 8 (2021) 195-208.

[174] A.J. Esswein, Y. Surendranath, S.Y. Reece, D.G. Nocera, Highly active cobalt phosphate and borate based oxygen evolving catalysts operating in neutral and natural waters, Energy & Environmental Science, 4 (2011) 499-504.

[175] D. Voiry, M. Chhowalla, Y. Gogotsi, N.A. Kotov, Y. Li, R.M. Penner, R.E. Schaak, P.S. Weiss, Best Practices for Reporting Electrocatalytic Performance of Nanomaterials, ACS Nano, 12 (2018) 9635-9638.

[176] O. Kasian, S. Geiger, K.J.J. Mayrhofer, S. Cherevko, Electrochemical On-line ICP-MS in Electrocatalysis Research, The Chemical Record, 19 (2019) 2130-2142.

[177] R. Frydendal, E.A. Paoli, I. Chorkendorff, J. Rossmeisl, I.E.L. Stephens, Toward an Active and Stable Catalyst for Oxygen Evolution in Acidic Media: Ti-Stabilized MnO2, Advanced Energy Materials, 5 (2015) 1500991.

[178] D. Li, H. Liu, L. Feng, A Review on Advanced FeNi-Based Catalysts for Water Splitting Reaction, Energy & Fuels, 34 (2020) 13491-13522.

[179] C.C.L. McCrory, S. Jung, I.M. Ferrer, S.M. Chatman, J.C. Peters, T.F. Jaramillo, Benchmarking Hydrogen Evolving Reaction and Oxygen Evolving Reaction Electrocatalysts for Solar Water Splitting Devices, Journal of the American Chemical Society, 137 (2015) 4347-4357.

[180] S. Anantharaj, S. Kundu, Do the Evaluation Parameters Reflect Intrinsic Activity of Electrocatalysts in Electrochemical Water Splitting, ACS Energy Letters, 4 (2019) 1260-1264.

[181] S.I. Perez Bakovic, P. Acharya, M. Watkins, H. Thornton, S. Hou, L.F. Greenlee, Electrochemically active surface area controls HER activity for Fe_xNi_{100-x} films in alkaline electrolyte, Journal of Catalysis, 394 (2021) 104-112.

[182] X. Shang, K.-L. Yan, Y. Rao, B. Dong, J.-Q. Chi, Y.-R. Liu, X. Li, Y.-M. Chai, C.-G. Liu, In situ cathodic activation of V-incorporated Ni_xS_y nanowires for enhanced hydrogen evolution, Nanoscale, 9 (2017) 12353-12363.

[183] K. Zhang, R. Zou, Advanced Transition Metal-Based OER Electrocatalysts: Current Status, Opportunities, and Challenges, Small, 17 (2021) 2100129.

[184] W.K. Chong, B.J. Ng, C.C. Er, L.L. Tan, S.P. Chai, Insights from density functional theory calculations on heteroatom P-doped $ZnIn_2S_4$ bilayer nanosheets with atomic-level charge steering for photocatalytic water splitting, Sci Rep, 12 (2022) 1927.

[185] S.H. Hsu, J. Miao, L. Zhang, J. Gao, H. Wang, H. Tao, S.F. Hung, A. Vasileff, S.Z. Qiao, B. Liu, An Earth-Abundant Catalyst-Based Seawater Photoelectrolysis System with 17.9% Solar-to-Hydrogen Efficiency, Adv Mater, 30 (2018) 1707261.

[186] J.S. Ko, J.K. Johnson, P.I. Johnson, Z. Xia, Decoupling Oxygen and Chlorine Evolution Reactions in Seawater using Iridium-based Electrocatalysts, ChemCatChem, 12 (2020) 4526-4532.

CHAPTER 2 Facile fabrication of O vacancy rich CuVO$_x$ nanobelt@NiO nanosheet array for hydrogen evolution reaction

2.1. Introduction

Hydrogen is regarded as one of clean fuels for a sustainable future. It can be produced from various processes including the thermochemical conversion of organic materials such as fossil fuels and biomass and water electrolysis. In particular, the water electrolysis is a clean way for the pure hydrogen production without direct CO$_2$ emission [1-3]. The water electrolysis process includes two half electrode reactions, i.e., oxygen evolution reaction (OER) and hydrogen evolution reaction (HER) [4]. For the HER in the alkaline condition, the limitation is the sluggish electrochemical reaction due to the Volmer step for the formation of adsorption proton (H$_{ads}$) during the water dissociation and the Heyrovsky step for the detaching of hydrogen molecule [5, 6]. In the alkaline electrolyte, the reaction starts from the catalytic cleavage of H$_2$O molecule into OH$^-$ and H$_{ads}$ (Volmer step; H$_2$O + e$^-$ $\rightarrow$ H$_{ads}$ + OH$^-$), followed by a Heyrovsky step with a hydrogen molecule detached from the surface of catalysts via either the interaction of the H$_{ads}$ atom and H$_2$O (Heyrovsky/Tafel step; H$_2$O + e$^-$ + H$_{ads}$ $\rightarrow$ H$_2$ + OH$^-$) or the recombination of two H atoms (Tafel step; H$_{ads}$ + H$_{ads}$ $\rightarrow$ H$_2$). Thus, it is important to improve both the Volmer and Heyrovsky steps for the enhancing electrocatalytic performance [7].

Currently, noble metal based electrocatalysts (mainly Pt-based ones) are still the most effective catalysts for the HER. However, they are too expensive and too scarce, and especially, their performances are still unsatisfactory owing to their inefficient HO-H

bond cleavage ability, limiting their widespread applications [8, 9]. Nowadays, numerous efforts have been paid to develop high-performance electrocatalysts with low cost. To date, various transition metal oxide based electrocatalysts such as NiO, CuO, V_2O_5, MnO_2, Fe_2O_3, Co_3O_4 and ZnO based ones and their mixtures have been widely studied since their electrocatalytic activities can be effectively improved by controllably adjusting their nanostructures and compositions [10-12]. Meanwhile, bi/tri-metal oxides have been studied as the promising HER electrocatalysts because of the synergistic effect from the formation of special nanostructures, the regulating of electronic structure, the exerting of the intrinsic properties for the enhancing electric/ionic conductivity, the balancing of intermediates adsorption/desorption energy for the hydrogen generation, the promoting of the capability towards the breaking of O-H bond, and/or the increasing of the electrochemical stability [11, 12]. For examples, Hao et al. [13] prepared an electrocatalyst of $Fe_{1.89}Mo_{4.11}O_7$/MoO_2 with a regulated Mo electronic structure, by which a Mo-H bond strength similar to the Pt-H bond strength was exhibited and a fast kinetics for the HER was achieved. Jiang et al. [14] doped cobalt on two-dimensional (2D) ceria nanosheets, which effectively promoted the generation of oxygen vacancies on ceria oxide nanosheets for the optimizing of hydrogen binding/water dissociation with the increased active sites, thereby exhibiting an outperformance even over Pt in alkaline HER with long-term durability. Besides, Peng et al. [15] found that the super-hydrophilic surface should be also benefit for the catalytic HER since the enhanced contact area between electrode and electrolyte can promote hydrogen desorption from the surface of catalyst.

However, the pure transition metal oxides generally exhibit not so high activity for catalyzing HER due to the unbefitting hydrogen adsorption energy [16]. Especially, although the metal oxide and hydroxide based catalysts are good at the splitting of the

75

HO-H bonds, they could not efficiently converse the obtained H* intermediates to H_2 [17, 18]. On the other hand, due to their good stability within a wide range of electrochemical window in alkaline solution, considerable efforts have been devoted to overcoming these barriers, and some efficient tactics are developed to synthesize the high active metal oxide based HER catalysts.

Recently, vanadium oxides (VO_x) including VO_2, V_2O_3, V_2O_5, V_2O_7 and V_3O_8 have gained great attention due to their high catalytic activities and excellent electrical properties with outstanding electronic structures, large conductivity as well as high charge transfer capability and multi-valence feature [19]. They have been widely investigated for the applications in lithium batteries and photocatalysis but seldomly considered for the HER since they always have low specific surface area and poor electronic conductivity [14, 20]. It is reported that the introduction of other metals in VO_x could be an effective way to increase the electronic conductivity and stabilize its structure during the redox reaction [21]. For example, Bai *et al*. [22] synthesized CuV_2O_5 via a hydrothermal way, and found that the obtained CuV_2O_5 had good electrical conductivity and structure stability. Meanwhile, it is found that V_2O_5 can reactivate the deactivated Ni cathode in water electrolysis, and based on this finding, Li *et al*. [3] implanted Ni-O-VO_x sites with Cu on the surface of nickel form (NF) to create a Ni(Cu)VO_x electrocatalysts with excellent HER activity and stability in alkaline solution. Herein, the combination of V and Ni species promoted the charge redistribution from Ni to VO_x, which greatly improved the kinetics for H_{ads} atom and fast release of H_2 from the catalyst surface. Moreover, VO_x resulted in the damper of Ni lattice and the generation of large electrochemically active surface area. Meena *et al*. [23] also prepared V_2O_5/Ni(OH)$_2$ electrocatalysts on NF (V_2O_5/Ni(OH)$_2$@NF) for HER in alkaline solution, which showed a Pt-like activity with a overpotential as low as 39

mV @ 10 mA cm^{-2} and long-term stability. Herein, assisting by V_2O_5, the near-zero adsorption free energy (ΔG_{H*}) for H_{ads} atom could be achieved on the active sites owing to the charge transfer resulted from the adsorbed O species on Ni (111) plane together with high conductivity of NF. While, the weak hydrogen binding strength due the downshifting of the d-band center by the O-adsorption on the Ni surface could lead to a favorable kinetics for H_{ads} atom and fast release of H_2 on the surface of catalysts. Similarly, Li. *et al*. [24] used VO_x clusters to modulate a metallic Co catalyst (denoted as Co(VO_x)) for HER, and found that the VO_x clusters can endow Co with a highly disordered lattice and decrease the particle size, and as a result, an optimal doping level of 3% effectively regulated the atomic structure, which not only provided more active sites and reduced the H* binding, but also enabled an efficient electron transferring from Co to VO_x to decrease the H* adsorption on V-Co(001) for enhancing HER.

Besides, defect engineering, e.g., O vacancy generation, is an efficient methodology to boost up the HER activity as well as stability [25]. For example, An *et al*. [26] modified the electronic structure of $NiMoO_4$ surface by doping N at the NiO_6 sites to concomitantly generate the oxygen vacancy defects by heteroatomic exchange with the electrical neutrality principle between $2N^{3-}$ and $3O^{2-}$ species, which led to the formation of multiple active sites with the improved metallic conductivity as well as the lowered adsorption energy barrier of Heyrovsky step. Similarly, Liu *et al*. [27] reported that the introduction of oxygen vacancies in the $NiCo_2O_4$ material effectively reduced the adsorption energy and dissociation energy barrier of H_2O, which was attributed to the low-coordinated metal sites derived from the oxygen vacancies, thereby promoting the Heyrovsky step of alkaline HER. Meanwhile, Wang *et al*. [28] used iridium (Ir) and ruthenium (Ru) to tune the electronic and atomic structure of NiV layered double hydroxide (LDH) to promote the water electrolysis kinetics, and found that the

synergistic electronic interactions existed among the Ru (Ir), V and Ni cations. Especially, the local coordination environments around the V and Ni cations were modulated, resulting in more V vacancies, which could optimize the adsorption energy of intermediates in the Volmer and Heyrovsky steps for the HER. Therefore, combining of VO_x with other metal oxide and/or metal catalysts could result in some unique atomic structure with more oxygen vacancies, thereby achieving highly catalytic performance for the HER.

Herein, a defect rich $CuVO_x$ nanobelt @ NiO nanosheet composite was synthesized on the pretreated carbon paper (CP) by using a facile hydrothermal process combined calcination method. The obtained $CuVO_x$-NiO electrocatalysts contained conductive a $CuVO_x$ layer with rich defects and active NiO nanosheets with high wettability, which resulted in favorable kinetics for H_{ads} atom and fast release of H_2 on the surface of catalysts. As a result, this novel $CuVO_x$-NiO@CP electrode exhibited high activity and stability for HER in the alkaline solution.

2.2 Experimental section

2.2.1 Chemicals and Materials

Ammonium metavanadate (V) (NH_4VO_3, 99%), nickel (II) nitrate hexahydrate ($Ni(NO_3)_2 \cdot 6H_2O$, 98%), copper (II) nitrate trihydrate ($Cu(NO_3)_2 \cdot 3H_2O$, 98%), nitric acid (HNO_3, 69%), potassium hydroxide (KOH, 85%) and ethanol (C_2H_5OH, 99.5%) were purchased from Wako, Japan. Deionized (DI) water (18.2 MΩ cm) was used to prepare the solution. Carbon paper (CP, TGP-H-060, thickness: 190 μm) was purchased from Toray, Japan.

2.2.2 Synthesis of $CuVO_x$@NiO based electrode

$CuVO_x$@NiO composite was directly grown on CP substrate by a hydrothermal process combined calcination method. In brief, a piece of carbon paper (2 x 2 cm^2) was

treated in 6 M HNO_3 solution under an ultrasonic condition for 3 h, and then washed with ethanol and DI water consecutively for the removal of those impurities. Meanwhile, the calculated amounts of NH_4VO_3, $Cu(NO_3)_2 \cdot 3H_2O$, $Ni(NO_3)_2 \cdot 6H_2O$, NH_4F and $CO(NH_2)_2$ were dissolved in DI water (20 mL) under stirring for 30 min and then, 6 M HNO_3 solution was slowly added into the above solution to adjust pH to 3. Thereafter, the solution was introduced into an autoclave with Teflon-line, in which the pretreated CP was vertically fixed. The hydrothermal reaction was performed at 180 °C for 12 h. Finally, the composite coated CP electrode was washed by ethanol and DI water consecutively for several times, and then dried at 80 °C in a vacuum oven overnight, and finally treated at 450 °C for 3 h with a 2 °C/min heating rate. As such, the $CuVO_x$-NiO@CP electrode was obtained (Figure 2.1). Herein, the chemical composition of $CuVO_x$-NiO was preliminarily optimized based on the HER performance and the molar ratio of Ni:Cu:V with 1:4:2.5 was selected as the optimal composition for further investigation. For comparison, Ni-Cu mixed oxide, Ni-V mixed oxide, Cu-V mixed oxide and pure V_2O_5 were also coated on CPs by the same methodology and conditions.
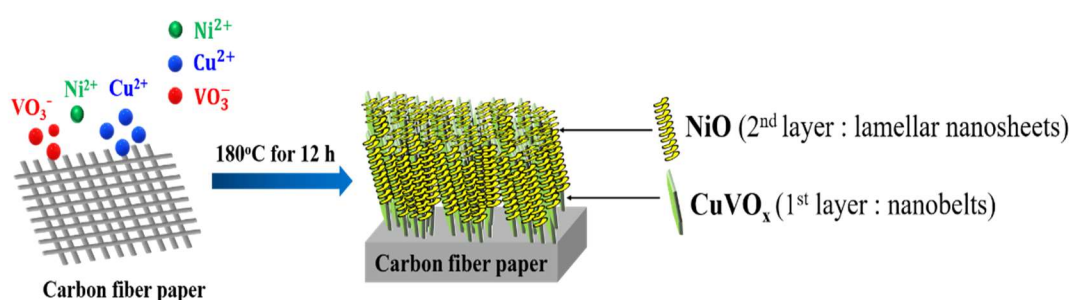
Figure 2.1 Schematic illustration for the preparation of $CuVO_x$-NiO@CP electrode via a one-step hydrothermal method.

2.2.3 Material Characterizations

Morphology and nanostructure of the as-synthesized electrocatalysts were observed by a scanning electron microscope (SEM, SU8010, HITACHI, JAPAN) and a transmission electron microscope (TEM, JEM-2100F, JEOL), respectively. Crystalline structure of the sample was determined by an X-ray diffraction (XRD, Rigaku Smartlab diffractometer, Japan) measurement in a 2θ range of $10°$-$80°$ using a Cu-Kα radiation source ($\lambda = 0.15406$ nm). The contact angle on the electrocatalyst surface was measured by a contact angle meter (DMe-201, Japan) using DI water drop. Raman spectrum was obtained using a JASCO NRS-5100 ($\lambda = 632$ nm). The XPS measurement was performed at ambient temperature on a VG Scientific ESCALab250i-XL XPS machine with an Al-Kα X-ray source.

2.2.4 Electrochemical performance tests

Electrochemical performance test was performed on an electrochemical workstation (Versa STAT4, Princeton, USA) with a three-electrode system. A standard Hg/HgO electrode and a carbon rod were used as the reference and counter electrodes, respectively. HER performance of the electrocatalyst was evaluated using a linear sweep voltammetry (LSV) at a scan rate of 1 mV s^{-1} in a potential range of -0.9~-1.5 V in 1 M KOH solution. The potential relating to the reversible hydrogen electrode (RHE) was determined by the following equation: E(RHE) = E(Hg/HgO) + 0.098 + 0059 pH [29]. LSV polarization curve was recorded with iR-compensation. Meanwhile, EIS (electrochemical impedance spectroscopy) measurement was performed at a frequency range of 100 kHz-0.1 Hz in 1 M KOH solution. The cyclic voltammetry test was carried out in a potential range of -0.2-0 V (*vs* RHE) at a scan rate range of 10-100 mVs^{-1} to obtain the electrochemical active surface area (ECSA). The stability test was performed by two methods: (i) chronopotentiometry analysis at 10 mA cm^{-2} for 30 h;

and (ii) cyclic voltammetry analysis at a potential range of 0.1~ -0.3 V (vs RHE) for 1000 cycles.

2.3. Results and discission

2.3.1 Morphology and structural characterizations

XRD patterns of the synthesized electrocatalysts before the calcination are presented in Figures 2.2(a-c). One can see that all of them show a hydroxide form. For the $CuVO_x$-NiO@CP before the calcination, $Cu_3V_2O_7(OH)_2 \cdot 2H_2O$ with hydroxyl groups exist, which can be completely changed to $Cu_3V_2O_8$ after the calcination at 450 ^{o}C based on the following equations;

$$3Cu(NO_3)_2 + 2NH_4VO_3 + 5H_2O \rightarrow Cu_3V_2O_7(OH)_2 \cdot 2H_2O + 2NH_4NO_3 + 4HNO_3 \quad (1)$$

$$Cu_3V_2O_7(OH)_2 \cdot 2H_2O \rightarrow Cu_3V_2O_8 + 3H_2O \quad (2)$$
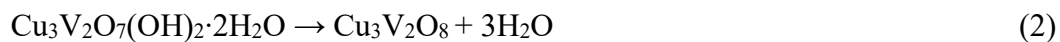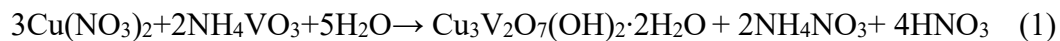
Figures 2.3 (a-d) displays XRD patterns of $CuVO_x$-NiO, $CuVO_x$, V_2O_5 and NiO after the calcination, the characteristic peaks located at 2θ of 37.2^o, 43.3^o and 62.9^o correspond to the (111), (200) and (220) planes of NiO (JCPDS No 71-1179), and the diffraction peaks at 2θ of 26.5^o, 32.3^o, 36.3, 37.1, 43.2^o and 49.2^o indicate the formation of monoclinic CuV_2O_5 phase (JCPDS No. 43-0080) while the small diffraction peaks at 2θ between 16.5^o and 66.3^o match well with those corresponding to the monoclinic $Cu_2V_2O_7$ (JCPDS No. 73-1032) and $Cu_3V_2O_8$ (JCPDS No. 74-1503) phases. Herein, in the crystal structures of monoclinic $Cu_2V_2O_7$ and $Cu_3V_2O_8$, a Cu atom is coordinated with five oxygen atoms while a V atom with four oxygen atoms forms the VO_4 tetrahedral structure [30]. It should be noted that it is difficult to find the main peak at 2θ of 26.1° corresponding to V_2O_5.
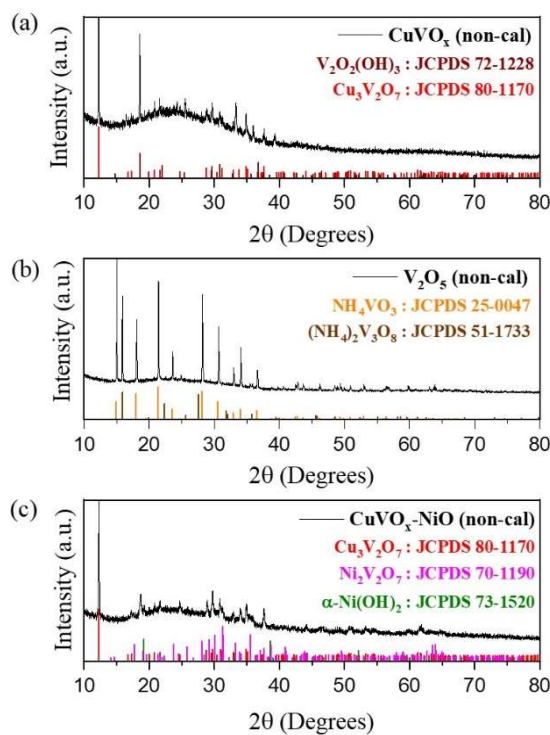
Figure 2.2 XRD patterns of all synthesized electrocatalysts before the calcination.
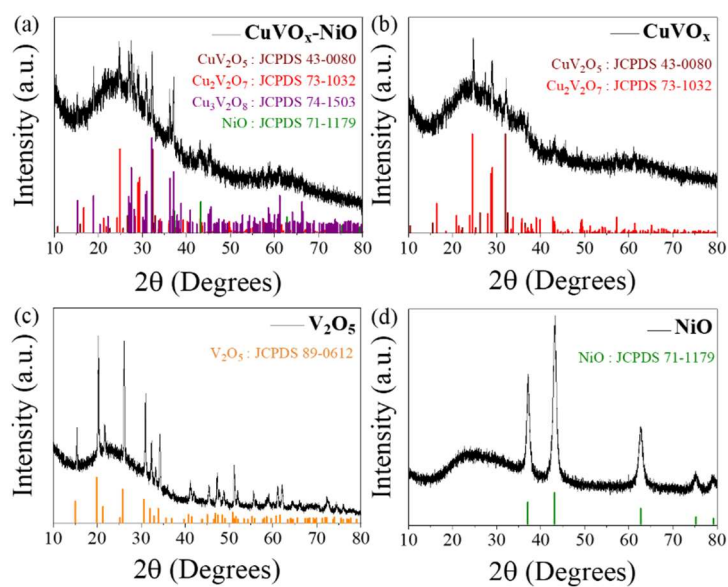
Figure 2.3 XRD patterns of (a) $CuVO_x$-NiO, (b) $CuVO_x$, (c) V_2O_5 and (d) NiO.

As presented in Figure 2.4a, $CuVO_x$ with a nanobelt structure (Figure 2.4b, thickness: ca. 0.43 μm) is formed on the CP with a smooth surface. While, pure NiO with a nanosheet structure (Figure 2.4c) is deposited in the CP. When Cu^{2+}, VO^{3-} and Ni^{2+} ions co-exist in the initial solution, the nanosheets seem to be grown on the nanobelt during the hydrothermal synthesis process, which could be a composite of $CuVO_x$-NiO formed on the CP (Figures 2.4(d-e)). As illustrated in Figure 2.1, $CuVO_x$ nanobelt seems to be formed on the CP initially, followed by NiO nanosheets growing on the surface of the $CuVO_x$ nanobelt layer. Herein, in the acid condition, the Cu^{2+} and VO^{3-} with higher molar concentrations than Ni^{2+} could react faster to form various compounds such as $Cu_3V_2O_7(OH)_2 \cdot 2H_2O$ with the nanobelt structure. In parallel, due to the hydrolysis of urea, Ni^{2+} ions would form $Ni(OH)_2$ layer anchoring on the surface of $CuVO_x$. After the calcination, the $CuVO_x$-NiO composite is generated. One can see that the nanosheet on the nanobelt has a thickness of 0.12 μm (Figure 2.4f). EDS elemental mappings of Ni, Cu, O and V on the surface of $CuVO_x$-NiO@CP are shown in Figures 2.5(d-h). One can see that the colour intensity of each element is fluctuating with the element concentration. Obviously, the purple colour corresponding to V element has a lower intensity than Ni due to that the V element is concentrated in the core part. In order to further confirm the distributions of various elements in the core and shell areas, EDS linear element scanning is performed. As shown in Figure 2.4 (g-h), more Ni elements in the nanosheet region (shell) than nanobelt part (core) are observed, revealing the formation of the $CuVO_x$ core and NiO shell. Combining with the XRD analysis, it can be confirmed that the composite is consisted of $CuVO_x$ nanobelt core and NiO nanosheet shell. Herein, as stated in the introduction section, the synergistic interaction between nickel and vanadium species should play a significant role in affecting the growth of such a special three-dimensional (3D) nano-flake

83

structure, which could provide high surface area, easily accessible active sites and shortened charge transfer route during the reaction [19]. In comparison, those surface morphologies of the prepared NiO-CuO@CP, NiO-VO$_x$@CP and V$_2$O$_5$@CP electrodes are presented in Figure 2.5. One can see that NiO-CuO@CP has a fluffy-like structure, which is different from that of CuVO$_x$-NiO@CP (Figure 2.4d). As shown in Figure 2.5c, the pure vanadium oxide (V$_2$O$_5$) grows along the carbon fiber with a denser layer microstructure, which should not be benefit for the electrocatalytic performance. However, as indicated in this study and other report [31], the coexistence of V and other metal species, the composite with 2D/3D structure could be more easily formed.
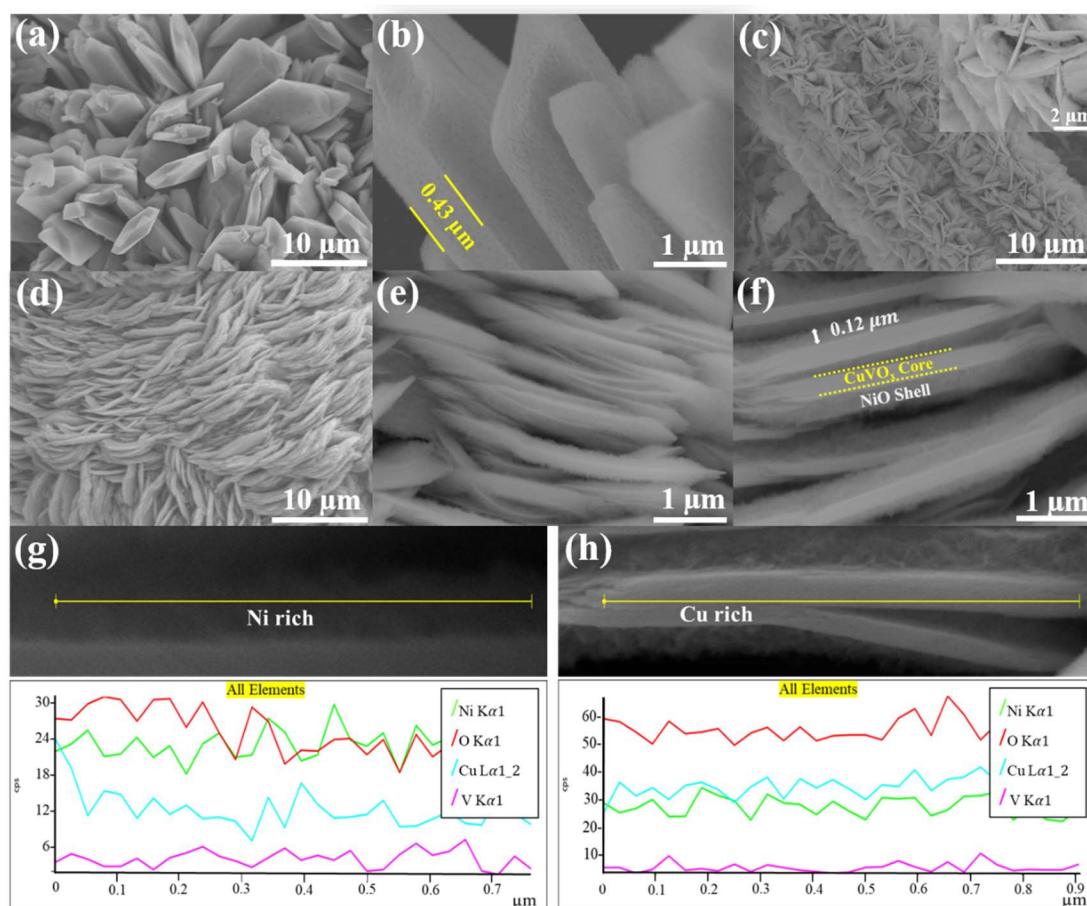
Figure 2.4 SEM images of (a-b) CuVO$_x$@CP, (c) NiO@CP, (d-f) CuVO$_x$-NiO@CP at different magnifications; (g-h) EDS line scan of Ni, Cu, O and V on CuVO$_x$-NiO@CP.
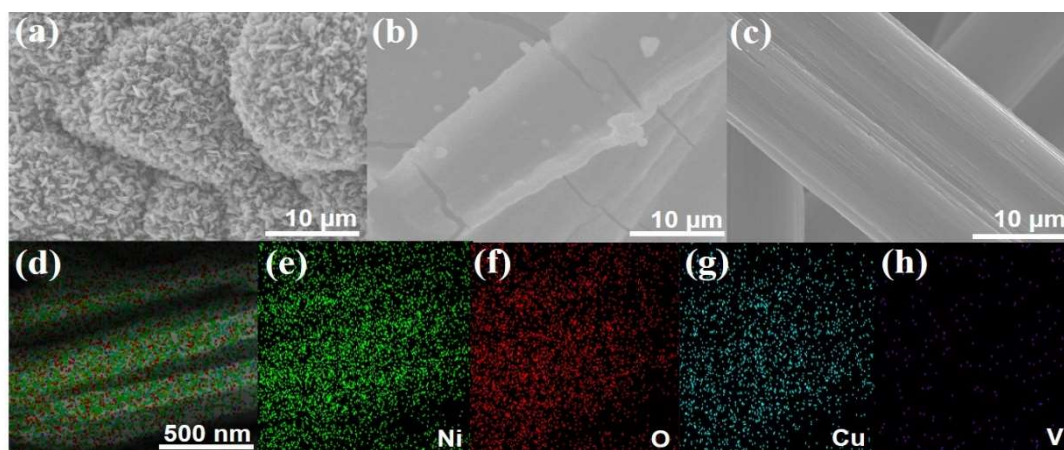
Figure 2.5 SEM images of (a) NiO-CuO@CP, (b) NiO-VO$_x$@CP and (c) V$_2$O$_5$@CP and (d-h) EDX elemental mappings of Ni, Cu, O and V on CuVO$_x$-NiO@CP at a scale bar of 500 nm.

TEM analysis was carried out to investigate nanostructure of the synthesized electrocatalysts. When CuVO$_x$ is synthesized on the CP, the interplanar spacing of 0.28 nm, which is assigned to the (003) plane of CuV$_2$O$_5$, is observed (Figure 2.6a). Herein, the edge dislocations, which should provide actives sites for HER, are also observed. Meanwhile, on the TEM image of CuVO$_x$-NiO supported on the CP (Figures 2.6(b-c)), the lattice fringes of 0.24 and 0.27 nm are in good agreement with the (131) and (012) planes of Cu$_2$V$_2$O$_7$ and Cu$_3$V$_2$O$_8$, respectively. While, the lattice spacings of 0.15 and 0.20 nm correspond to the (220) and (200) planes of NiO. It is reported that both Cu$_2$V$_2$O$_7$ and Cu$_3$V$_2$O$_8$ have highly distorted structures with rich-defects [32]. As illustrated in Figure 2.6d, the edge dislocation resulted from the Burgers vectors could be generated in these materials, which always accompanies by lots of vacancies [33]. In addition, the typical TEM-EDS mappings exhibit the uniform distributions of Cu, V and Ni on the electrocatalyst (Figures 2.6 (e-h)).
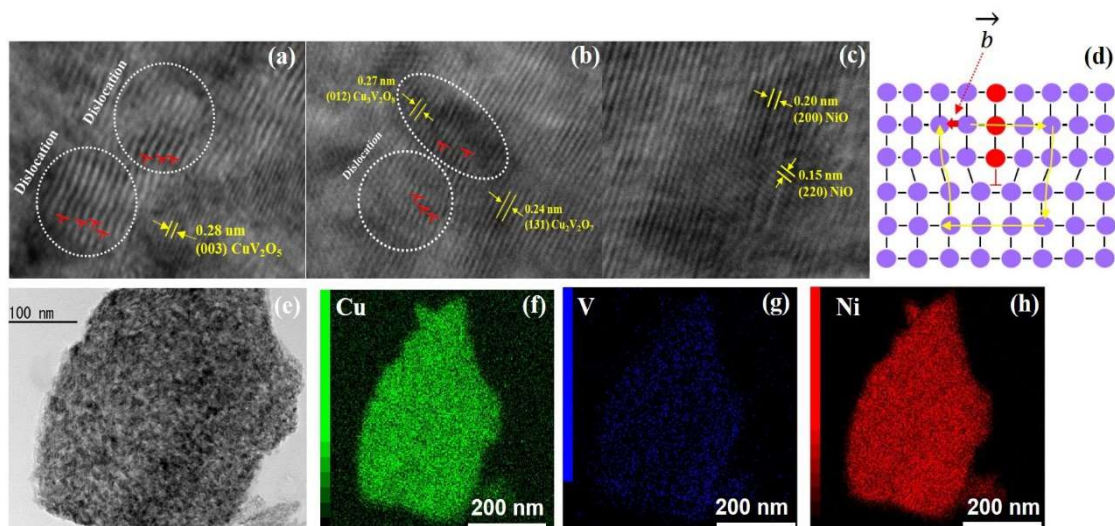
Figure 2.6 TEM images of (a) CuVO$_x$; (b) CuVO$_x$-NiO composite on CP with lattice fringes of CuVO$_x$; (c) lattice fringes of NiO on CuVO$_x$-NiO@CP; (d) Schematic illustrations of edge dislocations; (e-h) the corresponding EDS elemental mappings of Cu, V and Ni.

Chemical composition and elemental valences of CuVO$_x$-NiO on CP were further investigated by XPS analysis (Figure 2.7). The atomic percentages of Ni, Cu, V and O elements based on XPS analysis are presented in Table 2.1, which reveal that more Ni species exist on the surface of the electrocatalyst since NiO is anchored on the CuVO$_x$ surface. The peaks located at 856.1 and 873.9 eV with two satellite peaks (862.1 and 880.3 eV) on the XPS spectra of Ni 2p$_{3/2}$ and Ni 2p$_{1/2}$ indicate the presence of Ni^{2+} [34].

Table 2.1 Atomic composition of CuVO$_x$-NiO based on XPS analysis.

Electrocatalyst	% Atom			
	Ni	Cu	V	O
CuVO$_x$-NiO	31.8	6.82	2.75	58.63

The peaks located at 854.9 and 872.9 eV together with two peaks at 856.8 and 874.8 eV are indexed to the XPS spectra of Ni $2p_{3/2}$ and Ni $2p_{1/2}$, respectively, which indicate the presence of Ni^{2+} and Ni^{3+} (Figure 2.7b). While, as shown in Figure 2.7c, the fitted peaks located at 935.2 and 955.3 eV relating to Cu^{2+} accompanying with the peaks at 933.6 and 953.4 eV relating to Cu^+ on the XPS spectra of Cu $2p_{3/2}$ and Cu $2p_{1/2}$ are also observed, indicating the presence of mixed valences of Cu species. Herein, the splitting energy between Cu $2p_{3/2}$ and Cu $2p_{1/2}$ is 20.1 eV and three satellite peaks at 941.3, 943.8 and 962.6 eV are also found, which indicate that Cu species could be inserted into VO_x lattice [35]. In Figure 2.7d, two peaks of V $2p_{3/2}$ (516.9 eV) and V $2p_{1/2}$ (523.9 eV) are assigned to V^{4+} while the deconvolution of the V $2p_{3/2}$ peak located at 517.5 eV and the satellite peak of V $2p_{1/2}$ at 524.9 eV with the spin-orbital splitting energy of about 7.4 eV correspond to the V^{5+} oxidation state, which is well consistence with the XRD result [36]. For XPS spectrum of V 2p in V_2O_5@CP (Figure 2.8a), there are only two peaks of V $2p_{3/2}$ and V $2p_{1/2}$ at 517.3 and 524.3 eV, which correspond to V^{5+} of V_2O_5. It is reported that V^{4+} ion is always associated with the oxygen vacancy coupled with the V^{5+} ion [37]. As such, the presence of V^{4+} in both $CuVO_x$ and $CuVO_x$-NiO should play a crucial role in the generation of the defect structure associated with the oxygen vacancy. In other words, the recrystallization of vanadium pentoxide (V_2O_5) in the presence of Cu^{2+} and Ni^{2+} ions should have enhanced the oxygen deficiency and defect sites [38]. Additionally, for O 1s XPS spectrum in $CuVO_x$-NiO, the main peak appeared at 530.2 eV could be assigned to the lattice O^{2-} ions (O_L). Besides, the binding energy gap between O 1s and V 2p of about 12.7 eV confirms the existence of V^{5+} species [23, 39]. The peak at high binding energies at about 531.7 and 532.7 eV are assigned to the defect sites with low oxygen coordination (O_V) and surface adsorbed water (O_C), respectively [27, 40]. In order to confirm the relative ratios of oxygen vacancies, the

O1s peak areas between CuVO$_x$ and CuVO$_x$-NiO are compared in the Table 2.2. After NiO is composited with CuVO$_x$, the intensity of peak relating to oxygen vacancy is dramatically increased from 0.172 to 0.289, confirming that more O vacancies should be generated with the presence of NiO due to the structure reconstruction and recrystallization during the reaction [41]. Moreover, multivalent states of vanadium and rich-defect structure could either improve the electronic and ionic conductivities or accelerate the charge transfer kinetics for the electrochemical reactions [42]. Therefore, the co-existence of Cu^{2+}, Cu^{+}, V^{5+}, V^{4+} and Ni^{2+} species in the CuVO$_x$-NiO electrocatalyst is expected to exhibit the superior performance for HER. These results also correspond to the HRTEM observation.
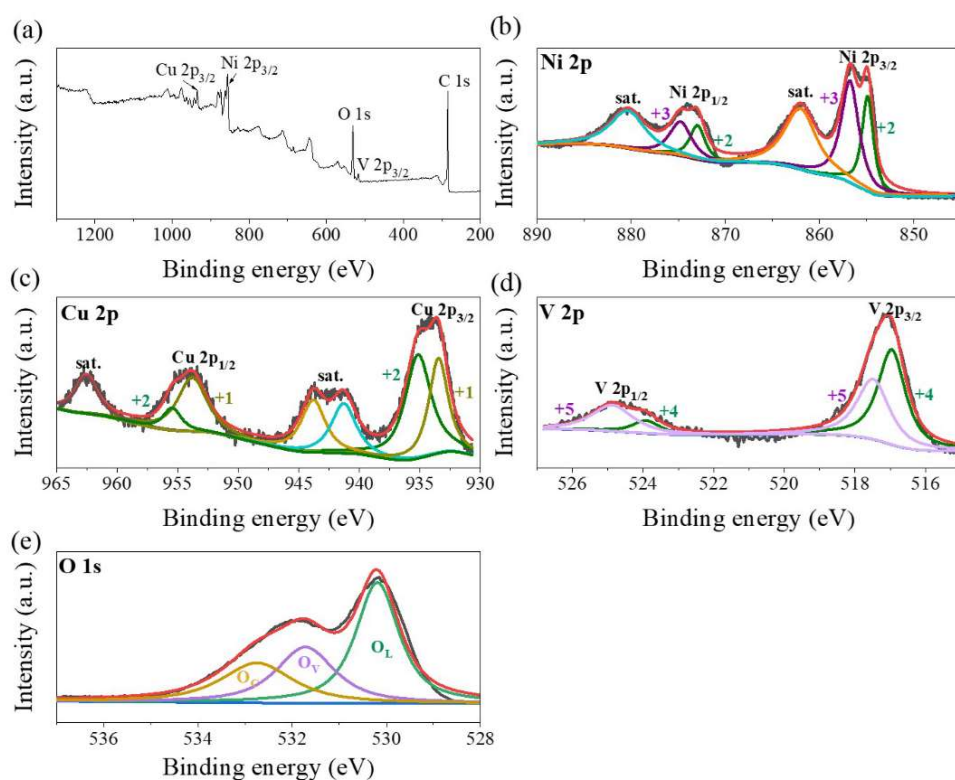
Figure 2.7 (a) Survey XPS spectrum; (b) Ni 2p XPS spectrum; (c) Cu 2p XPS spectrum; (d) V 2p XPS spectrum and (e) O 1s XPS spectrum of CuVO$_x$-NiO electrocatalyst.
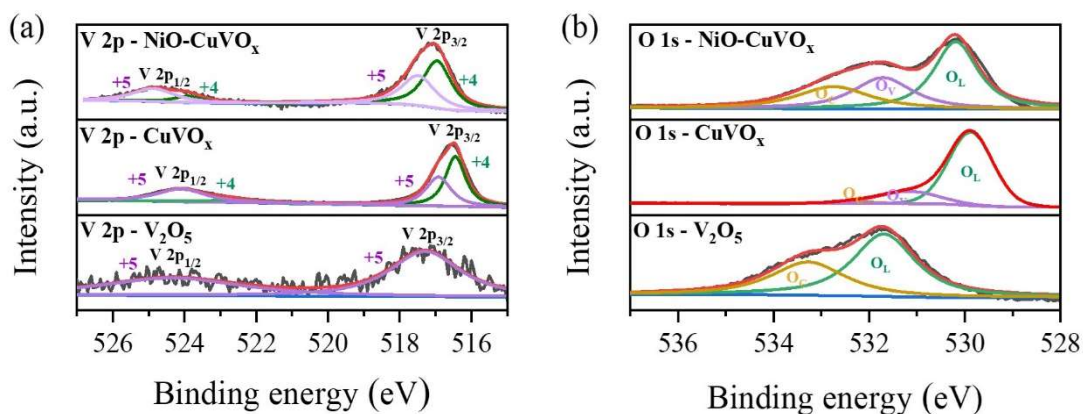
Figure 2.8 XPS spectra of (a) V 2p and (b) O 1s of V_2O_5, $CuVO_X$ and $CuVO_x$-NiO.

Table 2.2 The relative ratios of O1s peak areas based on XPS analysis

Electrode	Relative ratio of O1s peak areas		
	Lattice oxygen (O_L)	Oxygen vacancies (O_V)	Chemisorbed oxygen (O_C)
V_2O_5@CP	0.613	-	0.387
$CuVO_x$ @CP	0.753	0.172	0.075
$CuVO_x$-NiO@CP	0.459	0.289	0.252
$CuVO_x$-NiO@CP after HER	0.280	0.447	0.273

To further verify the composition of $CuVO_x$-NiO, Raman spectroscopy was also measured. As shown in Figure 2.9, the main peak of V-O stretching at 998 cm^{-1} in pure V_2O_5 (Figure 2.9a) shifts to 895 cm^{-1} in $CuVO_x$ (Figure 2.9b) and 820 cm^{-1} in $CuVO_x$-NiO (Figure 2.9c), which should be attributed to the substitution of Cu and/or Ni in the lattice of V_2O_5 [43]. In addition, the Raman scatterings at 263 and 340 cm^{-1} (Figure 2.9c) correspond to Cu-O stretching whereas the peak at 538 cm^{-1} is ascribed to the vibration of Ni-O [23]. These results also indicate the successful formation of $CuVO_x$-NiO electrocatalysts.

The contact angle was examined to understand the surface wettability and aerophobic properties of the catalyst surface for the HER [15]. As shown in Figure 2.10, the water contact angles (WCAs) of bare CP, V_2O_5@CP, $CuVO_x$@CP, NiO@CP and $CuVO_x$-NiO@CP are 131.5°, 124.1°, 48.3°, 0° and 0°, respectively, indicating that the $CuVO_x$-NiO@CP has super-hydrophilic property with a WCA of 0°. This super-hydrophilic surface of $CuVO_x$-NiO@CP should be due to the good water adsorption ability of NiO nanosheet shell, which could promote the Volmer step of HER in alkaline electrolyte. Simultaneously, the generated hydrogen gas could be more easily detached from the electrode surface during the HER process [44]. The fast hydrogen desorption is also beneficial for keeping the nucleation sites free for new hydrogen generation, inducing more favorable contact points around the catalytic active sites, thereby leading to sufficient contact between the electrode and electrolyte [45, 46].
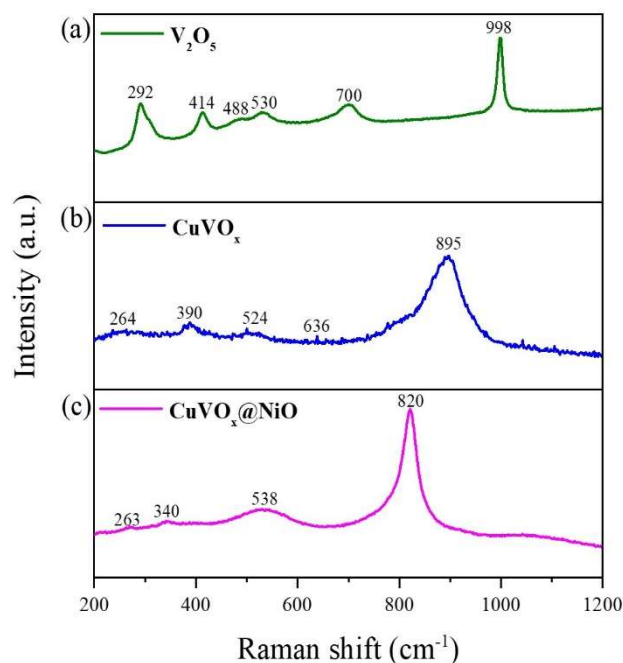
Figure 2.9 Raman spectra of prepared catalysts (a) V_2O_5, (b) $CuVO_x$ and (c) $CuVO_x$-NiO.
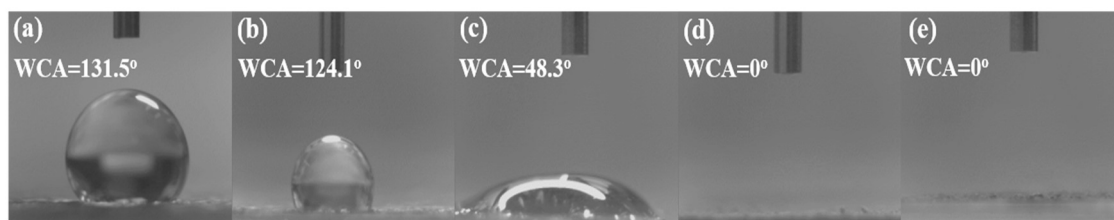
Figure 2.10 Contact angle measurements for (a) Bare CP, (b) V_2O_5 @CP, (c) $CuVO_x$ @CP, (d) NiO@CP and (e) $CuVO_x$-NiO@CP.

2.3.2 Catalytic HER performance and stability

HER performances of all fabricated electrodes were evaluated in 1 M KOH solution with a scan rate of 1 mVs^{-1} in the three-electrode system. As shown in Figure 2.11a, the $CuVO_x$-NiO@CP electrode exhibits an overpotential of 74 $mV@10$ $mAcm^{-2}$, which is lower than those of NiO-CuO@CP (83 $mV@10$ $mAcm^{-2}$) and $CuVO_x$@CP (124 $mV@10$ $mAcm^{-2}$). The overpotential of $CuVO_x$-NiO@CP catalyst is not only comparable to that of Pt/C but also lower than those recently reported data on the similar materials (Table 2.3).

Meanwhile, from Figure 2.11b, Tafel slopes relating to the NiO-CuO@CP, NiO-V_2O_5@CP, $CuVO_x$@CP, V_2O_5@CP and $CuVO_x$-NiO@CP electrodes are 75.8, 158.4, 132.5, 163.6 and 60.8 mV dec^{-1}, respectively. Herein, the $CuVO_x$-NiO@CP electrode also exhibits the lowest Tafel slope, implying that the fastest kinetics occur on this electrode. Based on the Tafel slope value (60.8 mV dec^{-1}) of $CuVO_x$-NiO@CP electrode, the HER over it should obey the Volmer-Heyrovsky mechanism. As stated above, the NiO shell is benefit for the H_2O adsorption and decomposition with the reduced energy barrier at the initial water dissociation step followed by a H_2 desorption step. It is reported that the NiO (111) site could accelerate water dissociation step due to the strong adsorption ability and hight surface wettability, where H_2O molecule can be easily dissociated into intermediate H_{ads} and OH^- (Volmer step ; H_2O + e^- → H_{ads} + OH^-) [16, [47-49]]. Then, the produced H_{ads} could be easily to absorb on the O

vacancies sites of VO_x-Cu_2O/Cu (the real active species), and subsequently combine with another H_{ads} from the water dissociation with a hydrogen desorption step (Heyrovsky step; $H_2O + e^- + H_{ads} \rightarrow H_2 + OH^-$). Therefore, the oxygen vacancy defects could promote the Heyrovsky step of HER in alkaline solution by facilitating the conversion of adsorbed H intermediate to H_2, and enhance electrical conductivity due to the electron hopping between different valence states of metal-O sites [26]. Thus, the synergistic effect of the NiO and $CuVO_X$ could promote water dissociation, especially hydrogen desorption step, thereby improving the HER activity.
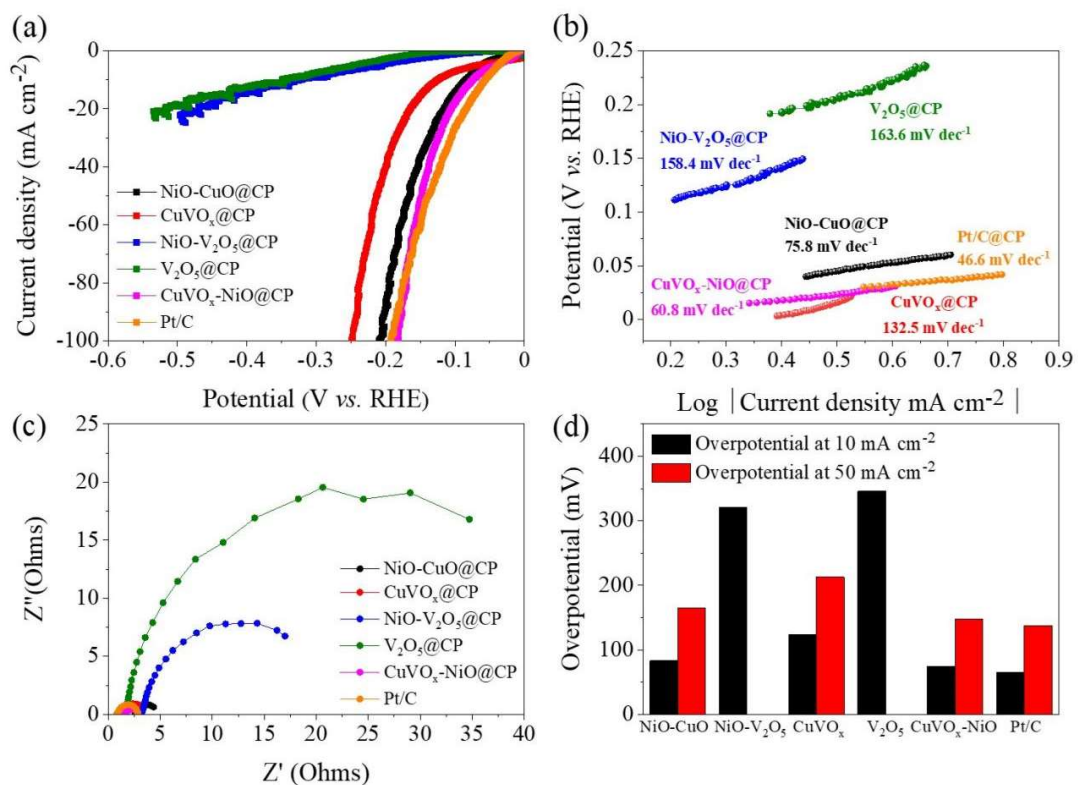
Figure 2.11 Electrocatalytic performances of the prepared electrodes in 1 M KOH solution. (a) LSV curves; (b) Corresponding Tafel plots; (c) EIS Nyquist plots; (d) Overpotentials at two different current densities of 10 and 50 mA cm^{-2}.

According to Butler-Volmer equation with microkinetic analysis, the Tafel slope value is in the range of 40-120 mV dec^{-1}, indicating that the amount of active sites does not limit the reaction rate while the Heyrovsky step could be determined as the rate

determined step [50, 51]. Figure 2.11c shows EIS analysis results, in which the spectrum at the high frequency stands for the internal resistance of electrode (R_s) while the semicircle radius indicates the charge-transfer resistance (R_{ct}). One can see that the R_s values of NiO-CuO@CP, NiO-V$_2$O$_5$@CP, CuVO$_x$@CP, V$_2$O$_5$@CP and CuVO$_x$-NiO@CP are 3.73, 3.20, 1.23, 1.68 and 1.55 Ω/cm^2 with the corresponding R_{ct} values of 2.09, 13.80, 2.11, 33.07 and 0.72 Ω/cm^2, respectively. It indicates that the CuVO$_x$-NiO@CP electrode has the lowest resistance for the charge transfer, which is also agreement with its electrocatalytic performance. These results confirm that the CuVO$_x$ binary metal oxides combined with the NiO lamellar nanosheets can effectively enhance the charge transfer properties. The synergetic coupling of the CuVO$_x$ with high conductivity and NiO lamellar nanosheets with a high surface area could provide effective electron transportation and sufficient contact area between the electrode and electrolyte, thereby resulting in the improved HER performance [43, 52]. In addition, the CuVO$_x$-NiO@CP electrode also shows an overpotential as low as 148 mV for the generation of a higher current density of 50 mA/cm^2 (Figure 2.11d), suggesting that it has the potential for the practical application.

Cyclic voltammetry (CV) at the non-faradic potential range was conducted in order to measure the electrochemical active surface area (ECSA) of all prepared electrodes (Figure 2.12). Figure 2.13a shows the electrochemical active surface areas (ECSAs) of different synthesized electrodes and Table 2.4 summarizes the related other parameters. The normalized ECSA was calculated by setting the ECSA of carbon paper as 1. As such, the normalized ECSA of NiO-CuO@CP, CuVO$_x$@CP and CuVO$_x$-NiO@CP are 86.2, 74.4 and 182, respectively, indicating that synergistic interaction between nickel and vanadium species should play a crucial role for improving the ECSA due to the formation of lamellar NiO nanosheets on the CuVO$_x$ layer. Obviously, the CuVO$_x$-

NiO@CP electrode displays 2.1 and 2.4 times higher ECSAs than those of NiO-CuO@CP and CuVO$_x$@CP electrodes, respectively, proving that this electrode has enriched active sites and high surface roughness. Moreover, the excellent intrinsic activity of CuVO$_x$-NiO@CP is further confirmed by ECSA-normalized current density. As shown in Figure 2.14, CuVO$_x$-NiO@CP obviously exhibits a higher electrocatalytic activity than others electrode, further implying its high intrinsic activity [65, 66].

Table 2.3 Comparison of HER activity of CuVO$_x$-NiO electrocatalysts with the recently reported data

Electrocatalysts	Electrolyte	Overpotential at 10 mA cm^{-2} (mV)	Reference
CuVO$_x$-NiO@CP	1M KOH	74	This work
In-Zn-Co ternary oxide	1M KOH	510	[53]
V-Ni$_3$S$_2$/CC	1M KOH	81	[54]
NiO/Co$_3$O$_4$	1M KOH	170	[55]
NiO@CoO/CC	1M KOH	149	[34]
Ni$_3$(VO$_4$)$_2$/NiCo$_2$O$_4$	1M KOH	113	[56]
MoS$_2$/Co$_3$S$_4$	1M KOH	90.3	[15]
Cu/Cu$_2$O-CuO/rGO	1M KOH	105	[57]
V-Ni$_2$P	1M KOH	85	[58]
V doped MoS$_2$	1M KOH	206	[59]
W-NiO/NiS$_2$	1M KOH	116	[60]
Mixed metal oxide (Co:W:Cu)	1M KOH	103	[61]
Ni-Mo-S@Co$_3$O$_4$/CF	1M KOH	85	[8]
Mo-Doped NiCu	1M KOH	95	[12]
PA-NiO	1M KOH	138	[62]
CuO@Ni/NiFe hydroxide	1M KOH	125	[63]
NiCu-P	1M KOH	175	[64]

Figure 2.13b shows multi-step chronopotentiometry measured from 10 to 300 mA cm^{-2} with a 50 mA cm^{-2} increment every 500 s and then going back to 10 mA cm^{-2} after 300 mA cm^{-2} operation for the CuVO$_x$-NiO@CP electrode. One can see that this electrode maintains the potentials at different constant current densities with excellent

recyclability due to its good electro-conductivity, superb mass transport property and mechanical robustness for HER in the alkaline solution. Moreover, as can be seen in Figure 2.13c, the LSV curve after 1000-cycle testing has no apparent change in the HER activity. Meanwhile, for the chronopotentiometry measurement at a constant current density of 10 mA cm^{-2} in 30 h, the potential to achieve the standard 10 mA cm^{-2} current density remains constant when the testing is performed in a continuous flowing 1 M KOH solution (Figure 2.13d).
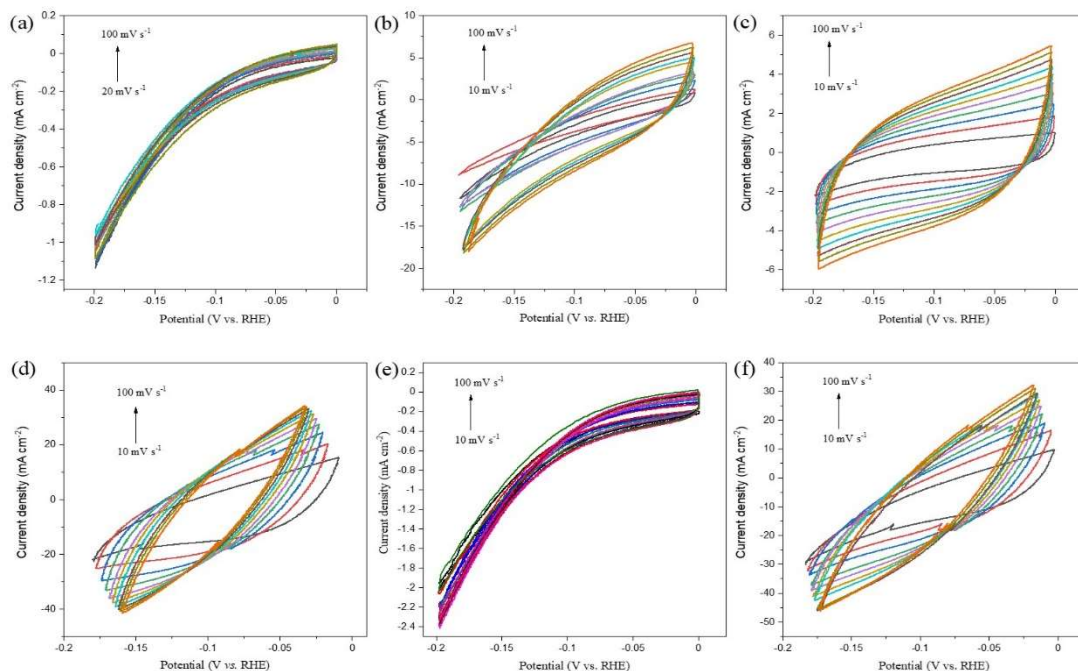
Figure 2.12 Cyclic voltammograms (CV) for the double-layer capacitance measurements of (a) Bare carbon paper, (b) NiO-CuO@CP, (c) NiO-V$_2$O$_5$@CP, (d) CuVO$_x$@CP, (e) V$_2$O$_5$@CP and (f) CuVO$_x$-NiO@CP electrodes with a potential range of -0.2-0V (*vs* RHE) at scan rates of 10-100 mVs^{-1} in 1 M KOH solution.

Table 2.4 Calculated electrochemical active surface area (ECSA) values and R_f of all electrodes

Electrode	C_{dl} (mF)	ECSA (x 10^3 cm^2)	R_f (x 10^3)	Normalized ECSA
Carbon paper	0.5	0.01	0.01	1.0
NiO-CuO@CP	43.1	1.08	1.08	86.2
NiO-V$_2$O$_5$@CP	28.45	0.71	0.71	56.9
CuVO$_x$@CP	37.2	0.93	0.93	74.4
V$_2$O$_5$@CP	1.4	0.04	0.04	2.80
CuVO$_x$-NiO@CP	91	2.28	2.28	182
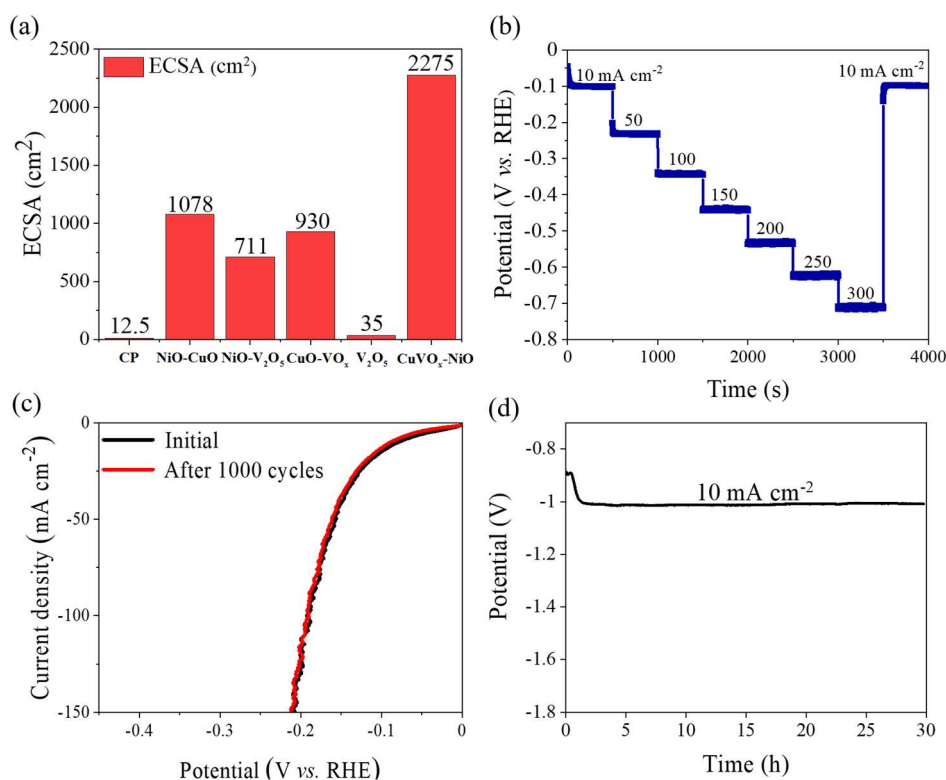
Figure 2.13 (a) ECSAs of the various prepared electrodes; (b) HER multi-step chronopotentiometric curve of the CuVO$_x$-NiO@CP electrode starting from a current density of 10 mA cm^{-2} and ending at 300 mA cm^{-2} with an increment of 50 mA cm^{-2} every 500 s; (c) Polarization curves for the CuVO$_x$-NiO@CP at the initial cycle and after 1000 cycles; (d) Chronopotentiometry test of CuVO$_x$-NiO@CP carried out at a constant current density of 10 mA cm^{-2} for 30 h.
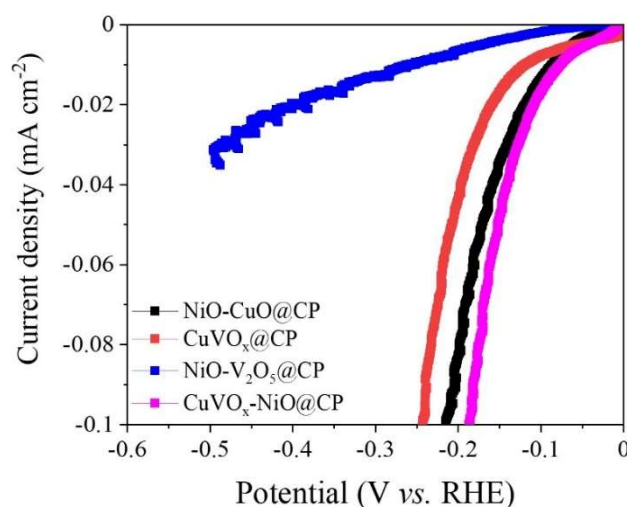
Figure 2.14 HER performance normalized by ECSA.

Post-characterization of $CuVO_x$-NiO@CP further supports the excellent stability of catalyst. As displayed in Figure 2.15a, the morphology of $CuVO_x$-NiO@CP after the stability testing maintains almost unchanged, especially the lamellar nanosheet layer is obviously observed. Herein, one can see that some tiny spherical particles appear in the space among the nanosheets, suggesting that some new phases should be formed during the HER process, which is also confirmed by the EDX elemental mapping (Figure 2.16). TEM image of the electrocatalysts after the HER is presented in Figure 2.17. Herein, the lattice spacing of 0.20 nm corresponding to the (200) plane of NiO is retained. Meanwhile, the lattice fringes assigned to (111) and (200) planes of Cu_2O and Cu are also observed, suggesting that the recrystallization of $CuVO_x$ occurred during the HER process. Moreover, XRD pattern of the spent $CuVO_x$-NiO@CP after the stability test is displayed in Figure 2.15b, in which the diffraction peaks located at 2θ of 43.4°, 50.6° and 74.2° relating to (111), (200) and (220) planes of Cu (JCPDS No. 04-0836) and the characteristics peaks at 36.5°, 42.4°, 61.5° and 73.7° corresponding to (111), (200), (220) and (311) planes of Cu_2O (JCPDS No 75-1531) are also found. The peaks of

97

Cu_2O and Cu should be generated from partial reduction of Cu species in $CuVO_x$ in alkaline solution, confirming by XRD peak of $CuVO_x/CP$ after HER [67]. Meanwhile, the diffraction peaks of NiO are remained.
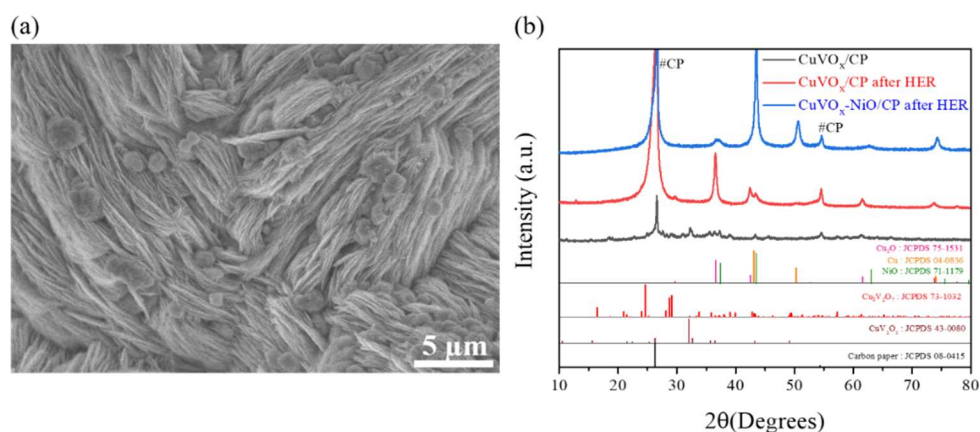
Figure 2.15 (a) SEM image and (b) XRD pattern of $CuVO_x$-$NiO@CP$ after long-term stability test.
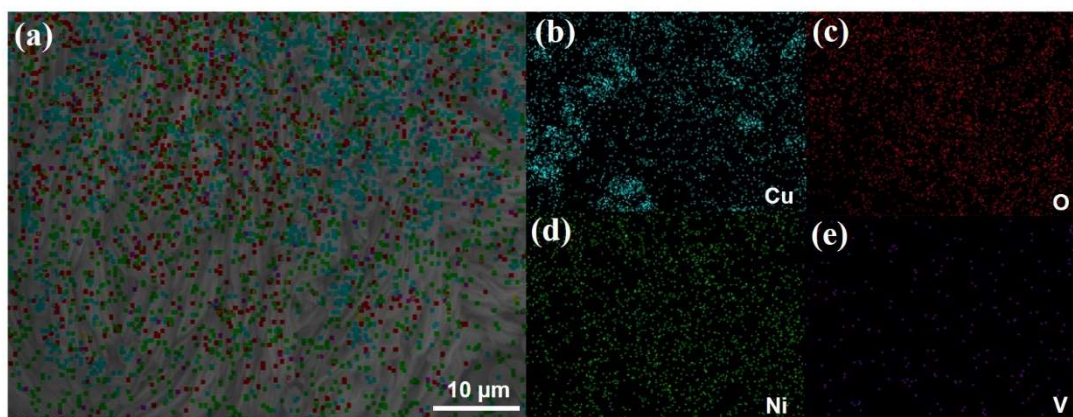
Figure 2.16 SEM images of (a) CuVOx-NiO@CP ; and (b-e) the corresponding EDX mappings of Cu, O, Ni and V after the stability test.
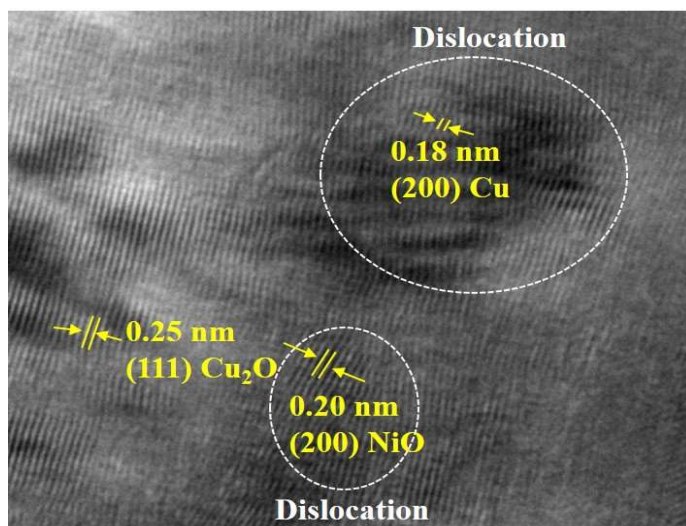
Figure 2.17 TEM image of $CuVO_x$-NiO@CP after the stability test.

This phenomenon is further analyzed by XPS analysis. As displayed in Figure 2.18a, the peaks located at 954.4 and 934.9 eV relating to Cu $2p_{1/2}$ and Cu $2p_{3/2}$ of Cu^{2+} still exist but the peak intensities of Cu $2p_{1/2}$ and Cu $2p_{3/2}$ after the stability test are increased sharply and shifted toward the lower binding energy, suggesting the transformation of CuO to Cu_2O (Cu^+) or metallic copper (Cu^0) at 932.9 and 952.8 eV because Cu (II) species can be reduced to Cu_2O (I) and Cu (0) driven by electron in the redox reaction [68]. However, it should be noted that it is difficult to distinguish the Cu_2O and metallic Cu with the XPS analysis results owing to the similar binding energies of Cu $2p_{3/2}$ and Cu $2p_{1/2}$ for the Cu_2O and Cu 2p for the Cu(0). Notably, the presences of both stable Cu_2O/Cu and/or Cu_2O/CuO composites could enhance the catalytic activity, leading to the good stability in alkaline solution [57, 69]. Onsten *et. al.* [70] reported that H from water prefers to be adsorbed at uncoordinated oxygen sites/defects of Cu_2O (111), and oxygen species in water can interact with the surface copper species, resulting in a weaker O-H bond, which can accelerate water dissociation. Hence, the presence of a small amount of Cu(I)/Cu(0) species with an oxophilic surface of NiO-$CuVO_X$ could promote water dissociation by lowering the energy barrier and enhancing the

recombination reaction of H_{ads} to H_2 at the metal surface, resulting in increased HER activity in alkaline condition [71, 72].
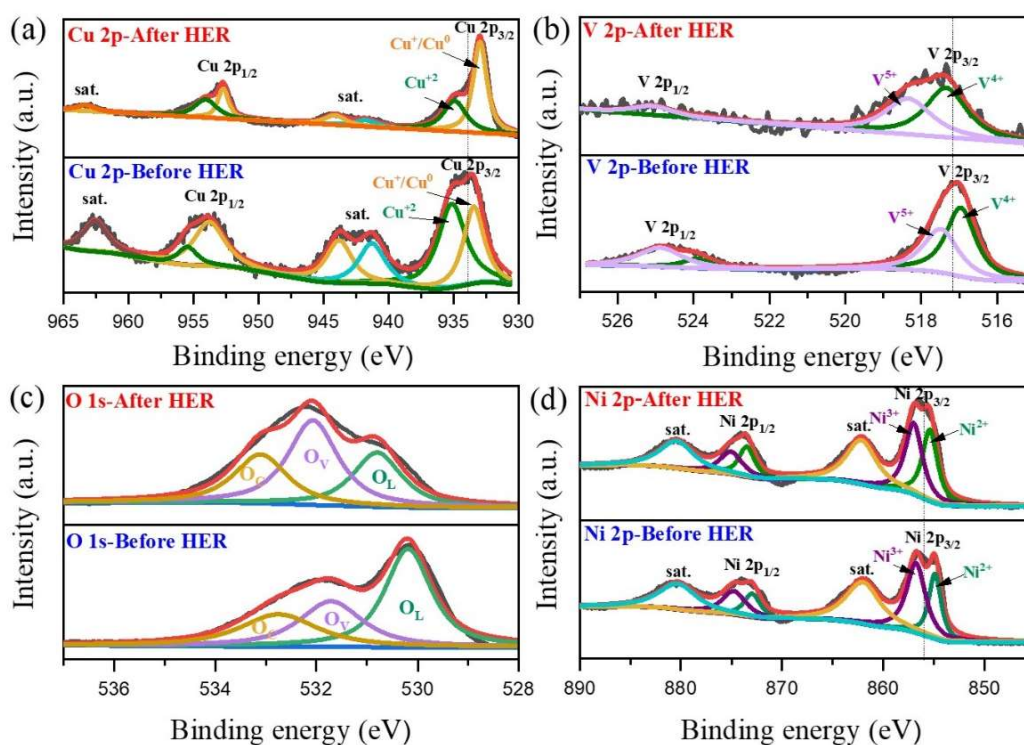
Figure 2.18 (a) Cu 2p XPS spectrum, (b) V 2p XPS spectrum, (c) O 1s XPS spectrum and (d) Ni 2p XPS spectrum of CuVO$_x$-NiO after the long-term stability test for 30 h.

Besides, the presence of metallic Cu(0) could enhance intrinsic conductivity of the electrode. As can be seen in Figure 2.18b, the peaks of V 2p spectra are slightly decreased, which can be attributed to the partial dissolution of VO$_x$ caused by the weak bonding between VO$_x$ and Ni species. However, the valence states of V^{5+} and V^{4+} at 517.3 and 518.3 eV are almost remained [3]. On the O 1s spectrum, three peaks at 530.8, 532.1 and 533.1 eV correspond to the lattice oxygen (O$_L$), the native defects of O^{2-} vacancies (O$_V$) and the chemisorbed oxygen closely related to -OH groups on the surfaces of metal oxides (O$_C$), respectively (Figure 2.18c) [71]. The intensities of peaks relating to the metal oxide on the surface are decreased while those corresponding to the oxygen vacancies and surface absorbed oxygens/hydroxide are increased,

100

confirming the transformation of CuO to Cu_2O/Cu species with the loss of oxygen atoms after recrystallization during the HER process. In addition, the relative ratios of O 1s peak areas are summarized in the Table 2.5. Notably, the fraction of oxygen vacancies is increased from 0.289 to 0.447 after the long-term operation, which might be caused by the weakening of M-O bonds. Herein, the generation of O vacancies could promote the Heyrovsky step since the O vacancies can promote H_{ads} adsorption kinetics as well as the desorption of H_2. Meanwhile, Ni 2p XPS spectrum maintains unchanged, implying that the valence states of Ni^{2+} and Ni^{3+} maintain stable in the alkaline condition (Figure 2.18d). Moreover, the relative Cu content is increased from 6.82% to 8.64%, also confirming the generation of Cu_2O and Cu species during the HER in alkaline solution. These post characterizations prove that the VO_x-Cu_2O/Cu and NiO species should act as the real active species for the HER. In addition, it should be noted that the response current density of HER does not decrease during the conversion of Cu based species according to the long-term stability test, which might be due to that the reaction current of $CuVO_x$ conversion is not obvious and the formed Cu_2O/Cu and VO_x are the stable forms. Here, the robust stability still observed after a long-term operation should rely on the recrystallization on the Cu species sites from $CuVO_x$-NiO to the stable VO_x-Cu_2O/Cu-NiO. As such, the presence of mixed valence states of Cu species and stable morphology from the strong interaction between $CuVO_x$ and NiO nanosheets with high surface roughness could provide an outstanding intrinsic activity with strong adsorption of electroactive species, which are beneficial for the HER [73, 74]. In addition, the hydrogen production during a certain period of water electrolysis was also investigated. As shown in Figure 2.19, the Faradaic efficiency of $CuVO_x$-NiO@CP electrode reaches 97%. Therefore, the $CuVO_x$-NiO@CP electrode can provide fast

charge transfer rate, quick hydrogen bubble releasing, thereby exhibiting good robustness and durability under HER in the alkaline electrolyte.

Table 2.5 The relative ratios of O1s peak areas based on XPS analysis

Electrodes	Relative ratio of O1s peak areas		
	Lattice oxygen (O_L)	Oxygen vacancies (O_V)	Chemisorbed oxygen (O_C)
V_2O_5@CP	0.613	-	0.387
$CuVO_x$ @CP	0.753	0.172	0.075
$CuVO_x$-NiO@CP	0.459	0.289	0.252
$CuVO_x$-NiO@CP after HER	0.280	0.447	0.273

Figure 2.19 Theoretical hydrogen evolution amount compared with the measured hydrogen evolution amount for HER over the $CuVO_x$-NiO@CP electrode.

2.4 Conclusions

By utilizing a simple hydrothermal process with a calcination step, an O vacancy-rich $CuVO_x$ nanobelt@NiO nanosheet composite was successfully coated on the carbon paper. Especially, the generation of real active species VO_x-Cu_2O and Cu-NiO during the HER could further increase the intrinsic activity with the maintained morphology. The composite had excellent electrocatalytic HER performance in the alkaline solution with an overpotential as low as 74 mV at 10 mA cm^{-2} and a fast kinetic reaction with a small Tafel slope of 60.8 mVdec^{-1}, as well as excellent stability and recyclability, significantly better than those reported similar bi-metal oxide based electrocatalysts. The outstanding catalytic performance could be attributed to the effective adsorption and decomposition of H_2O to H_{ads} intermediate by synergistic effect between hydrophilic surface of NiO and the O vacancy-rich $CuVO_x$, allowing the generated H_{ads} on the NiO to be easily adsorbed on the O vacancy of VO_x-Cu_2O, thereby converting to H_2. This innovative design could be useful in the development of low-cost electrocatalysts for the application in alkaline electrolyzers.

References

[1] S.A. Razek, M.R. Popeil, L. Wangoh, J. Rana, N. Suwandaratne, J.L. Andrews, D.F. Watson, S. Banerjee, L.F.J. Piper, Designing catalysts for water splitting based on electronic structure considerations, Electronic Structure, 2 (2020) 023001.

[2] P. Zhou, X. Lv, Y. Gao, Z. Cui, Y. Liu, Z. Wang, P. Wang, Z. Zheng, Y. Dai, B. Huang, Enhanced electrocatalytic HER performance of non-noble metal nickel by introduction of divanadium trioxide, Electrochim. Acta 320 (2019).

[3] Y. Li, X. Tan, R.K. Hocking, X. Bo, H. Ren, B. Johannessen, S.C. Smith, C. Zhao, Implanting Ni-O-VO$_x$ sites into Cu-doped Ni for low-overpotential alkaline hydrogen evolution, Nat Commun. 11 (2020) 2720.

[4] Y. Li, K. Dastafkan, Q. Sun, Y. Ma, X. Wang, X. Yang, Z. Wang, C. Zhao, Ni-based 3D hierarchical heterostructures achieved by selective electrodeposition as a bifunctional electrocatalyst for overall water splitting, Electrochim. Acta 379 (2021) 138042.

[5] J. Joo, T. Kim, J. Lee, S.-I. Choi, K. Lee, Morphology-Controlled Metal Sulfides and Phosphides for Electrochemical Water Splitting, Adv. Mater 31 (2019) 1806682.

[6] M. Zhou, Q. Weng, Z.I. Popov, Y. Yang, L.Y. Antipina, P.B. Sorokin, X. Wang, Y. Bando, D. Golberg, Construction of Polarized Carbon–Nickel Catalytic Surfaces for Potent, Durable, and Economic Hydrogen Evolution Reactions, ACS Nano 12 (2018) 4148-4155.

[7] J. Wei, M. Zhou, A. Long, Y. Xue, H. Liao, C. Wei, Z.J. Xu, Heterostructured Electrocatalysts for Hydrogen Evolution Reaction Under Alkaline Conditions, Nano-Micro Lett, 10 (2018) 75.

[8] T. Xiong, G. Li, D.J. Young, Z. Tan, X.-H. Yin, Y. Mi, F. Hu, In-situ surface-derivation of Ni-Mo bimetal sulfides nanosheets on Co$_3$O$_4$ nanoarrays as an advanced

overall water splitting electrocatalyst in alkaline solution, J. Alloys Compd. 791 (2019) 328-335.

[9] Q. Shao, P. Wang, X. Huang, Opportunities and Challenges of Interface Engineering in Bimetallic Nanostructure for Enhanced Electrocatalysis, Adv. Funct. Mater. 29 (2019).

[10] J.M. Gonçalves, M.I. da Silva, H.E. Toma, L. Angnes, P.R. Martins, K. Araki, Trimetallic oxides/hydroxides as hybrid supercapacitor electrode materials: a review, J. Mater. Chem. A 8 (2020) 10534-10570.

[11] Z. Fang, S.u. Rehman, M. Sun, Y. Yuan, S. Jin, H. Bi, Hybrid NiO–CuO mesoporous nanowire array with abundant oxygen vacancies and a hollow structure as a high-performance asymmetric supercapacitor, J. Mater. Chem. A 6 (2018) 21131-21142.

[12] Z. Wang, X. Ge, Z. Li, J. Wu, Z. Liang, S. Wang, Mo-Doped NiCu as an efficient and stable electrocatalyst for the hydrogen evolution reaction, New J. Chem 43 (2019) 9652-9657.

[13] Z. Hao, S. Yang, J. Niu, Z. Fang, L. Liu, Q. Dong, S. Song, Y. Zhao, A bimetallic oxide $Fe_{1.89}Mo_{4.11}O_7$ electrocatalyst with highly efficient hydrogen evolution reaction activity in alkaline and acidic media, Chem. Sci. 9 (2018) 5640-5645.

[14] S. Jiang, R. Zhang, H. Liu, Y. Rao, Y. Yu, S. Chen, Q. Yue, Y. Zhang, Y. Kang, Promoting Formation of Oxygen Vacancies in Two-Dimensional Cobalt-Doped Ceria Nanosheets for Efficient Hydrogen Evolution, J. Am. Chem. Soc. 142 (2020) 6461-6466.

[15] O. Peng, R. Shi, J. Wang, X. Zhang, J. Miao, L. Zhang, Y. Fu, P. Madhusudan, K. Liu, A. Amini, C. Cheng, Hierarchical heterostructured nickle foam–supported Co_3S_4

nanorod arrays embellished with edge-exposed MoS_2 nanoflakes for enhanced alkaline hydrogen evolution reaction, Mater. Today Energy 18 (2020) 100513.

[16] M. Gong, W. Zhou, M.-C. Tsai, J. Zhou, M. Guan, M.-C. Lin, B. Zhang, Y. Hu, D.-Y. Wang, J. Yang, S.J. Pennycook, B.-J. Hwang, H. Dai, Nanoscale nickel oxide/nickel heterostructures for active hydrogen evolution electrocatalysis, Nat Commun. 5 (2014) 4695.

[17] R. Subbaraman, D. Tripkovic, D. Strmcnik, K. Chang, M. Uchimura, A.P. Paulikas, V.R. Stamenkovic, N.M. Markovic, Enhancing Hydrogen Evolution Activityin Water Splitting by Tailoring Li^+-$Ni(OH)_2$-Pt Interfaces, Science, 334 (2011) 1256-1260.

[18] M.A. Henderson, The interaction of water with solid surfaces: fundamental aspects revisited, Surf. Sci. Rep. 46 (2002) 1-308.

[19] W. Zhang, Y. Sun, Q. Liu, J. Guo, X. Zhang, Vanadium and nitrogen co-doped CoP nanoleaf array as pH-universal electrocatalyst for efficient hydrogen evolution, J. Alloys Compd. 791 (2019) 1070-1078.

[20] L. Xu, J. Li, H. Sun, X. Guo, J. Xu, H. Zhang, X. Zhang, In situ Growth of Cu_2O/CuO Nanosheets on Cu Coating Carbon Cloths as a Binder-Free Electrode for Asymmetric Supercapacitors, Front. Chem. 7 (2019) 420.

[21] J. Yao, Y. Li, R.C. Massé, E. Uchaker, G. Cao, Revitalized interest in vanadium pentoxide as cathode material for lithium-ion batteries and beyond, Energy Stor. Mater. 11 (2018) 205-259.

[22] L. Bai, J. Zhu, X. Zhang, Y. Xie, Reducing hydrated protons co-intercalation to enhance cycling stability of CuV_2O_5 nanobelts: A new anode material for aqueous lithium ion batteries, J. Mater. Chem. 22 (2012) 16957-16963.

[23] A. Meena, M. Ha, S.S. Chandrasekaran, S. Sultan, P. Thangavel, Ahmad M. Harzandi, B. Singh, J.N. Tiwari, K.S. Kim, Pt-like hydrogen evolution on a $V_2O_5/Ni(OH)_2$ electrocatalyst, J. Mater. Chem. A 7 (2019) 15794-15800.

[24] Y. Li, X. Tan, W. Yang, X. Bo, Z. Su, T. Zhao, S.C. Smith, C. Zhao, Vanadium Oxide Clusters Decorated Metallic Cobalt Catalyst for Active Alkaline Hydrogen Evolution, Cell Rep. 1 (2020) 100275.

[25] T. Sun, G. Zhang, D. Xu, X. Lian, H. Li, W. Chen, C. Su, Defect chemistry in 2D materials for electrocatalysis, Mater. Today Energy 12 (2019) 215-238.

[26] L. An, Y. Zhang, R. Wang, H. Liu, D. Gao, Y.-Q. Zhao, F. Cheng, P. Xi, Activation of defective nickel molybdate nanowires for enhanced alkaline electrochemical hydrogen evolution, Nanoscale 10 (2018) 16539-16546.

[27] D. Liu, C. Zhang, Y. Yu, Y. Shi, Y. Yu, Z. Niu, B. Zhang, Hydrogen evolution activity enhancement by tuning the oxygen vacancies in self-supported mesoporous spinel oxide nanowire arrays, Nano Res.11 (2018) 603-613.

[28] D. Wang, Q. Li, C. Han, Q. Lu, Z. Xing, X. Yang, Atomic and electronic modulation of self-supported nickel-vanadium layered double hydroxide to accelerate water splitting kinetics, Nat Commun. 10 (2019) 3899.

[29] S. Li, S. Sirisomboonchai, A. Yoshida, X. An, X. Hao, A. Abudula, G. Guan, Bifunctional $CoNi/CoFe_2O_4$ /Ni foam electrodes for efficient overall water splitting at a high current density, J. Mater. Chem. A 6 (2018) 19221-19230.

[30] W. Guo, W.D. Chemelewski, O. Mabayoje, P. Xiao, Y. Zhang, C.B. Mullins, Synthesis and Characterization of CuV_2O_6 and $Cu_2V_2O_7$: Two Photoanode Candidates for Photoelectrochemical Water Oxidation, J. Phys. Chem. C 119 (2015) 27220-27227.

[31] L. Dong, L. Zhang, C. Sun, W. Yu, J. Zhu, L. Liu, B. Liu, Y. Hu, F. Gao, L. Dong, Y. Chen, Study of the Properties of $CuO/VO_x/T_{i0.5}Sn_{0.5}O_2$ Catalysts and Their Activities in NO + CO Reaction, ACS Catal. 1 (2011) 468-480.

[32] L. Zhou, Q. Yan, A. Shinde, D. Guevarra, P.F. Newhouse, N. Becerra-Stasiewicz, S.M. Chatman, J.A. Haber, J.B. Neaton, J.M. Gregoire, High Throughput Discovery of Solar Fuels Photoanodes in the $CuO-V_2O_5$ System, Adv. Energy Mater. 5 (2015).

[33] Y. Wang, Z. Liang, H. Zheng, R. Cao, Recent Progress on Defect-rich Transition Metal Oxides and Their Energy-Related Applications, Chem. Asian J. 15 (2020) 3717-3736.

[34] S. Li, R. Feng, M. Li, X. Zhao, B. Zhang, Y. Liang, H. Ning, J. Wang, C. Wang, P.K. Chu, Needle-like CoO nanowire composites with NiO nanosheets on carbon cloth for hybrid flexible supercapacitors and overall water splitting electrodes, RSC Adv.10 (2020) 37489-37499.

[35] R. Thangarasu, B. Babu, N. Senthil Kumar, M.-S. Ho, O.N. Balasundaram, T. Elangovan, Impact of Cu doping on the structural, morphological and optical activity of V_2O_5 nanorods for photodiode fabrication and their characteristics, RSC Adv. 9 (2019) 16541-16553.

[36] R.H. Zhang, T.S. Zhao, H.R. Jiang, M.C. Wu, L. Zeng, V_2O_5-NiO composite nanowires: A novel and highly efficient carbon-free electrode for non-aqueous Li-air batteries operated in ambient air, J. Power Sources. 409 (2019) 76-85.

[37] E. Gillis, E. Boesman, E. P. R.-Studies of V_2O_5 Single Crystals. I. Defect Centres in Pure, Non-stoichiometric Vanadium Pentoxide, Phys. Status Solidi B 14 (1966) 337-347.

[38] K. McColl, I. Johnson, F. Cora, Thermodynamics and defect chemistry of substitutional and interstitial cation doping in layered alpha-V_2O_5, Phys. Chem. Chem. Phys. 20 (2018) 15002-15006.

[39] P. Zhang, L. Li, D. Nordlund, H. Chen, L. Fan, B. Zhang, X. Sheng, Q. Daniel, L. Sun, Dendritic core-shell nickel-iron-copper metal/metal oxide electrode for efficient electrocatalytic water oxidation, Nat Commun. 9 (2018) 381.

[40] J.H. Kim, Y.J. Jang, J.H. Kim, J.-W. Jang, S.H. Choi, J.S. Lee, Defective $ZnFe_2O_4$ nanorods with oxygen vacancy for photoelectrochemical water splitting, Nanoscale 7 (2015) 19144-19151.

[41] H. Chen, D. Ge, J. Chen, R. Li, X. Zhang, T. Yu, Y. Wang, S. Song, In situ surface reconstruction synthesis of a nickel oxide/nickel heterostructural film for efficient hydrogen evolution reaction, Chem Commun (Camb) 56 (2020) 10529-10532.

[42] W. Fang, J. Zhao, T. Wu, Y. Huang, L. Yang, C. Liu, Q. Zhang, K. Huang, Q. Yan, Hydrophilic engineering of VO_x-based nanosheets for ambient electrochemical ammonia synthesis at neutral pH, J. Mater. Chem. A 8 (2020) 5913-5918.

[43] M. Przesniak-Welenc, M. Nadolska, B. Koscielska, K. Sadowska, Tailoring the Size and Shape-New Path for Ammonium Metavanadate Synthesis, Materials (Basel) 12 (2019).

[44] W.B. Jung, G.T. Yun, Y. Kim, M. Kim, H.T. Jung, Relationship between Hydrogen Evolution and Wettability for Multiscale Hierarchical Wrinkles, ACS Appl. Mater. Interfaces 11 (2019) 7546-7552.

[45] Z. Cai, A. Wu, H. Yan, Y. Xiao, C. Chen, C. Tian, L. Wang, R. Wang, H. Fu, Hierarchical Whisker-on-sheet NiCoP with Adjustable Surface Structure for Efficient Hydrogen Evolution Reaction, Nanoscale 10 (2018).

[46] F. Li, D. Zhang, R.-C. Xu, W.-F. Fu, X.-J. Lv, Superhydrophilic Heteroporous MoS$_2$/Ni$_3$S$_2$ for Highly Efficient Electrocatalytic Overall Water Splitting, ACS Appl. Energy Mater. 1 (2018) 3929-3936.

[47] C. Zhong, Q. Zhou, S. Li, L. Cao, J. Li, Z. Shen, H. Ma, J. Liu, M. Lu, H. Zhang, Enhanced synergistic catalysis by a novel triple-phase interface design of NiO/Ru@Ni for the hydrogen evolution reaction, J. Mater. Chem. A 7 (2019) 2344-2350

[48] K.L. Zhou, Z. Wang, C.B. Han, X. Ke, C. Wang, Y. Jin, Q. Zhang, J. Liu, H. Wang, H. Yan, Platinum single-atom catalyst coupled with transition metal/metal oxide heterostructure for accelerating alkaline hydrogen evolution   reaction, Nat. Commun. 12 (2021) 3783.

[49] W. Zhao, M. Bajdich, S. Carey, A. Vojvodic, J.K. Nørskov, C.T. Campbell, Water Dissociative Adsorption on NiO(111): Energetics and Structure of the Hydroxylated Surface, ACS Catal. 6 (2016) 7377-7384.

[50] T. Shinagawa, A.T. Garcia-Esparza, K. Takanabe, Insight on Tafel slopes from a microkinetic analysis of aqueous electrocatalysis for energy conversion, Sci. Rep. 5 (2015).

[51] B. Zhang, J. Liu, J. Wang, Y. Ruan, X. Ji, K. Xu, C. Chen, H. Wan, L. Miao, J. Jiang, Interface engineering: The Ni(OH)$_2$/MoS$_2$ heterostructure for highly efficient alkaline hydrogen evolution, Nano Energy 37 (2017) 74-80.

[52] X. Liu, J. Zeng, H. Yang, K. Zhou, D. Pan, V$_2$O$_5$-Based nanomaterials: synthesis and their applications, RSC Adv. 8 (2018) 4014-4031.

[53] P. Ilanchezhiyan, G.M. Kumar, C. Siva, A. Madhankumar, H.C. Jeon, T.W. Kang, D.Y. Kim, Evidencing enhanced oxygen and hydrogen evolution reactions using In–

Zn–Co ternary transition metal oxide nanostructures: A novel bifunctional electrocatalyst, Int. J. Hydrog. Energy 44 (2019) 23081-23090.

[54] L. Ma, K. Zhang, S. Wang, L. Gao, Y. Sun, Q. Liu, J. Guo, X. Zhang, Vanadium doping over Ni_3S_2 nanosheet array for improved overall water splitting, Appl. Surf. Sci. 489 (2019) 815-823.

[55] X. Wei, Y. Zhang, H. He, D. Gao, J. Hu, H. Peng, L. Peng, S. Xiao, P. Xiao, Carbon-incorporated NiO/Co_3O_4 concave surface microcubes derived from a MOF precursor for overall water splitting, Chem. Commun. 55 (2019) 6515-6518.

[56] X. Shang, J.-Q. Chi, S.-S. Lu, B. Dong, Z.-Z. Liu, K.-L. Yan, W.-K. Gao, Y.-M. Chai, C.-G. Liu, Hierarchically three-level $Ni_3(VO_4)_2$@$NiCo_2O_4$ nanostructure based on nickel foam towards highly efficient alkaline hydrogen evolution, Electrochim. Acta 256 (2017) 100-109.

[57] L. Ye, Z. Wen, Self-supported three-dimensional Cu/Cu_2O–CuO/rGO nanowire array electrodes for an efficient hydrogen evolution reaction, Chem. Commun. 54 (2018) 6388-6391.

[58] L. Wen, J. Yu, C. Xing, D. Liu, X. Lyu, W. Cai, X. Li, Flexible vanadium-doped Ni_2P nanosheet arrays grown on carbon cloth for an efficient hydrogen evolution reaction, Nanoscale 11 (2019) 4198-4203.

[59] S. Bolar, S. Shit, J.S. Kumar, N.C. Murmu, R.S. Ganesh, H. Inokawa, T. Kuila, Optimization of active surface area of flower like MoS_2 using V-doping towards enhanced hydrogen evolution reaction in acidic and basic medium, Appl. Catal. B: Environ. 254 (2019) 432-442

[60] H. Wang, T. Liu, K. Bao, J. Cao, J. Feng, J. Qi, W doping dominated NiO/NiS_2 interfaced nanosheets for highly efficient overall water splitting, J. Colloid Interface Sci. 562 (2020) 363-369.

[61] D. Gao, R. Liu, J. Biskupek, U. Kaiser, Y.F. Song, C. Streb, Modular Design of Noble-Metal-Free Mixed Metal Oxide Electrocatalysts for Complete Water Splitting, Angew. Chem. Int. Ed. Engl. 58 (2019) 4644-4648.

[62] Z. Li, W. Niu, L. Zhou, Y. Yang, Phosphorus and Aluminum Co doped Porous NiO Nanosheets as Highly Efficient Electrocatalysts for Overall Water Splitting, ACS Energy Lett. 3 (2018) 892-898.

[63] Y. Liu, Z. Jin, X. Tian, X. Li, Q. Zhao, D. Xiao, Core-shell copper oxide @ nickel/nickel–iron hydroxides nanoarrays enabled efficient bifunctional electrode for overall water splitting, Electrochim. Acta 318 (2019) 695-702.

[64] M. Asnavandi, B.H.R. Suryanto, W. Yang, X. Bo, C. Zhao, Dynamic Hydrogen Bubble Templated NiCu Phosphide Electrodes for pH-Insensitive Hydrogen Evolution Reactions, ACS Sustain. Chem. Eng. 6 (2018) 2866-2871.

[65] L. Wang, G. Zhou, H. Luo, Q. Zhang, J. Wang, C. Zhao, A.M. Rao, B. Xu, B. Lu, Enhancing catalytic activity of tungsten disulfide through topology, Appl. Catal. B: Environ. 256 (2019).

[66] L. Xie, L. Wang, W. Zhao, S. Liu, W. Huang, Q. Zhao, WS_2 moire superlattices derived from mechanical flexibility for hydrogen evolution reaction, Nat. Commun. 12 (2021) 5070.

[67] H.L.S. Santos, P.G. Corradini, M.A.S. Andrade, L.H. Mascaro, CuO/NiO_x thin film–based photocathodes for photoelectrochemical water splitting, J. Solid State Electrochem. 24 (2020) 1899-1908.

[68] Y. Wan, Y. Zhang, X. Wang, Q. Wang, Electrochemical formation and reduction of copper oxide nanostructures in alkaline media, Electrochem. Commun. 36 (2013) 99-102.

[69] P. Muthukumar, M. Pannipara, A.G. Al-Sehemi, S.P. Anthony, Highly enhanced bifunctional electrocatalytic activity of mixed copper–copper oxides on nickel foam via composition control, New J. Chem 44 (2020) 11993-12001.

[70] A. Önsten, J. Weissenrieder, D. Stoltz, S. Yu, M. Göthelid, U.O. Karlsson, Role of Defects in Surface Chemistry on Cu_2O (111), J. Phys. Chem. C 117 (2013) 19357-19364.

[71] Z. Guo, X. Wang, Y. Gao, Z. Liu, Co/Cu-modified NiO film grown on nickel foam as a highly active and stable electrocatalyst for overall water splitting, Dalton Trans. 49 (2020) 1776-1784.

[72] P. Farinazzo Bergamo Dias Martins, P. Papa Lopes, E.A. Ticianelli, V.R. Stamenkovic, N.M. Markovic, D. Strmcnik, Hydrogen evolution reaction on copper: Promoting water dissociation by tuning the surface oxophilicity, Electrochem. Commun. 100 (2019) 30-33.

[73] K. Fan, Y. Ji, H. Zou, J. Zhang, B. Zhu, H. Chen, Q. Daniel, Y. Luo, J. Yu, L. Sun, Hollow Iron-Vanadium Composite Spheres: A Highly Efficient Iron-Based Water Oxidation Electrocatalyst without the Need for Nickel or Cobalt, Angew. Chem. Int. Ed. Engl. 56 (2017) 3289-3293.

[74] K. Kannimuthu, K. Sangeetha, S. Sam Sankar, A. Karmakar, R. Madhu, S. Kundu, Investigation on nanostructured Cu-based electrocatalysts for improvising water splitting: a review, Inorg. Chem. Front. 8 (2021) 234-272.

CHAPTER 3 Highly durable FeNiS$_x$/NiFe(OH)$_x$ electrocatalyst for selective oxygen evolution reaction in alkaline simulated seawater at high current densities

3.1 Introduction

Hydrogen production via water electrolysis by using electricity produced from waste heat or renewable energy without CO_2 emission is a clean and secure technology [1]. However, fresh water is a limited resource while the seawater is an abundant one [2]. Water electrolysis consists of two main reactions, i.e., Hydrogen Evolution Reaction (HER) and Oxygen Evolution Reaction (OER). The sluggish OER at the anode generally requires a large overpotential to overcome the energy barrier and energy loss since it involves multiple steps to cleavage water molecule (H_2O) with a 4-electron pathway so that the electrocatalysts with high performance are highly required [3]. For seawater electrolysis, two 2-electron reactions, i.e., chlorine evolution reaction (ClER, $2Cl^- \rightarrow Cl_2 + 2e^-$) and hypochlorite generation reaction (HGR, $Cl^- + 2OH^- \rightarrow ClO^- + H_2O + 2e^-$), could competitively occur on the anode with the OER in the acidic and alkaline conditions, respectively, especially at a high current density, owing to the presence of large amount of chloride ions (~0.5 M) and kinetic advantage of them although OER is thermodynamically favored over either ClER or HGR [4-6]. In general, in the alkaline solution (pH >7.5), if those obtained electrocatalysts can be operated at an overpotential lower than 480 mV, HGR will not occur to compete with OER. In addition, the chlorine in seawater could result in electrode erosion and electrode degradation [7]. Therefore, the electrocatalysts for seawater electrolysis should have an overpotential lower than 480 mV to avoid the hypochlorite formation and corrosion in the alkaline condition [8]. Besides, to meet the practical industrial-scale requirements,

the electrocatalysts should be operated at a current density as high as 1 A·cm^{-2} or more to achieve a high hydrogen production rate under long-term operation [9, 10]. Unfortunately, to date, only a few works on OER catalysts have been explored at such highly-harsh conditions and most of the developed catalysts are always deactivated during the OER process, particularly at a high current density. For example, Zhou *et al.* [11] measured the stability of NiFe-LDH on Cu nanowires but this catalyst is not stable at a high current density (500 mA cm^{-2}) under alkaline solution (1 M KOH). Gupta *et al.* [12] investigated OER in saline water (1 M KOH + 0.5 M NaCl) using a bimetallic oxy-boride (Co-Fe-O-B) catalyst, which exhibited a low overpotential of 294 mV at 10 mAcm^{-2}, but the current lost nearly 35% after 20 hours of operation. While, the faradaic efficiency at a high current density (100 mA cm^{-2}) was also decreased from nearly 100% to ~74% due to Cl$^-$ oxidation. Herein, it is considered that the lower stability and performance was attributed to the presence of corrosive Cl$^-$ ions in the solution.

Among various OER electrocatalysts, Ni-Fe oxides, hydroxides, (oxy)hydroxide and their layered double hydroxides have been reported to be a class of electrocatalysts with excellent OER activity even in alkaline electrolytes [7, 13]. However, these electrocatalysts always have low conductivity, less active sites, insufficient intrinsic activity and poor stability especially in saline water at a high current density [14, 15]. To solve these issues, phosphorization, boronation, sulfidation and nitridation of them and incorporation them with other materials could tune the intrinsic activity [16]. For instance, Zou *et al.* [17] combined NiFe-LDH and NiFeS$_x$ as the electrocatalyst, which exhibited a low overpotential of 210 mV at 10 mA cm^{-2} for OER since the chemisorption free energy of O* (E (O*)) of NiFe-LDH can be reduced from 0.90 to 0.53 eV by the combination of it with NiFeS$_x$. Herein, the charge redistribution on the interface of the two materials contributed to the improvement of OER activity through

the enhancement of affinity to the O* intermediates and the improvement of electrical conductivity by the incorporated metallic $NiFeS_x$ species. Yuan *et al.* [18] reported that sulfur doping can increase the OER activity of FeCoOOH with a lowered catalytic overpotential (225.3 mV at 20 mA cm^{-2}). By density functional theory (DFT) calculations, it is revealed that a synergistic effect between two coordinating S and one adjacent Fe can optimize the electronic state of Co, resulting in the deceasing in binding energy of OH* (ΔE_{OH}) and tuning of the electronic structure. Shuang *et al.* [14] prepared $NiFe(OH)_x$ electrocatalyst with abundant oxygen vacancy-rich amorphous structure on the carbon paper (CP), which demonstrated a low overpotential of 303 mV at 100 mA cm^{-2} and high durability without the degradation for 50 h. Such a superior performance could be attributed to the synergistic effect between Ni and Fe species. Recently, Zhang *et al.* [19] doped S into FeOOH/IF to lower the energy barrier of rate determining step in OER, thereby improving the electrocatalytic performance. Liu *et al.* [20] embedded Ag on the NiFe-LDH, which exhibited superior activity by requiring a low overpotential of 303 mV at 1,000 mA cm^{-2} in 1 M KOH seawater solution. DFT calculations showed that the Ag doping improved the phase stability of NiFe-LDH with triggering lattice oxygen, implying high mechanical robustness. Yu *et al.* [21] successfully synthesized S-doped Ni/Fe(oxy)hydroxide, which displayed excellent OER performance in the seawater electrolyte with a low overpotential of 278 mV at 100 mA cm^{-2}. The excellent catalytic performance could be attributed to hydrophilic property, highly porous nanostructure and good corrosion resistance from metal(oxy)hydroxide. Dionigi *et al.* [6] also studied the NiFe-LDH for selective seawater electrolysis, achieving overpotentials of 360 and 359 mV at 10 mA cm^{-2} in alkaline freshwater and saline electrolytes, respectively. For scaling up from lab scale to industrial level using natural seawater as a water resource, it requires consideration

of either electrocatalytic performance or the catalyst preparation step as well as the cost of chemical substances need to be considered. Thus, searching for preparation of earth-abundant and cost-effective electrocatalysts with high durability, especially at a large current density for overall seawater electrolysis using a facile strategy is still full of challenges but necessary.

In this study, *in-situ* growing of $FeNiS_x/NiFe(OH)_x$ composite with a two-dimensional (2D) nanosheet structure on nickel foam (NF) is simply realized using a corrosion engineering process followed by a fast and mild sulfurization step in order to reduce catalyst preparation cost and time and simultaneously decrease interfacial resistance between the electrocatalyst and the substrate, increase electrical conductivity, and prevent electrocatalyst peeling off from the substrate during the long-term operation at a high current density. The evaluation of electrocatalytic performances is performed in the alkaline freshwater solution at first, and then a simulated seawater is used to confirm its suitability as a bifunctional electrocatalyst, especially as a selective OER electrocatalyst for the seawater electrolysis. It is found that the obtained $FeNiS_x/NiFe(OH)_x$ composite based electrode has excellent electrocatalytic activity with a low overpotential of 270 mV for the OER in alkaline simulated seawater at 100 mA cm^{-2} and it can even work stably over 100 h at a current density as high as 1 A cm^{-2}. For the overall seawater electrolysis using a two-electrode system, it is capable to sustain stable up to 1 A/cm^2 in the imitate seawater solution with a cell voltage of 2.81 V, achieving a high hydrogen productivity without the catalyst deterioration while the faradaic efficiencies of hydrogen and oxygen production are as high as 95% and 94% in the electrolysis of alkaline simulated seawater, respectively.

3.2 Experimental section

3.2.1 Chemical and Materials

Iron (III) chloride hexahydrate ($FeCl_3 \cdot 6H_2O$), sodium nitrate ($NaNO_3$, 99%), urea (CH_4N_2O), sodium sulfide (Na_2S, 98%), sodium chloride ($NaCl$, 99%), hydrochloric acid (HCl, 69%), potassium hydroxide (KOH, 85%) and ethanol (C_2H_5OH, 99.5%) were purchased from Wako, Japan. deionized (DI) water (<18.2 MΩ cm) was used to prepare the solution. Nickel foam (NF, 1.5 mm of thickness, 0.23 g/cm^3 bulk density and 110 pores/inch) was purchased from MTI, Japan.

3.2.2 Synthesis of FeNiS$_x$/NiFe(OH)$_x$/NF electrode

Before fabrication of FeNiS$_x$/NiFe(OH)$_x$/NF electrode, NF substrate (2 x 2 cm^2) was treated in 1 M HCl solution for 1 hour under sonication, and then washed with ethanol and DI water consecutively for 1 h in each step followed by drying for 1 hour in a vacuum oven at 60 °C to remove the oxide layer and other impurities. Thereafter, the treated NF was immersed into 50 ml of aqueous solution containing 0.5 mmol of $FeCl_3 \cdot 6H_2O$ and 2.5 mmol of $NaNO_3$ to perform the reaction at 100 °C for 2 h. Then, the electrode was washed with distilled water and ethanol successively for 3 times and dried in vacuum oven at 60°C for 12 h. As such, the obtained dark-yellow electrode is called NiFe(OH)$_x$/NF. Thereafter, the NiFe(OH)$_x$/NF electrode was mildly sulfurized by using 1 g of Na_2S with 10 mmol of CH_4N_2O in aqueous solution at 25°C for 1 h and then, dried in vacuum oven at 60°C for 12 h. As such, the FeNiS$_x$/NiFe(OH)$_x$ with a nanosheet structure in black color was uniformly coated on the NF skeleton. Herein, the loading amount of FeNiS$_x$/NiFe(OH)$_x$ was estimated to be ca. 0.30 mg cm^{-2} by weighing the electrode before and after the synthesis. For comparison, Ni$_x$S$_y$/NF electrode was also prepared using the similar method but not using Fe species in the initial stage.

3.2.3 Material Characterizations

Morphology and nanostructure of the electrocatalyst were determined by a scanning electron microscope (SEM, SU8010, Hitachi, Japan) and a transmission electron microscope (TEM, JEM-2100F, JEOL, Japan). Chemical valences and composition of the prepared electrocatalysts were characterized by XPS measurement using a VG Scientific ESCALab250i-XL instrument with an Al-Kα X-ray source and crystalline structure was analyzed by X-ray diffraction (XRD) measurement in a 2θ range of 10°-80° with a Rigaku Smartlab diffractometer (Japan) using a Cu-Kα as the radiation source (λ=0.15406 nm). Raman spectrum was recorded using a JASCO NRS-5100 (λ= 532 nm).

3.2.4 Electrochemical measurements

Performances of all prepared electrodes were examined using a three-electrode system on an electrochemical workstation (Versa STAT4, Princeton, USA). A standard Hg/HgO electrode was used as the reference electrode, a carbon rod was used as the counter electrode and the as-prepared catalysts were used directly as the working electrode. A linear sweep voltammetry (LSV) with a scan rate of 2 mV s^{-1} in a potential range of 0.176-1.076 V was used to evaluate the OER performance. Two different electrolytes including alkaline freshwater solution (1 M KOH) and alkaline-simulated seawater solution (1 M KOH + 0.5 M NaCl) were used in the experiment (pH ~14)[4]. The potential with respect to reversible hydrogen electrode (RHE) was calculated by the Nernst equation: E(vs RHE) = E(Hg/HgO) + 0.098 + 0.059 pH. The corresponding overpotential (η) for OER can also be calculated using the formula; η = E(RHE) - 1.23 V. Electrochemical impedance spectroscopy (EIS) measurement was performed at a frequency range of 100 kHz-0.1 Hz. The potential range of cyclic voltammetry (CV) measurement at a scan rate range of 10-100 mV s^{-1} was - 0.2-0 V (vs. RHE), which was

applied to evaluate the electrochemical active surface area (ECSA). The OER durability test was performed for 100 hours at room temperature with constant current densities of 100 and 1,000 mA cm^{-2} in alkaline freshwater solution and alkaline simulated sea water solution, as well as accelerate degradation test (ADT) for 2000 cycles at a potential range from 0.1 to -0.3 V (*vs* RHE), respectively. In addition, overall seawater electrolysis was tested using a two-electrode system with the FeNiS$_x$/NiFe(OH)$_x$/NF electrode for both anode and cathode, where the polarization curve was measured in a potential range of 1.0-2.2 V at a scan rate of 2 mVs^{-1} without iR-compensation and long-term durability was conducted using chronopotentiometry at 10, 100, 500 and 1,000 mA cm^{-2} for 12 hours in alkaline freshwater solution (1 M KOH) and alkaline-simulated seawater solution (1 M KOH + 0.5 M NaCl).

3.2.5 DFT calculation

The spin-polarized DFT calculations were performed using the Vienna Ab-initio Simulation Package (VASP) [22]. Exchange-correlation functional was expressed using the generalization gradient approximation of Perdew, Burke and Ernzerhof (PBE) functional [23]. The U-J terms of Ni and Fe were set as 3.8 and 4.0 eV, respectively [24]. The plane wave energy cut-offs were set at 450 eV. A Monkhorst-Pack grid was used and the k-point mesh was thoroughly tested for structure relaxation and energy calculation. The Ni/Fe ratio of NiFe(OH)$_x$ was considered to be 3:1 in construction of the models. The (001) facet was used as the calculation models for NiFe(OH)$_2$ and NiFeS(OH)$_2$. A vacuum region of 15 Å was applied to avoid interactions between two images along c axis and the layer space of 7 Å was set based on the experimental experience [25]. Residual forces were within 0.02 eV/Å for geometry optimizations. The adsorption energy relating to Cl atom is defined as follows;

$$E_{abs}=E_{tot}-E_{slab}-E_{cl\_atom}, \qquad\qquad \text{Eq. (1)}$$

where E_{tot}, E_{slab} and E_{cl_atom} are the total energy of adsorbed system, the energy of clear surface and the energy of isolated Cl atom in a large cell, respectively.

3.3 Results and discussion

3.3.1 Characterization of FeNiS$_x$/NiFe(OH)$_x$/NF electrode

As indicated in the experimental section, the NiFe(OH)$_x$/NF electrode was prepared by submerging of the NF substrate in a solution containing oxidants including Fe^{3+}, NO$_3^-$ and dissolved oxygen at 100°C for 2 hours, in which the surface of NF can be oxidized spontaneously to NiFe(OH)$_x$. This is an oxidation effect of NaNO$_3$, which can change the near-surface chemical environment and allow more active sites to be formed on the NF surface. In this study, the NF was used as both nickel source and substrate. The effect of corrosion reaction time on the preparation of NiFe(OH)$_x$ was also studied. As displayed in Figure 3.1, NiFe(OH)$_x$ with a nanosheet structure was grown uniformly after 120-min corrosion reaction. Moreover, as shown in Figure 3.2, the optimal condition was chosen based on the lowest overpotential and charge transfer resistance. The results shows that NiFe(OH)$_x$ performs best when synthesized at 100°C for 2 hours.
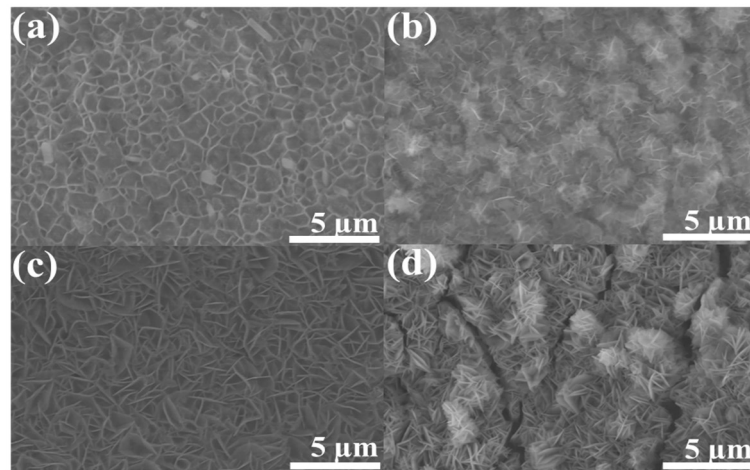
Figure 3.1 SEM images of (a) NiFe(OH)$_x$-30 min, (b) NiFe(OH)$_x$-60 min, (c) NiFe(OH)$_x$-120 min and (d) NiFe(OH)$_x$-180 min.

To generate FeNiS$_x$/NiFe(OH)$_x$ on the NF, the obtained NiFe(OH)$_x$/NF electrode was further submerged in a 0.1 M Na$_2$S solution for anion-exchange. As shown in Figure 3.3a, in order to form the NiFe(OH)$_x$ on the NF, the NO_3^- ions are reduced to hydroxide ions on the NF surface with the aid of electrons and subsequently interacted with Ni^{2+} from the dissolution of NF substrate. Then, in the presence of Fe^{3+} ions from FeCl$_3$ precursor, bimetallic hydroxide, i.e., NiFe(OH)$_x$, could be formed on the NF surface as indicated in the following equations: [26-28]

$$Ni \rightarrow Ni^{2+} + 2e^- \qquad\qquad\qquad \text{Eq. (2)}$$

$$Fe^{3+} + e^- \rightarrow Fe^{2+} \qquad\qquad\qquad \text{Eq. (3)}$$

$$NO_3^- + 7H_2O + 8e^- \rightarrow NH_4^+ + 10OH^- \qquad\qquad\qquad \text{Eq. (4)}$$

$$Ni^{2+} + Fe^{3+} + xOH^- \rightarrow NiFe(OH)_x \qquad\qquad\qquad \text{Eq. (5)}$$
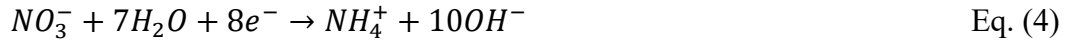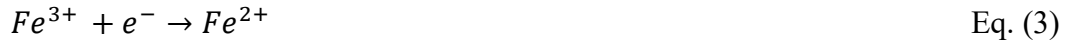
After the mild sulfurization with Na$_2$S, the color of obtained electrode is changed from dark-yellow to black, indixating that the FeNiS$_x$/NiFe(OH)$_x$/NF is obtained (Figure 3.3a).
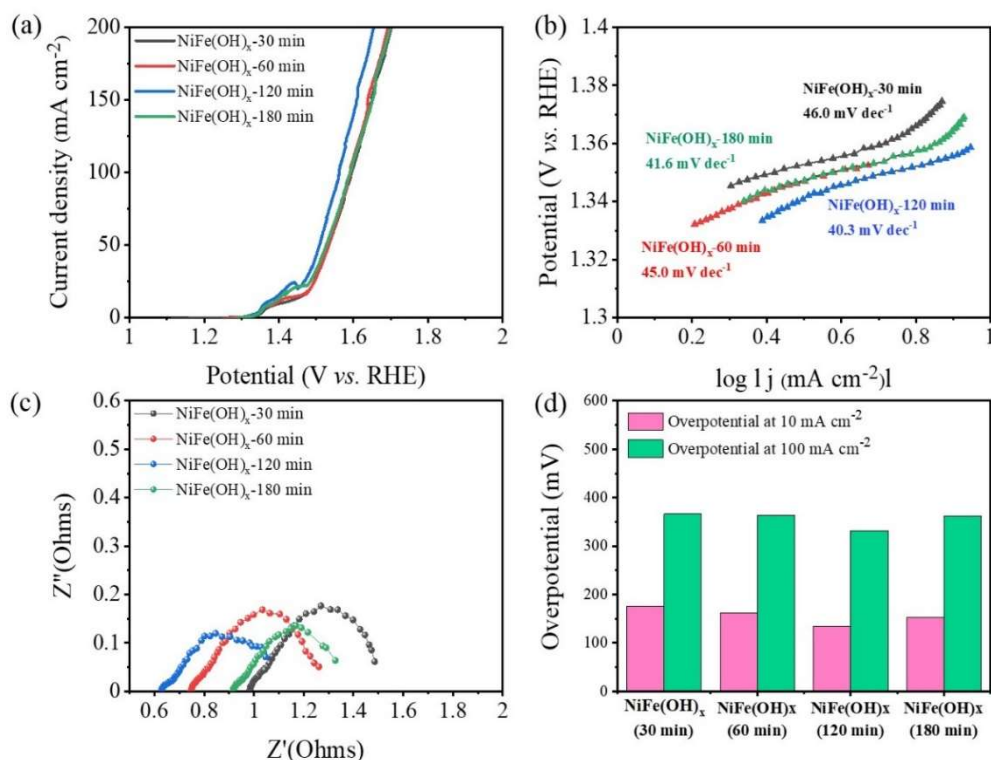
Figure 3.2 LSV polarization curves; (b) corresponding Tafel slopes; (c) Nyquist plots NiFe(OH)$_x$/NF for OER in alkaline freshwater with 1.0 M KOH (corrosion time: 30, 60, 120 and 180 min are); and (d) overpotentials at 10 and 100 mA cm^{-2} of all prepared electrodes.

As shown in Figures 3.3(b-c), NiFe(OH)$_x$ nanosheets uniformly grow on the surface of NF without the addition of additional nickel source, ensuring robust physical contact of active catalyst layer to the substrate. After the mild sulfurization by anion-exchange reaction between S^{2-} (from Na$_2$S) and OH$^-$ of NiFe(OH)$_x$, the original morphology is maintained (Figure 3.3c). Herein, since the solubility constant (K_{sp}) of sulfide is lower than that of hydroxide, the S^{2-} could partially substitute the OH$^-$ to form FeNiS$_x$ on the surface of NiFe(OH)$_x$. From the EDS elemental mapping (Figures 3.3(d-e)), one can see that Ni, Fe, O and S exist on the NF substrate and all these elements are homogeneously distributed. However, due to the high intensity peak of the nickel foam

substrate, no diffraction peaks corresponding to both metal hydroxides and metal sulfides are observed in the XRD patterns of the obtained $NiFe(OH)_x$ and $FeNiS_x/NiFe(OH)_x$ (Figure 3.4). However, from the TEM images as shown in Figures. 3.5(a-c), it can be found that FeS, $Ni(OH)_2$ and $Fe(OH)_3$ exist in the electrocatalysts with lattice spacings of 0.28 (111), 0.26 (101) and 0.27 (102) nm, respectively. More interestingly, lattice distortion is observed, implying that the sulfurization allows S atoms incorporating into the $NiFe(OH)_x$ structure, which could improve the intrinsic activity of the obtained electrocatalysts. The corresponding nano-scale elemental mappings as shown in Figures 3.5(d-g) also confirm the uniform distribution of Ni, Fe, S and O elements on the nanosheets. The obtained $FeNiS_x/NiFe(OH)_x$ electrocatalyst was further characterized by Raman analysis. As shown in Figure 3.6a, the representative bands at around 470 and 540 cm^{-1} correspond to Fe^{3+}-Ni^{2+}-O-Ni^{2+} and Fe^{3+}-O-Fe^{3+} bonds in $NiFe(OH)_x$, respectively. While, the Raman center-band at 685 cm^{-1} could be attributed to the Fe^{3+}-O vibration in the disordered Fe-OH clusters [29]. The broad peak with low intensity at 475 cm^{-1} also confirms the amorphous nature of $NiFe(OH)_x$ [30]. After the sulfurization, the peaks at 330 and 355 cm^{-1} corresponding to the mackinawite FeS are observed, indicating that the S atoms has been doped into $NiFe(OH)_x$ structure successfully [31].
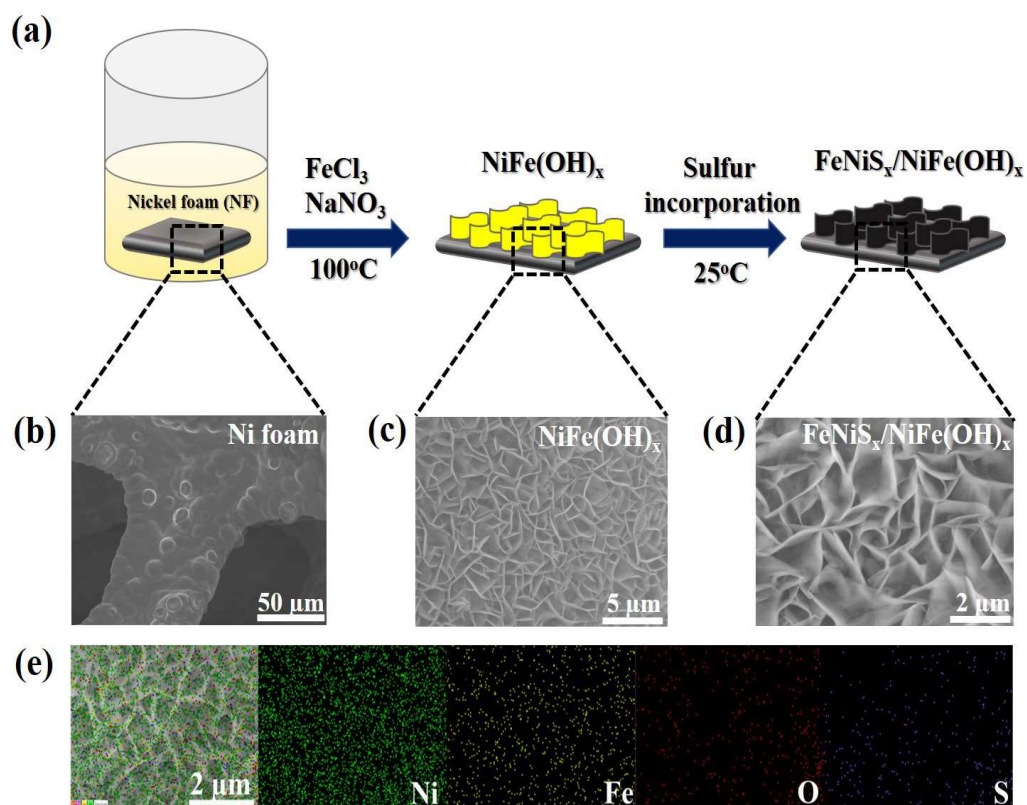
Figure 3.3 (a) Schematic illustration of the FeNiS$_x$/NiFe(OH)$_x$/NF electrode fabrication procedure; (b) SEM images of the pre-treated NF; (c) surface of NiFe(OH)$_x$/NF electrode; (d) surface of FeNiS$_x$/NiFe(OH)$_x$/NF electrode; and (e) EDS elemental mappings of FeNiS$_x$/NiFe(OH)$_x$/NF electrode.
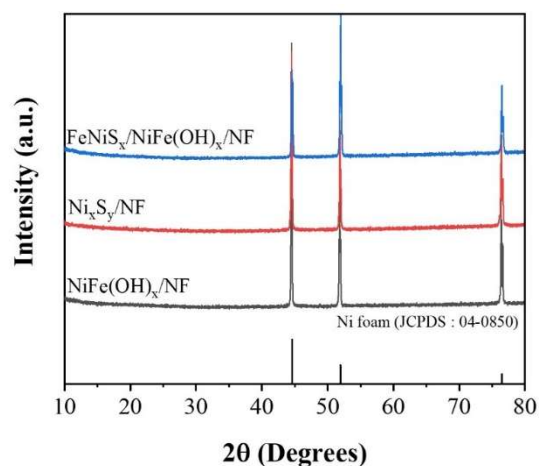
Figure 3.4 XRD patterns of as-prepared catalysts.
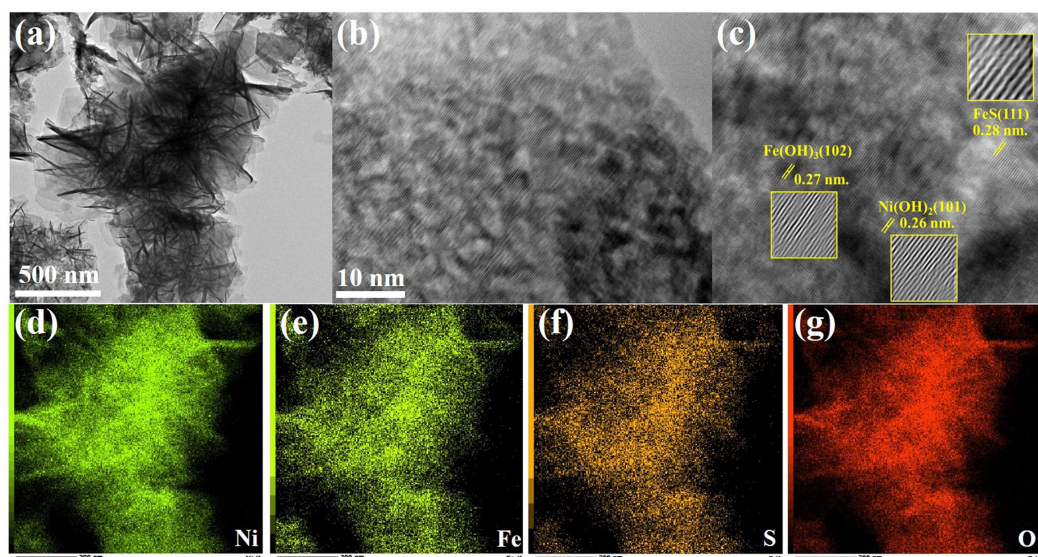
Figure 3.5 TEM images of (a) FeNiS$_x$/NiFe(OH)$_x$; (b,c) HR-TEM images and (d-g) corresponding EDS elemental mappings of Ni, Fe, S and O on FeNiS$_x$/NiFe(OH)$_x$ surface

Figure 3.6b displays XPS survey spectrum of the obtained FeNiS$_x$/NiFe(OH)$_x$, which further demonstrates the presence of Ni, Fe, O and S elements in this electrocatalyst. The high-resolution Ni *2p* spectrum in Figure 3.6c shows two peaks at the binding energies of 855.9 and 857.1 eV, which correspond to Ni^{2+} and Ni^{3+} species, confirming the presence of Ni^{2+} and Ni^{3+} in FeNiS$_x$/NiFe(OH)$_x$. After the sulfurization, the peak

126

intensity corresponding to Ni^{2+} is increased when compared to that of $NiFe(OH)_x$. Furthermore, compared with $NiFe(OH)_x$ (Ni^{2+}: 856.3 eV), the Ni^{2+} peak position of $FeNiS_x/NiFe(OH)_x$ (Ni^{2+}: 855.9 eV) shifts to the lower binding energy direction since the electronegativity of S (2.58) is lower than that of O atom (3.44). It also indicates that incorporating S into $NiFe(OH)_x$ crystal lattice via O site substitution can effectively improve electrocatalytic activity by creating more adsorption sites with high electron density and asymmetric charge density distribution, lowering OER overpotential [32]. As can be seen in Figure 3.6d, Fe *2p3/2* and Fe *2p1/2* of Fe^{2+} species are ascribed to the two peaks at 711.7 and 721.5 eV, respectively, whereas those of Fe^{3+} species are assigned to the coexistence peaks at 714.0 and 726.2 eV, respectively. Furthermore, after the sulfurization, the corresponding peak intensity of Fe^0 metal species at 707.0 eV is increased while the Fe *2p* spectrum shifts about 0.30 eV higher than that in the $NiFe(OH)_x$, implying that the incorporating of S atoms can enhance the coordination ability of Fe and formation of FeS ($Fe^{2+} + S^{2-} \rightarrow FeS$) species on the surface of $NiFe(OH)_x$, which could considerably improve the conductivity, thereby benefiting for OER. The O *1s* peak can be decomposed into three peaks at 530.7, 531.4 and 532.1 eV, corresponding to O^{2-} , OH and surface absorbed water/oxygen defect sites, respectively (Figure 3.6e) [33]. On the high-resolution S *2p* spectrum, the peaks at 162.1 and 163.3 eV correspond to S^{2-} (S-S) and S_2^{2-} (S-M) in $FeNiS_x$, respectively (Figure 3.6f). Moreover, the peak at 168.6 eV should be attributed to surface oxidation with the formation of S-O bond relating to the sulfurization. As can be seen from Figure 3.6c, after the sulfurization, the binding energy of Ni is shifted negatively because the sulphur (S) has a lower electronegativity with higher polarization degree so that it is easier to be polarized and shares more electrons with the foreign metal in order to balance the strong positive field of Ni. Herein, the lowering of binding energy could make Ni

receive more electrons from the S after the sulfurization step. Meanwhile, in the O *1s* spectrum, the binding energy also shifts negatively, which should be attributed to the partial substitution of hydroxyl anions with S anion caused by the polarization effect. As such, the incorporation of S into the $NiFe(OH)_x$ can effectively modulate the electronic structure by anionic regulation and generation of S/O hetero-anionic structure with the formation of $FeNiS_x$ on the surface of $NiFe(OH)_x$, which should be beneficial to the electrocatalytic activity.
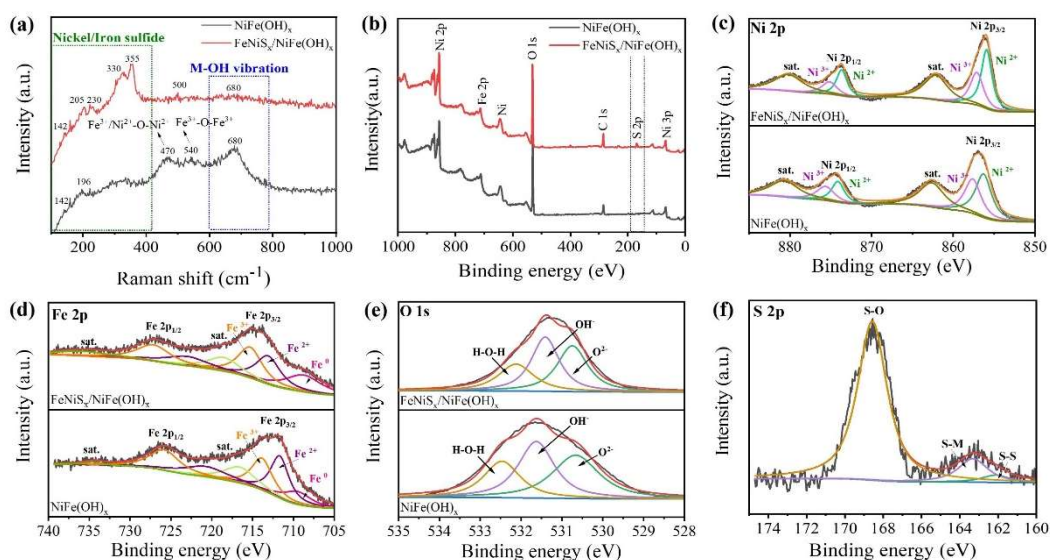
Figure 3.6 (a) Raman spectra of $NiFe(OH)_x$ and $FeNiS_x/NiFe(OH)_x$; (b) Survey spectrum; and high-resolution XPS spectra of (c) Ni *2p*, (d) Fe *2p*, (e) O *1s* and (f) S *2p*.

3.3.2 Electrocatalytic performance for OER in alkaline freshwater

Performance of as-prepared electrocatalysts for OER in alkaline freshwater solution was investigated at first in a three-electrode system in 1 M KOH freshwater solution. Figure 3.7a shows the polarization curve of $FeNiS_x/NiFe(OH)_x/NF$ electrode comparing with the related ones as well as benchmark RuO_2 based electrode. To avoid the influence of the oxidation peak on the overpotential range of 1.3-1.5 V (*vs.* RHE), a high current density was employed for the comparison of overpotentials. As shown in

Figure 3.7b, the FeNiS$_x$/NiFe(OH)$_x$/NF electrode exhibits superior performance with a lowest overpotential of 277 mV at 100 mA cm^{-2}, which is much lower than those of NiFe(OH)$_x$/NF (332 mV), Ni$_x$S$_y$/NF (410 mV) and RuO$_2$/NF (407 mV) electrodes, indicating that the sulfurization effectively improves the intrinsic activity of NiFe(OH)$_x$, reduces the free energy between O* and OOH*, and optimizes the Ni- and/or Fe-O bonding, which are beneficial for the improving of OER activity. While, the corresponding Tafel slopes are also calculated from the LSV curves, and as shown in Figure 3.7c, the Tafel slope of FeNiS$_x$/NiFe(OH)$_x$/NF electrode is 35.3 mV dec^{-1}, which is much lower than those of NiFe(OH)$_x$/NF (40.3 mV dec^{-1}), Ni$_x$S$_y$/NF (48.3 mV dec^{-1}), bare NF(70.4 mV dec^{-1}) and RuO$_2$/NF (46.5 mV dec^{-1}) electrodes, suggesting that the FeNiS$_x$/NiFe(OH)$_x$/NF electrode results in a fastest kinetic reaction since the S incorporation effectively improves the electronic structure of electrode, thereby adjusting the adsorption/desorption energy on the electrode surface and reducing the gap between the free energy of formation of the O^* and OOH^* intermediates [31]. EIS analysis was further performed to determine the charge transfer resistance (R_{ct}) on the electrode. Nyquist plots in Figure 3.7d reveal that the R_{ct} of FeNiS$_x$/NiFe(OH)$_x$/NF electrode (0.4 Ω) is also much lower than those of other electrodes such as NiFe(OH)$_x$/NF (0.6 Ω), indicating that the incorporation of S effectively improves the conductivity and the *in-situ* growth with sulfurization strategy also effectively reduces the charge transfer resistance between electrocatalyst layer and substrate. In addition, the electrochemical active surface areas (ECSAs) calculated from the double layer capacitances (C_{dl}) by measuring cyclic voltammetry at different scan rates (Figure 3.7e) show that the FeNiS$_x$/NiFe(OH)$_x$ electrocatalyst has the highest C_{dl} value of 9.2 mF cm^{-2}, which is approximately 1.2 times higher than those of NiFe(OH)$_x$. This result also

indicates that the sulfurization improves the ECSA significantly by increasing the surface area and exposing/generating more active sites.

A multi-step chronopotentiometry test was carried out to identify the stability of FeNiS$_x$/NiFe(OH)$_x$ electrocatalyst. As can be seen from Figure 3.7f, the current density is increased from 100 mA cm^{-2} and ended at 1,000 mA cm^{-2} with an increment of 100 mA cm^{-2} per 600 s, the relating potential at each condition remains constant without any fluctuation. Moreover, the reverse operation by changing the current density back to 100 mA cm^{-2} from 1,000 mA cm^{-2} also exhibits the same initial potential response as the initial process at the same current density, demonstrating superior mechanical robustness throughout a wide range of current densities, which indicates its applicable for a practical process.

The durability of FeNiS$_x$/NiFe(OH)$_x$/NF electrode for OER in alkaline freshwater solution containing 1 M KOH was further investigated by cyclic voltammetry at a scan rate of 100 mV/s for 2000 cycles as well as chronopotentiometry at a constant current density of 100 mA cm^{-2} for 100 hours. As can be seen in Figure 3.7g, the LSV curves before and after the accelerated degradation test are identical after 2,000 cycles, suggesting high mechanical robustness. While, as indicated in Figure 3.7h, the FeNiS$_x$/NiFe(OH)$_x$/NF electrode maintains its initial potential for at least 100 h without the degradation, confirming its superior activity and stability of this electrocatalyst in alkaline solution compared to the NiFe based ones (Table 3.1). Figure 3.7i shows the morphology of spent electrocatalyst after the 100-h stability test. One can see that the nanosheet structure maintains almost unchanged after the long-time stability test. The presence of Ni, Fe, and S on the spent electrocatalyst is also confirmed (Figure 3.8). The XRD analysis indicates the amorphous nature of the spent electrocatalysts (Figure 3.9a). Furthermore, the XPS analysis (Figure 3.10) also displays that the composition

and oxidation states of the main elements in the spent electrocatalyst remain almost unchanged. Especially, the Fe *2p* profile at 708.7 eV corresponding to Fe^0 is still retained, implying that the chemical composition and the valence state are not changed after the stability test.
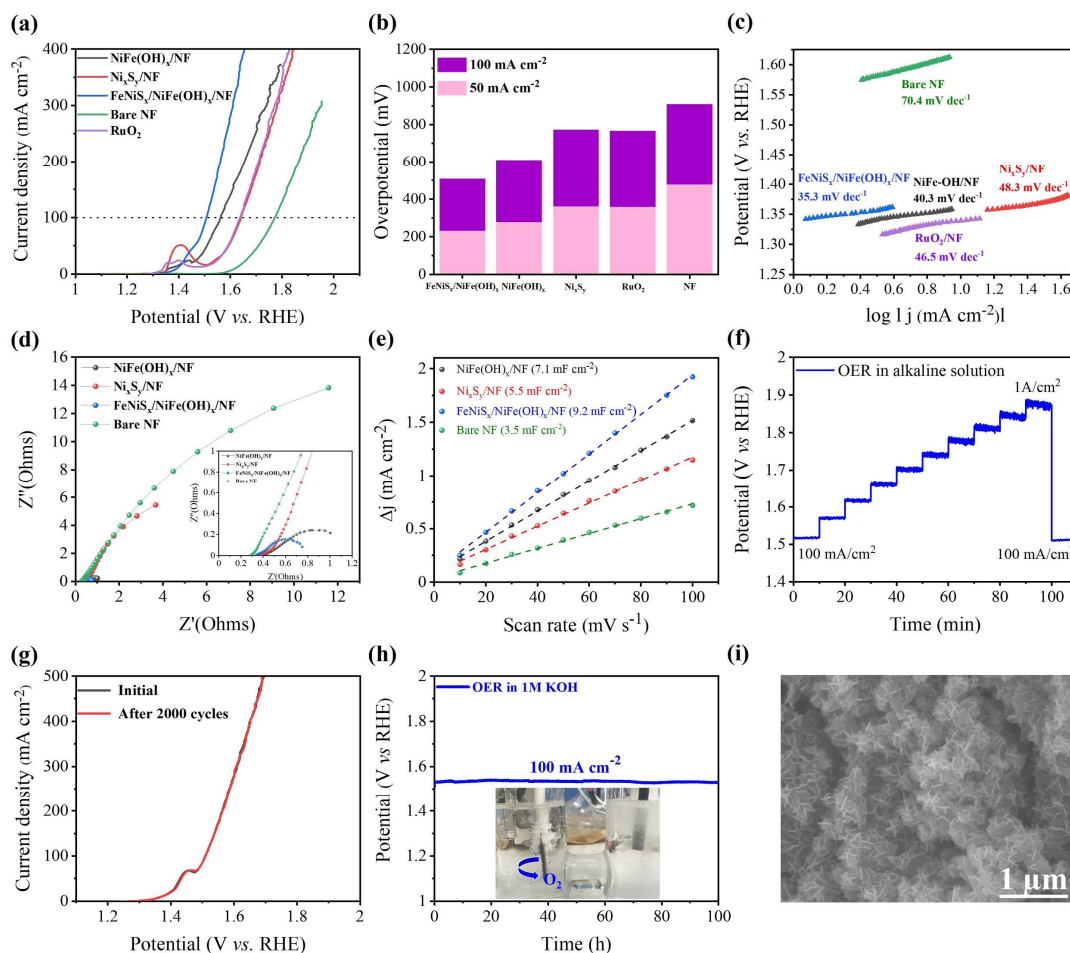
Figure 3.7 OER performance in alkaline freshwater solution containing 1 M KOH. (a) LSV curves; (b) overpotentials at 50 and 100 mA cm^{-2}; (c) Tafel plots; (d) Nyquist plots; (e) capacitive current density as a function of scan rate; (f) Multiple-step chronopotentiometry test started from 100 mA cm^{-2} and ended at 1,000 mA cm^{-2} with an increment of 100 mA cm^{-2} in every 600 s, then returning back to 100 mA cm^{-2}; (g) LSV polarization curves of FeNiS$_x$/NiFe(OH)$_x$/NF electrode before and after the accelerated durability test (ADT) for 2000 cycles; (h) durability test at a constant current density of 100 mA cm^{-2} for 100 h; and (i) SEM image of spent FeNiS$_x$/NiFe(OH)$_x$ after the stability test.

131

Table 3.1 Comparison of OER activities of various NiFe based electrocatalysts for the electrolysis of alkaline freshwater solution (1 M KOH)

Electrocatalyst	Electrolyte	Overpotential at 10 mA cm^{-2} (mV)	Overpotential at 100 mA cm^{-2} (mV)	Stability	Reference
FeNiS$_x$/NiFe(OH)$_x$/NF	1 M KOH	164	277	100	This work
NiFe(OH)$_x$/CP	1 M KOH	261	303	50	[14]
Ni–Fe–OH@Ni$_3$S$_2$/NF	1 M KOH	165	300	-	[44]
Ni-Co-Fe/Cu	1 M KOH	316	375	5	[45]
Fe$_3$O$_4$/FeS$_2$	1 M KOH	253	306	36	[46]
NiFe LDH	1 M KOH	243	N/A	-	[39]
NiFe LDH/CuO	1 M KOH	270 (at 20 mA cm^{-2})	N/A	-	[47]
(Ni-Fe)S$_x$/NiFe(OH)$_y$	1 M KOH	-	290	-	[29]
(Ni, Fe)S$_2$@MoS$_2$	1 M KOH	270	330	-	[48]
Ni–Fe–OH/Ni$_3$S$_2$/NF	1 M KOH	268	324	-	[49]
FeS-NiS/TM	1 M KOH	260	N/A	25	[50]
Co–NiFe LDH	1 M KOH	278	N/A	24	[51]
NiFe-LDH-Ni(III)Li	1 M KOH	248	N/A	24	[52]
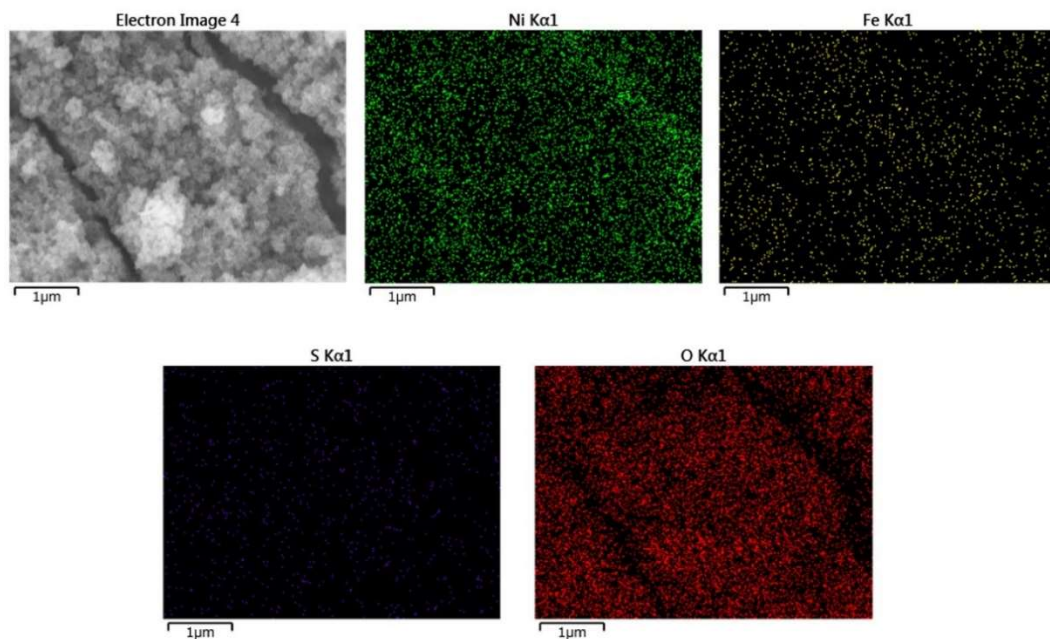
Figure 3.8 Corresponding EDS elemental mapping of FeNiS$_x$/NiFe(OH)$_x$ electrocatalyst after the stability test in alkaline freshwater solution for 100 h.
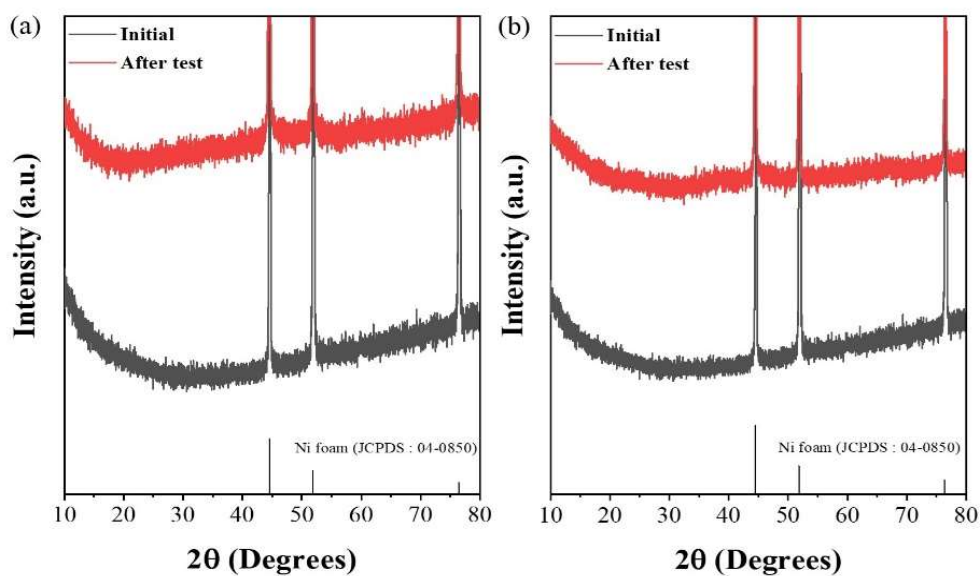
Figure 3.9 XRD patterns of FeNiS$_x$/NiFe(OH)$_x$/NF electrode before and after the stability test in (a) alkaline freshwater and (b) alkaline simulated seawater solutions.
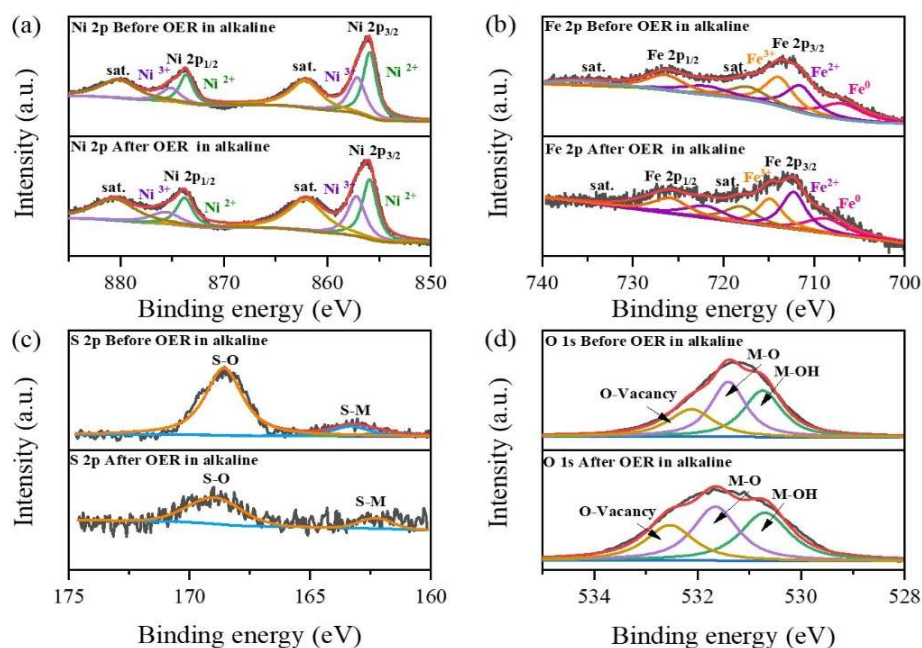
Figure 3. 10 (a) Ni 2p XPS spectrum, (b) Fe 2p XPS spectrum, (c) S 2p XPS spectrum and (d) O 1s XPS spectrum of $FeNiS_x/NiFe(OH)_x$ electrocatalyst after long-term stability test for 100 h in alkaline freshwater solution.

3.3.3 Selectively of OER performance in alkaline simulated seawater

The OER performance of the $FeNiS_x/NiFe(OH)_x/NF$ electrode in an alkaline simulated seawater electrolyte was further investigated by adding 0.5 M NaCl into 1 M KOH freshwater solution [34]. As shown in Figures 3.11(a-b), only overpotentials of 270, 440 and 614 mV are required to achieve current densities of 100, 500 and 1,000 mA cm^{-2}, respectively, which are even slightly better than the case using alkaline freshwater solution containing 1 M KOH, and better performance than those recently reported electrocatalysts for seawater electrolysis (Table 3.2). Multi-step chronopotentiometry measurements with various current density inputs were also performed to test its stability working at different environments such as those in the practical process. As shown in Figure 3.11c, notably, this electrode demonstrates a consistent response potential in each step, implying that this electrocatalyst has

134

excellent mass transfer and charge transfer property as well as stability in the simulated seawater environment over a wide range of current densities. While, as displayed in Figure 3.11d, the electrode can maintain its initial potential of 1.53 V *vs* RHE in the alkaline simulated seawater at 100 mA cm^{-2} for 100 hours without degradation and/or corrosion. Moreover, even at a current density of 500 mA cm^{-2}, it also shows no obvious change comparing to the initial potential after 100-h stability test. In addition, no chlorine gas and hypochlorite are detected and no catalyst dissolution and/or the catalyst peeling off from NF substrate is observed during OER process. Therefore, the prepared FeNiS$_x$/NiFe(OH)$_x$/NF electrode has superior durability and high selectivity towards OER in the electrolysis of alkaline simulated seawater. Herein, it should be noted that the overpotential of this electrode is much lower than 480 mV, and the pH value after stability test even at a high current density is around 10, which are the favorable conditions to achieve high selectivity towards OER in a seawater electrolyzer [6]. Moreover, the nanosheet structure of the spent catalyst after the durability test for over 100 h is still maintained (Figures 3.11(e-f)), suggesting the mechanical stability and anti-corrosion of this electrode in simulated seawater solution. Furthermore, as displayed in Figure 3.9b, the XRD pattern of the electrocatalysts after long-term OER stability test is similar to the initial state, showing that the amorphous nature is also stable in the simulated seawater solution. Moreover, as shown in Figure 3.12, except for S species, the chemical valence states of other main elements are essentially unchanged, also indicating the chemical stability of Ni and Fe species. However, for the EDS elemental mapping, it is confirmed that the S element is still remained in the spent electrocatalyst (Figure 3.13). The superior stability of this electrode could be attributed to the intercalating of sulfate ions into the NiFe(OH)$_x$ structure since it can enhance OER activity as well as corrosion resistance to chloride anions in seawater [4].

The generation of multivalent anions such as sulfite during the reaction could enhance cation selectivity and thus block the chloride anions.

To investigate the possibility of this electrode used in an industrial scale condition, the durability test at a constant current density as high as 1 A cm^{-2} was also carried out for 100 h in the simulated seawater solution. Interestingly, as shown in Figure. 3.14a, the prepared FeNiS$_x$/NiFe(OH)$_x$/NF electrode also exhibits outstanding stability for over 100 hours without performance drop or catalyst corrosion. Notably, because of the cavitation of produced gas (O$_2$) and Cl$^-$ in the solution caused by the high current density input, the surface morphology changes after the stability test, implying surface damage [35]. However, the TEM observation (Figure 3.14b) confirms the presence of FeS and NiFe(OH)$_x$ in the initial form. In the present electrocatalyst, the existing of FeNiS$_x$ and NiFe(OH)$_x$ should have a synergetic effect to provide stable active species for OER in the alkaline simulated solution, and especially FeNiS$_x$ could improve the electrical conductivity and prevent corrosion by chloride anions whereas the NiFe(OH)$_x$ accelerates water molecule dissociation step in the electrolysis of simulated seawater, thereby resulting in superior stability in the imitate seawater electrolysis.
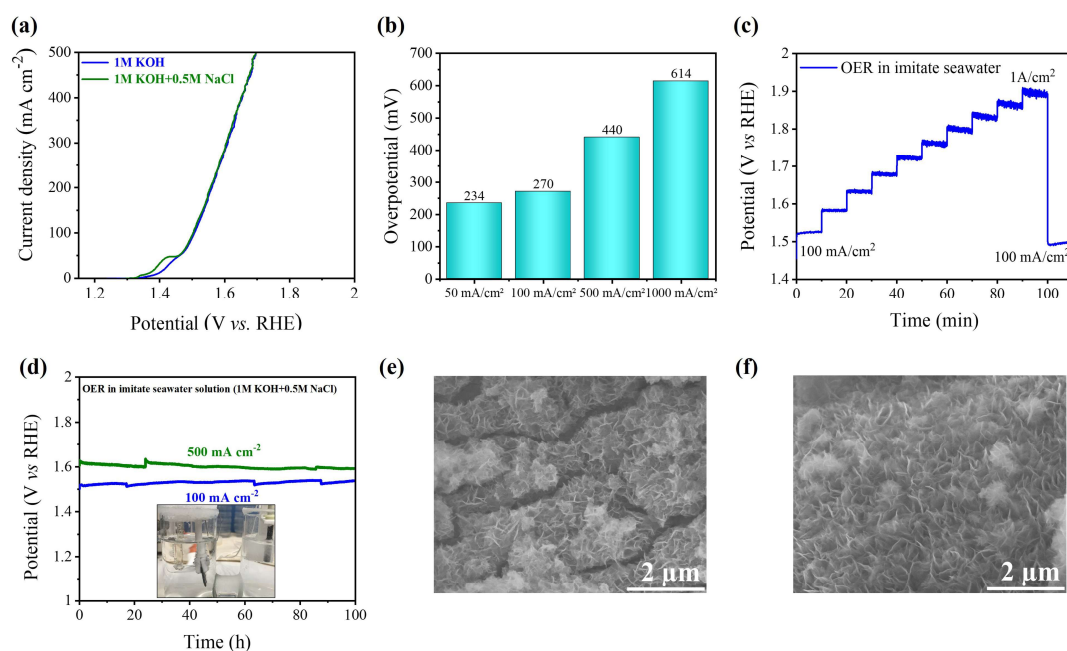
Figure 3.11 OER performance of FeNiS$_x$/NiFe(OH)$_x$ in imitate seawater (1M KOH+0.5M NaCl) electrolysis. (a) Comparison of LSV curves for OER in the alkaline freshwater solution containing 1 M KOH 1M KOH and the alkaline imitate seawater (1 M KOH + 0. 5M NaCl); (b) OER overpotentials at different current densities; (c) Multi-step chronopotentiometry measurements   started from 100 mA cm^{-2} and ended at 1,000 mA cm^{-2} with an increment of 100 mA cm^{-2} in every 600 s, then returning back to 100 mA cm^{-2}; (d) Durability test at constant current densities of 100 and 500 mA cm^{-2} for 100 h (inset: the photo showing the OER during the stability test); and (e-f) SEM images of FeNiS$_x$/NiFe(OH)$_x$ after the stability test at current densities of 100 and 500 mA/cm^2.
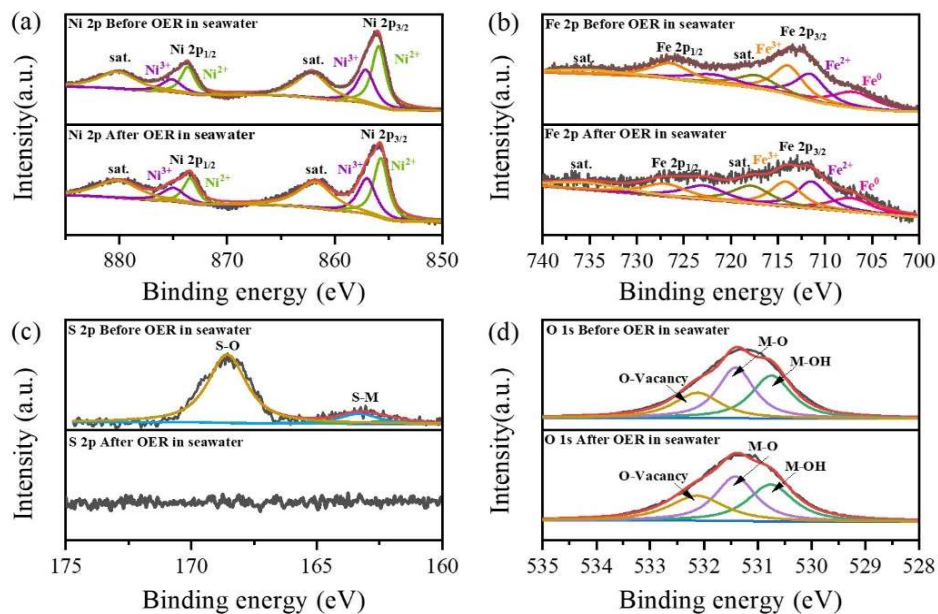
Figure 3.12 (a) Ni 2p XPS spectrum, (b) Fe 2p XPS spectrum, (c) S 2p XPS spectrum and (d) O 1s XPS spectrum of FeNiS$_x$/NiFe(OH)$_x$ /NF after long-term stability test for 100 h in imitate seawater solution.
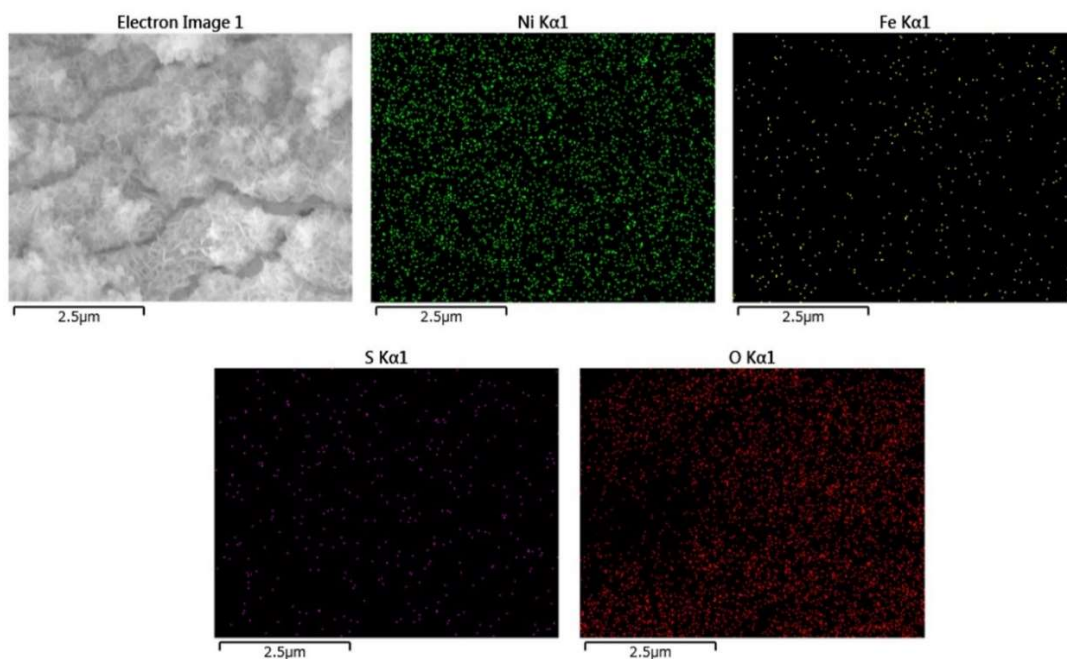
Figure 3.13 Corresponding EDS elemental mapping of FeNiS$_x$/NiFe(OH)$_x$ /NF after the stability test in simulated seawater solution for 100 h.

138
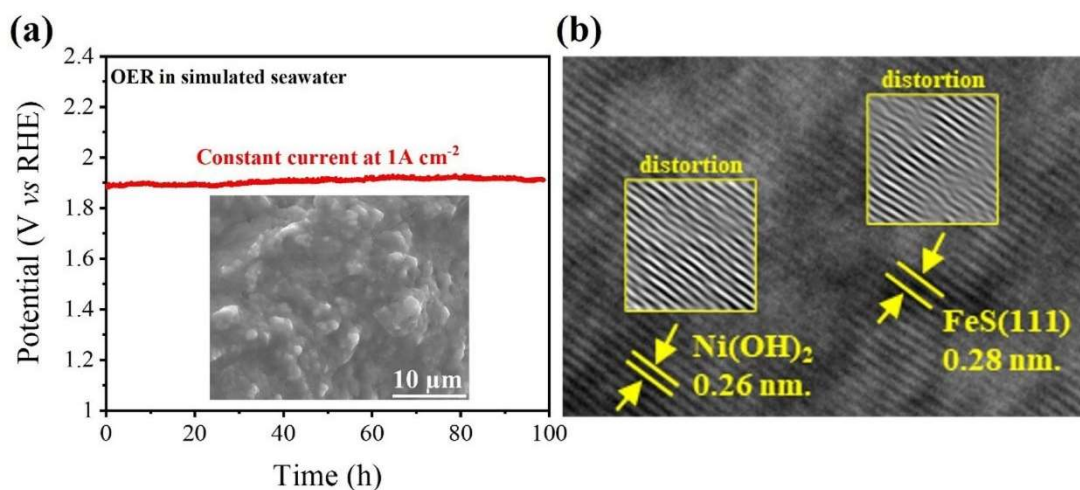
Figure 3.14 (a) Durability test in alkaline simulated seawater at a high current density (1 A cm^{-2}) for 100 h (inset: SEM image after the stability test for OER) and (b) TEM image after the stability test for OER.

Table 3.2 Comparisons of OER activities of various NiFe based electrocatalysts for the electrolysis of alkaline simulated seawater electrolyte

Electrocatalyst	Electrolyte	Overpotential at 100 mA cm^{-2} (mV)	Stability	Reference
FeNiS$_x$/NiFe(OH)$_x$/NF	1 M KOH+0.5 M NaCl	270	100	This work
NiFeN @NiMoN	1 M KOH+0.5 M NaCl	286	48	[53]
NiFe LDH/Carbon	0.1 M KOH+0.5 M NaCl	359 (at 10 mA/cm^2)	2	[6]
Fluorine-doped tin oxide (FTO)/NiO	0.1 M KOH+0.5 M NaCl	340	~3	[54]
S-(Ni,Fe)OOH	0.1 M KOH+0.5 M NaCl	278	100	[21]

3.3.4 Elucidation of the OER mechanism by DFT calculations

The DFT calculations were also carried out to identify the OER mechanism and catalytic active sites on FeNiS$_x$/NiFe(OH)$_x$ electrocatalyst. Theoretically, the OER

mechanism under alkaline condition can be described by four steps using the following equations: [36]

$$OH^- + * \rightarrow OH^* + e^-$$
Eq. (6)

$$OH^* + OH^- \rightarrow O^* + e^- + H_2O$$
Eq. (7)

$$O^* + OH^- \rightarrow HOO^* + e^-$$
Eq. (8)

$$HOO^* + OH^- \rightarrow * + O_2 + e^- + H_2O$$
Eq. (9)

Where the * denotes catalytic active sites on the catalyst surface while OOH^*, O^* and OH^* represent adsorption intermediates.

The catalytic active sites were studied by DFT calculations using Ni and Fe atoms with S substitutions on the O site. The three models are including $NiFe(OH)_x$, $FeNiS_x$-$NiFe(OH)_x$-Fe sites and $FeNiS_x$-$NiFe(OH)_x$-Ni sites with refer to single phase $NiFe(OH)_x$, S substitution on O (Fe active sites) and S substitution on O (Ni active sites), respectively, are proposed (Figure 3.15).
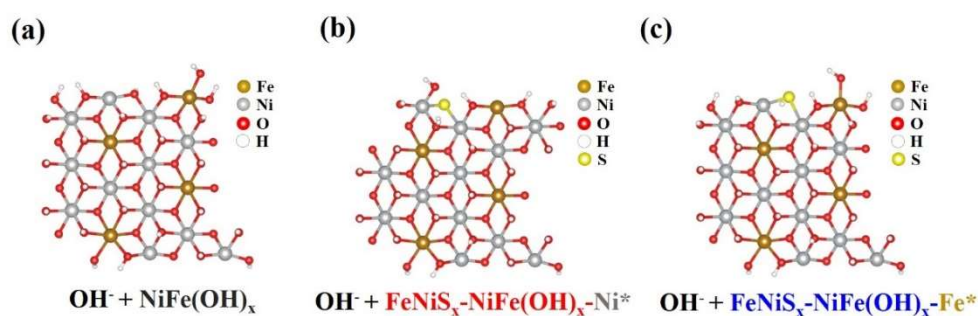
Figure 3.15 Structure models of (a) $NiFe(OH)_x$; (b) $FeNiS_x$-$NiFe(OH)_x$-Ni sites; and (c) $FeNiS_x$-$NiFe(OH)_x$-Fe sites.

According to OER in Figure 3.16a, the intermediates *OH, *O, and *OOH bound to the active sites through oxygen species with a single bond should be in correspondence with four-electron mechanism. Basically, OER overpotential is directly related to the free energies of the reaction intermediates, especially at the second step

(*OH to *O), and the adsorption free energy difference between *OH and *O is proposed to be the main descriptor for the OER activity [32]. As shown in Figure 3.16b, the transformation of *OH to *O can be defined as a rate determining step due to its larger gap of free energy than other steps. As a result, the Gibbs free energy difference value of FeNiS$_x$-NiFe(OH)$_x$-(*Fe) ($\Delta G_{II} = 1.61\ eV$) is lower than those of FeNiS$_x$-NiFe(OH)$_x$- (*Ni) ($\Delta G_{II} = 2.21\ eV$) and NiFe(OH)$_x$ ($\Delta G_{II} = 1.74\ eV$), suggesting that Fe sites should be the active sites and S substitution on the O site can effectively reduce the free energy, thereby enhancing the electrocatalytic properties. In other words, S doping can decrease free energy gap between *OH to *O, making OER more efficient (Figure 3.16c). Moreover, Cl$^-$ adsorption energy on the Ni and Fe sites in FeNiS$_x$-NiFe(OH)$_x$ electrode were also calculated by DFT. As shown in Figure 3.16d, the free energy of Cl$^-$ adsorption on Ni sites (-3.30 eV) is higher than that on Fe sites (-3.19 eV and -2.65 eV), indicating that Cl$^-$ adsorption on Ni sites should be more thermodynamically favorable since it is more negative than that of two Fe sites on FeNiS$_x$-NiFe(OH)$_x$-(*Fe). As such, more free available sites on the Fe surface could be provided for OER, implying higher OER selectivity against ClER on the FeNiS$_x$-NiFe(OH)$_x$-(*Fe) (Figure 3.17).
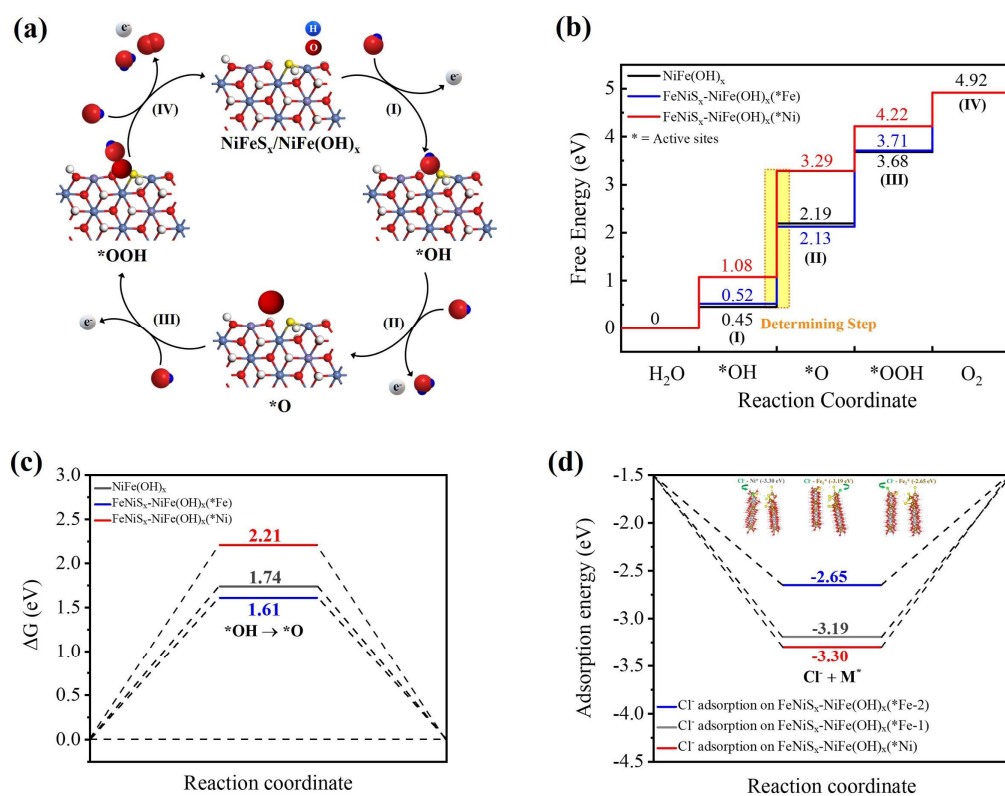
Figure 3.16 (a) Schematic illustration for OER mechanism, (b) Gibbs free energy diagram; (c) The energy barrier for *OH to *O transition reaction step and, (d) the energy barrier for Cl- adsorption.
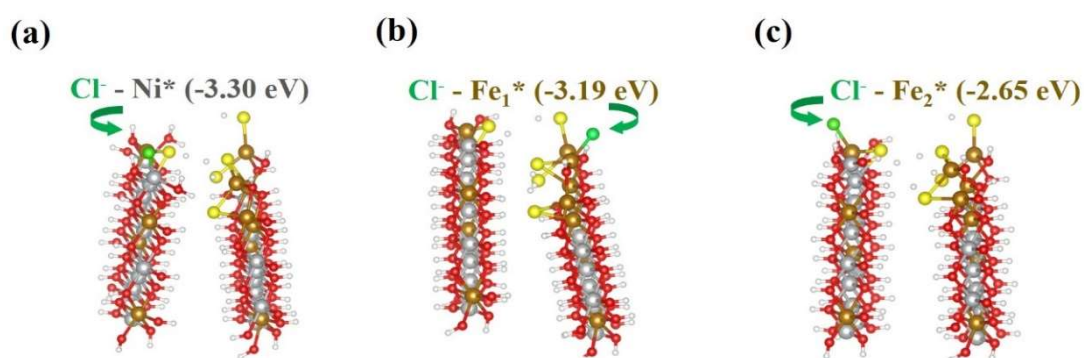
Figure 3.17 Structure models of Cl⁻ adsorption ; (a) on Ni sites and (b and c) on and Fe sites in FeNiS$_x$/NiFe(OH)$_x$.

3.3.5 Overall alkaline freshwater and seawater electrolysis

Since the obtained $FeNiS_x/NiFe(OH)_x$ electrocatalyst shows excellent performances for the OER in both alkaline freshwater and simulated seawater electrolysis processes, a try was performed by using it as the bifunctional electrocatalyst for the overall alkaline freshwater and seawater electrolysis. Figure 3.18 shows a photo of overall water electrolysis cell. Both HER and OER activities of $FeNiS_x/NiFe(OH)_x$ electrocatalyst are demonstrated in Figure 3.19. It is observed that the potential differences (ΔE) between HER and OER at a current density of 100 mA cm^{-2} are 1.82 and 1.80 V for the electrolysis of alkaline freshwater and simulated seawater, respectively. Comparing to the theoretical decomposition voltage of 1.23 V for water electrolysis, this bifunctional electrode requires only 590 and 570 mV overpotentials for the electrolysis of alkaline freshwater and simulated seawater, respectively, which are even lower than those of the cell with noble metal-based catalysts (i.e., Pt/C and RuO_2).
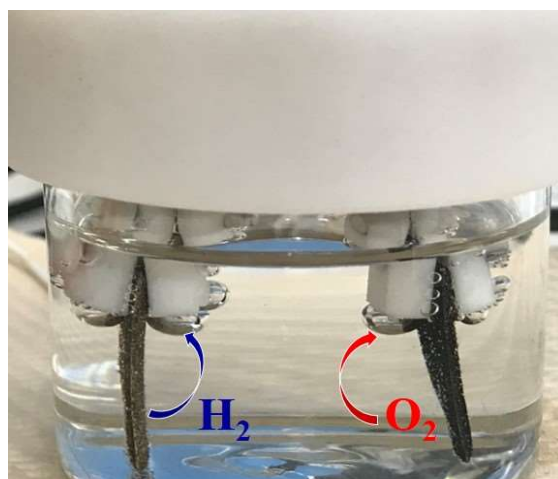
Figure 3.18 Digital photograph show in O_2 and H_2 gas bubbles on the electrode surface.
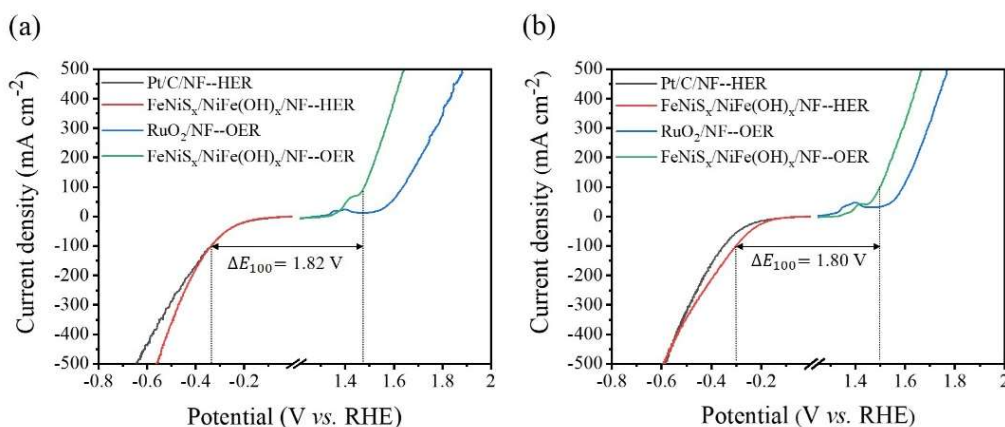
Figure 3.19 Electrocatalytic activities of $FeNiS_x/NiFe(OH)_x/NF$ electrode for OER and HER; (a) in alkaline freshwater and (b) in alkaline simulated solution.

Due to the outstanding OER and HER activities of this catalyst, a two-electrode cell by using it for both cathode (+) and anode (-) (denoted as $FeNiS_x/NiFe(OH)_x/NF \parallel FeNiS_x/NiFe(OH)_x/NF$) was investigated. As can be seen in Figures 3.20a and 3.20d, this electrolysis system only requires a low cell voltage of 1.58 and 1.60 V at 10 mA cm^{-2} in the alkaline freshwater and simulated seawater solutions, respectively. Notably, for the alkaline freshwater electrolysis, the cell with the bifunctional $FeNiS_x/NiFe(OH)_x/NF$ electrode exhibits superior performance over other reported ones (Figure. 3.20c NiFe-LDH/(Ni(OH)$_2$ (1.6 V) [30], Ar-NiCo$_2$O$_4$/S (1.63 V) [37], NiFe-(oxy)sulfide (1.64 V) [38] , NiFe-LDH (1.70 V) [39] NiFe-LDH/FeCoS$_2$ (1.74 V) [40], NiFe-LDH/Ni$_3$S$_2$ (1.65 V)[41] and Ni-CoS$_2$ (1.66 V)[42]). While, for the simulated seawater solution electrolysis, it also shows a comparable performance to those reported ones (Figure 3.20f. NiMoN//NiMoN@NiFeS (1.58 V), Karst Ni Foam (1.79 V) and NiFe-NiS$_x$-Ni//Ni-NiO-Cr$_2$O$_3$ (1.56 V) [43]).

Long-term stability test of this two-electrode system was also carried out in both alkaline freshwater and simulated seawater solutions at different constant current densities of 10, 100, 500 and 1,000 mA cm^{-2}. As shown in Figure 3.20b, constant cell

voltages of 1.58, 2.00, 2.90 and 3.54 V are obtained without electrocatalyst dissolution and apparent degradation for 12 h in the alkaline freshwater solution. Similarly, in the imitate seawater solution, the cell voltages of 1.60, 1.93, 2.41 and 2.81 V are also remained for over 12 h (Figure 3.20e). Particularly, this two-electrode system is capable to sustain stable up to 1 A/cm^2 in the imitate seawater solution with an overall water electrolysis voltage of 2.81 V, achieving a high hydrogen productivity without the catalyst deterioration, which should be attributed to that the polyatomic anion on the anode could block the Cl$^-$ and protect the corrosion of electrode. While, it is reported that the S incorporation into the NiFe(OH)$_x$ structure could decrease OH* adsorption energy as well as free energy gap between O* and OH* for the enhancing OER at a lower overpotential, which is consistent with the above DFT results and those in the literature [32]. Moreover, chronopotentiometry measurements with a power on-off condition was also performed to investigate the stability of this electrolysis system in order to mimic the practical operation condition in the large-scale application using intermittent energy sources such as wind and solar power. As shown in Figure 3.20g, the chronopotentiometry measurements were carried out in a simulated seawater solution by continuously applying a current density of 100 mA cm^{-2} for 1 h, then turning off the current for 0.5 h, and repeating this process for 4 cycles. As a result, the cell voltage remains steady at 1.82 V during the power-on period with a good recovery property in each cycle, implying the stability of electrocatalytic performance and mechanical robustness in an unstable power supply system for seawater electrolysis. Besides, the faradaic efficiency is calculated from theoretical and measured hydrogen and oxygen evolution amounts during the electrolysis in the two-electrode system for overall water electrolysis by using this bifunctional electrode as both cathode and anode. As shown in Figure 3.21, the faradaic efficiencies of hydrogen/oxygen production are

as high as 94/95% and 93/94% in the electrolysis of alkaline freshwater and simulated seawater, respectively. Therefore, it could be one of the most promising candidates for hydrogen production from seawater in a large-scale application using a system as illustrated in Figure 3.20h.
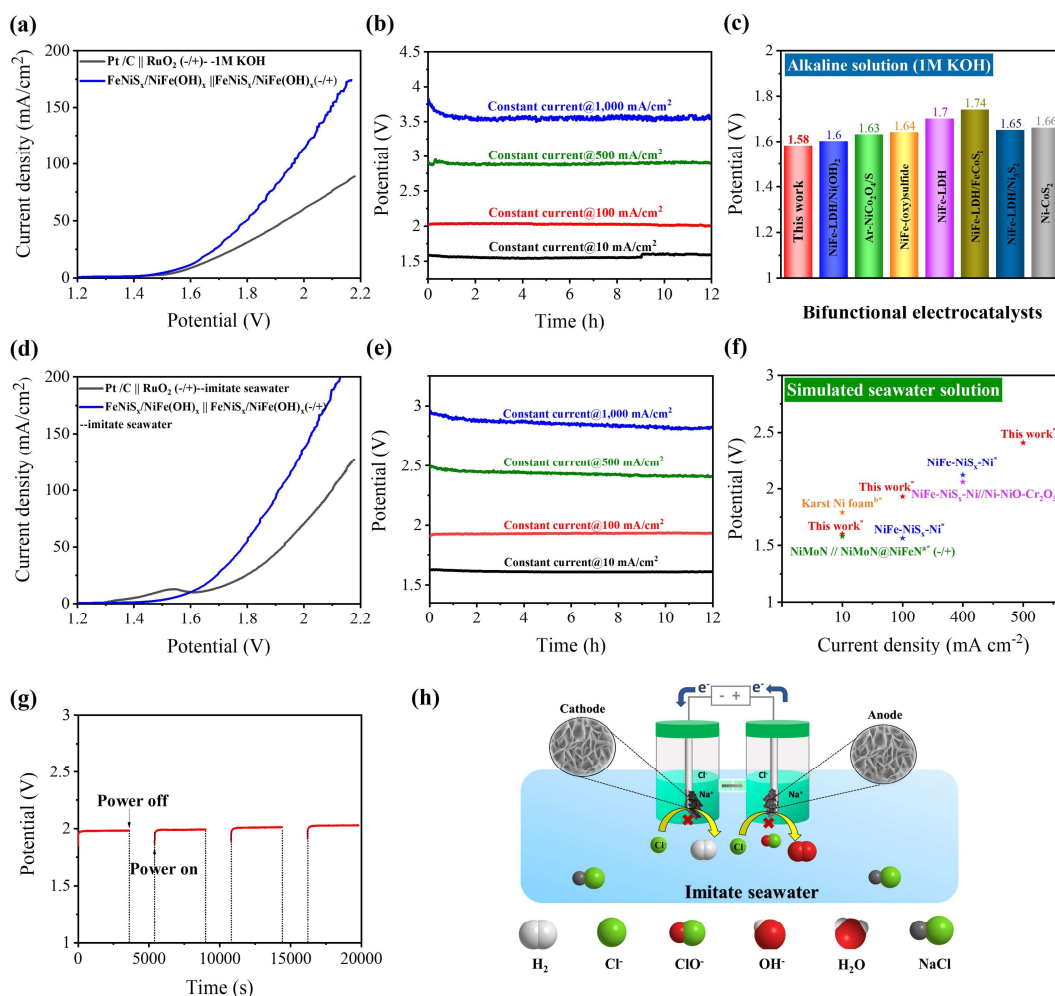
Figure 3.20 (a) LSV curves of two-electrode systems of FeNiS$_x$/NiFe(OH)$_x$/NF ‖ FeNiS$_x$/NiFe(OH)$_x$ /NF and Pt/NF//RuO$_2$/NF for alkaline freshwater electrolysis at a scan rate of 2 mV/s in 1 M KOH solution; (b) Stability tests at 10,100,500 and 1,000 mA cm^{-2} for 12 h in alkaline freshwater solution containing 1 M KOH; (c) Comparison of the performances of various bifunctional electrocatalysts in electrolysis of alkaline freshwater solution; (d) LSV curves of alkaline freshwater solution containing 1 M KOH at a scan rate of 2 mV/s in alkaline imitate seawater solution; (e) Stability tests.

146
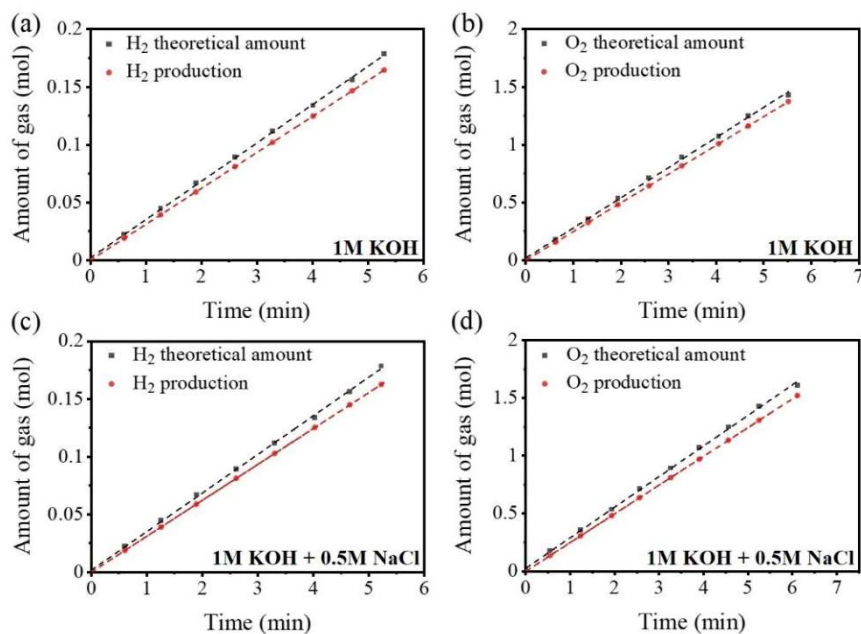
Figure 3.21 Theoretical hydrogen and oxygen evolution amounts and the measured gas amounts during the electrolysis in the two-electrode system for overall water electrolysis by using FeNiS$_x$/NiFe(OH)$_x$/NF electrode as both cathode and anode; (a,b) in alkaline freshwater (1M KOH) and (c,d) in alkaline simulated seawater (1 M KOH+0.5 M NaCl).

3.4 Conclusions

A FeNiS$_x$/NiFe(OH)$_x$ electrocatalyst with a 2D nanosheet structure is successfully *in-situ* grown on nickel foam by using a facile corrosion engineering process followed by a fast and mild sulfurization step. This electrode exhibits excellent electrocatalytic performance with a low OER overpotential of 270 mV at 100 mA cm^{-2} and remarkable stability even at a large current density of 1 A cm^{-2} without catalyst dissolution and erosion for over 100 h in alkaline simulated seawater solution. Moreover, it can also be served as a bifunctional electrocatalysts for both HER and OER in the electrolysis of seawater. As a result, for the overall seawater electrolysis using a two-electrode system, it is capable to sustain stable up to 1 A/cm^2 in the imitate seawater solution with a cell voltage of 2.81 V, achieving a high hydrogen productivity without the catalyst

deterioration while the faradaic efficiencies of hydrogen and oxygen production are as high as 95% and 94% in the electrolysis of alkaline simulated seawater, respectively. The superior activity and durability of this electrode should be attributed to the synergistic interaction between highly conductive $FeNiS_x$ species and the highly catalytic active sites on both $FeNiS_x$ and $NiFe(OH)_x$. In particular, the incorporated sulfur species could function as a protective coating layer for the blockage Cl^- from the electrolyte, preventing catalyst degradation and/or erosion over the long-term operation under a high current density condition by intercalated it into the $NiFe(OH)_x$ layer instead of Cl^-. DFT calculations proves that the low energy barrier on $FeNiS_x/NiFe(OH)_x$ makes *OH to *O transition step more kinetically promoted and the bonding between Fe and OER intermediates improved. The DFT calculations reveal that Cl^- has a high adsorption energy on the non-active Ni sites, implying that more free available Fe sites can be provided for OER, thereby resulting in a high OER selectivity. Therefore, this economical electrode could be a promising candidate for seawater electrolysis even in an industrial-scale application.

References

[1] F. Zhang, H. Zhang, M. Salla, N. Qin, M. Gao, Y. Ji, S. Huang, S. Wu, R. Zhang, Z. Lu, Q. Wang, J. Am. Chem. Soc. 143 (2021) 223-231.

[2] F.S. Hegner, F.A. Garcés-Pineda, J. González-Cobos, B. Rodríguez-García, M. Torréns, E. Palomares, N. López, J.-R. Galán-Mascarós, ACS Catal. 11 (2021) 13140-13148.

[3] M. Kim, J. Park, M. Wang, Q. Wang, M.J. Kim, J.Y. Kim, H.-S. Cho, C.-H. Kim, Z. Feng, B.-H. Kim, S.W. Lee, Appl. Catal. B: Environ. 302 (2022) 120834.

[4] Y. Kuang, M.J. Kenney, Y. Meng, W.H. Hung, Y. Liu, J.E. Huang, R. Prasanna, P. Li, Y. Li, L. Wang, M.C. Lin, M.D. McGehee, X. Sun, H. Dai, Proc. Natl. Acad. Sci. U. S. A. 116 (2019) 6624-6629.

[5] J.N. Hausmann, R. Schlögl, P.W. Menezes, M. Driess, Energy Environ. Sci. 14 (2021) 3679-3685.

[6] F. Dionigi, T. Reier, Z. Pawolek, M. Gliech, P. Strasser, ChemSusChem 9 (2016) 962-972.

[7] Y. Liu, X. Liang, L. Gu, Y. Zhang, G.-D. Li, X. Zou, J.-S. Chen, Nat. Commun. 9 (2018) 2609.

[8] S.H. Hsu, J. Miao, L. Zhang, J. Gao, H. Wang, H. Tao, S.F. Hung, A. Vasileff, S.Z. Qiao, B. Liu, Adv. Mater. 30 (2018) 1707261.

[9] G. Liu, Y. Xu, T. Yang, L. Jiang, Nano Materials Science (2020).

[10] L. Chen, Y. Wang, X. Zhao, Y. Wang, Q. Li, Q. Wang, Y. Tang and Y. Lei, J. Mater. Sci. Technol. 110 (2022) 128-135.

[11] H. Zhou, F. Yu, Q. Zhu, J. Sun, F. Qin, L. Yu, J. Bao, Y. Yu, S. Chen, Z. Ren, Energy Environ. Sci. 11 (2018) 2858-2864.

[12] S. Gupta, M. Forster, A. Yadav, A.J. Cowan, N. Patel, M. Patel, ACS Appl. Energy Mater. 3 (2020) 7619-7628.

[13] P.M. Bodhankar, P.B. Sarawade, G. Singh, A. Vinu, D.S. Dhawale, J. Mater. Chem. A 9 (2021) 3180-3208.

[14] W. Shuang, X. Ge, C. Lv, C. Hu, H. Guan, J. Wu, Z. Wang, X. Yang, Y. Shi, J. Song, Z. Zhang, A. Watanabe, J. Cai, Nanoscale 12 (2020), 9557-9568.

[15] H.J. Song, H. Yoon, B. Ju, D.-Y. Lee, D.-W. Kim, ACS Catal. 10 (2019) 702-709.

[16] C. Xuan, J. Wang, W. Xia, J. Zhu, Z. Peng, K. Xia, W. Xiao, Huolin L. Xin, D. Wang, J. Mater. Chem. A 6 (2018) 7062-7069.

[17] Y. Zou, B. Xiao, J.-W. Shi, H. Hao, D. Ma, Y. Lv, G. Sun, J. Li, Y. Cheng, Electrochim. Acta 348 (2020) 136339.

[18] D. Yuan, Y. Dou, C.-T. He, L. Yu, L. Xu, D. Adekoya, Q. Xia, J. Ma, S. X. Dou and S. Zhang, Cell Rep. Physical Science, 2 (2021) 100331.

[19] X.-Y. Zhang, F.-T. Li, Y.-W. Dong, B. Dong, F.-N. Dai, C.-G. Liu, Y.-M. Chai, Appl. Catal. B: Environ 315 (2022).

[20] S. Liu, S. Ren, R.-T. Gao, X. Liu, L. Wang, Nano Energy 98 (2022) 107212.

[21] L. Yu, L. Wu, B. McElhenny, S. Song, D. Luo, F. Zhang, Y. Yu, S. Chen, Z. Ren, Energy Environ. Sci. 13 (2020) 3439-3446.

[22] G. Kresse, J. Furthmüller, J. Comput. Mat. Sci. 6 (1996) 15-50.

[23] J.P. Perdew, K. Burke, M. Ernzerhof, Phys. Rev. Lett. 77 (1996) 3865-3868.

[24] P. Li, X. Duan, Y. Kuang, Y. Li, G. Zhang, W. Liu, X. Sun, Adv. Energy Mater 8 (2018) 1703341.

[25] C. Kuai, Y. Zhang, D. Wu, D. Sokaras, L. Mu, S. Spence, D. Nordlund, F. Lin, X.-W. Du, ACS Catal. 9 (2019) 6027-6032.

[26] Y. Sun, C. Liu, L. Zhang, P. Wan, S. Zhuang, Y. Tang, Y. Chen and J. Pan, Chem

Electro Chem 4 (2017) 1044-1050.

[27] S. Zhuang, L. Wang, H. Hu, Y. Tang, Y. Chen, Y. Sun, H. Mo, X. Yang, P. Wan and Z. U. H. Khan, Chem Electro Chem 5 (2018) 2577-2583.

[28] H. Yang, L. Gong, H. Wang, C. Dong, J. Wang, K. Qi, H. Liu, X. Guo and B. Y. Xia, Nat Commun. 11 (2020) 5075.

[29] Q. Che, Q. Li, Y. Tan, X. Chen, X. Xu, Y. Chen, Appl. Catal. B: Environ 246 (2019) 337-348.

[30] N.S. Gultom, H. Abdullah, C.-N. Hsu, D.-H. Kuo, Chem. Eng. J. 419 (2021) 129608.

[31] Y.-N. Zhou, W.-L. Yu, Y.-N. Cao, J. Zhao, B. Dong, Y. Ma, F.-L. Wang, R.-Y. Fan, Y.-L. Zhou, Y.-M. Chai, Appl. Catal. B: Environ 292 (2021) 120150.

[32] T. Wang, G. Nam, Y. Jin, X. Wang, P. Ren, M.G. Kim, J. Liang, X. Wen, H. Jang, J. Han, Y. Huang, Q. Li, J. Cho, Adv. Mater. 30 (2018) 1800757.

[33] G. Xi, L. Zuo, X. Li, Y. Jin, R. Li and T. Zhang, J. Mater. Sci. Technol. 70 (2021) 197-204.

[34] Y. Xu, H. Lv, H. Lu, Q. Quan, W. Li, X. Cui, G. Liu, L. Jiang, Nano Energy 98 (2022) 107295.

[35] S.-J. Kim, S.-J. Lee and S.-O. Chong, Mater. Res. Bull. 58 (2014) 244-247.

[36] M. Plevová, J. Hnát, K. Bouzek, J. Power Sources 507 (2021) 230072.

[37] J.H. Lin, Y.T. Yan, T.X. Xu, C.Q. Qu, J. Li, J. Cao, J.C. Feng, J.L. Qi, J. Colloid Interface Sci. 560 (2020) 34-39.

[38] B.Q. Li, S.Y. Zhang, C. Tang, X. Cui, Q. Zhang, Small 13 (2017) 1700610.

[39] C. Wu, H. Li, Z. Xia, X. Zhang, R. Deng, S. Wang, G. Sun, ACS Catal. 10 (2020) 11127-11135.

[40] Z. Zhang, J. Zhou, H. Wei, Y. Dai, S. Li, H. Shi, G. Xu, J. Mater. Sci. 55 (2020) 16625-16640.

[41] L. Ren, C. Wang, W. Li, R. Dong, H. Sun, N. Liu, B. Geng, Electrochim. Acta. 318 (2019) 42-50.

[42] W. Fang, D. Liu, Q. Lu, X. Sun, A.M. Asiri, Electrochem. Commun. 63 (2016) 60-64.

[43] J. Mohammed-Ibrahim, H. Moussab, Mater. Sci. Energy Technol. 3 (2020) 780-807.

[44] X. Zou, Y. Liu, G.D. Li, Y. Wu, D.P. Liu, W. Li, H.W. Li, D. Wang, Y. Zhang, X. Zou, Adv. Mater. 29 (2017) 1700404.

[45] G. Barati Darband, M. Aliofkhazraei, A.S. Rouhaghdam, J. Colloid Interface Sci. 547 (2019) 407-420.

[46] M.J. Wang, X. Zheng, L. Song, X. Feng, Q. Liao, J. Li, L. Li, Z. Wei, J. Mater. Chem. A 8 (2020) 14145-14151.

[47] B. Lin, H. le, F. Xu, S. Mu, RSC Adv. 10 (2020) 27424-27427.

[48] Y. Liu, S. Jiang, S. Li, L. Zhou, Z. Li, J. Li, M. Shao, Appl. Catal. B: Environ 247 (2019) 107-114.

[49] W. He, G. Ren, Y. Li, D. Jia, S. Li, J. Cheng, C. Liu, Q. Hao, J. Zhang, H. Liu, Catal. Sci. Technol. 10 (2020) 1708-1713.

[50] X. Luan, H. Du, Y. Kong, F. Qu, L. Lu, Chem. Commun. 55 (2019) 7335-7338.

[51] S. Si, H.-S. Hu, R.-J. Liu, Z.-X. Xu, C.-B. Wang, Y.-Y. Feng, Int. J. Hydrog. Energy 45 (2020) 9368-9379.

[52] Z. Xu, Y. Ying, G. Zhang, K. Li, Y. Liu, N. Fu, X. Guo, F. Yu, H. Huang, J. Mater. Chem. A 8 (2020) 26130-26138.

[53] L. Yu, Q. Zhu, S. Song, B. McElhenny, D. Wang, C. Wu, Z. Qin, J. Bao, Y. Yu, S. Chen, Z. Ren, Nat Commun, 10 (2019) 5106.

[54] J. Juodkazytė, B. Šebeka, I. Savickaja, M. Petrulevičienė, S. Butkutė, V. Jasulaitienė, A. Selskis, R. Ramanauskas, Int. J. Hydrog. Energy 44 (2019) 5929-5939.

CHAPTER 4 Modification of spinel MnCo₂O₄ nanowire with NiFe-layered double hydroxide nanoflakes for stable seawater oxidation

4.1 Introduction

According to the report of the International Energy Agency, the market share of hydrogen from water electrolysis will reach about 22% in 2050 [1]. Thus, water resource for the electrolysis is becoming more and more important since the fresh water resource is limited in our daily life. In contrast, high-salinity *seawater* accounts for 97% of *total water* reserves on the earth [2]. If seawater can be directly electrolyzed for the hydrogen production, the use of hydrogen in various equipments such as fuel cells can generate freshwater, which will not only save the limited fresh water resource but also solve the freshwater problem in the world [3]. Moreover, the seawater electrolysis is beneficial for the storage of those unstable ocean energy such as offshore wind power and tidal and wave energy [4]. However, unlike the fresh water electrolysis, in the seawater electrolysis, it contains competitive reactions between chlorine evolution reaction (ClER ; $2Cl^- \rightarrow Cl_2 + 2e^-, E^0 = 1.36\,V_{RHE}$) or hypochlorite generation reaction and oxygen evolution reaction (OER ; $4OH^- \rightarrow O_2 + 2H_2O + 4e^-; E^0 = 1.23V_{RHE}$) since ClER is more kinetically favorable than OER, especially at a high current density [5]. The difference in electrode thermodynamical potential between ClER and OER is fixed at 0.480 V. The hypochlorite will be not formed if the overpotential is less than 480 mV [6]. Furthermore, considering for a large-scale application at a high current density, catalyst corrosion and degradation should be taken into account. Sometimes, even though there is a lower overpotential, those accumulated Cl⁻ ions would limit anode lifetime because high-concentration Cl⁻ ions at the

electrode/electrolyte interface tend to accelerate the corrosion process through metal chloride-hydroxide formation, leading to catalyst deactivation [7]. Therefore, the designing criteria for the electrocatalysts in the seawater electrolysis should be (i) high OER selectivity and stability, (ii) high corrosion resistance, (iii) high temperature tolerance [8], and especially (iv) stable performance at high current density (~0.4-1 A cm^{-2}).

Spinel-type cobalt-based binary metal oxides such as $MnCo_2O_4$ [9], $CuCo_2O_4$ [10], and $NiCo_2O_4$ [11] have been studied for OER because of their redox stability, synergy of two metals and mixed variance states of each metal. Especially, for $MnCo_2O_4$, it has an abundance active sites, in which the cobalt species provides a high oxidation potential while the manganese species affords high electron transfer ability along with defined morphology [12]. However, its performance is still unsatisfactory since it suffers from poor ionic conductivity and partial dissolution in those alkaline electrolytes, resulting in poor stability. Many strategies have been proposed to improve OER activity and stability such as modified $MnCo_2O_4$ with cation substitution [13], anchored on a highly conductive material [14] and surface modification [15]. To date, $MnCo_2O_4$ has never been used in a seawater electrolysis system [16]. In the presence of chlorine ions, it is reported that MnO_x based catalysts always have high OER selectivity since MnO_x can block Cl^- transportation [17, 18]   While, it is found that some Layered Double Hydroxide (LDH) materials also have the ability to block chlorine ions due to higher Cl^- adsorption free energy on their surfaces [19]. Among those LDH materials, NiFe-LDH is the most active one for the OER in alkaline electrolytes. However, inferior electrical activity, limited active sites, intrinsically poor catalytic activity, metal dissolution and instability during the OER at current densities higher than 100 mA cm^{-2} are the key barriers for industrial applications [20]. Recently,

it is found that uniformly coating of NiFe-LDH on a sulfide layer formed on a nickel substrate led to superior catalytic activity and corrosion resistance in alkaline seawater electrolysis [21]. Inspired by these reported results, in this study, modification of the $MnCo_2O_4$ nanowire with a NiFe-LDH layer was proposed in the preparation of electrocatalysts for the stable seawater electrolysis. It is expected that the combination of NiFe-LDH active material with Cl^- blocking property and $MnCo_2O_4$ with rich active sites could significantly boost the activity and extend the stability in seawater electrolysis due to the synergy effect between the two materials.

4.2 Experimental section

4.2.1 Chemical and materials

Manganese (II) nitrate tetrahydrate ($Mn(NO_3)_2·4H_2O$, $\geq$ 97%) and ruthenium (IV) oxide (RuO_2, 99.9%) were purchased from Sigma-Aldrich, Japan. Cobalt (II) nitrate hexahydrate ($Co(NO_3)_2·6H_2O$, 99.5%), ammonium fluoride (NH_4F, 97%), urea (CH_4N_2O, 99%), iron (III) chloride hexahydrate ($FeCl_3·6H_2O$, 99%), sodium nitrate ($NaNO_3$, 99%), sodium chloride (NaCl, 99%) hydrochloric acid (HCl, 69%), potassium hydroxide (KOH, 85%) and ethanol (C_2H_5OH, 99.5%) were purchased from Wako, Japan. Deionized (DI) water (18.2 MΩ cm) was used to prepare the solution. Nickel foam (NF; 1.5 mm of thickness, 0.23 g/cm^3 bulk density and 110 pores/inch) was purchased from MTI, Japan.

4.2.2 Preparation of MnCo2O4@NiFe-LDH on nickel foam (NF)

To remove oxide layer and other impurities, NF sheet (2 x 2 cm^2) was ultrasonically cleaned in 1 M HCl, ethanol and deionized water consecutively for 1 h in each step, and then dried for 1 h in a vacuum oven at 60 $^\circ$C. For the preparation of MnCO2O4@NiFe-LDH on the NF, 1 mmol of $Mn(NO_3)_2·4H_2O$, 2 mmol of $Co(NO_3)_2 ·6H_2O$, 6 mmol of NH_4F and 12 mmol of CH_4N_2O were dissolved in 30 ml of DI water, and then the pre-

treated NF sheet was immersed into the above solution in a Teflon-lined autoclave, which was heated for 4 h at 120 °C followed by naturally cooling down. The resulting electrode was rinsed with ethanol and DI water sucessively, dried in vacuum oven at 60 °C for 12 h, and continuously calcined in air atmosphere at 350 °C for 2 h. As such the $MnCo_2O_4$ nanowires were formed on the NF substrate. The obtained $MnCo_2O_4$/NF was then placed in an autoclave with a solution containing 2 mmol of $FeCl_3 \cdot 6H_2O$ and 2 mmol of $NaNO_3$ in 30 ml of DI water, which was heated at 120 °C for 2 h. Thereafter, the obtained electrode was rinsed with DI water and ethanol sucessively for 3 times before being dried in a vacuum oven at 60 °C for 12 h. As such, the NiFe-LDH nanosheets were deposited on each $MnCo_2O_4$ nanowire was obtained, which is denoted as $MnCo_2O_4$@NiFe-LDH@/NF electrode. For comparison, $MnCo_2O_4$/NF and NiFe-LDH/NF electrodes were also prepared by using the same hydrothermal method.

4.2.3 Catalyt characterization

A scanning electron microscope (SEM, SU8010, HITACHI, JAPAN) and a transmission electron microscope (TEM, JEM-2100F, JEOL) were used to examine the morphology and nanostructure of the prepared electrocatalysts, respectively. The phase compositions and crystalline structures were characterized by an X-ray photoelectron spectroscopy measurement (XPS) using a VG Scientific ESCALab250i-XL instrument with an Al-Kα X-ray source and X-ray diffraction (XRD) measurement in a 2θ range of 10°-80° with a Rigaku Smartlab diffractometer (Japan) using a Cu-Kα radiation source ($\lambda = 0.15406$ nm), respectively.

4.2.4 Electrochemical measurements

All prepared electrodes were examined using a three-electrode system on an electrochemical workstation (Versa STAT4, Princeton, USA). A standard Hg/HgO electrode was used as the reference electrode, a carbon rod was used as the counter

electrode and the as-prepared electrode was used directly as the working electrode. The potential with respect to reversible hydrogen electrode (RHE) was calculated by the Nernst equation: E(V *vs.* RHE) = E(V *vs.* Hg/HgO) + 0.098 + 0.059pH. The corresponding overpotential (η) for OER was calculated using the formula: η = E(*vs* RHE) - 1.23 V. The polarization curve was measured in a potential range of 0.924-2.324 V vs RHE at a scan rate of 2 mVs^{-1} in both a simulated seawater alkaline solution (1 M KOH + 0.5 M NaCl) and a natural seawater based alkaline solution (the natural seawater was collected from Pacific Ocean, Aomori Prefecture, Japan) without iR-compensation. The electrochemical impedance spectroscopy (EIS) measurement was performed at a frequency range of 100 kHz-0.1 Hz. The cyclic voltammetry (CV) was conducted in a potential range of 0.1-0.2 V at a scan rate range of 10-100 mVs^{-1} to determine the electrochemical double layer capacitance (C_{dl}) for the determination of electrochemical active surface area (ECSA). OER durability was evaluated by using the chronopotentiometry testing for 20 h. at 10°C with constant high current densities of 100 and 1,000 mA cm^{-2} in an alkaline simulated seawater solution (1M KOH + 0.5M NaCl).

4.3 Results and discussion

4.3.1 Characterization of MnCo$_2$O$_4$@NiFe-LDH electrocatalyst

A two-step hydrothermal method was used to prepare the MnCo$_2$O$_4$@NiFe-LDH electrocatalyst on NF (Figure 4.1a). As shown in Figure 4.1b, the MnCo$_2$O$_4$ nanowires have been successfully grown on the surface of NF substrate. Then, the NiFe-LDH layer has been also deposited on the MnCo$_2$O$_4$ nanowire via a reduction reaction between NaNO$_3$ and FeCl$_3$: $NO_3^- + H_2O + 2e^- \rightarrow NO_2^- + 2OH^-$, where the OH^- results in the precipitation of Ni and Fe species to form NiFe-LDH nanosheets on the surface of each nanowire (Figure 4.1c) [22]. One can see that the NiFe-LDH nanosheets are fully

158

covered on the surface of each $MnCo_2O_4$ nanowire (Figure 4.1d). The presences of Mn, Co, Ni, Fe and Ni elements on the NF have been also confirmed by the EDS elemental mapping (Figures. 4.1e-j). Fig. 2a shows the XRD patterns, on which the peaks at 18.8^o, 31.0^o, 36.5^o, 38.2^o, 44.4^o, 54.8^o, 58.3^o and 64.2^o are contributed to the (111), (220), (311), (222), (400), (422), (511) and (440) planes of $MnCo_2O_4$ with cubic spinel structure (JCPDS 23-1237) whereas the peaks corresponding to the NiFe-LDH are well matching with the typical pattern (JCPDS 38-0715) [23]. Herein, the observed shoulder peaks at 10° and 78° are the main characteristic peaks of NiFe-LDH, confirming the generation of NiFe-LDH on the $MnCo_2O_4$.

TEM image of the $MnCo_2O_4$@NiFe-LDH (Fig. 2b) clearly indicate a $MnCo_2O_4$ core with a NiFe-LDH shell structure. The lattice spacings of 0.29 and 0.23 nm in Figs. 2c-d are consistent with the (220) and (015) planes of $MnCo_2O_4$ and NiFe-LDH, respectively [24]. One can see that the coating of NiFe-LDH nanoflakes on the $MnCo_2O_4$ nanowire causes defects on the parent $MnCo_2O_4$, which could promote electrochemical activity due to the generation of active sites as well as oxygen vacancies with the modifying of the electronic structure. Herein, the strong chemical bonding between metal species and absorbed oxygen species on the oxygen vacancy sites could facilitate oxygen activation and partial dissociation of the adsorbed H_2O molecules [25].
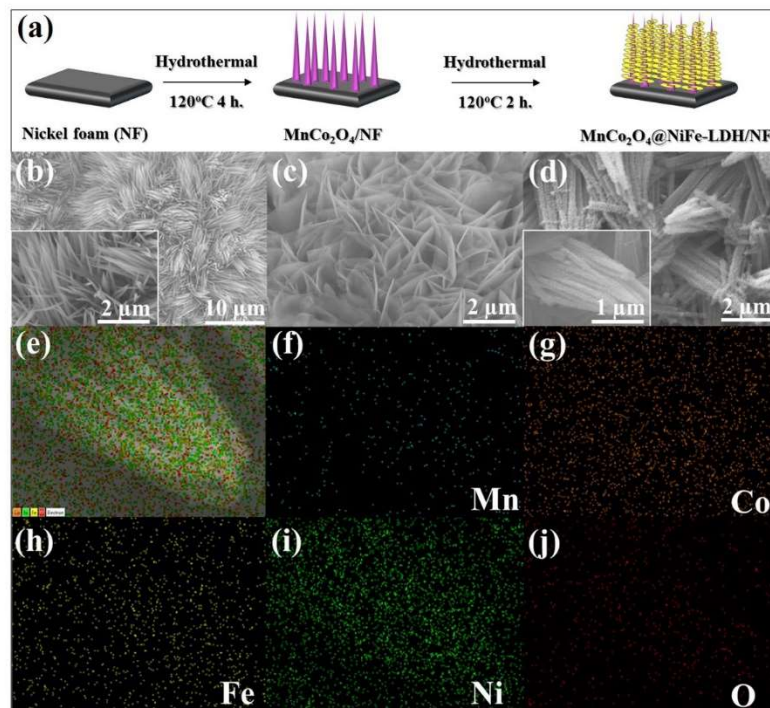
Figure 4.1 Fabrication and characterizations of MnCo$_2$O$_4$@NiFe-LDH electrocatalyst. (a) Schematic illustration of the fabrication route of MnCo$_2$O$_4$@NiFe-LDH/NF electrode; (b) SEM surface images of MnCo$_2$O$_4$/NF, (c) NiFe-LDH/NF, and (d) MnCo$_2$O$_4$@NiFe-LDH/NF; and (e-j) EDS elemental mappings of Mn, Co, Fe, Ni and O elements.
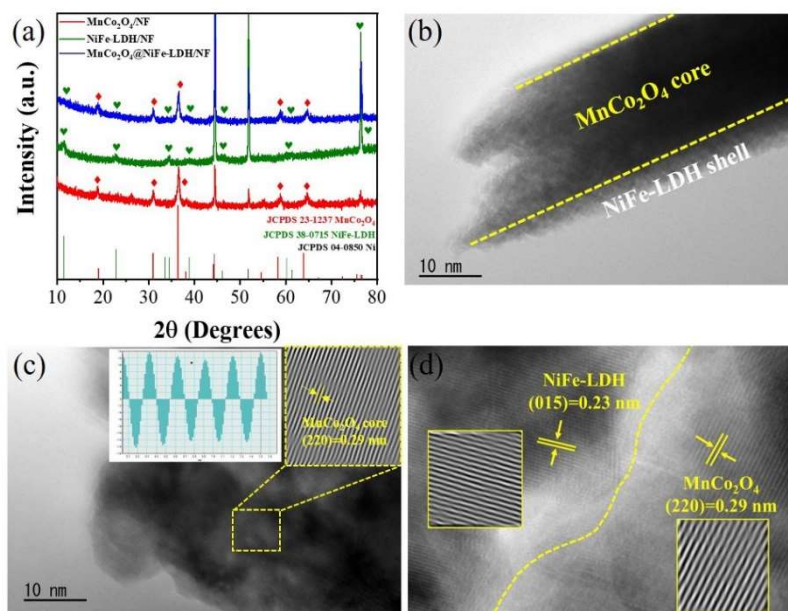
Figure 4.2 (a) XRD patterns and (b)TEM image with a low magnification of MnCo$_2$O$_4$@NiFe-LDH; (c-d) HR-TEM images of MnCo$_2$O$_4$@NiFe-LDH.

Figure 4.3 shows the XPS spectra of as-prepared $MnCo_2O_4$@NiFe-LDH electrocatalyst (Figure. 4.3a). The deconvolution peaks for the parent $MnCo_2O_4$ nanowires (Figure. 4.3b) confirm the presence of Mn^{2+} (641.7 and 653.0 eV) and Mn^{3+} (643.6 and 654.5 eV) species. The Co 2p spectra show two spin-orbital doublets at 780.4 and 795.5 eV, which are attributed to Co $2p_{3/2}$ and Co $2p_{1/2}$ of Co^{3+}, respectively [26]. While, the peaks at 782.5 and 797.6 eV are related to Co $2p_{3/2}$ and Co $2p_{1/2}$ of Co^{2+}, respectively (Figure 4.3c). As shown in Figure 4.3d, the binding energies of 855.7 and 873.3 eV are ascribed to Ni $2p_{3/2}$ and Ni $2p_{1/2}$, which correspond to Ni^{2+} of NiFe-LDH [27]. As summarized in Table 4.1, the relative ratio of Mn^{3+} was reduced relating the increases in that of Mn^{2+} after the growing of NiFe-LDH nanosheets on $MnCo_2O_4$ nanowire due to the chemical reduction process. Furthermore, the peak of Co 2p 3/2 shifts toward the lower binding energy direction, indicating that Fe incorporation changs the electronic structure of Co species in comparison to the pure $MnCo_2O_4$ (Figure 4.3c). Notably, the relative ratio of Co^{3+} species is increased after the growth of NiFe-LDH, implying an increase in OER active sites [29]. Most importantly, as indicated in Table 1, the $MnCo_2O_4$@NiFe-LDH has a higher Co^{3+}/Co^{2+} ratio (1.32) than $MnCo_2O_4$ (1.21), implying a higher OER activity for the promoting of water dissociation to active OH* intermediate species and the accelerating of OER kinetics [30]. While, a higher Ni^{3+}/Ni^{2+} on the $MnCo_2O_4$@NiFe-LDH (0.83) than that on the NiFe-LDH (0.79) could lower the overpotential of the electrode for OER because higher Ni^{3+} concentration on the electrocatalyst is beneficial for the OER with Fe^{3+}. However, as shown in Figures 4.3d-e, it should be noted that the oxidation states of Ni and Fe species are not noticeably changed comparing to those on the initial NiFe-LDH. According to the report by Steven *et al*.[31], only those surface Fe^{3+} species at the edge/defect sites could be responsible for the enhancement of OER activity relating to

Ni^{2+} species. Based on the above XPS analysis results, the incorporation of NiFe-LDH could effectively improve electrocatalytic activity of $MnCo_2O_4$. In addition, the O 1s spectrum (Figure 4.3f) can be fitted into three characteristic peaks at 530.0, 531.1 and 532.0 eV, which agree well with the binding energies of lattice oxygen (O_L), oxygen vacancies (O_v) and surface adsorbed water (O_{ads}), respectively [32]. Interestingly, the concentration of O vacancies (O_v) is increased after the incorporation of NiFe-LDH on $MnCo_2O_4$, implying that more O vacancies have been formed on the electrocatalyst. Herein, the positive shift of O 1s might be caused by the interaction between NiFe-LDH and $MnCo_2O_4$. Notably, the electronic configuration of $MnCo_2O_4$ is changed through the incorporation of NiFe-LDH, which could also significantly improve the OER activity due to the synergistic effect of Ni^{2+} and Fe^{3+} on the promoting of surface OER dynamics [19, 33]. In conclusion, the multiple oxidation states in $MnCo_2O_4$@NiFe-LDH composite electrocatalyst should have rich redox characteristics, resulting in higher activity.
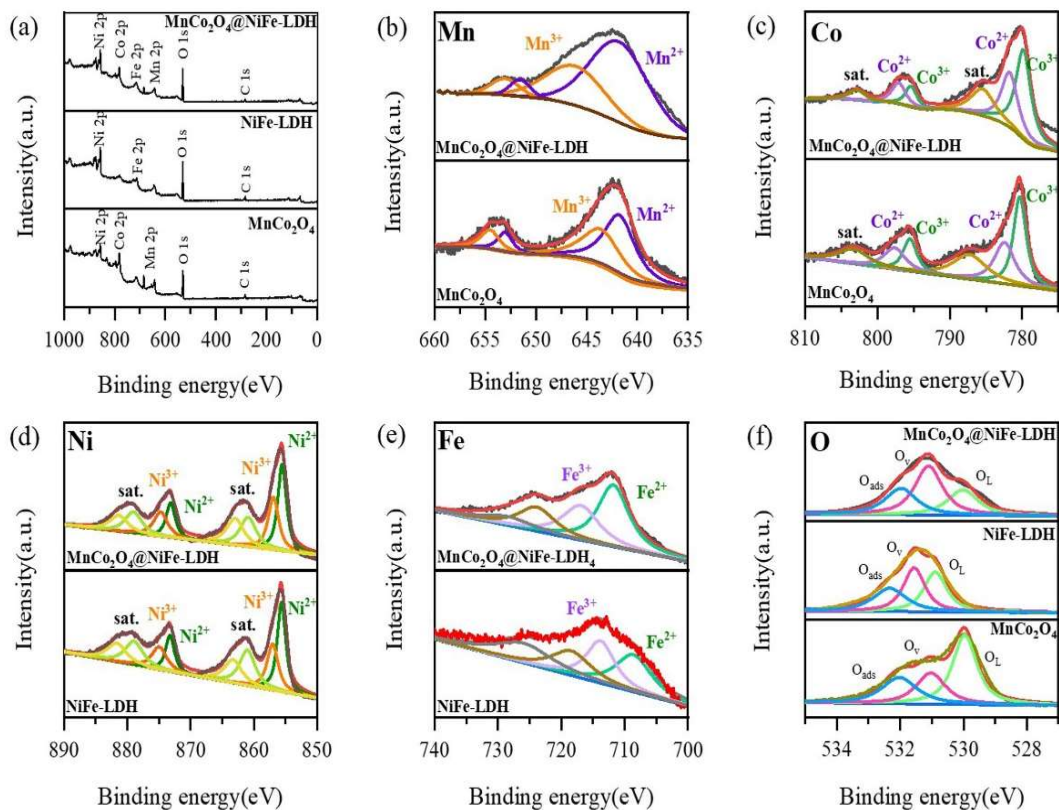
Figure 4.3 XPS spectra of the as-prepared electrocatalysts. (a) Survey spectra, (b) Mn 2p, (c) Co 2p, (d) Ni 2p, (e) Fe 2p and (f) O 1s.

Table 4.1 Elemental valence states of Mn, Co, Ni, Fe and O species of as-prepared electrocatalysts and their relative percentage ratios based on the deconvolution of peak areas.

Catalyst	Peak area ratio of Mn species (%)	Peak area ratio of Co species (%)	Peak area ratio of Ni species (%)	Peak area ratio of Fe species (%)	Relative ratio of O1s peak area (%)
	Mn^{2+}/Mn^{3+}	Co^{2+}/Co^{3+}	Ni^{2+}/Ni^{3+}	Fe^{2+}/Fe^{3+}	$O^{2-}/OH^-/H\text{-}O\text{-}H$
MnCo$_2$O$_4$/NF	55.4/44.6	45.2/54.8	-	-	47.8/25.9/26.3
NiFe-LDH/NF	-	-	55.8/44.2	50.3/49.7	34.6/36.2/29.2
MnCo$_2$O$_4$@NiFe-LDH@ /NF	64.6/35.4	43.0/57.0	54.5/45.5	62.0/38.0	26.1/45.8/28.1

Note: The ratios of elemental valence states were calculated by the deconvoluted peak areas from XPS spectra.

4.3.2 Electrochemical performance for OER

The electrocatalytic activity was measured in 1 M KOH containing 0.5 M NaCl solution as the simulated seawater electrolyte [21] and compared with the RuO_2 benchmark electrocatalyst for OER. To avoid the influence of the oxidation peak at the potential range of 1.3-1.4 V (*vs* RHE), a high current density at 100 mA/cm^2 is employed for the comparison of overpotentials in this study. As shown in Figure 4a, the $MnCo_2O_4$@NiFe-LDH composite electrocatalyst based electrode exhibits the superior performance with a lowest overpotential of 219 mV, which is lower than those of $MnCo_2O_4$/NF (395 mV), NiFe-LDH/NF (285 mV), and RuO_2/NF (362 mV) electrodes at the current density of 100 mA cm^{-2}. These results suggest that the modification of $MnCo_2O_4$ with NiFe-LDH greatly can improve the electrocatalytic activity for OER. The corresponding Tafel slopes were calculated based on the LSV curves (Fig. 4b). One can see that the Tafel slope of the $MnCo_2O_4$@NiFe-LDH/NF electrode is 45.4 mV dec^{-1}, which are lower than those of $MnCo_2O_4$/NF (115.8 mV dec^{-1}), NiFe-LDH/NF (56.4 mV dec^{-1}) and RuO_2/NF (75.4 mV dec^{-1}), indicating that the OER over the $MnCo_2O_4$@NiFe-LDH has a fastest kinetics, and more oxygen intermediates could be adsorbed on it. Generally, the OER on the catalysts in the alkaline solution could occur as follows [34, 35]:

$$M + OH^- \rightarrow MOH_{ads} + e^- \qquad \text{(Tafel slope = 120 mV dec}^{-1}\text{)} \qquad (1)$$

$$MOH_{ads} + OH^- \rightarrow MO_{ads} + e^- + H_2O \quad \text{(Tafel slope = 40 mV dec}^{-1}\text{)} \qquad (2)$$

$$2MO_{ads} \rightarrow 2M + O_2 \qquad \text{(Tafel slope = 15 mV dec}^{-1}\text{)} \qquad (3)$$

$$MOH_{ads} + OH^- \rightarrow MOOH + e^- \qquad (4)$$

$$MOOH + OH^- \rightarrow M + O_2 + H_2O + e^- \qquad (5)$$
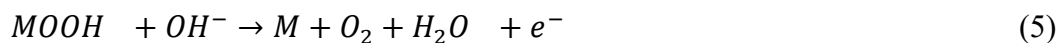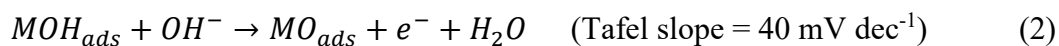
For the $MnCo_2O_4$@NiFe-LDH/NF electrode, since its Tafel slope was 45.4 mV dec^{-1}, the possible OER over it could follow Eqs. (1), (2), (4) and (5). That is, the reaction

starts with the adsorption of OH^- in alkaline solution on metal sites (M) on the surface of MnCo$_2$O$_4$@NiFe-LDH. Then, MOH_{ads} undergoes a proton coupling electron transfer process, transforming into MO_{ads}. The following O-O bond formation step allows MO_{ads} to react with another water molecule to form $MOOH$. Finally, $MOOH$ is oxidized, resulting in the release of O$_2$ and the recovery of an initial metal active site on the surface of electrode. Considering for the surface adsorption sites of electrode, the XPS analysis reveals that more O vacancy sites are generated on the MnCo$_2$O$_4$@NiFe-LDH, which could promote the separation of H atoms from MOH$_{ads}$ (Eq. 2) and the formation of FeOOH , thereby improving OER kinetics [36-38].

In order to reveal the charge transfer resistance (R_{ct}), the electrochemical impedance spectroscopy was further analysed in a frequency range of 100 kHz-0.1 Hz (Figure 4.4c). One can see that the charge transfer resistance (R_{ct}) of the MnCo$_2$O$_4$@NiFe-LDH/NF electrode (0.56 Ω) is lower than those of MnCo$_2$O$_4$/NF (0.65 Ω) and NiFe-LDH/NF (0.60 Ω). In addition, the MnCo$_2$O$_4$@NiFe-LDH/NF electrode also showed the smallest solution resistance (R_s) of 0.32 Ω, demonstrating the superior conductivity over other electrodes. Therefore, the MnCo$_2$O$_4$@NiFe-LDH/NF electrode had a lowest charge transfer resistance with a better electronic property, which led to a faster reaction rate.

The performances of the MnCo$_2$O$_4$@NiFe-LDH/NF electrode were further investigated at different operating temperatures. As shown in Figure 4.4d, when the operating temperature was increased from 10 to 80°C, the overpotential of the MnCo$_2$O$_4$@NiFe-LDH/NF electrode decreased to some extent (also see: Figure 4.5 and Table 4.2). Notably, this electrode can remain stable until the temperature was raised to 80 °C. In addition, this electrode worked stably at 80 °C for 14 h at a high current density of 100 mA cm^{-2} (Figure 4.6), suggesting that it is applicable even at a high operating temperature as well as a large current density.

A multi-step chronopotentiometry test was used to assess the mechanical robustness of this electrode, in which the current density was increased from 100 until 1,000 mA cm^{-2} with an increment of 100 mA cm^{-2} every 600 seconds. As shown in Figure 4.4e, the response potential remaines steady without any fluctuation in each step whereas the reverse process also exhibites the same initial potential response as the forward process, indicating superior mass transport properties and mechanical robustness over a wide range of current densities, which is very important for a practical process.

Additionally, the electrochemical active surface area (ECSA), which was calculated from the double layer capacitance (C$_{dl}$) measured using the cyclic voltammetry at various scan rates (Figure 4.4f). One can see that the MnCo$_2$O$_4$@NiFe-LDH electrocatalyst has a highest C$_{dl}$ value of 12.0 mF cm^{-2}, which is higher than those of MnCo$_2$O$_4$ (9.4 mF cm^{-2}) and NiFe-LDH (6.7 mF cm^{-2}), implying that this MnCo$_2$O$_4$@NiFe-LDH electrocatalyst has higher active surface area, allowing more active sites to be exposed for the facilitating the formation of more oxygen-containing intermediates during the OER process.
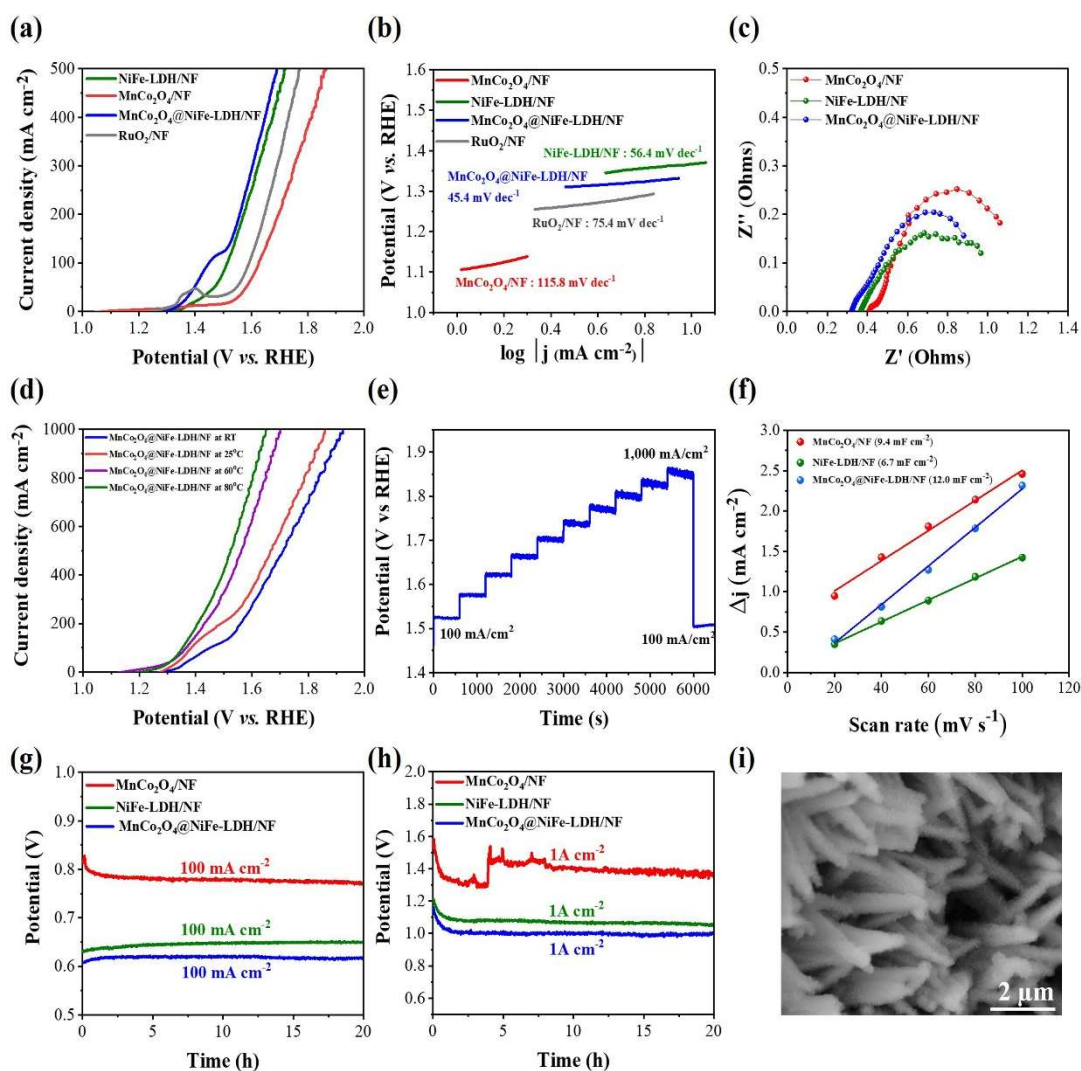
Figure 4.4 OER performance in simulated alkaline seawater solution (1 M KOH+0.5 M NaCl solution). (a) LSV curves; (b) Tafel plots; (c) EIS Nyquist plots; (d) LSV curves of the $MnCo_2O_4$@NiFe-LDH/NF electrode working at different temperatures; (e) Multiple-step chronopotentiometry test; (f) Capacitive current density as a function of scan rate; (g) Chronopotentiometry response at a constant current density of 100 mA cm^{-2}; (h) Chronopotentiometry response at an industrial-level constant current density of 1,000 mA cm^{-2} for 20 h; and (i) SEM surface image of the spent $MnCo_2O_4$@NiFe-LDH/NF electrode after the stability test.
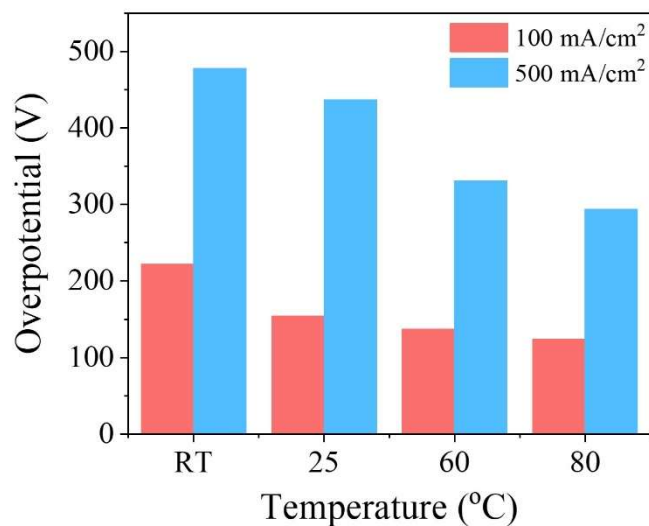
Figure 4.5 Overpotentials of OER over MnCo$_2$O$_4$@NiFe-LDH electrocatalyst at room temperature (~10 °C), 25 °C, 60 °C and 80 °C in alkaline simulated seawater solution.
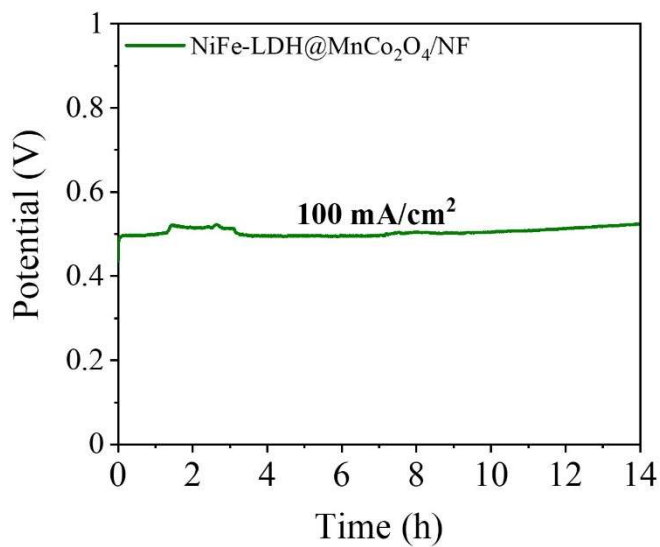
Figure 4.6 Durability test of MnCo$_2$O$_4$@NiFe-LDH/NF electrode for OER at 80 °C in alkaline simulated seawater solution for 14 h.

In addition, the stability was also evaluated for 20 hours using a chronopotentiometry test at a constant current density of 100 mA cm^{-2}. It is found that all the prepared electrodes maintain stable (Figure 4.4g). In order to examine the feasibility of such electrodes for an industrial process, the durability test at 1 A cm^{-2} were also investigated [39]. As shown in Figure 4h, the MnCo$_2$O$_4$@NiFe-LDH/NF electrode remains its initial potential in the alkaline simulated seawater at 1 A cm^{-2} for 20 h without degradation and potential drop. In comparison, the MnCo$_2$O$_4$/NF electrode showed unstable potential especially in the first 5-h testing (Figure 4.4h). Herein, it is found that the fluctuating potentials of the MnCo$_2$O$_4$/NF electrode were caused by the dissolution of MnCo$_2$O$_4$ in the solution containing NaCl (Figure 4.7). However, after the covering of NiFe-LDH nanosheets on the surface of MnCo$_2$O$_4$ nanowire, the catalyst degradation or MnCo$_2$O$_4$ dissolution problems can be well solved. It is considered that the NiFe-LDH layer on the MnCo$_2$O$_4$ can serve as a Cl$^-$ diffusion barrier to protect the MnCo$_2$O$_4$ nanowires from Cl$^-$ erosion while it allows the diffusion of other ions and O$_2$ transportation between electrode and electrolyte. Furthermore, after the stability test, the spent MnCo$_2$O$_4$@NiFe-LDH electrocatalyst retaines its initial morphology (Figure 4.4i), also implying its high mechanical robustness and tolerance in the harsh conditions.

Table 4.2 Electrocatalytic activity of the MnCo$_2$O$_4$@NiFe-LDH electrocataly at different temperatures in alkaline simulated seawater solution (1 M KOH+0.5 M NaCl)

Temperature (°C)	η_{100} (mV)	η_{500} (mV)
RT (~10 °C)	222	478
25 °C	154	437
60 °C	137	331
80 °C	124	294
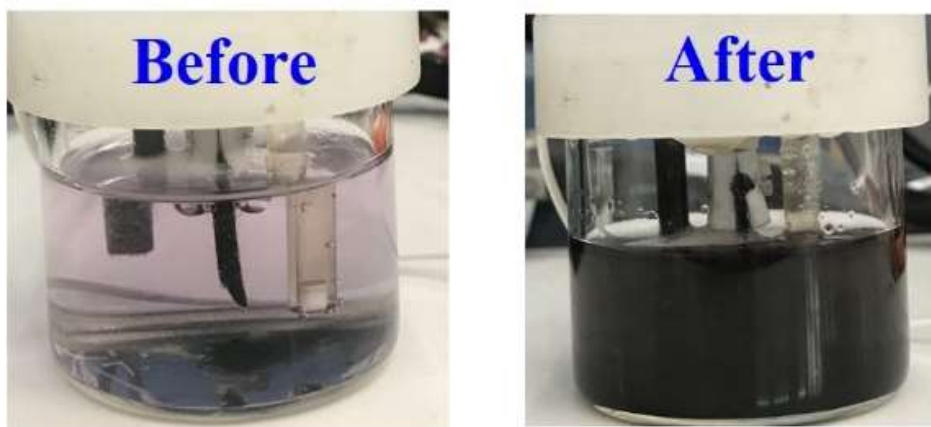
Figure 4.7 Digital photographs of MnCo$_2$O$_4$/NF electrode before and after the stability test for 20 h in alkaline simulated seawater solution (1 M KOH + 0.5 M NaCl).

4.3.3 Electrochemical performance for OER in alkaline natural seawater

The OER performance of MnCo$_2$O$_4$@NiFe-LDH/NF electrode in an alkaline natural seawater (1 M KOH + Natural seawater, pH = 13.7) was also investigated (Figure 4.8). As presented in Figure 4.8a, the MnCo$_2$O$_4$@NiFe-LDH/NF electrode shows low overpotentials of 245 and 578 mV at current densities of 100 and 500 mA cm^{-2}, respectively. Notably, as shown in Figure 4.8b, the overpotentials are slightly higher than those evaluated in the simulated seawater, which should be due to the existence of some impurities in the natural seawater, especially those insoluble precipitates such as Ca(OH)$_2$ and Mg(OH)$_2$ formed in the alkaline natural seawater condition could poison the electrode, resulting in the decrease in the performance for OER (Figure 4.8b) [40].

However, this electrode is still highly durable in the alkaline natural seawater more than 25 h at a relatively high current density of 100 mA cm^{-2} (Figure 4.8c). According to the theoretical calculations in the previous report [19], the higher Cl$^-$ adsorption energy on the surface of NiFe-LDH could make ClER more difficult to occur, which can simultaneously prevent inner MnCo$_2$O$_4$ corrosion from Cl$^-$ ions and improve anti-corrosion property, thereby enhancing the stability of such catalysts in the natural seawater based electrolytes.
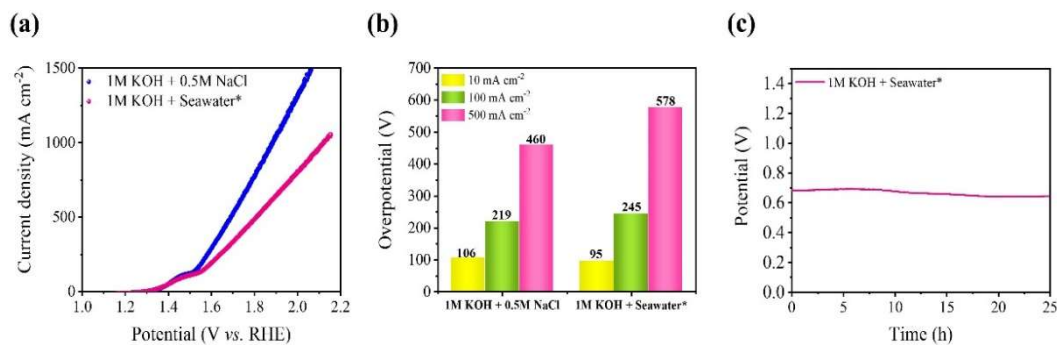
Figure 4.8 (a) OER performances of the MnCo$_2$O$_4$@NiFe-LDH/NF electrode in simulated seawater (1 M KOH+0.5 M NaCl) and alkaline natural seawater (1 M KOH + Natural seawater); (b) Comparison of overpotentials based on the results shown in Figure 4.8a; and (c) Chronopotentiometry response at a high current density of 100 mA cm^{-2} for 25 h in alkaline natural seawater solution.

The XPS analysis of the spent electrocatalysts after the stability test was further performed. From the high resolution XPS spectra in the Mn 2p regions (Figure 4.9a), the peaks relating to the Mn^{2+} species decreases whereas those corresponding to Mn^{3+} species increased after the OER reaction, implying partial oxidation of the electrocatalyst during the OER (also see: Table 4.3). While, the relative ratio of Co^{3+}/Ni^{3+} (Figures 4.9b-c) were slightly changed. In addition, the relative peak area of Fe^{3+} species increased, suggesting the formation of FeOOH active species during the OER process (Figure 4.9d). Moreover, the characteristic peaks of O 1s spectra of the spent catalysts in both cases corresponding to the lattice oxygen (Figure 4.9e) shift to higher binding energy, indicating the oxidation of lattice oxygen (O$_L$) (Table 4.3). These surface lattice sites can be exposed to adsorb the intermediates, resulting in lower kinetic barriers, which is better for OER activity [41].

Similar phenomena were also reported by Huang *et al.*, in which they implied that the optimal activity could be tuned via a barrier symmetry regulation between O-H bond cleavage and OOH* formation on the lattice oxygen sites, which can improve the OER

performance [42]. While, as stated above, the Mn^{3+}, Co^{3+}, Ni^{3+}, and Fe^{3+} with higher oxidation states could also play an important role in maintaining the excellent durability in the alkaline natural seawater solution. Moreover, as indicated by Cheng *et al.* [43], chloride ions could act as a bridge ligand between Co and Fe by inserting into the interlayer of CoFe-LDH, which can stabilize the higher valence state of the Co element for retaining active sites for OER. In this study, for the NiFe-LDH, the similar function could also exist for the improving of OER in the alkaline natural seawater solution.

The SEM image (Figure 4.9f) also showes that the $MnCo_2O_4$ nanowire coated with NiFe-LDH nanosheet structure is well maintained after the stability test, indicating its mechanical stability in the alkaline natural seawater solution during the OER process.
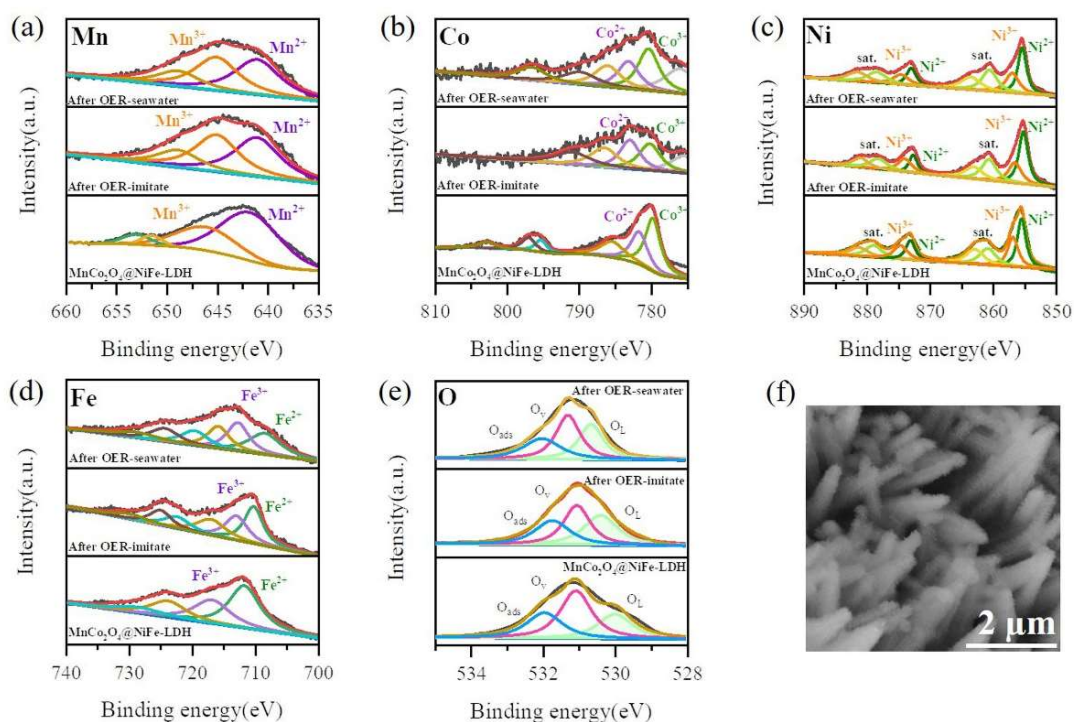
Figure 4.9 XPS spectra of the $MnCo_2O_4$@NiFe-LDH electrocatalyst before and after OER stability test in the alkaline simulated and natural seawater solutions: (a) Mn 2p, (b) Co 2p, (c) Ni 2p, (d) Fe 2p, (e) O 1s; and (f) SEM image after the long-term stability test in alkaline natural seawater solution.

Moreover, TEM images (Figures 4.10(a-f)) confirm that the lattice fringe of (015) plane of NiFe-LDH and (220) plane of $MnCo_2O_4$ are remained. Interestingly, the crystal lattice of Fe-OOH can be observed due to the surface reconstruction of NiFe-LDH during the OER process, indicating that NiFe-LDH lattice distortion can accelerate the formation of Fe-OOH active species (Figures 4.10(g-i)) [44]. Based on these results, the present core-shell structure with two synergetic electrocatalytic components can effectively endow the catalyst with high activity and stability, which is ranked the top-level in the developed OER electrocatalysts for seawater electrolysis (Table 4.4).
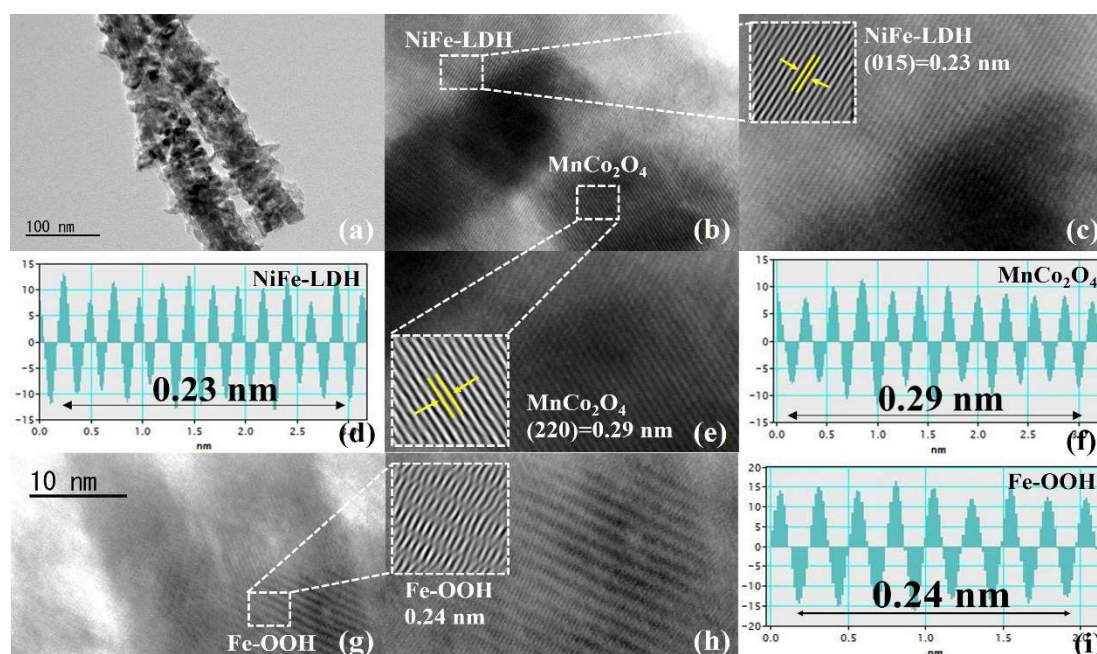
Figure 4.10 TEM images of $MnCo_2O_4$@NiFe-LDH after the stability test: (a-b) $MnCo_2O_4$@NiFe-LDH; (c) NiFe-LDH layer; (d) lattice distance of NiFe-LDH layer; (e) $MnCo_2O_4$ layer; (f) lattice distance of $MnCo_2O_4$; (g-h) Fe-OOH; and (i) Lattice distance of Fe-OOH.

Table 4.3 Elemental valence states of Mn, Co, Ni, Fe and O species of spent MnCo$_2$O$_4$@NiFe-LDH electrocatalyst after the stability test comparing with the fresh one and their relative percentage ratios based on the deconvolution of peak areas.

Catalyst	Peak area ratio of Mn species (%)	Peak area ratio of Co species (%)	Peak area ratio of Ni species (%)	Peak area ratio of Fe species (%)	Relative ratio of O1s peak area (%)
	Mn^{2+}/Mn^{3+}	Co^{2+}/Co^{3+}	Ni^{2+}/Ni^{3+}	Fe^{2+}/Fe^{3+}	O^{2-}/OH^{-}/H-O-H
MnCo$_2$O$_4$@NiFe-LDH - initial	64.6/35.4	43.0/57.0	54.5/45.5	62.0/38.0	26.1/45.8/28.1
MnCo$_2$O$_4$@NiFe-LDH - after the stability test in alkaline simulated seawater solution	57.0/43.0	48.2/51.8	58.7/41.3	46.5/53.5	34.9/35.9/29.2
MnCo$_2$O$_4$@NiFe-LDH - after the stability test in alkaline natural seawater solution	52.3/47.7	41.5/58.5	56.9/43.1	47.9/52.1	31.6/39.6/28.8

Moreover, the HER performance of MnCo$_2$O$_4$@NiFe-LDH was also investigated. As shown in Figure 4.11, MnCo$_2$O$_4$@NiFe-LDH exhibits the lowest overpotential as 90 mV at the standard current density of 10 mA cm^{-2}. Finally, overall seawater electrolysis was performed by using MnCo$_2$O$_4$@NiFe-LDH as the bifunctional electrocatalyst for both anode and cathode (MnCo$_2$O$_4$@NiFe-LDH (-) ll MnCo$_2$O$_4$@NiFe-LDH (+), which requires low cell voltages of 1.54 and 1.56 V at the standard current density of 10 mA cm^{-2} in the alkaline simulated and natural seawater solutions, respectively. Furthermore, its initial potentials can be maintained for 100 h at

a relatively high current density of 100 mA cm^{-2} without degradation or catalyst corrosion (Figures 4.12(a-c)). It confirms that such an electrocatalyst can also serve as the bifunctional electrocatalyst for seawater electrolysis with high stability against chloride corrosion.
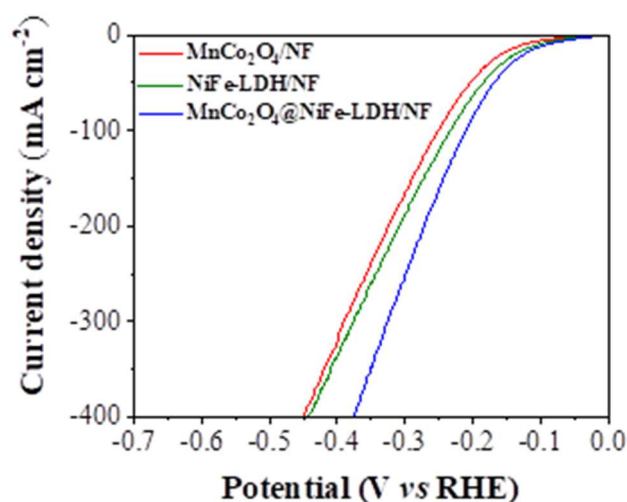
Figure 4.11 LSV curves for HER over MnCo$_2$O$_4$/NF, NiFe-LDH and MnCo$_2$O$_4$@NiFe-LDH/NF electrocatalyst at room temperature in alkaline simulated seawater solution.
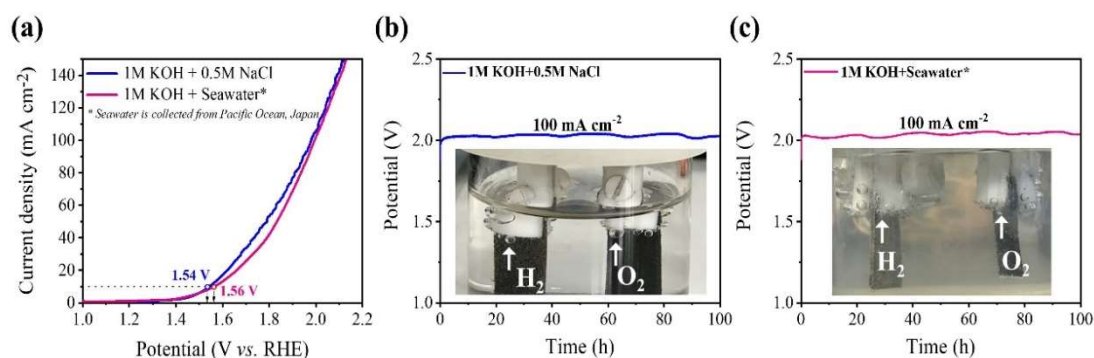
Figure 4.12 (a) LSV curves of MnCo$_2$O$_4$@NiFe-LDH (-) ll MnCo$_2$O$_4$@NiFe-LDH (+) cell in the alkaline simulated and natural seawater solutions; (b) Chronopotentiometry test of MnCo$_2$O$_4$@NiFe-LDH (-) ll MnCo$_2$O$_4$@NiFe-LDH (+) cell at a high current density of 100 mA cm^{-2} in the alkaline simulated seawater solution (1 M KOH+0.5 M NaCl) and (c) in the alkaline natural seawater solution (1 M KOH + Natural seawater).

4.4 Conclusions

In summary, a rational design of $MnCo_2O_4$@NiFe-LDH electrocatalyst with a core@shell structure was successfully performed and fabricated on NF substrate via a facile two-step hydrothermal method. The obtained electrode exhibited excellent electrocatalytic performance for OER with low overpotentials as 219 and 245 mV at a relatively high current density of 100 mA cm^{-2} in the alkaline simulated and natural seawater solutions, respectively. Moreover, the $MnCo_2O_4$@NiFe-LDH/NF electrode exhibited high stability at different seawater conditions without corrosion even at an industrial scale level (> 500 mA cm^{-2}). Besides, this electrocatalyst can also serve as the bifunctional electrocatalyst for the seawater electrolysis with high durability against chloride corrosion for over 100 h. The outstanding activity and durability of this electrode should be attributed to that (i) the NiFe-LDH shell on the $MnCo_2O_4$ core can enhance electron transfer and act as a protective layer against Cl$^-$ erosion ; (ii) the $MnCo_2O_4$ core can provide rich active sites for OER with the assistance of the NiFe-LDH shell; (iii) the incorporation of NiFe-LDH nanosheets on the $MnCo_2O_4$ core can effectively increase the active surface area, enhance the charge transfer property of $MnCo_2O_4$ nanowires, and maintain higher valence states of the Mn, Co, Ni and Fe species in the electrocatalyst, which is beneficial for the retaining of rich active sites for long-term OER; and (iv) the generation of Fe-OOH on the lattice oxygen sites of NiFe-LDH during the OER process can effectively promote water dissociation and reduce the kinetics barrier, thereby improving OER kinetics. Therefore, the synergistic effect between $MnCo_2O_4$ and NiFe-LDH played a crucial role for maintaining the catalytic activity and stability against chloride corrosion in alkaline natural seawater solution since Cl$^-$ could be inserted into the interlayer of NiFe-LDH, which can stabilize the higher valence state of the Mn^{3+}, Co^{3+}, Ni^{3+}, and Fe^{3+} elements for retaining active sites

for OER and preventing the catalyst corrosion. This pioneer electrode could be a promising candidate for industrial-scale alkaline natural seawater electrolysis.

Table 4.4 Comparison of OER performance of the present electrocatalyst with those recently reported ones for seawater electrolysis

Electrocatalyst	Electrolyte	Overpotential at 100 mA cm^{-2} (mV)	Reference
MnCo$_2$O$_4$@NiFe-LDH	1 M KOH+0.5 M NaCl	219	This work
	1 M KOH + Natural seawater	245	
NiFeN @NiMoN	1 M KOH+0.5 M NaCl	286	[37]
NiFe-CuCo-LDH	6M KOH seawater	259	[14]
NiFe-NiS$_x$-Ni activated	1 M KOH+0.5 M NaCl	~300 (at 400 mA/cm^2)	[16]
NiFe LDH/C	0.1 M KOH+0.5 M NaCl	359 (at 10 mA/cm^2)	[38]
FTO/NiO	0.1 M KOH+0.5 M NaCl	340	[39]
S-NiMoO$_4$@NiFe-LDH/NF	1 M KOH+0.5 M NaCl	273	[40]
	1 M KOH + seawater	315	

References

[1] J. Wang, Y. Gao, H. Kong, J. Kim, S. Choi, F. Ciucci, Y. Hao, S. Yang, Z. Shao, J. Lim, Non-precious-metal catalysts for alkaline water electrolysis: operando characterizations, theoretical calculations, and recent advances, Chem Soc Rev. 49 (2020) 9154-9196.

[2] P. Gayen, S. Saha, V. Ramani, Selective Seawater Splitting Using Pyrochlore Electrocatalyst, ACS Appl. Energy Mater. 3 (2020) 3978-3983.

[3] L. Li, G. Zhang, B. Wang, D. Zhu, D. Liu, Y. Liu, S. Yang, Fe_2O_3/NiO Interface for the Electrochemical Oxygen Evolution in Seawater and Domestic Sewage, ACS Appl. Mater. Interfaces 13 (2021) 37152-37161.

[4] S. Shit, S. Chhetri, W. Jang, N.C. Murmu, H. Koo, P. Samanta, T. Kuila, Cobalt Sulfide/Nickel Sulfide Heterostructure Directly Grown on Nickel Foam: An Efficient and Durable Electrocatalyst for Overall Water Splitting Application, ACS Appl. Mater. Interfaces 10 (2018) 27712-27722.

[5] L. Bigiani, D. Barreca, A. Gasparotto, T. Andreu, J. Verbeeck, C. Sada, E. Modin, O.I. Lebedev, J.R. Morante, C. Maccato, Selective anodes for seawater splitting via functionalization of manganese oxides by a plasma-assisted process, Appl. Catal. B: Environ. 284 (2021) 119684.

[6] F. Dionigi, T. Reier, Z. Pawolek, M. Gliech, P. Strasser, Design Criteria, Operating Conditions, and Nickel–Iron Hydroxide Catalyst Materials for Selective Seawater Electrolysis, ChemSusChem, 9 (2016) 962-972.

[7] M. Yu, J. Li, F. Liu, J. Liu, W. Xu, H. Hu, X. Chen, W. Wang, F. Cheng, Anionic formulation of electrolyte additive towards stable electrocatalytic oxygen evolution in seawater splitting, J. Energy Chem. 72 (2022) 361-369.

178

[8] F.M. Sapountzi, J.M. Gracia, C.J. Weststrate, H.O.A. Fredriksson, J.W. Niemantsverdriet, Electrocatalysts for the generation of hydrogen, oxygen and synthesis gas, Prog. Energy Combust. Sci. 58 (2017) 1-35.

[9] A. Amirzhanova, N. Akmanşen, I. Karakaya, Ö. Dag, Mesoporous $MnCo_2O_4$, $NiCo_2O_4$, and $ZnCo_2O_4$ Thin-Film Electrodes as Electrocatalysts for the Oxygen Evolution Reaction in Alkaline Solutions, ACS Appl. Energy Mater. 4 (2021) 2769-2785.

[10] G. Wei, J. He, W. Zhang, X. Zhao, S. Qiu, C. An, Rational Design of Co(II) Dominant and Oxygen Vacancy Defective $CuCo_2O_4$@CQDs Hollow Spheres for Enhanced Overall Water Splitting and Supercapacitor Performance, Inorg. Chem. 57 (2018) 7380-7389.

[11] Q. Ouyang, Z. Lei, Q. Li, M. Li, C. Yang, A self-supported $NiCo_2O_4/Cu_xO$ nanoforest with electronically modulated interfaces as an efficient electrocatalyst for overall water splitting, J. Mater. Chem. A 9 (2021) 14466-14476.

[12] B.J. Rani, R. Yuvakkumar, G. Ravi, S.I. Hong, D. Velauthapillai, R.K. Guduru, M. Thambidurai, C. Dang, W.A. Al-onazi, A.M. Al-Mohaimeed, Electrochemical water splitting exploration of $MnCo_2O_4$, $NiCo_2O_4$ cobaltites, New J. Chem. 44 (2020) 17679-17692.

[13] A. Rebekah, E. Ashok Kumar, C. Viswanathan, N. Ponpandian, Effect of cation substitution in $MnCo_2O_4$ spinel anchored over rGO for enhancing the electrocatalytic activity towards oxygen evolution reaction (OER), Int. J. Hydrog. Energy 45 (2020) 6391-6403.

[14] H. Yang, M. Zhu, X. Guo, C. Yan, S. Lin, Anchoring $MnCo_2O_4$ Nanorods from Bimetal-Organic Framework on rGO for High-Performance Oxygen Evolution and Reduction Reaction, ACS Omega 4 (2019) 22325-22331.

179

[15] K. Zeng, W. Li, Y. Zhou, Z. Sun, C. Lu, J. Yan, J.-H. Choi, R. Yang, Multilayer hollow $MnCo_2O_4$ microsphere with oxygen vacancies as efficient electrocatalyst for oxygen evolution reaction, Chem. Eng. J. 421 (2021) 127831.

[16] A.N. Naveen, S. Selladurai, A 1-D/2-D hybrid nanostructured manganese cobaltite–graphene nanocomposite for electrochemical energy storage, RSC Adv. 5 (2015) 65139-65152.

[17] J.E. Bennett, Electrodes for generation of hydrogen and oxygen from seawater, Int. J. Hydrog. Energy 5 (1980) 401-408.

[18] J.G. Vos, T.A. Wezendonk, A.W. Jeremiasse, M.T.M. Koper, MnO_x/IrO_x as Selective Oxygen Evolution Electrocatalyst in Acidic Chloride Solution, J. Am. Chem. Soc. 140 (2018) 10270-10281.

[19] L. Yu, J. Xiao, C. Huang, J. Zhou, M. Qiu, Y. Yu, Z. Ren, C.W. Chu, J.C. Yu, High-performance seawater oxidation by a homogeneous multimetallic layered double hydroxide electrocatalyst, Proc. Natl. Acad. Sci. U. S. A. 119 (2022) 2202382119.

[20] L. Peng, N. Yang, Y. Yang, Q. Wang, X. Xie, D. Sun-Waterhouse, L. Shang, T. Zhang, G.I.N. Waterhouse, Atomic Cation-Vacancy Engineering of NiFe-Layered Double Hydroxides for Improved Activity and Stability towards the Oxygen Evolution Reaction, Angew Chem Int Ed Engl 60 (2021) 24612-24619.

[21] Y. Kuang, M.J. Kenney, Y. Meng, W.H. Hung, Y. Liu, J.E. Huang, R. Prasanna, P. Li, Y. Li, L. Wang, M.C. Lin, M.D. McGehee, X. Sun, H. Dai, Solar-driven, highly sustained splitting of seawater into hydrogen and oxygen fuels, Proc. Natl. Acad. Sci. U. S. A. 116 (2019) 6624-6629.

[22] Z. Yan, H. Sun, X. Chen, H. Liu, Y. Zhao, H. Li, W. Xie, F. Cheng, J. Chen, Anion insertion enhanced electrodeposition of robust metal hydroxide/oxide electrodes for oxygen evolution, Nat. Commun. 9 (2018) 2373.

[23] A. Ashok, A. Kumar, J. Ponraj, S.A. Mansour, Preparation of Mesoporous/Microporous $MnCo_2O_4$ and Nanocubic $MnCr_2O_4$ Using a Single Step Solution Combustion Synthesis for Bifunction Oxygen Electrocatalysis, J. Electrochem. Soc. 167 (2020) 054507.

[24] X.-P. Li, W.-K. Han, K. Xiao, T. Ouyang, N. Li, F. Peng, Z.-Q. Liu, Enhancing hydrogen evolution reaction through modulating electronic structure of self-supported NiFe LDH, Catal. Sci. Technol. 10 (2020) 4184-4190.

[25] T.Y. Ma, Y. Zheng, S. Dai, M. Jaroniec, S.Z. Qiao, Mesoporous $MnCo_2O_4$with abundant oxygen vacancy defects as high-performance oxygen reduction catalysts, J. Mater. Chem. A 2 (2014) 8676-8682.

[26] X. Zheng, Y. Ye, Q. Yang, B. Geng, X. Zhang, Hierarchical structures composed of $MnCo_2O_4$@MnO_2 core–shell nanowire arrays with enhanced supercapacitor properties, Dalton Trans. 45 (2016) 572-578.

[27] B. Lin, H. le, F. Xu, S. Mu, NiFe LDH/CuO nanosheet: a sheet-on-sheet strategy to boost the active site density towards oxygen evolution reaction, RSC Adv. 10 (2020) 27424-27427.

[28] Z. Cai, X. Bu, P. Wang, W. Su, R. Wei, J.C. Ho, J. Yang, X. Wang, Simple and cost effective fabrication of 3D porous core–shell Ni nanochains@NiFe layered double hydroxide nanosheet bifunctional electrocatalysts for overall water splitting, J. Mater. Chem. A 7 (2019) 21722-21729.

[29] G. Guo, D. Zhong, T. Zhao, G. Liu, J. Li, Q. Zhao, NiCo-BDC derived Co^{3+} enriched $NiCo_xO_y$/NF nanosheets for oxygen evolution reaction, Int. J. Hydrog. Energy 47 (2022) 23094-23105.

[30] R. Chen, Y. Tan, Z. Zhang, Z. Lei, W. Wu, N. Cheng, S. Mu, Hydrazine Hydrate Induced Two-Dimensional Porous Co^{3+} Enriched Co_3O_4 Nanosheets for Enhanced Water Oxidation Catalysis, ACS Sustain. Chem. Eng. 8 (2020) 9813-9821.

[31] M.B. Stevens, C.D.M. Trang, L.J. Enman, J. Deng, S.W. Boettcher, Reactive Fe-Sites in Ni/Fe (Oxy)hydroxide Are Responsible for Exceptional Oxygen Electrocatalysis Activity, J. Am. Chem. Soc. 139 (2017) 11361-11364.

[32] C. Hou, Z. Cui, S. Zhang, W. Yang, H. Gao, X. Luo, Rapid large-scale synthesis of ultrathin NiFe-layered double hydroxide nanosheets with tunable structures as robust oxygen evolution electrocatalysts, RSC Adv. 11 (2021) 37624-37630.

[33] Y. Lin, A. Qin, W. Fang, R. Xv, L. Fu, Synergistic Effect of Ni^{2+} and Fe^{3+} of Bimetallic Oxyhydroxide NiFeOOH as OER Cocatalyst for Fe_2O_3 Photoanode with Enhanced Photoelectrochemical Water Splitting, Energy & Fuels 36 (2022) 2890-2900.

[34] Y. Yang, J. Yang, P. Liang, Z. Zhang, Z. Li, Z. Hu, V_2O_3/FeOOH with rich heterogeneous interfaces on Ni foam for efficient oxygen evolution reaction, Catal. Commun. 162 (2022) 106393.

[35] M. Plevová, J. Hnát, K. Bouzek, Electrocatalysts for the oxygen evolution reaction in alkaline and neutral media. A comparative review, J. Power Sources 507 (2021) 230072.

[36] J. Hu, S. Li, J. Chu, S. Niu, J. Wang, Y. Du, Z. Li, X. Han, P. Xu, Understanding the Phase-Induced Electrocatalytic Oxygen Evolution Reaction Activity on FeOOH Nanostructures, ACS Catal. 9 (2019) 10705-10711.

[37] L. Gao, X. Cui, C.D. Sewell, J. Li, Z. Lin, Recent advances in activating surface reconstruction for the high-efficiency oxygen evolution reaction, Chem Soc Rev 50 (2021) 8428-8469.

[38] J. Feng, M. Chen, P. Zhou, D. Liu, Y.-Y. Chen, B. He, H. Bai, D. Liu, W.F. Ip, S.

Chen, D. Liu, W. Feng, J. Ni, H. Pan, Reconstruction optimization of distorted FeOOH/Ni hydroxide for enhanced oxygen evolution reaction, Mater. Today Energy 27 (2022) 101005.

[39] Y. Luo, Z. Zhang, M. Chhowalla, B. Liu, Recent Advances in Design of Electrocatalysts for High-Current-Density Water Splitting, Adv. Mater. (2021) 2108133.

[40] M. Ning, L. Wu, F. Zhang, D. Wang, S. Song, T. Tong, J. Bao, S. Chen, L. Yu, Z. Ren, One-step spontaneous growth of NiFe layered double hydroxide at room temperature for seawater oxygen evolution, Mater. Today Phys. 19 (2021) 100419.

[41] X. Du, H. Su, X. Zhang, 3D $MnCo_2O_4$@CoS nanoarrays with different morphologies as an electrocatalyst for oxygen evolution reaction, Int. J. Hydrog. Energy 44 (2019) 21637-21650.

[42] Z.F. Huang, S. Xi, J. Song, S. Dou, X. Li, Y. Du, C. Diao, Z.J. Xu, X. Wang, Tuning of lattice oxygen reactivity and scaling relation to construct better oxygen evolution electrocatalyst, Nat Commun. 12 (2021) 3992.

[43] F. Cheng, X. Feng, X. Chen, W. Lin, J. Rong, W. Yang, Synergistic action of Co-Fe layered double hydroxide electrocatalyst and multiple ions of sea salt for efficient seawater oxidation at near-neutral pH, Electrochim. Acta 251 (2017) 336-343.

[44] J. Feng, M. Chen, P. Zhou, D. Liu, Y.-Y. Chen, B. He, H. Bai, D. Liu, W.F. Ip, S. Chen, D. Liu, W. Feng, J. Ni, H. Pan, Reconstruction optimization of distorted FeOOH/Ni hydroxide for enhanced oxygen evolution reaction, Mater. Today Energy 27 (2022)101005.

CHAPTER 5 Conclusions and Prospects

5.1 Conclusions

Water splitting is a clean and secure process for producing hydrogen by decomposing water using various power sources such as electrical (current), thermal (heat) and light (electromagnetic radiation). In this study, electricity is used to cleave H-O-H bonds, resulting in the production of hydrogen and oxygen via the HER and OER. The major challenge to the implementation of electrochemical water splitting applications is the energy-efficiency loss with high overpotential during HER, OER and competitive reaction between OER and ClER, as well as economic inefficiencies including high-cost nobel metal catalysts used and complicated processes. Additionally, the most important criteria for scaling up the application of electrocatalysts from laboratory scale to industrial scale is related to the catalytic activity, stability, suitability for a wide range of current sensities and high corrosion resistance. Therefore, minimizing the production cost but maximizing the performance by three different development strategies are used in this study, including the introduction of O vacancies on transition metal oxides by combining nanoengineering and defect engineering, sulfurized transition metal hydroxides, and nanostructured engineering for spinel oxide modification, to improve intrinsic activity, electrocatalytic activity and stability, especially at high and harsh conditions comparable to industrial scale. The key performances of all electrocatalysts are summarized as follows ;

(1) The obtained $CuVO_x$@NiO/CP composite electrode is successfully synthesized via a facile hydrothermal process combined with a calcination step. This electrode exhibits a remarkable HER activity in alkaline solution with an overpotential as low as 74 mV at 10 mA cm^{-2}, which also shows excellent stability for 30 hours and a fast

kinetic reaction with a Tafel slope of 60.8 mVdec^{-1}. Moreover, it can work stably in a wide range of current densities (10-300 mA cm^{-2}). It is found that real active species are generated during HER due to CuVO$_x$ is reduced to VO$_x$-Cu$_2$O/Cu with increased O vacancies. Besides, the NiO shell also improved a number of active sites as well as super-hydrophilic surface, which effectively facilitate the H$_2$O adsorption and decomposition to H$_{ads}$ intermediates, suggesting accelerate HER performace.

 (2) In order to reduce catalyst preparation cost and time and simultaneously decrease interfacial resistance between the electrocatalyst and the substrate, increase electrical conductivity, and prevent electrocatalyst peeling off from the substrate during the long-term operation at a high current density in seawater solution, a simple corrosion engineering process followed by a fast and mild sulfurization step is used for *in-situ* growing of FeNiS$_x$/NiFe(OH)$_x$ composite on nickel foam (NF) substrate. The obtained electrode has an outstanding electrocatalytic activity with a low overpotential of 277 and 270 mV for the OER in alkaline and alkaline simulated seawater at 100 mA cm^{-2} , respectively. Furthermore, it can operate continuously for 100 hours at a current density of 1 A cm^{-2}, which is comparable to industrial scale. Furthermore, this catalyst was used for both anode and cathode in a two-electrode system for overall seawater electrolysis, and it was capable of sustaining stable up to 1 A/cm^2 in the imitate seawater solution with a cell voltage of 2.81 V, achieving a high hydrogen productivity without catalyst deterioration, while the faradaic efficiencies of hydrogen and oxygen production were as high as 95% and 94% in the electrolysis of alkaline simulated seawater. In this study, incorporated sulfur species could function as a protective coating layer for the blockage Cl$^-$ from the seawater electrolyte, preventing catalyst degradation over the long-term operation under a high current density condition by intercalated it into the NiFe(OH)$_x$ layer instead of Cl$^-$ and DFT calculations proves that S substitution on the O site

(NiFe(OH)$_x$) can effectively lower energy barrier on FeNiS$_x$/NiFe(OH)$_x$ makes *OH to *O transition step more kinetically promoted, implying improve OER activity. Besides, DFT calculations reveal that Cl$^-$ has a high adsorption energy on the non-active Ni sites, implying that more free available Fe sites can be provided for OER, thereby resulting in a high OER selectivity. Therefore, this economical electrode could be a promising candidate for seawater electrolysis even in an industrial-scale application.

(3) A simple two-step hydrothermal method at low temperature is used for synthesized MnCo$_2$O$_4$ core @NiFe-LDH shell structure. This electrode exhibits low overpotentials of 219 and 245 mV at a high current density of 100 mA cm^{-2} in alkaline simulated and natural seawaters (collected from Pacific ocean, Aomori, Japan), respectively. It is found that the NiFe-LDH function as Cl$^-$ protective layer against catalyst corrosion via ClER and active sites for OER, while MnCo$_2$O$_4$ nanowires provides a high active surface area and stable core structure. This electrode not only works consistently at room temperature, but also when the temperature is raised to 80 ^{o}C for 14 hours at a high current density of 100 mA cm^{-2}, implying high thermal tolerance in a harsh condition. Moreover, when MnCo$_2$O$_4$ @NiFe-LDH is utilized as the bifunctional electrocatalyst for overall seawater electrolysis. It shows a low cell voltages of 1.54 and 1.56V at the standard current density of 10 mA cm^{-2} in the alkaline simulated and natural seawater solutions, respectively, and highly stable for 100 hours at a high current density of 100 mA cm^{-2} without degradation or catalyst corrosion. In conclusion, the incorporation of NiFe-LDH nanosheets on the MnCo$_2$O$_4$ core can effectively increase the active surface area, enhance the charge transfer property of MnCo$_2$O$_4$ nanowires, and maintain higher valence states of the Mn, Co, Ni and Fe species in the electrocatalyst, which is beneficial for retaining rich active sites for long-term OER. These outstanding results provide a promosing candidate for sustain seawater splitting.

5.2 Prospects

Even though significant efforts have been performed for the developing of the electrocatalysts for water splitting application, most of developed electrocatalysts were rarely used in an industrial scale due to limitations such as durability and catalyst dissolution. Moreover, some parameters require further investigation in order to prove the reaction mechanism.

The following points should be considered for further development of electrocatalysts in order to step up the water electrolysis system to a practical scale;

(1) Alternative corrosion resistance substrates

Currently, carbon paper, nickel foam and copper foam are commonly used as a substrate for water electrolysis application. However, the durability in a wide range of pH values are still unsatisfied. Therefore, seeking for the alternative substrates such as Ti foil, FTO and Iron foam or surface modification of substrate are suggested.

(2) Seeking for novel electrocatalysts with higher performance and low cost

Novel electrocatalysts with higher performance and low cost are still desired. For example, those carbon-based electrocatalysts like MXene and ZIF-67, which are commonly used in supercapacitors and lithium-ion batteries (LIBs), could be also applied in water electrolysis because they can work stably in acid and neutral conditions. While, those developed electrocatalysts such as transition metal oxides/hydroxides, transition metal sulfide, and transition metal phosphide could be further modified so that they can be more suitable for HER/OER in harsh conditions, especially for seawater electrolysis.

(3) More efficient electrocatalysts for seawater electrolysis

How to improve the selectivity and erosion resistance of electrocatalysts for seawater electrolysis is still full of challenges.The way for the detecting of Cl-related products in the seawater electrolysis should be considered for confirming the catalytic selectivity

the chlorine evolution (ClER)

(4) Energy saving hydrogen production system

To complete the life cycle of sustainable development by utilizing abundant natural resources, seawater electrolysis coupling with another system such as sulfion degradation, hybrid seawater electrolyzer with a solar cell, combined with zinc-air battery are interesting for new opportunities in sustainable hydrogen production.

CURRICULUM VITAE

Personal details

Name: NUTTHAPHAK KITIPHATPIBOON

Nationality: THAI

Date of birth: 26 February 1989

Email: nkitiphatpiboon@gmail.com

Educations

April, 2020-March, 2023	D.Eng. (Safety Science and Technology), Hirosaki University, Japan
May, 2012- January, 2015	M.Sc. (Fuel Technology), Chulalongkorn University, Thailand
June, 2007- April, 2011	B.Sc. (Biotechnology), Mahidol University, Thailand

Experiences

September, 2022	Presentation on the event that held by Hirosaki City : Talks about the world directly from internationals students, Hirosaki Museum of Contemporary Art.
August, 2015- August, 2019	Researcher at Kao Consumer Products (Southeast Asia) Co., Ltd.
November, 2013	Exchange student (Twin College Envoys Program: TWINCLE) at Chiba University.

Scholarship and Awards

1) 令和 4 年度 弘前大学学生表彰,令和 5 年 3 月 7 日.

2) 学生奨励賞, 令和 3 年度化学工学会秋田大会, 令和 3 年 7 月 1 日.

3) Japanese Government (Monbukagakusho：MEXT) Scholarship, Doctoral course, Hirosaki University, Japan (2019-2023).

List of Publications and Presentations

Publications

1. **Nutthaphak Kitiphatpiboon**, Meng Chen, Changrui Feng, Yifan Zhou, Changlin Liu, Zhongbao Feng, Qiang Zhao, Abuliti Abudula, Guoqing Guan, "Modification of spinel $MnCo_2O_4$ nanowire with NiFe-layered double hydroxide nanoflakes for stable seawater oxidation", Journal of Colloid and Interface Science, 632 (2023) 54-64.

2. **Nutthaphak Kitiphatpiboon**, Meng Chen, Xiumin Li, Changlin Liu, Shasha Li, Junli Wang, Shang Peng, Abuliti Abudula, Guoqing Guan, "Heterointerface engineering of Ni_3S_2@NiCo-LDH core-shell structure for efficient oxygen evolution reaction under intermittent conditions", Electrochimica Acta, 435 (2022) 141438.

3. **Nutthaphak Kitiphatpiboon**, Suchada Sirisomboonchai, Meng Chen, Shasha Li, Xiumin Li, J. Wang, Xiaogang Hao, Abuliti Abudula, Guoqing Guan, "Facile fabrication of O vacancy rich $CuVO_x$ nanobelt@NiO nanosheet array for hydrogen evolution reaction", Electrochimica Acta, 405 (2022) 139623.

4. Meng Chen, Qing Su, **Nutthaphak Kitiphatpiboon**, Juan Zhang, Changrui Feng, Shasha Li, Qiang Zhao, Abuliti Abudula, Yufei Ma and Guoqing Guan,

"Heterojunction engineering of Ni_3S_2/NiS nanowire for electrochemical hydrogen evolution," Fuel, 331 (2023), 125794.

5. Meng Chen, Jianbin Liu, **Nutthaphak Kitiphatpiboon**, Xiumin Li, Junli Wang, Xiaogang Hao, Abuliti Abudula, Yufei Ma and Guoqing Guan, "Zn-VO_x-Co nanosheets with amorphous/crystalline heterostructure for highly efficient hydrogen evolution reaction", Chemical Engineering Journal, 43 (2022) 134329.

6. Suchada Sirisomboonchai, **Nutthaphak Kitiphatpiboon**, Meng Chen, Shasha Li, Xiumin Li, Suwadee Kongparakul, Chanatip Samart, Lei Zhang, Abuliti Abudula and Guoqing Guan, "Multi-hierarchical Porous Mn Doped CoP Catalyst on Nickel Phosphide Foam for Hydrogen Evolution Reaction," ACS Applied Energy Material, 5 (2022) 149-158.

7. Suchada Sirisomboonchai, Xiumin Li, **Nutthaphak Kitiphatpiboon**, Rinrada Channoo, Shasha Li, Yufei Ma, Suwadee Kongparakul, Chanatip Samart, Abuliti Abudula, Guoqing Guan, "Fabrication of CuO_x nanowires@$NiMnO_x$ nanosheets core@shell-type electrocatalysts: crucial roles of defect modification and valence state for overall water electrolysis", Journal of Materials Chemistry A, 8 (2020) 16463-16476.

8. Changlin Liu, Yang He, Xiaowei An, **Nutthaphak Kitiphatpiboon**, Xiao Du, Xiaogang Hao, Abuliti Abudula, and Guoqing Guan, "A poly(ether block amide) based solid polymer electrolyte for solid-state lithium metal batteries", Journal of Colloid & Interface Science, 630 (2023), 595-603.

9. Amar M. Patil, **Nutthaphak Kitiphatpiboon**, Xiaowei An, Xiaoqiong Hao, Shasha Li, Xiaogang Hao, Abuliti Abudula, and Guoqing Guan, "Fabrication of High Energy Flexible All-Solid-State Supercapacitor Using Pseudocapacitive 2D-

Ti$_3$C$_2$T$_x$-MXene and Battery-Type Reduced Graphene Oxide/Nickel-Cobalt Bimetal Oxide Electrode Materials," ACS Applied Materials & Interfaces,12 (2020) 52749–52762.

International presentations

1. **Kitiphatpiboon Nutthaphak**, Chen Meng, 阿布 里提,官 国清," Developing a dual-functional electrocatalyst for sustained seawater electrolysis" 12th International Conference on Environmental Catalysis (ICEC2022), 2022 年 7 月 30 日-2022 年 8 月 2 日(On line).

2. Amar M. Patil, Jiajia Wang, **Nutthaphak Kitiphatpiboon**, Xiyan Yue, Akihiro Yoshida, Abuliti Abudula, Guoqing Guan, "Bilateral growth of monoclinic tungsten oxide and 2D Ti$_3$C$_2$T$_x$-Mxene on3D free-standing multilayer hollow graphene foam for flexible all-solid-state pseudocapacitor," PRiME 2020, Hawii, USA, October 4-9, 2020 (On line).

3. Suchada Sirisomboonchai, Rinrada Channoo, **Nutthaphak Kitiphatpiboon**, Akihiro Yoshida, Suwadee Kongparakul, Chanatip Samart, Abuliti Abudula, Guoqing Guan, "In-situ construction of 3D core-shell structure on Cu foam electrode for driven hydrogen production via overall water splitting," The Pure and Applied Chemistry International Conference 2020 (PACCON 2020), February 13th – 14th, 2020 in Bangkok, Thailand.

Domestic presentations

1. **Kitiphatpiboon Nutthaphak**, Chen Meng, 阿布 里提,官 国清,"Highly durable S-NiFe(OH)$_x$ electrocatalyst for oxygen evolution reaction in alkaline seawater at high current density" 令和 4 年度化学系学協会東北大会, 岩手大学 2022 年 9 月 17-18 日.

2. **Kitiphatpiboon Nutthaphak**, Chen Meng, 阿布 里提,官 国清," Development of novel electrocatalysts for highly-efficient seawater splitting" 11th JACI/GSC SYMPOSIUM, 2022 年 6 月 15-16 日(On line).

3. **Kitiphatpiboon Nutthaphak**, Chen Meng, 阿布 里提,官 国清,"Hierarchical NiFe- LDH@MnCo$_2$O$_4$ electrocatalyst for oxygen evolution reaction in electrolysis of imitate seawater" 化学工学会第 87 年会(神戸), 2022 年 3 月 16-18 日(On line).

4. **Kitiphatpiboon Nutthaphak**, Chen Meng, 阿布 里提,官 国清,"NiFeS$_x$/NF nanosheets as electrocatalysts for oxygen evolution reaction" 化学工学会秋田大会、2021 年 7 月 1 日（On-line）.

5. **Kitiphatpiboon Nutthaphak**, Sirisomboonchai Suchada, Chen Meng, Yu Tao, Yoshida Akihiro, Abuliti Abudula, Guan Guoqing "Designing Ni$_3$S$_2$@NiCo nano-grasses with core-shell structure for accelerating oxygen evolution reaction" 化学工学会第 86 年会、2021 年 3 月 20-22 日(On line).

6. Sirisomboonchai Suchada, **Kitiphatpiboon Nutthaphak**, Chen Meng, Yu Tao, Yoshida Akihiro, Abuliti Abudula, Guan Guoqing "Nanostructured CoMnP/P-NF electrocatalysts with long-duration for hydrogen evolution reaction" 化学工学会第 86 年会、2021 年 3 月 20-22 日(On line).

7. **Kitiphatpiboon Nutthaphak**, Sirisomboonchai Suchada, Akihiro Yoshida, Abuliti Abudula, Guoqing Guan "Fabrication of Ni-Cu mixed oxide with three-dimensional flower bush-like structure on carbon paper　for hydrogen evolution reaction" 令和 2 年度化学系学協会東北大会, 八戸, 2020 年 9 月 26-27 日（On-line）.

8. **Kitiphatpiboon Nutthaphak**, Sirisomboonchai Suchada, Patil Amar, Yu Tao, Yoshida Akihiro, Abuliti Abudula, Guan Guoqing "Facile synthesis of NiO-CuO/CP electrocatalysts with 3D architecture for Hydrogen Evolution Reaction" 化学工学会第 51 回秋季大会、岩手大学、2020 年 9 月 24-26 日(On line).

9. Sirisomboonchai Suchada, **Kitiphatpiboon Nutthaphak,** Patil Amar, Yu Tao, Yoshida Akihiro, Abuliti Abudula, Guan Guoqing "Fabrication of defect-rich Cu nanowire@bimetallic oxides with core@shell structure as electrocatalysts for oxygen evolution reaction" 化学工学会第 51 回秋季大会、岩手大学、2020 年 9 月 24-26 日(On line).

List of Patents

1. **ナッタパック・ギティパットピブーン**、官国清、陳萌、関和治、阿布里提、"酸素発生電極及びその製造方法、並びに酸素発生電極及び水の電気分解方法"、日本特許、出願番号：特願 2022-022392、出願日：2022 年 2 月 16 日

2. **ナッタパック　ギティパットピブーン**、官国清、陳萌、関和治、阿布里提、"電極触媒、酸素発生電極及び水の電気分解方法"、日本特許、出願番号：特願 2021-25200、出願日：2021 年 7 月 30 日.

3. **ナッタパック　ギティパットピブーン**、官国清、陳萌、関和治、阿布里提、"新規酸素発生電極"、日本特許、出願番号：特願 2021-123675、出願日：2021 年 7 月 28 日.

4. **ナッタパック　ギティパットピブーン**、 官国清, シリソムブンチャイ　スチャダ, 関和治, 阿布里提, "電極触媒及びその製造方法、並びに水素の製造方法", 出願番号：特願 2020-172736, 出願日：2020 年 10 月 13 日.

5. 陳萌、官国清、**ナッタパック　ギティパットピブーン**、関　和治、阿布里提、"酸素発生電極、水の電気分解方法及び酸素発生電極の製造方法、"出願番号：特願 2022-062000、出願日：2022 年 4 月 1 日.

6. 陳萌、官国清、**ナッタパック　ギティパットピブーン**、関　和治、阿布里提、"電極触媒及びその製造方法、"出願番号：特願 2021-093897、出願日：2021 年 6 月 3 日.